Western Graduate&PostdoctoralStudies

Western University
Scholarship@Western

Electronic Thesis and Dissertation Repository

4-12-2018 10:00 AM

A numerical tool for predicting the spatial decay of freestream turbulence.

Dwaipayan Sarkar
The University of Western Ontario

Supervisor
Savory, Eric
The University of Western Ontario

Graduate Program in Mechanical and Materials Engineering
A thesis submitted in partial fulfillment of the requirements for the degree in Master of Engineering Science
© Dwaipayan Sarkar 2018

Follow this and additional works at: https://ir.lib.uwo.ca/etd

Part of the Other Mechanical Engineering Commons

Recommended Citation

Sarkar, Dwaipayan, "A numerical tool for predicting the spatial decay of freestream turbulence." (2018). *Electronic Thesis and Dissertation Repository*. 5331.
https://ir.lib.uwo.ca/etd/5331

This Dissertation/Thesis is brought to you for free and open access by Scholarship@Western. It has been accepted for inclusion in Electronic Thesis and Dissertation Repository by an authorized administrator of Scholarship@Western. For more information, please contact wlswadmin@uwo.ca.

Abstract

The present numerical work is an attempt towards modelling of freely decaying homogeneous isotropic turbulence with its application in experimental modelling of the effect of incident turbulence on flow around 2D and 3D bluff-bodies. Both steady, Reynolds Averaged Navier Stokes (RANS) and unsteady, Large Eddy simulation (LES), 3-D numerical computational fluid dynamics (CFD) techniques have been employed to characterise the inviscid decay of large-scale turbulence in terms of the characteristic rms turbulent velocity fluctuations (u') and the local integral length scale (L_u). The large-scale turbulent properties extracted from the current numerical simulations are inter-related and are shown to behave predominantly as Saffman turbulence, which states $\overline{u'^2}L_u^3 \approx$ constant. The other focus from the current study was on modelling inlet conditions for bluff-bodies in a freestream flow. A set of three-correlation equations are formulated based on the large-scale turbulent properties that are effective in estimating the initial and local freestream turbulence conditions. The set of prediction equations can be deemed useful for researchers developing wind-tunnel models in the presence of freestream turbulence. Additionally, the set of equations is also reliable in determining appropriate near-constant turbulent conditions based on the upstream inlet conditions. The current study aims at designing the region of constant turbulent properties of a desired magnitude that can be helpful for boundary layer and heat transfer studies over a bluff-body.

Keywords

Homogeneous, Isotropic, Reynolds Averaged Navier-Stokes (RANS), Large Eddy Simulation (LES), Decay, Computational Fluid Dynamics (CFD), Freestream turbulence, Bluff-body

Co-Authorship Statement

This thesis has been prepared in accordance with the regulations for an Integrated-Article format thesis, as stipulated by the School of Graduate and Postdoctoral studies at The University of Western Ontario. This thesis includes co-authored articles and the following passages explicitly state the contributors, and the nature and extent of their contribution.

Chapter 2: Numerical modelling of spatially decaying isotropic homogeneous turbulence

The simulations conducted for this study were designed and carried out by D. Sarkar, with the assistance of E. Savory. The text was primarily written by D. Sarkar with guidance from E. Savory. All comparisons with literature were done by D. Sarkar, while the derivation of the decay correlation was provided by E. Savory.

Chapter 2 will be submitted for publication under the co-authorship of Sarkar, D and Savory, E.

Chapter 3: Comparison of RANS modelling against LES and experimental measurements of spatially decaying isotropic homogeneous turbulence

The simulations performed for this study were carried out by D. Sarkar, with recommendations from E. Savory. All the data processing was performed by D. Sarkar, with guidance from E. Savory. The first draft of the text was written by D. Sarkar, whilst E. Savory contributed to the final version of the manuscript by providing important comments and providing recommendations for editing the text.

Chapter 3 will be submitted for publication under the co-authorship of Sarkar, D and Savory, E.

Acknowledgments

First and foremost, I would like to express my sincere gratitude to my research supervisor Dr. Eric Savory, who has been very supportive throughout the completion of the thesis with his patience, valuable knowledge, feedback and constant encouragement throughout the course of my MESc. program. This has helped me a lot to develop my learning and understanding skills. I am thankful to him for providing me opportunities whilst allowing the room to work in my own way. Professor Savory has always been available for constructive discussions on my research and different other topics. Almost every time, I met him, I learned something new. His advice on different avenues of research, as well as on my approach to graduate studies in general, has been of great value over the past two years and I truly am grateful to all the supports provided by him. I would also like to thank my thesis advisory committee Professor Anthony Straatman and Professor Kamran Siddiqui. They have helped the progression of the thesis by providing new research insights and different perspective of the research outcomes.

I would also like to acknowledge the support, I received from my colleagues in the Advanced Fluid Mechanics Group. They have been very supportive throughout my research progression and always been available for discussion. I am also grateful to Dr. Shady Ali who helped me a lot to get familiar with the different commercial CFD codes and was supportive while working on the CFD simulations.

I would like to thank the Shared Hierarchical Academic Research Computing Network (www.sharcnet.ca) and Compute/Calcul Canada for their facilities.

I would also like to acknowledge the financial support I received from the department of Mechanical and Materials Engineering at Western University and Natural Sciences Engineering Research council discovery (NSERC) discovery grants.

Last but not the least; I owe my thanks to my parents Dulal Chandra Sarkar and Luna Sarkar. Without their mental support and constant encouragement, it would not have been possible for me to finish this work.

Table of Contents

Abstract i

Co-Authorship Statement ii

Acknowledgments iii

Table of Contents iv

List of Tables viii

List of Figures x

List of Appendices xviii

List of Abbreviations, Symbols, and Nomenclature xix

Chapter 1 1

1 Introduction 1

1.1 General Introduction 1

1.1.1 Grid-generated turbulence decay 7

1.2 Objective of the Thesis 9

1.3 Scope of the Thesis 10

1.4 Thesis layout 11

1.5 Summary 12

References 14

Chapter 2 20

2 Numerical modelling of spatially decaying isotropic homogeneous turbulence 20

2.1 Background 20

2.2 Introduction 27

2.3 Computational Domain 28

2.4 Grid generation 29

2.5 Methodology 30

2.5.1 Solver 30

2.5.2 Turbulence Models 31

2.5.3 Governing equations 32

2.5.4 Shear Stress Transport k-ω model 35

2.5.5 Large Eddy Simulation 38

2.5.6 Dynamic Smagorinsky-Lilly Model 40

2.5.7 Solution Parameters 42

2.6 Boundary Conditions 45

2.6.1 Boundary conditions for Steady Reynolds Averaged Navier-Stokes Model (RANS) 45

2.6.2 Inflow and Boundary conditions for Large Eddy Simulation (LES) 45

2.7 Flow Characteristics at the Inlet 46

2.7.1 Isotropy 47

2.7.2 Probability Density Function 51

2.7.3 Inertial sub-range of Spectral Energy Transfer 54

2.8 Model Convergence 55

2.8.1 Grid-Independence Test 55

2.8.2 Homogeneity and Isotropy of the velocity fields (LES) 61

2.8.3 Batchelor Turbulence or Saffman Turbulence? 67

2.8.4 Influence of the Time-Step Size 70

2.9 Comparison with previous studies (Validation of the CFD model) 74

2.9.1 Predictive methods for spatial decay of turbulent kinetic energy (TKE) . 79

2.9.2 Set of prediction correlation equations 98

2.9.3 Sensitivity of the virtual origin (x_0) 100

2.9.4 Identification of nearly constant TKE conditions 105

2.9.5 Influence of the different Reynolds number, integral length scales and turbulence intensities on the spatial decay rate of TKE 108

2.10 Summary 119

2.11 Conclusion 121

References 123

Chapter 3 133

3 Comparison of RANS modelling against LES and experimental measurements of spatially decaying isotropic homogenous grid-generated turbulence 133

3.1 Introduction 133

3.2 Comparison between different commercial CFD codes against the spatial decay of isotropic homogeneous turbulence 135

3.3 Investigation of the differences between the solver (FLUENT, STAR-CCM+ and CFX) results 137

3.3.1 Limitations of the RANS based CFD solvers 139

3.4 Generic optimized SST-k-ω model for FLUENT, STAR-CCM+ and CFX 141

3.4.1 New optimized SST-k-ω models for FLUENT 141

3.4.2 New optimized SST-k-ω models for STAR-CCM+ 144

3.4.3 New optimized SST-k-ω models for CFX 145

3.5 Applicability of the proposed generic SST-k-ω model for varying initial conditions 147

3.5.1 Applicability of the improved SST-k-ω model in predicting the turbulence decay for varying turbulence intensities at the inlet 147

3.5.2 Applicability of the improved SST-k-ω in predicting the turbulence decay model for varying integral length scales at the inlet 149

3.6 Boundary layer validation for new optimized SST-k-ω model 151

3.6.1 Introduction 151

3.6.2 Computational domain 152

3.6.3 Grid-generation 153

3.6.4 Methodology 153

3.6.5 Boundary conditions 156

3.6.6 Grid-Independence study 156
3.6.7 Boundary layer validation 163
3.7 Summary 174
3.8 Conclusion 175
References 176
Chapter 4 179
4 Conclusions and Recommendations 179
4.1 Conclusions 179
4.2 Contributions 181
4.3 Recommendations 182
References 183
Appendix A 184
Appendix B 188
Appendix C 195
Appendix D 207
Appendix E 210
Appendix F 212
Curriculum Vitae 215

List of Tables

Table 2.1 Spanwise and normal variation of the root-mean square of the velocity fields at the inlet with initial condition of $\overline{U}$ = 4m/s, TI =10% and L_u =0.1m 49

Table 2.2 Percentage variation of root-mean square velocities at the inlet plane..... 50

Table 2.3 Comparison between probability density function and normal distribution..... 52

Table 2.4 Properties of the different grids used in the current study 56

Table 2.5 Grid independence study on three different grids for steady RANS predicting the turbulent kinetic energy decay along the streamwise distance 58

Table 2.6 Grid independence study on three different grids for steady RANS predicting the growth of integral length scales along the streamwise centreline..... 58

Table 2.7 Grid independence study on three different grids for LES simulations predicting the turbulence kinetic energy decay at 11 points along the streamwise centreline 61

Table 2.8 Grid independence study on three different grids for LES predicting the growth of integral length scales at 11 points along the streamwise centreline..... 61

Table 2.9 Spanwise and normal variation of the root-mean square of the streamwise velocity fields at the centre plane ($\overline{U}$ = 4m/s, TI = 10% and L_u = 0.10m) 65

Table 2.10 Overview of performed simulations on the time-step independence 70

Table 2.11 Summary of the virtual origin location (x_0) with respect to the physical grid location for both experimental results of Kang *et al.* (2003) and LES 76

Table 2.12 Initial TKE and length scale magnitudes for experimental data of Kang *et al.* (2003) and the present LES study..... 77

Table 2.13 Summary of the virtual origin location (x_0) with respect to the physical grid location obtained from earlier relevant experimental data 84

Table 2.14 Constants obtained from best regression curve fitting procedure to equations 2.49 and 2.50 using the method of Non-linear least squares 99

Table 2.15 Constants obtained from best regression curve fitting procedure to equation 2.60 using the method of Non-linear least squares 99

Table 2.16 Constants obtained from best regression fit curve procedure using the method of Non-linear Least Squares (shift in virtual origin) 104

Table 2.17 Constants obtained from best regression fit curve procedure using the method of Non-linear Least Squares (shift in virtual origin) 104

Table 3.1 Non-dimensional distances of the four different locations along the centreline of the plate 159

Table 3.2 Comparison between the dimensionless momentum thickness, displacement thickness and the shape factor obtained from the improved SST-k-ω model and the theoretical laminar velocity profiles 168

Table 3.3 Comparisons between the dimensionless velocity shape factor obtained from the improved SST-k-ω model and the theoretical turbulent velocity profiles 173

List of Figures

Figure 1.1 A schematic of a typical air-based open loop BIPV/T system (adapted from Athienitis, 2008). 1

Figure 1.2 Pictorial representation of a turbomachine and downstream airfoil components ("Rolls Royce Infographic" 2014) 2

Figure 1.3 A schematic of the oncoming wind flow over a flat plate 3

Figure 1.4 Turbulence generating grid having circular rods of diameter d and mesh width M (adapted from Pope (2000)) 7

Figure 1.5 Schematic representation of the turbulence generating grid with wake vortices being convected along the streamwise direction. The virtual origin (x_0) is shown to be point where turbulence roughly re-organizes itself and complete mixing between the turbulent structures has taken place 8

Figure 1.6 A schematic of the decay of turbulent kinetic energy in the streamwise distance x 9

Figure 2.1 Schematic of the 3D computational domain with specific boundary conditions .. 29

Figure 2.2 A schematic of the hexahedral grid distribution over the entire computational domain 30

Figure 2.3 Comparisons between different RANS turbulence models showing the decay of TKE in the streamwise direction (FLUENT simulations). 35

Figure 2.4 Comparison between the 1st order and 2nd order discretization schemes of the SST k-ω model with respect to the spatial decay of TKE ($\overline{U}$ = 4m/s, TI = 10% and L_u = 0.10m) 43

Figure 2.5 Skewness coefficient of the streamwise velocity component obtained from LES simulations with an initial condition of $\overline{U}$ = 4m/s, TI = 10% and L_u = 0.10m 48

Figure 2.6 Transverse distribution of turbulence intensity laterally across the inlet plane obtained from LES simulations with an initial condition of $\overline{U}$ = 4m/s, TI = 10% and L_u = 0.10m 50

Figure 2.7 Normal Distribution of turbulence intensity vertically across the inlet plane obtained from LES simulations with an initial condition of $\overline{U}$ = 4m/s, TI = 10% and L_u = 0.10m 51

Figure 2.8 Kurtosis function of the streamwise velocity component obtained from LES simulations with an initial condition of $\overline{U}$ = 4m/s, TI = 10% and L_u = 0.10m..... 53

Figure 2.9 Probability density function plotted against the normal Gaussian distribution normalized by mean velocity ($\overline{U}$ = 4m/s, TI = 10% and L_u = 0.10m)..... 53

Figure 2.10 Turbulent kinetic energy spectra at the inlet plane plotted with a reference line of slope (-5/3) representing Kolmogorov decay ($\overline{U}$ = 4m/s, TI = 10% and L_u = 0.10m) 55

Figure 2.11 Comparison of streamwise decay of non-dimensional TKE for coarse, medium and finer mesh (Steady RANS) ($\overline{U}$ = 4m/s, TI = 10% and L_u = 0.10m) 57

Figure 2.12 Comparison of streamwise evolution of length scales for coarse, medium and finer grids (Steady RANS) ($\overline{U}$ = 4m/s, TI =10% and L_u = 0.10m) 57

Figure 2.13 Comparison of streamwise decay of non-dimensional TKE for coarse, medium and fine grids (LES) ($\overline{U}$ = 4m/s, TI = 10% and L_u = 0.10m) 59

Figure 2.14 Comparison of streamwise evolution of length scales for coarse, medium and finer grids (LES) ($\overline{U}$ = 4m/s, TI =10% and L_u = 0.10m)..... 60

Figure 2.15 Streamwise distribution of $\overline{U}$ along the centreline normalized by the mean velocity at the inlet i.e. U_0 ($\overline{U}$ = 4m/s, TI = 10% and L_u = 0.10m) 62

Figure 2.16 Streamwise distribution of turbulent Reynolds number (Re_λ) based on Taylor microscale along the centreline ($\overline{U}$ = 4m/s, TI = 10% and L_u = 0.10m) 64

Figure 2.17 Downstream variation of velocity skewness S(u) along the centreline of the domain ($\overline{U}$ = 4m/s, TI = 10% and L_u = 0.10m) 66

Figure 2.18 Downstream variation of Kurtosis coefficient, K(u) along the centreline of the domain ($\overline{U}$ = 4m/s, TI = 10% and L_u = 0.10m) 67

Figure 2.19 Downstream variation of $\overline{u'^2}L_u^5$ along the centreline of the domain ($\overline{U}$ = 4m/s, TI = 10% and L_u = 0.10m) 69

Figure 2.20 Downstream variation of $\overline{u'^2}L_u^3$ along the centreline of the domain ($\overline{U}$ = 4m/s, TI = 10% and L_u = 0.10m) 69

Figure 2.21 Influence of the time-step size on the profiles of normalized mean velocity component at different locations along the centreline ($\overline{U}$ = 4m/s, TI = 10% and L_u = 0.10m) 71

Figure 2.22 Influence of the time step size on the streamwise turbulent kinetic energy spectrum at the inlet ($\overline{U}$ = 4m/s, TI = 10% and L_u = 0.10m) 72

Figure 2.23 Influence of the time-step size on the profiles of integral length scales at different locations along the centreline ($\overline{U}$ = 4m/s, TI = 10% and L_u = 0.10m) 73

Figure 2.24 Influence of the time-step size on the TKE decay along the centreline in the streamwise direction ($\overline{U}$ = 4m/s, TI = 10% and L_u = 0.10m) 74

Figure 2.25 Comparison of decay of TKE in the streamwise direction between Kang *et al.* (2003) and the present LES results. 78

Figure 2.26 Physical distances of the virtual origin(x_0) with respect to the physical grid location plotted against the ratio of physical grid element size (M/d), for all the experimental studies of Kang *et al.* (2003); Krogstad & Davidson (2011); Torrano *et al.* (2015) 85

Figure 2.27 Quantitative comparisons of the spatial decay of TKE profiles between earlier experimental studies and the present LES study..... 86

Figure 2.28 Spatial decay of TKE profiles of earlier experimental studies and present LES study, scaled with local integral length scale (L_u) plotted with a solid line that shows the best fit power law 87

Figure 2.29 Spatial decay of TKE profiles for different experiments and the present LES study scaled with initial integral length scale (L_{u0}) plotted with a solid line that shows the best fit power law 88

Figure 2.30 Comparison of the dissipation rate of turbulent kinetic energy computed as: $\varepsilon_q = \frac{1}{2}\bar{U}\frac{\overline{du'^2}}{dx}$) ; $\varepsilon_{iso} = 15\nu\frac{\overline{u'^2}}{\lambda^2}$ ($\bar{U}$ = 4m/s, TI = 10% and L_u = 0.10m) 92

Figure 2.31 Ratio of the dissipation rate of turbulent kinetic energy, $\frac{\varepsilon_{iso}}{\varepsilon_q}$ ($\bar{U}$ = 4m/s, TI = 10% and L_u = 0.10m) 93

Figure 2.32 Streamwise distribution of D along the centreline of the domain obtained from $D_q = \frac{\varepsilon_q}{(u')^3 / L_u}$ and $D_{iso} = \frac{\varepsilon_{iso}}{(u')^3 / L_u}$ 94

Figure 2.33 Variation of the dimensionless dissipation constant D along the streamwise distance of the domain plotted to compare with the variation of the turbulent Reynolds number (R_λ) along the same direction 96

Figure 2.34 Spatial decay of TKE profiles for different experiments and the present LES data with the x abscissa scaled with local k and L_u plotted with a sold line that shows the best fit linear curve 98

Figure 2.35 Spatial decay of TKE profiles for different experiments and the present LES study scaled with local integral length scale (L_u) with a different choice of virtual origin (x_0) plotted with a solid line that shows the best fit power law 101

Figure 2.36 Spatial decay of TKE profiles for different experiments and the present LES study scaled with initial integral length scale (L_{u0}) with a different choice of virtual origin(x_0) plotted with a solid line that shows the best fit power law 102

Figure 2.37 Spatial decay of TKE profiles for different experiments and the present LES study scaled with local TKE (k) and local integral length scale (L_u), with a different choice of virtual origin(x_0) plotted with a solid line that shows the best fit power law 103

Figure 2.38 Spatial decay of TKE profile (LES) plotted against the streamwise distance x ($\overline{U}$ = 4m/s, TI = 10% and L_u = 0.10m) 107

Figure 2.39 Rate of spatial decay of TKE profile (LES) along the streamwise distance x ($\overline{U}$ = 4m/s, TI = 10% and L_u = 0.10m) 107

Figure 2.40 Rate of spatial decay of TKE profile in the form of $d(k/k_0)/d((x-x_0)*(k_0')^{0.5}/L_u$ plotted against $(x-x_0)*(k_0')^{0.5}/L_u$ for all the experimental data and the LES results ($\overline{U}$ = 4m/s, TI = 10% and L_u = 0.10m) 108

Figure 2.41 Spatial decay of TKE profiles for different Reynolds number (Re) prescribed at the inlet (RANS) 110

Figure 2.42 Spatial decay of TKE profiles (RANS) for different integral length scales (L_u) prescribed at the Inlet 111

Figure 2.43 Spatial Decay of TKE profiles (RANS) for different turbulence Intensities prescribed at the Inlet 111

Figure 2.44 Spatial decay of TKE profiles (RANS) for different turbulence intensities and integral length scales plotted with a solid line that shows the best fit power law 112

Figure 2.45 Spatial decay of TKE profiles for different integral length scales (L_u) prescribed at the inlet (LES) 113

Figure 2.46 Spatial decay of TKE profiles for different turbulence intensities at the inlet (LES) 114

Figure 2.47 Downstream variation of $\overline{u'^2}L_u^3/\overline{U^2}L_{u0}^3$ along the centreline of the domain (LES) 114

Figure 2.48 Spatial decay of TKE profiles for different Turbulence Intensities and Integral length scales plotted with a solid line that shows the best fit power law..... 115

Figure 2.49 Spatial decay of TKE profiles for different turbulence intensities and integral length scales compared with the relevant experimental results plotted with a solid line that shows the best fit power law..... 117

Figure 2.50 Spatial decay of TKE profiles for different inlet turbulence intensities (TI) and integral length scales (L_u) along the streamwise distance x 118

Figure 2.51 Rate of spatial decay of TKE profiles for different inlet turbulence intensities (TI) and integral length scales (L_u) along the streamwise distance x 119

Figure 3.1 Spatial decay of TKE profiles obtained from three different commercial codes (FLUENT, STAR-CCM+ and CFX) compared with the LES and the previous experimental studies 136

Figure 3.2 Spatial decay of TKE profiles obtained from the different optimized SST-k-ω RANS model compared with the LES and the earlier experimental studies, (FLUENT simulations)..... 142

Figure 3.3 Spatial decay of TKE profiles obtained from the different optimized SST-k-ω RANS model compared with the LES and the earlier experimental studies, (FLUENT simulations)..... 143

Figure 3.4 Spatial decay of TKE profiles obtained from the different optimized SST-k-ω RANS model compared with the present LES study along the streamwise distance x (FLUENT simulations)..... 144

Figure 3.5 Spatial decay of TKE profiles obtained from the different optimized SST-k-ω RANS model compared with the present LES and the earlier experimental studies (STAR-CCM+ simulations)..... 145

Figure 3.6 Spatial decay of TKE profiles obtained from the different optimized SST-k-ω RANS model compared with the LES and the earlier experimental studies, (CFX simulations)..... 146

Figure 3.7 Spatial decay of TKE profiles from different optimized SST-k-ω model compared with the LES and the earlier experimental studies (TI = 20%, L_{u0} = 0.1m) 148

Figure 3.8 Spatial decay of TKE profiles from different optimized SST-k-ω model compared with the LES and the earlier experimental studies (TI = 20%, L_{u0} = 0.1m) 148

Figure 3.9 Spatial decay of TKE profiles from different optimized SST-k-ω model compared with the LES and the earlier experimental studies (TI = 30%; L_{u0} = 0.1m) 149

Figure 3.10 Spatial decay of TKE profiles obtained from optimized SST-k-ω model compared with the LES and the earlier experimental studies (TI = 10%; L_{u0} = 0.1m) 150

Figure 3.11 Spatial decay of TKE profiles obtained from optimized SST-k-ω model compared with the LES and the earlier experimental studies (TI = 10%; L_{u0} = 0.05m) 150

Figure 3.12 Spatial decay of TKE profiles obtained from the optimized SST-k-ω model compared with the LES and the earlier experimental studies (TI= 10%; L_{u0} = 0.02m) 151

Figure 3.13 Schematic of the computational domain with the plate along with the relevant boundary conditions 152

Figure 3.14 Local skin-friction profiles plotted for three different grids measured along the centreline of the plate 158

Figure 3.15 Schematic of the flat plate showing the location of four different measurement points along the centreline of the plate 159

Figure 3.16 Normalized velocity profile plotted for three different grids along the centreline of the plate at x = 2.0m (right) and x = 2.5m (left) 160

Figure 3.17 Normalized velocity profile plotted for three different grids along the centreline of the plate at x = 1.0m (right) and x = 1.5m (left) 161

Figure 3.18 Local skin-friction profiles plotted for three different grids measured along the centreline of the plate 162

Figure 3.19 Normalized velocity profile plotted for three different grids along the centreline of the plate at x = 2.0m (right) and x = 2.5m (left) 163

Figure 3.20 Comparison of the local skin-friction profiles obtained from the standard and the improved SST-k-ω model plotted against the theoretical laminar skin-friction profiles, measured along the centreline of the plate 164

Figure 3.21 Normalized velocity profile obtained from the standard and the improved SST-k-ω model plotted against the theoretical laminar velocity profiles, measured along the centreline of the plate at x = 2.0m (right) and x = 2.5m (left) 166

Figure 3.22 Normalized velocity profile obtained from the standard and the improved SST-k-ω model plotted against the theoretical laminar velocity profiles, measured along the centreline of the plate at x = 1.0m (right) and x = 1.5m (left) 167

Figure 3.23 Normalized velocity profile obtained from the standard and the improved k-kl-ω model plotted against the theoretical turbulent velocity profiles, measured along the centreline of the plate at x = 2.0m (right) and x = 2.5m (left) 171

Figure 3.24 Plot of normalized velocity profile in the logarithmic form obtained from the standard and the improved k-kl-ω model measured at x = 2.5m 172

Figure 3.25 Plot of normalized velocity profile in the logarithmic form obtained from the standard and the improved k-kl-ω model measured at x = 2.0m 172

Figure 3.26 Comparison of the local skin-friction profiles obtained from the standard and the improved k-kl-ω model plotted against the theoretical turbulent skin-friction profiles, measured along the centreline of the plate 174

List of Appendices

Appendix A - Solution method of the linear dependency of (k/k_0) with $(x-x_0)*(k'_0)^{0.5}/L_u$ 184

Appendix B - Sample calculations to estimate the initial turbulent scales (k'_0) and L_{u0}) based on the local TKE (k) and the integral length scale (L_u)……188

Appendix C - Comparisons between three different commercial codes against the spatial decay of isotropic homogeneous turbulence……195

Appendix D - Near-wall treatment of boundary layer……207

Appendix E - Low Reynolds Number modelling approach……210

Appendix F - Governing equations of the k-kl-ω transitional model……212

List of Abbreviations, Symbols, and Nomenclature

Latin Symbols

a_1, c_1	SST-k-ω model constants that are used to compute the turbulent viscosity
A	Decay coefficient
c_f	Local skin-friction coefficient
c_p	Specific heat capacity of the fluid (J/kg-K)
C_μ	Turbulence model constant (β_∞^* for SST-k-ω model)
C_k, C_ε	Model constants for LES
C_s	Smagorinsky-Lilly constant
d	Diameter of the round-grid elements/Bar-width (m)
D	Dimensionless dissipation constant
D_ω	Cross -Diffusion term
D_ω^+	Positive portion of the cross-diffusion term
F_1, F_2	Blending functions for the SST-k-ω turbulence model
G_b	Generation of turbulent kinetic energy due to buoyancy
G_k	Generation of turbulent kinetic energy due to the mean velocity gradients
G_ω	Generation of ω

h	Convective heat-transfer coefficient
k	Turbulent kinetic energy (m^2/s^2)
$k^{'}$	Non-dimensional TKE
kl	Laminar kinetic energy (m^2/s^2)
k_P	Turbulent kinetic energy at centre point P of wall-adjacent wall (m^2/s^2)
k_{sgs}	Sub-grid scale kinetic energy (m^2/s^2)
L_s	Mixing-length for the sub-grid scales (m)
L_u	Integral length scale of an eddy (m)
L_x, L_y, L_z	Physical dimensions of the computational domain in x, y and z direction
M	Mesh-width (m)
n	Decay exponent
Nu	Nusselt number
P	Centre point of the wall adjacent wall
p	Pressure (Pa)
Pr	Prandtl number
Pr_t	Turbulent Prandtl number
Re_d	Reynolds number based on the grid-dimension d
Re_θ	Momentum-thickness Reynolds number

Re_L	Average Reynolds number based on the plate length in the streamwise direction
Re_{Lu0}	Turbulent Reynolds number based on the integral length scale at the inlet (L_{u0})
Re_t	Local turbulent Reynolds number
Re_X	Reynolds number based on the distance from the leading edge of the plate
Re_λ	Turbulent Reynolds number based on the Taylor length scale
R_k	Constant used in the low Reynolds number correction factor for the SST-k-ω model
S_1	Scalar measure of the deformation tensor
S_{ij}	Mean rate-of-strain rate tensor
S_k	User defined source term for turbulent kinetic energy
St	Stanton number
S_ε	User defined source term for turbulence dissipation rate
S_ω	User defined source term for turbulence specific dissipation rate
t	Flow time (s)
T_{pv}	Temperature of the photovoltaic panel (K)
T_{surr}	Temperature of the surroundings (K)
TI	Turbulence intensity in percentage (%)

Tu	Turbulence intensity in fraction
u_i	Velocity vector component along the i-th base coordinates (x direction)
u_j	Velocity vector component along the j-th base coordinates (y direction)
u^*	Boundary-layer friction velocity (m/s)
u, v, w	Velocity component in x, y, z direction (m/s)
u', v', w'	Root-mean square velocity fluctuations in x, y and z direction (m/s)
$u'(t), v'(t), w'(t)$	Time-dependent velocity fluctuations in x, y and z direction (m/s)
$\overline{u'u'}, \overline{v'v'}$	Reynolds normal stress components (m^2/s^2)
$\overline{u'v'}$	Reynolds shear stress component (m^2/s^2)
du/dy	Streamwise velocity gradient (s^{-1})
$\overline{U}$	Mean velocity (m/s)
$\vec{v}$	Velocity vector
x	Distance along the streamwise direction (m)
x_0	Virtual origin (m)
x_j	Cartesian coordinate component along the j-th base vector
X	Distance from the leading edge of the plate (m)
Y_k	Dissipation of k due to turbulence

Y_M	Contribution of the fluctuating dilatation in compressible turbulence to the overall dissipation rate
Y_ω	Dissipation of ω due to turbulence
y	Distance from the closest no-slip wall in the normal direction (m)
y_P	Distance (normal) of centre point P of wall-adjacent cell to the wall (m)
y^+	Dimensional wall normal distance

Greek symbols

α^*	Coefficient for Low-Reynolds number correction for the SST-k-ω turbulence model
α^*_∞, β_i	Constants used in computation of α^*
Δ	Local grid scale (m)
Δt	Time-step (s)
$\Delta x.\Delta y, \Delta z$	Grid-cell size (m)
ΔT	Temperature difference (K)
ε	Turbulent kinetic energy dissipation rate (m^2/s^3)
κ	Wave-number of an eddy/Von-Kármán constant
μ	Dynamic viscosity (N-s/m^2)
μ_t	Turbulent viscosity (N-s/m^2)
ν	Kinematic viscosity (m^2/s)

ρ	Density (kg/m^3)
λ	Taylor micro-length scale (m)
σ_{ij}	Stress tensor due to molecular viscosity (N/m^2)
σ_k	Turbulent Prandtl number of turbulent kinetic energy
σ_ε	Turbulent Prandtl number of turbulent dissipation rate
σ_ω	Turbulent Prandtl number of turbulent specific dissipation rate
ω	Specific dissipation rate of turbulent kinetic energy (s^{-1})
τ_{ij}	Sub-grid scale stresses (N/m^2)
τ_{kk}	Isotropic part of the sub-grid scale stresses (N/m^2)
δ	Boundary layer thickness (m)
θ	Momentum thickness (m)
$\sigma_n, \sigma_{k1}, \sigma_{k2}, \alpha_{\omega 1}, \alpha_{\omega 2}, \beta_n, \beta_1, \beta_2, \beta^*, \gamma_1, \gamma_2$	SST-k-ω model constants

Abbreviations

ABL	Atmospheric Boundary Layer
BIPV/T	Building Integrated Photo-voltaic/Thermal systems
CFD	Computational Fluid Dynamics
CFL	Courant–Friedrichs–Lewy condition
CHTC	Convective heat transfer coefficient

COST	European Cooperation in Science and Technology
DNS	Direct Numerical Simulation
LES	Large Eddy Simulation
LRC	Low Reynolds Number Correction
LRNM	Low Reynolds Number Modelling
PISO	Pressure-Implicit with Splitting of Operators
PV	Photovoltaic
PV/T	Photovoltaic/Thermal
RANS	Reynolds-Averaged Navier Stokes
RSM	Reynolds Stress Model
SIMPLE	Semi-Implicit Method for Pressure-Linked Equations
SST	Shear-Stress Transport
TKE	Turbulent Kinetic Energy
WF	Wall Function

Chapter 1

1 Introduction

1.1 General Introduction

The performance of thermally integrated solar panel systems e.g. (building integrated photo-voltaic thermal system (BIPV/T)) largely depends on the way the atmospheric wind interacts with these panels. It is mainly due to the surface roughness of the ground and abrupt bluff-body obstructions, that the incident wind profiles on these panels are highly intermittent, turbulent and fluctuating in nature. The exterior layer of a (BIPV/T) represents a smooth surface according to ASHRAE classification (ASHRAE (American Society of Heating Refrigerating and Air-Conditioning Engineers), 2009). Figure (1.1) is a schematic of the BIPV/T system and the heat transfer terms responsible for heat transfer over the panels.

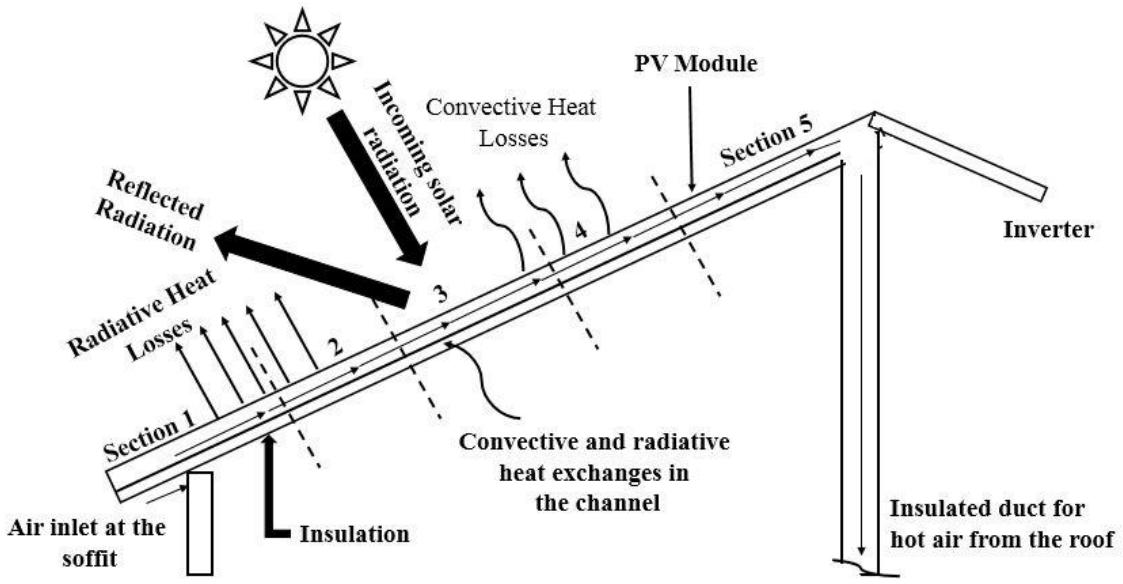

Figure 1.1 A schematic of a typical air-based open loop BIPV/T system (adapted from Athienitis, 2008).

Velocity and thermal boundary layers are formed at the immediate vicinity of the smooth surface at the onset of any fluid flow having different temperature than the surface

temperature. It is well known that boundary layers have a pronounced effect (drag, lift) upon any object immersed in a fluid and, in many cases, they govern the dynamics of the flow around three-dimensional bluff bodies, such as a cylinder (Geidt, (1951); Kestin & Maeder, (1957); Smith, (1964); Bearman & Morel, (1983)) or sphere (Moradian *et al.*, 2009). The effect of turbulent free stream fluctuations on the boundary layer development and its characterization is important in many thermal engineering applications such as turbomachinery, reactors and the combustion chamber of engines. There are a number of practical industrial situations where the boundary layers evolve differently in the presence of an external free stream having high turbulence intensities. A most common example is turbo-machinery flow where the wake of stators interacts with the downstream rotors whose developing boundary layers experience that oncoming turbulence (Fig 1.2). Similar flow patterns are also observed in heat exchanger and combustor flows. As far as these different objects are concerned, flat plates have the advantage of developing thicker boundary layers than those developing over rotor surface or spheres, whose structures can be analyzed, which makes it possible to consider the mechanisms responsible for the effect of turbulence on near wall heat transfer from these bodies (Kondjoyan *et al.* (2002)).

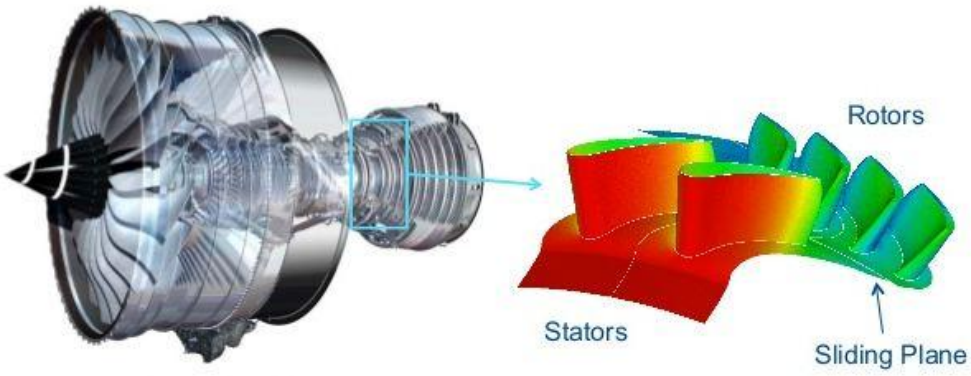

Figure 1.2 Pictorial representation of a turbomachine and downstream airfoil components ("Rolls Royce Infographic" 2014)

Figure (1.3) shows a schematic of the fundamental problem examined in this thesis where the oncoming flow interacts with the plate and alters the convective heat transfer rate

from it. In the figure, the term Re_L represents the Reynolds number of the flow based on the plate length L given by

$$Re_L = \frac{\overline{U}L}{\nu} \tag{1.1}$$

where $\overline{U}$ is the mean velocity of the flow, TI represents the turbulence intensity in percentage given by

$$(TI = \frac{\sqrt{\frac{1}{3}(\overline{u'^2} + \overline{v'^2} + \overline{w'^2})}}{\overline{U}} \times 100 \tag{1.2}$$

where u', v', w' are the r.m.s of the turbulent velocity fluctuations in each of the x, y and z directions), L_u represents the streamwise integral length scale of an eddy, TKE represents the turbulent kinetic energy, T_{surr} is the temperature of the surroundings , T_{pv} is the temperature of the photovoltaic thermal panel and BIPV/T represents building integrated photo-voltaic thermal system.

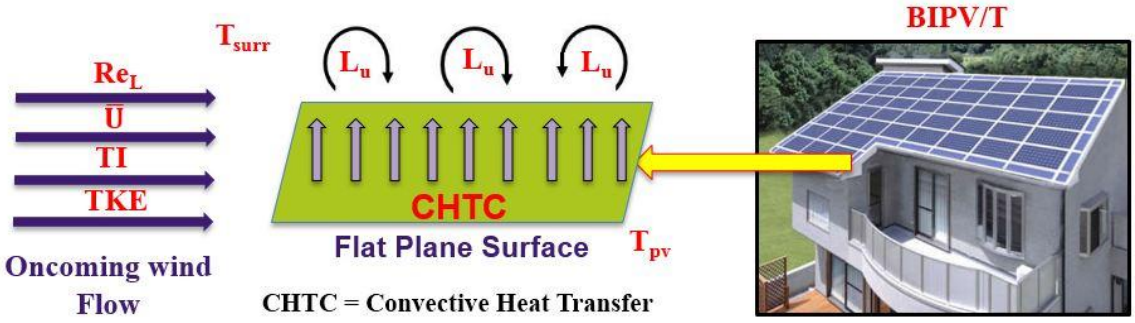

Figure 1.3 A schematic of the oncoming wind flow over a flat plate

The investigation of convective modes of heat transfer has been an important aspect in the empirical design of different geometrical structures under various external flow conditions (Wang & Peng (1994); Ambatipudi & Rahman (2000); Tian *et al.* (2004)). Convection coefficients determined analytically **(**Eckertf & Carlson, (1961); Foli *et al.*, (2006)) and empirically (Kestin *et al.*, (1961); Büyüktür *et al.*, (1964); Simonich & Bradshaw (1978)) exist for different geometries assuming simple boundary layer

approximations with negligible freestream turbulence levels and invariant properties of the fluid with temperature and pressure. The available correlations serve as a benchmark for problems of steady, incompressible, low-speed, uniform flows over simple systems such as smooth plane and curved surfaces. However, the correlations formulated include negligible disturbances of the freestream flow which cannot be extended to problems of a surrounding turbulent atmosphere.

For many years it has been recognized that the disturbances in the mean freestream flow can alter the heat transfer rate within the boundary layer. The freestream conditions can cause a change in the flow regime of the boundary layer and can also shift the position of the transition point upstream. Previous experimental studies have confirmed the augmentation in heat transfer from certain wall geometries (both plane and curved surfaces) in the presence of freestream turbulence in the mean flow (Fage and Falkner (1931); Comings *et al.* (1948); Edwards and Furber (1956); Reynolds *et al.* (1958); Van Der Hegge Zijnen, (1958); Sugawara *et al.* (1988)). Most of these studies have also been the subject of review articles (e.g. Kondjoyan *et al.* (2002)). However, due to a large scatter in the published results (Reynolds *et al.* (1958); Simonich and Bradshaw, (1978); Sugawara *et al.*, (1988); Maciejewski and Moffat, (1992)) on the effect of freestream turbulence on forced convective heat transfer, a fundamental challenge is presented to correctly predict the enhanced thermal dynamics in the laminar and turbulent region of a developing boundary layer. Earlier studies have reported that the velocity flow field in a boundary layer, alters significantly when there is an entrainment of the freestream turbulence into the boundary layer (Kline *et al.* (1960)**;** Charnay *et al.* (1976)). Studies have also shown that the thermal field is much more sensitive to the freestream turbulence than the dynamic field (Reynolds *et al.* (1958); Kondjoyan *et al.* (2002); Péneau *et al.* (2004)). A careful inspection of the previous studies leads to the fact that there were many discrepancies and contradictions involved in the reported findings, mainly due to the variability in the range of Reynolds number (Re), imprecise identification of an isotropic and homogeneous field of turbulent flows, different initial turbulent conditions and the influence of the different experimental set-ups used in those experiments.

The first experimental quantification of the effect of the freestream turbulence on a flat plate boundary layer was carried out by Fage and Falkner, (1931) who considered the laminar regime. Their study concluded that the laminar boundary layer mostly remains unperturbed by the freestream turbulence. Similar results were also reported by Edwards and Furber, (1956) who showed that that the oncoming turbulent flow had no effect on the rate of heat transfer for a laminar boundary layer but significantly relocated the transition point further upstream. However, studies by Dyban *et al.* (1977,1985) showed an increase in local skin-friction coefficient (c_f) (where c_f is the ratio between the local shear stress and the characteristic dynamic pressure given by $c_f = \frac{\tau_w}{0.5 * \rho * \overline{U}^2}$) by 56% at low Reynolds number flow (Re_L<20000) with a freestream turbulence (TI) of 12.5%, contradicting the aforementioned previous studies. Subsequently, numerous experimental studies (Simonich and Bradshaw, (1978); Sugawara *et al.*, (1988); Maciejewski and Moffat, (1992); have been carried out to understand the relationship between the heat transfer enhancement (expressed in terms of Stanton number (St) ,where Stanton number (St) is a dimensionless number given by the ratio of the heat transferred into the fluid to the thermal capacity of the fluid given by $St = \frac{h}{\rho \overline{U} c_p}$, where h is convective heat transfer coefficient, c_p is the specific heat capacity of the fluid) and the freestream turbulent fluctuations (TI) within the turbulent boundary layer regime. But there was a considerable variation in the magnitude of the heat transfer enhancement in each of those cases. The analysis of turbulent boundary layer skin friction (c_f) and heat transfer rate (St) by Blair, (1983a;1983b) showed that these effects were, indeed, a function of freestream turbulence intensity (TI), integral length scale (L_u) (where L_u gives the average size of an energy containing eddy) and Re_θ (where Re_θ is the momentum thickness Reynolds number given by $Re_\theta = \frac{\overline{U}.\theta}{\nu}$, θ is the momentum thickness of the boundary layer . New correlations for the effect of freestream turbulence on skin friction, heat transfer and the Reynolds analogy factor were also presented by Blair (1983a ;1983b), which will be later used in the future work for comparisons. A review by Kondjoyan *et al.*, (2002) concluded that despite the apparent contradictions, the heat transfer does increase consistently from

a turbulence level of 5% to 10% either in a laminar or turbulent boundary layer. The alterations of the velocity log law and the law of the wake may make it possible to explain a few of the disparities in the existing experimental results; Fage and Falkner, (1931); Charnay *et al*., (1976); Dyban *et al.*, (1977); Blair, (1983a; 1983b) Dyban *et al.*, (1985)). However, Palyvos, (2008) in his study pointed out the lack of generality of the existing heat transfer correlations relating Nusselt number (Nu), Reynolds number (Re) and Prandtl number (Pr) and concluded that there is an obvious lack of physical equivalence, because of the diverse experimental conditions under which they have been measured. Test and Lessmann, (1980) and Loveday and Taki, (1996) anticipated that the turbulence intensity (TI) of the approach flow might be one of the primary sources of some of the discrepancies between the experimental studies. Thus, the turbulent properties of the freestream flow approaching and passing the flat plate need to be quantified in order to begin to understand their influence on heat transfer rates from flat plates.

It is however, now well known that in absence of any external turbulent energy generating source, the freestream eddy fluctuations exhibit continuous decay of kinetic energy due to inertial eddy interactions at high Reynolds number. At low Reynolds number the decay occurs mostly due to the molecular viscosity of the eddies. Thus, the freestream turbulent kinetic energy (TKE) decay becomes an important factor of consideration before invoking any heat transfer study related to it, since its decay will have a direct effect on the evolution of the flow around any bluff body. It is hoped that quantifying the incidence TKE over the leading edge of a flat plate will help in precise estimation of the effect of freestream turbulence on boundary layer heat transfer in a comprehensive manner and thereby reconcile some of the differences observed in the earlier studies. Therefore, in the current study, attempts have been made to quantify the streamwise decay of the freestream turbulent fluctuations in order to identify a region of nearly uniform oncoming turbulent properties, so that any bluff body aerodynamics study can be suitably carried out under those constant TKE conditions.

1.1.1 Grid-generated turbulence decay

Stationary grids or perforated screens are often used to generate turbulence in typical wind-tunnel experiments where the Reynolds number ($Re_d = \frac{\overline{U}d}{\nu}$) based on the grid - dimension (d) is high enough (order of few hundreds) in magnitude. Grid-generated turbulence has served as a benchmark test case for turbulent theories and simulations over several decades and continues to do so in the present. Turbulence generated by grids decays downstream with a typical power-law of the form $TI = A*(\frac{x - x_0}{M})^{-n}$ (Batchelor and Townsend, (1948), Pope, (2000)) (where x is the streamwise distance, x_0 is the virtual origin, M is the mesh width, exponent n gives the decay rate and A gives the decay coefficient for a specific grid and Reynolds number (Re_d)). For a better understanding of the variables related to the power law form of the grid-generated turbulence, figures (1.4) and (1.5) have been shown which gives a clear visual representation of the grid elements and the importance of the virtual origin (x_0).

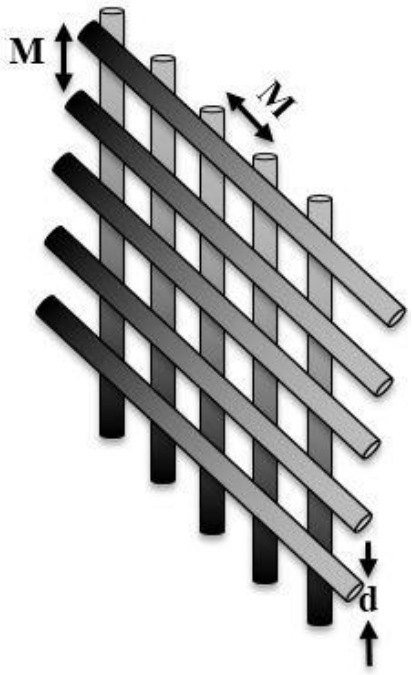

Figure 1.4 Turbulence generating grid having circular rods of diameter d and mesh width M (adapted from Pope (2000))

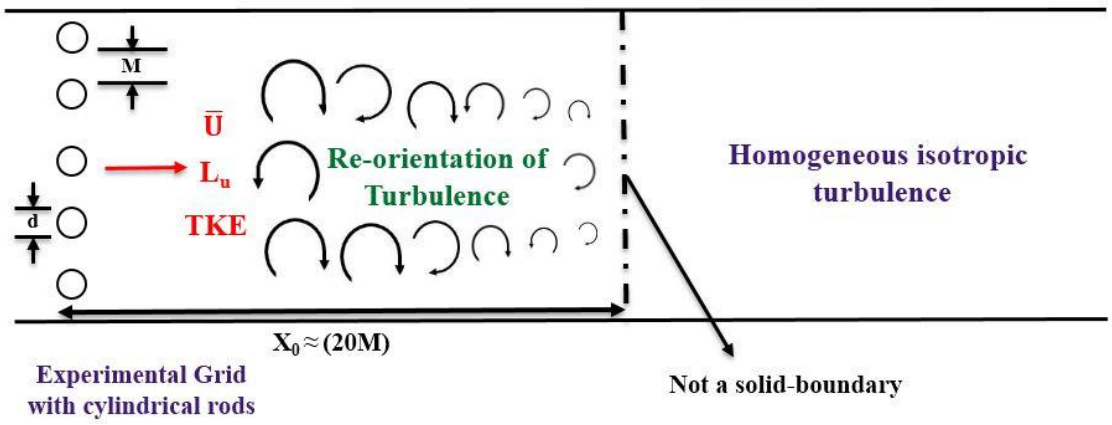

Figure 1.5 Schematic representation of the turbulence generating grid with wake vortices being convected along the streamwise direction. The virtual origin (x_0) is shown to be point where turbulence roughly re-organizes itself and complete mixing between the turbulent structures has taken place

However, it has been observed that different sets of geometrical grids introduce a variation in the magnitude of the exponent (n) of the kinetic energy decay that affects the structure of turbulence at small scales (Tan-atichat *et al.*, (1982); Lavoie *et al.*, (2005)). In recent years, numerous wind tunnel experiments have been focused on generating homogeneous turbulence by different type of grids; passive (Ishida *et al.*, (2006); Krogstad and Davidson, (2010)), active (Kang *et al.*, (2003); Mordant, (2008)) and multiscale (fractal) (Mazzi and Vassilicos, (2004), Seoud and Vassilicos, (2007), Hurst and Vassilicos, (2007), Krogstad and Davidson, (2011)). However, from this literature, concerning both numerical simulations and experiments, a marked scatter of the exponent (n) in the range (-1.0: -1.4) (Mohamed and Larue, 1990) is discovered which implies there may not be a universal state for grid turbulence decay.

It is very clear from the bluff body heat transfer studies mentioned above, that none of those studies commented on the streamwise decay of freestream turbulence prior to the bluff-body interaction (e.g. plate) nor do they discuss this issue while reporting the experimental setups or heat transfer results. As pointed out by Corrsin and Kistler, (1955), Townsend, (1956) and Mobbs, (1968), that turbulence intensity (TI), integral length scale ($L_{u)}$ and Reynolds number, are the three important parameters that should be

quantified accurately before making any correct predictions for any interacting turbulent mechanisms including convective heat transfer (CHTC) . Karava *et al.*, (2011) in their study tried to overcome the previous gaps and propose correlations for exterior convective heat transfer coefficient for flat plates and, hence, the present work is an implicit continuation of that study quantifying the effect of freestream decay before the leading-edge incidence occurs. A conceptual schematic is shown in (fig. 1.6) that illustrates the basic problem of the current investigation. The figure gives a perception of the decay of TKE in the streamwise direction for the comprehensive understanding of the reader.

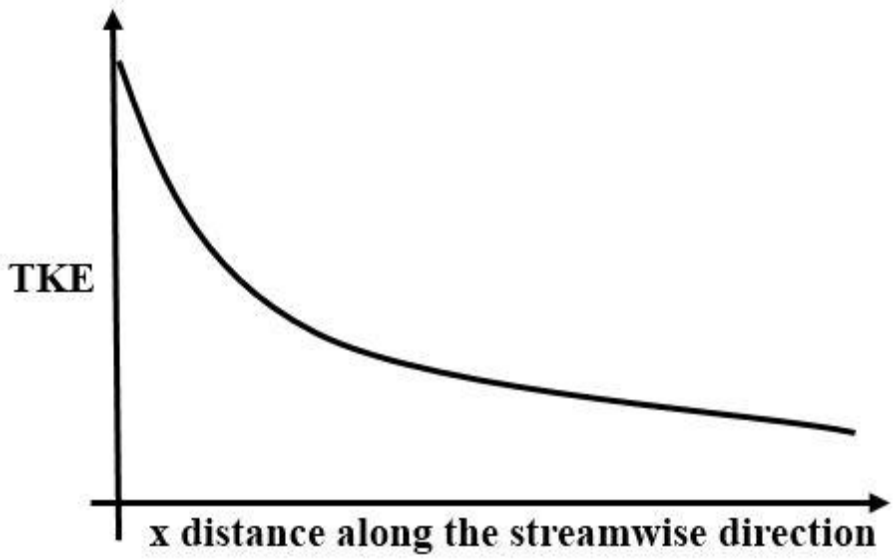

Figure 1.6 A schematic of the decay of turbulent kinetic energy in the streamwise distance x

1.2 Objective of the Thesis

The three main objectives of this thesis are: -

- To strengthen the understanding of the nature of the decay of the freestream turbulence in terms of various inlet freestream parameters (Re, L_u, TI) and to develop a simple predictive method for establishing leading edge TKE and L_u values for bluff-body aerodynamics based on specified upstream inlet conditions.

- To identify a region having negligible changes in the turbulent properties (such as TKE and the integral length scale) along the streamwise distance.

- To highlight the differences and limitations of the different numerical CFD formulations that are used as a computational tool to carry out the objectives and, finally, to optimise those numerical models (if required) to have the correct behaviour of turbulence decay.

However, it should be noted that this thesis only presents the objectives of the current study which in turn attempts to fill the gap prior to addressing a larger objective, which is to examine the influence of the freestream turbulence on convective heat transfer from heated flat plate. Heat transfer studies are currently in progress and the analysis of the results will form a part of future work.

In this research, three-dimensional (3D) based steady Reynolds Averaged Navier Stokes (RANS) and unsteady Large Eddy Simulation (LES) formulations have been employed to numerically predict the statistical properties of turbulent flows in order to overcome a few of the challenges presented by experimental grid-generated turbulence. The RANS study is expected to give quicker time-averaged results in comparison to LES but without any instantaneous information of the flow variables, which will be provided by the corresponding LES study. The RANS study also covers a wider range of turbulent flow Reynolds number ($Re_{L_{u0}}$) (where $Re_{L_{u0}} = \frac{\overline{U}L_{u0}}{\nu}$, $\overline{U}$ is the mean velocity, L_{u0} is the inlet integral length scale and ν is the kinematic viscosity of the fluid) flows that cannot be covered in LES owing to the limiting constraint of available computational resources. This is followed by a parametric analysis of the RANS and LES simulations to develop a simple yet powerful predictive correlations of spatial decay of TKE using dimensionless parameters.

1.3 Scope of the Thesis

The present thesis is aimed at studying and quantifying the streamwise decay of homogeneous isotropic turbulence from the point of generation until the leading edge of

the plate. Downstream evolution of turbulent kinetic energy (TKE) in the presence of different initial turbulence intensities (TI) and inlet integral length scales (L_u) are also examined. Henceforth, a quantitative prediction methodology of the turbulence decay mechanism is formulated that helps one to estimate both the local and initial values of the turbulent parameters (TKE and L_u) in the flow field of the domain. Additionally, the study has been extended to identify regions of near constant TKE conditions in order to allow bluff body studies in that region.

To this end, both 3-D steady RANS simulation and unsteady LES simulations have been performed to evaluate the turbulent kinetic energy decay rate (TKE) downstream from the inlet. The range of velocities covered in the RANS study are 4m/s, 10m/s, 20m/s, 30m/s, and 40m/s, whereas only one flow velocity (4m/s) has been simulated in the current LES study. The corresponding turbulent Reynolds numbers based on the inlet integral length scale ($Re_{L_{u0}}$) are 2.55×10^3, 6.38×10^3, 1.28×10^4, 1.91×10^4 and 2.55×10^4 which fall under the category of moderate turbulent Reynolds number flows. The inlet turbulence intensities covered in this study were 10%, 20%, 30% and the range of integral length scales specified at the inlet were from 0.02m, 0.05m and 0.10m. The turbulent parameters were varied at the inlet to quantify their influence on the decay rate of TKE over the domain. The range of length scales studied here are of the order of the boundary layer thickness that would impinge the leading edge of the plate and so would be energetic enough to perturb the dynamic and the thermal boundary layer completely, which is part of the heat transfer study. As a part of the future work, related to heat transfer models, only the forced convection regime with a temperature difference (ΔT) of 30K, will be studied, as including all of free and mixed convective heat transfer regimes is outside the scope of the study and proposed as future work.

1.4 Thesis layout

The numerical study presented herein is in the form of an Integrated Article format that includes only statistically converged results for decaying isotropic homogeneous turbulent flows.

Chapter 2 discusses the characteristic nature of the turbulence decay in an empty numerical grid domain and a region of nearly constant incident turbulence intensity is identified. The freestream decay of turbulent flow field is validated with the previous experimental and numerical studies and a new form of decay law is suggested considering the effect of inlet turbulence intensity (TI) and length scales (L_u). Attempts have also been made to model the turbulent inlet conditions that govern the decay rate of free stream turbulent flows and, henceforth, a set of new correlation equations characterizing the spatial decay of isotropic homogeneous turbulence has been formulated. A region of nearly constant incident turbulent conditions has been identified based on the above predictive correlation model so that the aerodynamic features of any bluff body can be suitably studied under near constant TKE conditions. Finally, a comprehensive review of its dependence on the initial TKE and length scales is presented that extends our understanding of the dependence of turbulence decay on the initial conditions.

Chapter 3 solely focuses on the qualitative and quantitative differences observed between three different CFD commercial codes while employing RANS model in the current study. The differences are highlighted in terms of the model constants used in these codes and the limitations of the models are brought forward. Improvements are also suggested for these commercial CFD codes that can be used to unify the results obtained for the streamwise decay of isotropic homogeneous turbulence from LES. Finally, results have been presented from these improved models to validate its prediction of the flat plate boundary layer growth in presence of negligible free stream turbulence intensity.

The Conclusions from the present work and recommendations for future work are presented in Chapter 4.

1.5 Summary

In summary, this chapter introduces the general nature of the current problem along with the motivation that drives the necessity of the present study to be carried out on the freestream decay of homogeneous isotropic turbulence. The present study is expected to assist the future work, in quantifying the convective heat transfer rates over a flat plate in

presence of freestream turbulent flow. As stated earlier, the current study only analyses the freestream decay of isotropic homogeneous turbulence, but the final goal is to develop relationships between the upstream incident turbulent parameters (TI, L_u and Re) and the dimensionless heat transfer variables (Nusselt number (Nu), Stanton number (St)). Currently, investigations are being carried as a part of the future work out to identify the fundamental features of turbulent flow over a smooth flat plate, in the presence of freestream turbulence and, therefore, that work is not presented in the subsequent chapters. The main intent of this current chapter was to introduce the broader topic related to the field of convective heat transfer studies with the final aim of quantifying the nature of thermal boundary layers in presence of freestream turbulence. It is hoped that the present study will contribute to the fields of Environmental Fluid Mechanics and Convective Heat Transfer to enhance our understanding of the responses of the velocity fields and the heat transfer to incident turbulence in atmospheric boundary layer flows.

The next chapter discusses the freestream decay of turbulence downstream of grids in a more detail, including the limitations of the existing literature and with numerical simulation results validated with the experiments for better understanding.

References

ASHRAE (American Society of Heating Refrigerating and Air-Conditioning Engineers) (2009) '2009 Ashrae Handbook: Fundamentals, I-P Edition', *ASHRAE Journal*, 30329(404), p. 926.

Ambatipudi, K.K. and Rahman, M.M., (2000).'Analysis of conjugate heat transfer in microchannel heat sinks'. *Numerical Heat Transfer: Part A: Applications*, 37(7), pp.711-731.

Athienitis, A. K. (2008) 'Design of advanced solar homes aimed at net-zero annual energy consumtion in Canada', in *3rd International Solar Energy Society Conference - Asia Pacific Region*. Sydney, Australia, pp. 1–14.

Batchelor, G. K. and Townsend, A. A. (1948a) 'Decay of isotropic turbulence in the initial period', *Proceedings of the Royal Society of London, Series A, Mathematical and Physical Sciences*, 193(1035), pp. 539–558.

Bearman, P. W. and Morel, T. (1983) 'Effect of free stream turbulence on the flow around bluff bodies', *Progress in Aerospace Sciences*, 20(2–3), pp. 97–123.

Blair, M. F. (1983a) 'Influence of free-stream turbulence on turbulent boundary layer heat transfer and mean profile development, Part I—Experimental Data', *Journal of Heat Transfer*, 105, pp. 33–40.

Blair, M. F. (1983b) 'Influence of free-stream turbulence on turbulent boundary layer heat transfer and mean profile development, Part II—Analysis of Results', *Journal of Heat Transfer*, 105, pp. 41–47.

Büyüktür, A.R., Kestin, J. and Maeder, P.F., (1964). 'Influence of combined pressure gradient and turbulence on the transfer of heat from a plate'. *International Journal of Heat and Mass Transfer*, 7(11), pp.1175-1186.

Charnay, G., Mathieu, J. and Comte-Bellot, G. (1976) 'Response of a turbulent boundary layer to random fluctuations in the external stream', *Physics of Fluids*, 19(9), pp. 1261-

1272.

Comings, E. W., Clapp, J. T. and Taylor, J. F. (1948) ‘Air turbulence and transfer processes’, *Industrial and Engineering Chemistry*, 40(6), pp. 1076–1082.

Corrsin, S. and Kistler, A. L. (1955) ‘Free-stream boundaries of turbulent flows’, *NACA-report-1244*, pp. 1–35.

Dyban, E. P., Epik, E. Y. and Surpun, T. T. (1977) ‘Characteristics of the laminar layer with increased turbulence of the outer stream’, *Int. Chem. Eng.*, 17(3), pp. 501–504.

Dyban, E. P., Epik, E. Y., Zuzine, in: N. and (Eds.), A. K. (1985) ‘Transferts de chaleur et hydrodynamique dans les écoulements rendus turbulents’, in *Monographie Traduite du Russe par l’I.N.R.A.* Naukova Dumka, Kiev.

Eckertf, E.R.G. and Carlson, W.O., (1961). 'Natural convection in an air layer enclosed between two vertical plates with different temperatures'. *International Journal of Heat and Mass Transfer*, 2(1-2), pp.106-120.

Edwards, A. and Furber, B. (1956) ‘The influence of free-stream turbulence on heat transfer by convection from an isolated region of a plane surface in parallel air flow’, *Proc. Inst. Mech.*, E 170, pp. 941–954.

Fage, A. and Falkner, V. (1931a) ‘Further experiments on the flow around a circular cylinder’, *Reports and memoranda (Great Britain. Aeronautical Research Committee)*, (1369).

Fage, A. and Falkner, V. M. (1931b) ‘On the relationship between heat transfer and surface friction for laminar flow’, *British. Aeronautical Research Council Reports and Memoranda*, 1408(London: HMSO).

Foli, K., Okabe, T., Olhofer, M., Jin, Y. and Sendhoff, B., (2006). 'Optimization of micro heat exchanger: CFD, analytical approach and multi-objective evolutionary algorithms'. *International Journal of Heat and Mass Transfer*, 49(5-6), pp.1090-1099.

Geidt, W. H. (1951) ‘Effect of turbulence level of incident air stream on local heat transfer and skin friction on a cylinder’, *Journal of the Aeronautical Sciences*, 18(11), pp. 725–730.

Hurst, D. and Vassilicos, J. C. (2007) ‘Scalings and decay of fractal-generated turbulence’, *Physics of Fluids*, 19, pp. 1–31.

Ishida, T., Davidson, P. a. and Kaneda, Y. (2006) ‘On the decay of isotropic turbulence’, *Journal of Fluid Mechanics*, 564, pp. 455-475.

Kestin, J. and Maeder, P.F., (1957). Influence of turbulence on transfer of heat from cylinders, *NACA Tech. Note 4018*, pp. 1-78.

Kestin, J., Maeder, P.F. and Wang, H.E., (1961). 'Influence of turbulence on the transfer of heat from plates with and without a pressure gradient'. *International Journal of Heat and Mass Transfer*, 3(2), pp.133-154.

Kang, H. S., Chester, S. and Meneveau, C. (2003) ‘Decaying turbulence in an active-grid-generated flow and comparisons with large-eddy simulation’, *Journal of Fluid Mechanics*, 480, pp. 129–160.

Karava, P., Jubayer, C. M. and Savory, E. (2011) ‘Numerical modelling of forced convective heat transfer from the inclined windward roof of an isolated low-rise building with application to photovoltaic/thermal systems systems’, *Applied Thermal Engineering*, 31, pp. 1950–1963.

Kline, S. J., Lisin, A. V. and Waitman, B. A. (1960) ‘Preliminary experimental investigation of the effect of free stream turbulence on turbulent boundary layer growth’, *NACA, Technical note*, D-368, pp. 1–62.

Kondjoyan, A., Péneau, F. and Boisson, H. C. (2002) ‘Effect of high free stream turbulence on heat transfer between plates and air flows: A review of existing experimental results’, *International Journal of Thermal Sciences*, 41(1), pp. 1–16.

Krogstad, P. and Davidson, P. A. (2011) ‘Freely-Decaying, Homogeneous Turbulence

Generated by Multi-scale Grids', *Journal of Fluid Mechanics*, 32042(680), pp. 417–434.

Lavoie, P., Burattini, P., Djenidi, L. and Antonia, R. A. (2005) 'Effect of initial conditions on decaying grid turbulence at low R_λ', *Experiments in Fluids*, 39(5), pp. 865–874.

Loveday, D. L. and Taki, A. H. (1996) 'Convective heat transfer coefficients at a plane surface on a full-scale building facade', *International Journal of Heat and Mass Transfer*, 39(8), pp. 1729–1742.

Maciejewski, P. K. and Moffat, R. J. (1992) 'Heat transfer with very high free-stream turbulence: Part I - Experimental Data', *Journal of Heat Transfer*, 114, pp. 827–833.

Mazzi, B. and Vassilicos, J. C. (2004) 'Fractal-generated turbulence', *J. Fluid Mech*, 502, pp. 65–87.

Mobbs, F. R. (1968) 'Spreading and contraction at the boundaries of free turbulent flows', *Journal of Fluid Mechanics*, 33, pp. 227–239.

Mohamed, M. S. and Larue, J. C. (1990) 'The decay power law in grid-generated turbulence', *Journal of Fluid Mechanics*, 219, pp. 195-214.

Moradian, N., Ting, D. S. K. and Cheng, S. (2009) 'The effects of freestream turbulence on the drag coefficient of a sphere', *Experimental Thermal and Fluid Science*. Elsevier Inc., 33(3), pp. 460–471.

Mordant, N. (2008) 'Experimental high Reynolds number turbulence with an active grid', *American Journal of Physics*, 76(12), pp. 1092–1098.

Palyvos, J. A. (2008) 'A survey of wind convection coefficient correlations for building envelope energy systems' modeling', *Applied Thermal Engineering*, 28(8–9), pp. 801–808.

Péneau, F., Boisson, H.C., Kondjoyan, A. and Djilali, N., (2004). 'Structure of a flat plate boundary layer subjected to free-stream turbulence'. *International Journal of*

Computational Fluid Dynamics, 18(2), pp.175-188.

Pope, S. B. (2000) *Turbulent Flows, Measurement Science and Technology*. Cambridge University Press. pp. 1-754.

Reynolds, W. C., Kays, W. M. and Kline, S. J. (1958) 'Heat Transfer in the Turbulent Incompressible Boundary layer I- Constant Wall Temperature', *NASA Memorandum*, 12–1–58W, pp. 1–37.

Rolls Royce Infographic (2014) *Computational Science and Engineering Grand Challenges in Rolls-Royce Leigh Lapworth Networkshop, University of Leeds*. Available at: https://www.slideshare.net/alimayar/rollsroyce-40221248.

Seoud, E. R. and Vassilicos, C. J. (2007) 'Dissipation and decay of fractal-generated turbulence', *Physics of Fluids*, 19(10). pp. 1-12.

Simonich, J. C. and Bradshaw, P. (1978) 'Effect of free-stream turbulence on heat transfer through a turbulent boundary layer', 100(4), pp. 671–677.

Smith, M. C. (1964) The effect of free stream turbulence on the laminar boundary layer heat transfer of flat plates and circular cylinders. *PhD. Thesis*, Aeronautical and Astronautical Engineering Department, University of Michigan.

Sugawara, S., Sato, T., Komatsu, H. and Osaka, H. (1988) 'Effect of free stream turbulence on flat plate heat transfer', *International Journal of Heat and Mass Transfer*, 31(1), pp. 5–12.

Tabor, G. R. and Baba-Ahmadi, M. H. (2010) 'Inlet conditions for large eddy simulation: A review', *Computers and Fluids*. Elsevier Ltd, 39(4), pp. 553–567.

Tan-atichat, J., Nagib, H. M. and Loehrke, R. I. (1982) 'Interaction of free-stream turbulence with screens and grids : a balance between turbulence scales', *Journal of Fluid Mechanics*, 114, pp. 501–528.

Test, F. L. and Lessmann, R. C. (1980) 'An experimental study of heat transfer during

forced convection over a rectangular body', *Journal of Heat Transfer*, 102, pp. 146–151.

Tian, J., Kim, T., Lu, T.J., Hodson, H.P., Queheillalt, D.T., Sypeck, D.J. and Wadley, H.N.G., 2004. 'The effects of topology upon fluid-flow and heat-transfer within cellular copper structures'. *International Journal of Heat and Mass Transfer*, 47(14-16), pp. 3171-3186.

Townsend, A. A. (1956) *The structure of turbulent shear flow*. pp. 1-315. Cambridge University Press.

Van Der Hegge Zijnen, B. G. (1958). "Heat transfer from horizontal cylinders to a turbulent air flow." Applied Scientific Research, Section A 7 (2-3): pp. 205–223.

Wang, B.X. and Peng, X.F., (1994). 'Experimental investigation on liquid forced-convection heat transfer through microchannels'. *International Journal of Heat and Mass Transfer*, 37, pp.73-82.

Chapter 2

2 Numerical modelling of spatially decaying isotropic homogeneous turbulence

2.1 Background

Streamwise dissipation of isotropic homogenous freestream turbulence is one of the fundamental and widely explored problems in turbulent theories and its effect on various bluff-body aerodynamics and thermal physics has been one of the topics of intense discussion over the past few decades. Although our understanding of turbulence scales of motion has increased over the years, there has been a lot of apparent inconsistencies observed on the decay development of turbulent kinetic energy (TKE) in the limit of infinite Reynolds number. In absence of any external turbulent kinetic energy generating mechanism, the observed kinetic energy carried by the integral length scales of motion will decay due to the inviscid dissipation of energy mostly due to inertial eddy interaction. Similarly, for Low Reynolds number flows, molecular viscous forces dominate which causes the decay of turbulent kinetic energy (TKE) carried by the small scale dissipative eddies (Pope, 2000). This decay of turbulence fluctuations has an influential impact on the development of laminar and turbulent boundary layers over bluff bodies which in turn alters the heat and mass transfer rates from them (Mizushina *et al.* (1972); Simonich and Bradshaw (1978); Blair (1983a; 1983b); Maciejewski and Moffat, (1992)). The impact of the decaying freestream turbulence on the separating and re-attaching flows over bluff-bodies are also important because of the large aerodynamic loads that these freestream flows are known to have caused (Gartshore, (1973); Hillier and Cherry, (1981); Saathhoff and Melbourne, (1989); Saathhoff and Melbourne, (1997)). Therefore, quantitative prediction of the magnitude of the freestream turbulent flow parameters incident on any bluff-body based on upstream inlet conditions becomes an important factor to accurately estimate the dynamic properties of fluid and thermal responses in laminar, turbulent and transitional boundary layers.

Quasi-homogeneous isotropic turbulence has been one of the recognized problems in classical turbulence, since it provides the centrepiece for the investigation of the large

scale physical properties of turbulence (Dryden, 1943). It is also by far the most documented configuration of turbulence used, as an attempt towards numerical modelling of turbulent flows. One may argue that isotropic and homogeneous turbulence are not encountered in most industrial situations, and yet its idealization helps make the analysis of the problem manageable and guide model development. Despite all the efforts made in the last few decades, a unifying theory describing the isotropic decay of homogeneous turbulence has not been instituted conveniently. However, a great deal of experimental data containing the information of turbulent energy spectra have been published, (Comte-Bellot and Corrsin, 1966); (Uberoi and Wallis, 1969); (Comte-Bellot and Corrsin, 1971a). Those results establish the foundation of the three-dimensional spectra from which the temporal decay of turbulence can be predicted.

Homogeneous isotropic turbulence is known to have been closely achieved in grid-generated turbulence, as noted by (Pope, 2000). A very close approximation to the decaying isotropic homogenous turbulence can be achieved in wind-tunnel experiments, by placing a grid upstream of the test-section and then passing a uniform flow stream through the grid. Both stationary and moving grids can be used in the experiments which would create passive and active turbulence downstream of the grid. Due to the resultant wakes created from the geometrical structure of the grids, turbulence is produced, which increases the fluctuations in the freestream. In the absence of a mean velocity gradient or external body forces causing turbulence, the freestream fluctuations will dissipate due to the inertial frictional forces acting amongst the large-scale turbulent eddies. The downstream velocity field generated from the wake interaction of the grids has been empirically known to become statistically homogeneous and isotropic at least at 20 mesh widths (M) from the grid (known as the virtual origin x_0) where the wake vortices from the grids coalesces completely (Hinze, 1975). However, a length of 40 mesh widths has been considered as a safe limit for turbulence reaching effective homogeneity (Corrsin, 1963). If a laboratory framework is considered, then the flow is statistically stationary, and statistics only vary in the x (streamwise) direction as turbulence decays.

Figure 1.4 (refer to chapter 1) shows a typical turbulence generating grid with circular rods embedded with each other. The mesh width is M and the diameter of the rod is

represented by d. Similarly, figure 1.5 (refer to chapter 1) shows a conceptual diagram of a grid-generated turbulence along with the eddies generated by the grid, mixing of eddies, re-orientation of turbulence, and virtual origin (x_0) after which the turbulence becomes nearly homogeneous and isotropic in nature. A schematic graph showing the decay of turbulent kinetic energy (TKE) in the streamwise direction has been represented previously in figure (1.6) (refer to chapter 1) for a better illustration of the current problem.

Numerous theoretical and experimental investigations on the decay of homogenous isotropic turbulence followed the influential work by Taylor (1935) and Kolmogorov (1941a, b). The earliest work was by Kármán and Howarth (1938) which showed that the energy decays as t^{-1} where ($t = x / \overline{U}$), x is the distance in the streamwise direction, $\overline{U}$ is the mean velocity and t represents time. But the apparent failure of the von-Kármán-Howarth similarity analysis to adequately describe the turbulence behind the grid led Batchelor (1948) to propose turbulence as a multilength scale phenomenon, described by local similarity laws at the energy containing large scales and the dissipative scales. Batchelor and Townsend (1947) analyzed the rate of change of mean square vorticity in isotropic turbulence during various stages of decay of the turbulence. They show that, theoretically, two separate physical processes contribute to the change in vorticity. The first process is an average extension of the vortex lines due to the random diffusion motion of the large scales, whereas the second process is the dissipation of vorticity due to the effect of the viscosity. The agreement in their results made it permissible to apply the theory of isotropy to the turbulence generated behind the grids. Batchelor and Townsend, (1948a) then reported that in grid-generated turbulence, there exists an initial period of decay, during which the energy decays according to the simple law, $\overline{u'^2} \propto t^{-1}$ where $\overline{u'^2}$ is the mean of the square of the velocity fluctuations and t represents time. In this period, the energy transfer between the large scales and the small scales, which maintains a high rate of dissipation, is chiefly due to the inertial actions, the dynamics of which are represented by the inertial terms in the Navier-Stokes equation, whereas the smaller eddies are dissipated mainly due to the action of viscosity. They even postulated that, after a certain period of time (Batchelor and Townsend, 1948b), there is a

transitional period of decay during which the decay law changes. During the transitional period the inertia terms continue to play some part in the transfer of energy from the larger eddies, but the Reynolds number decreases, and viscosity dominates during the final period of the decay. The decay law is modified according to $\overline{u'^2} \propto t^{-\frac{5}{2}}$ in the final period. It was also shown that such a self-preserving velocity correlation function can only exist when the inertia forces are negligible and is, necessarily an asymptotic solution under such conditions.

The variation of turbulence intensity in the streamwise direction has been discussed by several authors making various assumptions (Simmons and Salter, (1934); Dryden, (1943) where they found out that the rate of energy decay is almost equal to the work done against the eddying stresses due to viscosity. These early experiments seem to have consistency with the von-Kárman-Howarth predictions which states $\overline{u'^2} \propto t^{-1}$ or $\frac{\overline{u'^2}}{\overline{U^2}} \sim \frac{(x - x_0)}{M}$, where $\overline{U}$ is the mean velocity in the streamwise direction and x_0 represents the virtual origin (refer to figure. (1.5)). Comte-Bellot and Corrsin (1966) showed that the isotropy of the turbulent flow was improved by using a contraction downstream of a grid and indicated that a better fit to all the earlier experimental data could be obtained through a power law of the form

$$\frac{\overline{u'^2}}{\overline{U^2}} = D\left(\frac{x - x_0}{M}\right)^{-n} \qquad (2.1)$$

where D is the decay coefficient and n is the decay exponent which depends on the grid-geometry and Reynolds number of the grid flow.

The prediction of these decay exponents led to an extensive reanalysis of the previous experimental data by Skrbek and Stalp (2000)**.** After scrutinizing the previous theoretical predictions of decaying turbulence, it has been found that there is sometimes very little agreement between the available data sets, even after years of investigation, on the decay of homogeneous, isotropic turbulence. Mohamed and Larue (1990) presented an

extensive review of all the relevant studies done on the decay mechanism of grid-generated turbulence and showed that although the analyses of Kármán and Howarth (1938); Kolmogorov (1941a); Saffman (1967) leads to the same form of power law (eq. 2.1), the predicted value of the decay exponent varies as n = 1, $\frac{10}{7}$ and $\frac{6}{5}$, respectively. There have also been contrasting theories regarding the behaviour of large turbulent scales in grid generated flows. Batchelor (1953) and Saffman (1967) provide two variants of turbulent flows where the energy decay rates varies as, $\overline{u'^2} \sim t^{-\frac{10}{7}}$ for Batchelor turbulence and $\overline{u'^2} \sim t^{-\frac{6}{5}}$ for Saffman turbulence. In contrast George (1992) suggested that the decay rate of turbulence depends on the initial conditions and that the decay rate constants (A and n) cannot be universal, except possibly in the limit of infinite Reynolds number. Earlier studies also support George's theory as Batchelor and Townsend (1947), Batchelor and Townsend (1948b), Stewart and Townsend (1951), Portfors and Keffer (1969) found that n = 1, whereas Corrsin (1963), Uberoi, (1963), Uberoi and Wallis, (1967), Uberoi and Wallis (1969), and Comte-Bellot and Corrsin (1971a) found that 1.16 $\leq$ n $\leq$ 1.37. A higher magnitude of decay exponent (n = 1.43) was also found in the studies of Baines and Peterson, (1951). In most cases, the irreconcilable differences in the magnitude of the exponent observed is linked to (a) the unknown virtual origin x_0, (b) imprecise identification of the isotropic homogenous regime of grid-generated turbulence and (c) the decay coefficients and the exponents not being determined in a consistent and objective manner. The above discussions expose the fact that a complete theoretical understanding of the physical mechanisms of turbulence decay is yet to be achieved, despite more than 80 years of research. However, new approaches based on the Langevin equation of large structures have already been introduced by Llor (2011) which may offer an interesting unifying framework for homogeneous isotropic turbulence. The Langevin equations are based on the stochastic evolution of Loitsyankiis integral (Loitsyanskii, 1945) as the angular momentum variance of an asymptotically large sphere of size D_1 interpreted by Landau as Landau's large scale angular momentum or Landau's integral (Landau and Lifshitz, 1959). Besides this, a very slow unsteady turbulence decay has

been recently observed by (Llor, 2011) which might be able to explain some of the estimation errors related to the variability of D and n.

Decaying turbulence has long-served as an important benchmark test case for numerous theories, models and computer simulations. Although various wind tunnel experiments have provided worthwhile information on the time-resolved scales of turbulence over the years, it becomes essential to examine full three-dimensional structures of turbulence numerically to avoid the experimental difficulties and to better understand and visualize its underlying physics. Referring to the computational resources presently available, Direct Numerical Simulations (DNS) of homogeneous isotropic turbulence have also been carried out by Ishihara *et al.* (2009) where they created a mesh of 4096^3 resolution to achieve the finest spatial resolution of turbulence at very high turbulent Reynolds number (Re_λ) of 1131, where turbulent Reynolds number (Re_λ) is based on the Taylor microscale (λ) given by $\mathrm{Re}_\lambda = \overline{U}\lambda / \nu$ (where ν is the kinematic viscosity of the fluid). However, DNS models are extremely demanding computationally and are often limited with the lack of adequate computer power which is why they are not practiced for small computational runs. A less computationally expensive study using LES (Large eddy simulation) of active grid-generated turbulence was conducted by Kang *et al.* (2003) which showed good agreement between their results and the classical experiment of Comte-Bellot and Corrsin (1966). Consequently Detached Eddy Simulation (DES) of fractal grid generated turbulence (Medjroubi *et al.*, 2013) and Reynolds Averaged Navier Stokes simulations (RANS) (Torrano *et al.*, 2015) of grid-generated turbulence relating to passive grids have been done where they have assessed the capability of various numerical models to capture the main trends of turbulence decay. However, it should be noted that RANS models are only good for capturing the mean turbulent properties without providing any information about the various spatial and temporal scales embedded in a turbulent flow.

It is generally agreed that the large-scale turbulent properties; turbulence intensity (in percentage given by $TI = \frac{\sqrt{\frac{1}{3}(\overline{u'^2} + \overline{v'^2} + \overline{w'^2})}}{\overline{U}} \times 100$) and integral length scales (L_u) are the decisive factors in governing the decay laws for a quasi-static homogeneous isotropic turbulence, since both the parameters evolve according to power laws (Pope, 2000) and play an intrinsic role in dictating the dissipation rate of the turbulent kinetic energy ($\varepsilon \approx -\frac{u'^3}{L_u}$) where u', v' and w' are the r.m.s velocity fluctuations in x, y and z directions and L_u is the size of the average energy containing eddy. However, reviewing the earlier studies on decaying grid-generated turbulence, the present discussion concludes that the contribution of length scales on the decay rate of turbulence kinetic energy have been neglected since Taylor's first proposal (Taylor, 1938a) where it was assumed that, L_u (average size of an eddy which represents the scale of the turbulent flow system) is independent of x and proportional to the mesh width M of the grid that gives rise to turbulence. However, when the measured values of L_u became available (Hall, 1938) it was found that L_u increased with streamwise distance x. A further review by Dryden (1943) hypothesized that, if dimensional reasoning is taken into account, then $\frac{du'}{dt}$, the rate of change of turbulent fluctuation and $\frac{dL_u}{dt}$, the rate of change of integral length scale are determined solely by the values of L_u and u', i.e. viscosity and other upstream conditions have no effect on the rate of turbulence decay. However, if one considers the complete system of geometrical grids and the turbulent field, dimensional considerations suggests that for geometrically similar grids whose scale is fixed by some characteristic dimension, such as the mesh width M, the ratios $\frac{u'}{\overline{U}}$ and $\frac{L_u}{M}$ would be a function of $\frac{x}{M}$. Again, if the grids are not geometrically similar, the intensity and scale will then also depend on solidity, mesh shape and the surface roughness (Uberoi and Wallis, 1967). The effects of these parameters have not yet been fully investigated and a part of the discrepancy (dependency of turbulent parameters on grid-dimensions) between

the available results is yet to be described, including the influence of these factors. The underlying fact that develops out of the present discussion is that, if turbulence is truly isotropic in nature, then its characteristics can be adequately described by the two quantities, intensity and scale, and its behaviour of decay can only depend on the local values of characteristic intensity and scale at some point in the turbulent flow domain, i.e. the decay of free stream turbulence should be accountable in the values of u' and L_u at any point in the flow system. Previous relevant studies (Batchelor and Townsend, (1947); Batchelor and Townsend, (1948a); Batchelor and Townsend, (1948b); Batchelor, (1953); Comte-Bellot and Corrsin, (1966); Comte-Bellot and Corrsin, (1971b); Bennett and Corrsin, (1978); Sreenivasan *et al.* (1980)) on the spatial decay of homogeneous isotropic turbulence made almost no attempt to include the effects of length scale on the decay characteristics of turbulent kinetic energy, thereby only relating the length scale to the corresponding characteristic mesh size M, which is again different for different grid widths. So, it becomes increasingly necessary to formulate a set of correlation functions that would take both the turbulence parameters, viz. turbulence intensity (in %) (TI) and length scales (L_u) into account before invoking any predictions for spatial turbulence decay.

Hence, the motivation of the current study is to employ numerical RANS and LES simulation models, to develop simple yet powerful correlation equations that would systematically quantify the spatial decay of turbulence, based on upstream inlet conditions, in a nearly isotropic and homogenous regime of turbulence. The final goal from the current study is to use the correlation equation as a prediction tool to estimate local and initial values of turbulence intensity and turbulence length scale and predict a nearly uniform region of incident turbulent kinetic energy (TKE) where the changes in the turbulent properties in the streamwise direction are insignificant.

2.2 Introduction to numerical modelling

A detailed explanation of the CFD models used to assess the free stream turbulence decay in an empty three-dimensional (3D) grid domain are presented in the following section. A schematic representation of the computational domain with dimensional details is

presented in Section 2.3. The grid generation techniques are discussed in Section 2.4. Section 2.5 presents the methodology used for the CFD modelling of the current problem, which includes description of the CFD solver, different types of turbulence models used, and various solution parameters that affect the stability and accuracy of the solution. Boundary conditions for this problem are discussed in section 2.6. Section 2.7 discusses the flow characteristics at the inlet, in terms of directional isotropy and spatial homogeneity. A very detailed description of the model convergence along with its validation with the previous studies are given in Section 2.8. Section 2.8 also discusses the research contribution from the present work in terms of modelling the inlet turbulent conditions for bluff body flows. At the end, a comprehensive summary and the important conclusions from the present chapter are presented in Sections 2.9 and 2.10, respectively.

2.3 Computational Domain

Turbulence is a 3D phenomenon and to accurately capture the details of the turbulent motions across a wide range of eddy scales, a 3D computational domain is required to establish a realistic simulation set-up. A 3D computational domain (Fig. 2.1) was created with sufficient length in the streamwise direction for the decay of turbulence to develop fully. The top and the span-wise boundaries were at a distance of 1m from each other which is long enough to allow eddies of scale of 0.1m in sufficient number to pass through the domain. The particular eddy size was chosen to be quite large and, hence, energetic enough to perturb the boundary layer scale of the same order, with relevance to the boundary layer heat transfer study that will be carried out in the future. The physical dimensions of the computational domain are L_x = 4m, L_y = 1m, L_z =1m. The outflow boundary was free from any kind of recirculation zone. It is pointed out here that all the data extracted and presented in the current study are taken along the centreline of the domain in the streamwise direction. Additionally, turbulence data were also extracted along the spanwise and normal directions to check for uniformity.

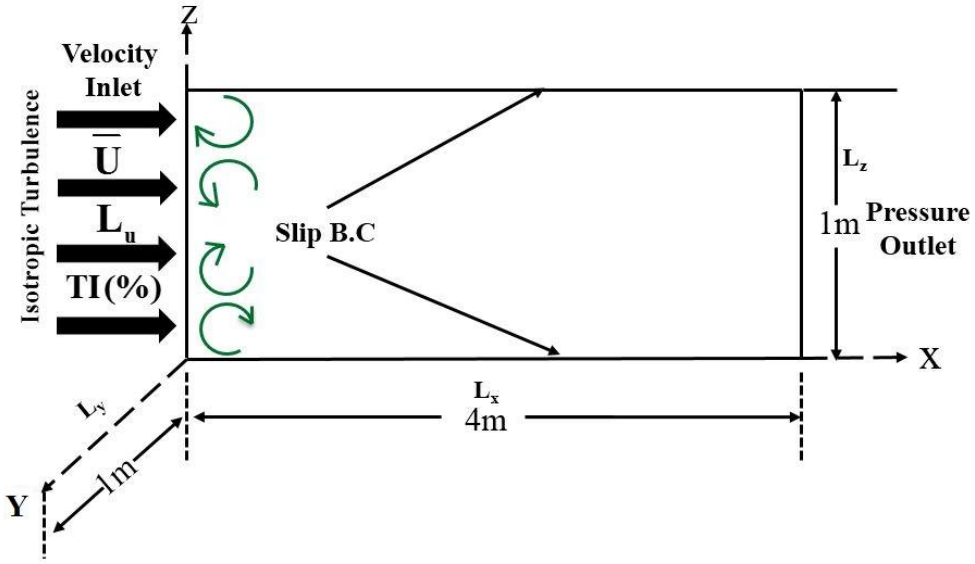

Figure 2.1 Schematic of the 3D computational domain with specific boundary conditions

2.4 Grid generation

A commercial mesh generating software ANSYS ICEM CFD™ 16.0 was used to generate the grid. The whole domain was discretized using a perfect structured orthogonal hexahedral mesh (fig. 2.2) in all three directions for accurate interpolation of the mean flow quantities and to be consistent with the cut-off scales for the spatial filtering. Hexahedral meshes offer an improved order of accuracy for wall bounded unidirectional flows since orthogonal grids can be maintained in the wall normal direction with regular connectivity. Orthogonal meshes offer minimal skewness which provides better numerical and computational efficiency for effective 1st order and 2nd order gradient approximation over the cells.

Polyhedral meshes can be used which would provide less computationally intensive calculations but the range of frequency of length scales convected through the domain will be inconsistent in nature since the local grid scale (Δ) of each computational cell will be different that would capture different frequency of the integral scales circulating through the flow.

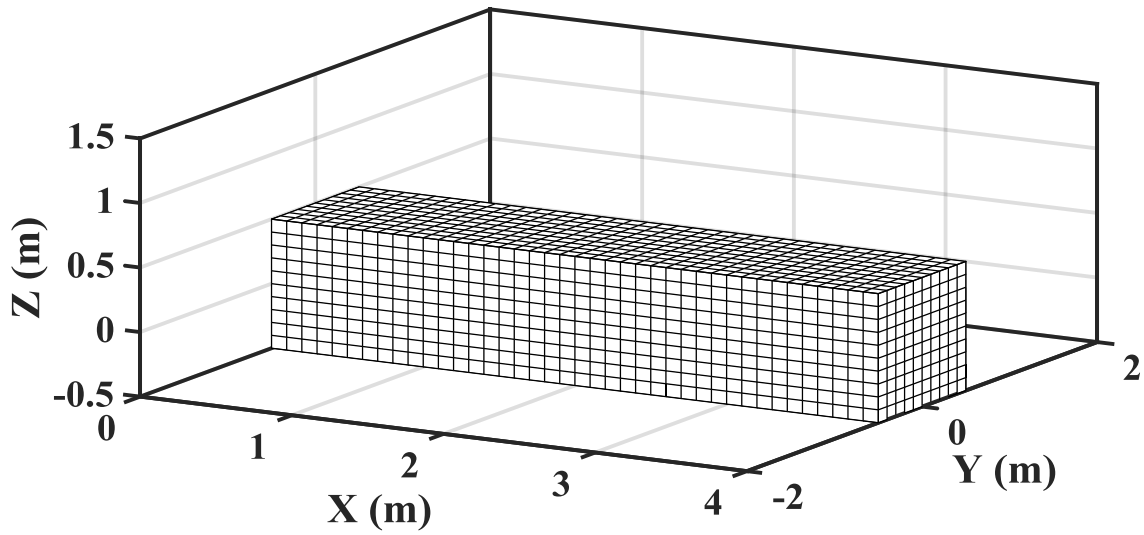

Figure 2.2 A schematic of the hexahedral grid distribution over the entire computational domain

2.5 Methodology

2.5.1 Solver

Three different types of commercial CFD software packages ANSYS FLUENT 16.0, ANSYS CFX 16.0 and CD-ADAPCO Star-CCM+ 10.02.012 were used in the current problem all of which use the finite volume technique to solve the equations with double precision which provides increased accuracy due to less round-off error.

FLUENT acts as cell-based solver computing variables at the cell-centres of any discretized control volumes and offers two different types of solvers; pressure-based solver and density-based solver. The pressure-based approach was developed for low-speed incompressible flows and mildly compressible flows, while the density-based approach is mainly used for high-speed compressible flows. In the current study, the pressure-based solver is used since the flow falls within the category of moderate speed incompressible flows. The pressure based solver employs an algorithm which belongs to a general class of methods called the projection method (Chorin, 1968)**.** In the projection method, the mass conservation (solving the continuity equation) of the velocity field is achieved by solving a pressure (or pressure correction) equation. The pressure equation is

derived from the continuity and the momentum equations in such a way that the velocity field, corrected by the pressure satisfies continuity. Since the governing equations are non-linear and are coupled to one another, the solution process involves iterations wherein the entire set of governing equations is solved repeatedly until the solution converges.

CFX is a vertex (node)-centred solver and, hence, the flux through each face is based on the nodal values of the discretized control volume using finite element shape functions. CFX only offers a coupled pressure-based solver where the continuity and the momentum equations are solved in a coupled matrix simultaneously in a single step which delivers a faster convergence rate with respect to the total number of iterations solved. The built-in pressure-based algorithm used in CFX operates in a similar manner as in FLUENT.

Star-CCM+ is a finite volume cell-based solver computing the variable gradients at the cell centre of the control volume. Segregated solvers offer a pressure-based solution algorithm and can be used for incompressible and mildly compressible flows whereas the coupled flow algorithm is used for compressible flows, natural convection problems and flows with large body forces and energy sources. The segregated flow solver controls the solution update for the segregated flow model according to the SIMPLE algorithm.

2.5.2 Turbulence Models

A turbulent flow itself is irregular, chaotic, randomly diffusive, dissipative and time dependent in nature, characterized by velocity and vorticity fluctuations in all directions possessing a wide range of length scales (degrees of freedom). Thus, an enormous amount of information in the form of complete time histories over all spatial co-ordinates for every flow property is required to completely describe a turbulent flow. In such cases a complete solution of the Navier-Stokes equations is required with full numerical resolution of the flow field to capture the complete time histories of every aspect of a turbulent flow which usually requires vast computing resources. Hence, efforts have been made over decades ((Prandtl, 1925); Kármán, (1930); Kolmogorov, (1942); Prandtl, (1945)) to model a set of realistic mathematical algorithms that greatly simplifies the transport equations associated with the physical behaviour of turbulent flows. An ideal

turbulence model should have a minimal degree of complexity while capturing the essence of the relevant physics. A desirable type of turbulence model would be one that can be applied to a given turbulent flow by prescribing the appropriate initial and boundary conditions with no pre-defined knowledge of turbulence required.

2.5.3 Governing equations

Turbulence consists of time varying random fluctuations of flow properties in all the directions. Since this fluctuation can be of small scale magnitude with various frequencies, they are computationally too expensive to simulate directly for any practical engineering applications. A general statistical approach can be employed where the governing transport equations of fluid flow (conservation of mass, momentum and energy) can be time-averaged, spatially-averaged or ensembled-averaged to reduce the effect of the small scales, resulting in a modified set of equations that are computationally less expensive to solve. This is achieved by performing Reynold's decomposition of a scalar field or vector field where any time-varying generic variable (ϕ) (ϕ can be a scalar or a vector such as velocity, pressure, energy or species concentration) such can be written as the sum of an average and fluctuation, i.e. $\phi(t) = \bar{\phi} + \phi'(t)$, where the over-bar denotes the time-average and the prime denotes the time varying fluctuation of the property with time. The following decomposition yields a set of governing equations that governs the turbulent mean flow field. The new set of equations will be exact for an average flow field and not for the exact details of turbulent flow field. The resulting equations derived from the Navier-Stokes equation after the time averaging equations are called the Reynolds averaged Navier-Stokes equations (RANS equations).

The equations for conservation of mass and momentum for incompressible, constant property flow are

$$\frac{\partial u_i}{\partial x_i} = 0 \tag{2.2}$$

$$\frac{\partial}{\partial t}(\rho u_i) + \frac{\partial}{\partial x_j}(\rho u_j u_i) = -\frac{\partial p}{\partial x_i} + \frac{\partial t_{ji}}{\partial x_j} \tag{2.3}$$

The vectors u_i and x_i are the instantaneous velocity at position x_i, t is time, p is pressure, ρ is density and t_{ij} is the viscous stress tensor defined by

$$t_{ij} = 2\mu s_{ij} \tag{2.4}$$

where μ is molecular viscosity and s_{ij} is the strain rate tensor,

$$s_{ij} = \frac{1}{2}\left(\frac{\partial u_i}{\partial x_j} + \frac{\partial u_j}{\partial x_i}\right) \tag{2.5}$$

It is to be noted that $s_{ij} = s_{ji}$, so that $t_{ji} = t_{ij}$ for simple viscous fluids (but not for some anisotropic fluids). Substituting expressions of the form $\phi(t) = \bar{\phi} + \phi'(t)$ into the equation of mass and momentum conservation equations and taking a time (or ensemble) average and dropping the overbar on the mean profile quantity (velocity, pressure and strain) yields the ensemble-averaged mass and momentum equations usually referred to as Reynolds-averaged Navier-Stokes equations (RANS). They can be written in cartesian tensor form as:

$$\frac{\partial U_i}{\partial x_i} = 0 \tag{2.6}$$

$$\frac{\partial}{\partial t}(\rho U_i) + \frac{\partial}{\partial x_j}(\rho U_j U_i) = -\frac{\partial p}{\partial x_i} + \frac{\partial}{\partial x_j}(2\mu s_{ji}) + \frac{\partial}{\partial x_j}(-\rho\overline{u_i' u_j'}) \tag{2.7}$$

The time averaged mass and momentum equations are identical to the instantaneous mass and momentum conservation equations with the mean velocity replacing the instantaneous velocity. Aside from replacement of instantaneous variables by mean values, the only difference between the time-averaged and instantaneous momentum equations is the appearance of the correlation $\overline{u_i' u_j'}$. This is the time-averaged rate of momentum transfer due to turbulence also known as Reynolds-stress tensor term denoted by τ_{ij} where $\tau_{ij} = -\rho\overline{u_i' u_j'}$. τ_{ij} is a symmetric tensor that includes six different independent components. Hence, because of Reynolds averaging, six unknown quantities

have been produced with no additional equations added to solve them. The RANS equations denote an open set of equations that need to be closed to solve for the unknowns. The need for additional equations to model the new unknowns is called Turbulence Modelling. FLUENT, CFX and Star-CCM+ offers several turbulence models to solve the closure problem which are Spalart-Allmaras, k-ε, k-ω, v^2-f, Reynolds stress model (RSM), Detached eddy simulation (DES) and Large Eddy simulation models (LES) models. Some of these models also have variants.

In order to choose a relevant RANS turbulence model, a relative comparison between the different models predicting the decay of turbulent kinetic energy (TKE) along the streamwise distance is presented in figure (2.3). The comparisons are shown for an inlet mean velocity ($\overline{U}$) of 4m/s, initial turbulence intensity (TI) of 10% with an integral length (L_u) of 0.1m specified at the inlet. The x abscissa represents the streamwise distance and the y ordinate represents the turbulent kinetic energy (k) normalized with initial turbulent kinetic energy (k_0). From figure (2.3), it is evident that the predicted rate of decay of TKE is very similar (<1% difference) for each of the different RANS models and the choice of one model variant over other will really not affect the spatial rate of decay of the TKE in the streamwise direction. Since the chosen turbulence model will be extended for the flat plate heat transfer study in the future, thus, the shear stress transport k-ω model has been selected over other variants of turbulence models for simulating isotropic decaying homogeneous turbulence. It has been found that the SST k-ω closure with low Reynolds number (Re) modelling have performed better in predicting both the velocity profiles over a windward roof slope and the standard Nusselt number (Nu) correlation with Re for uniform flow over an isothermal flat plate (Karava *et al.* 2011) which provides another reason to choose the SST k-ω model for carrying out numerical simulations for isotropic decaying turbulence**.**

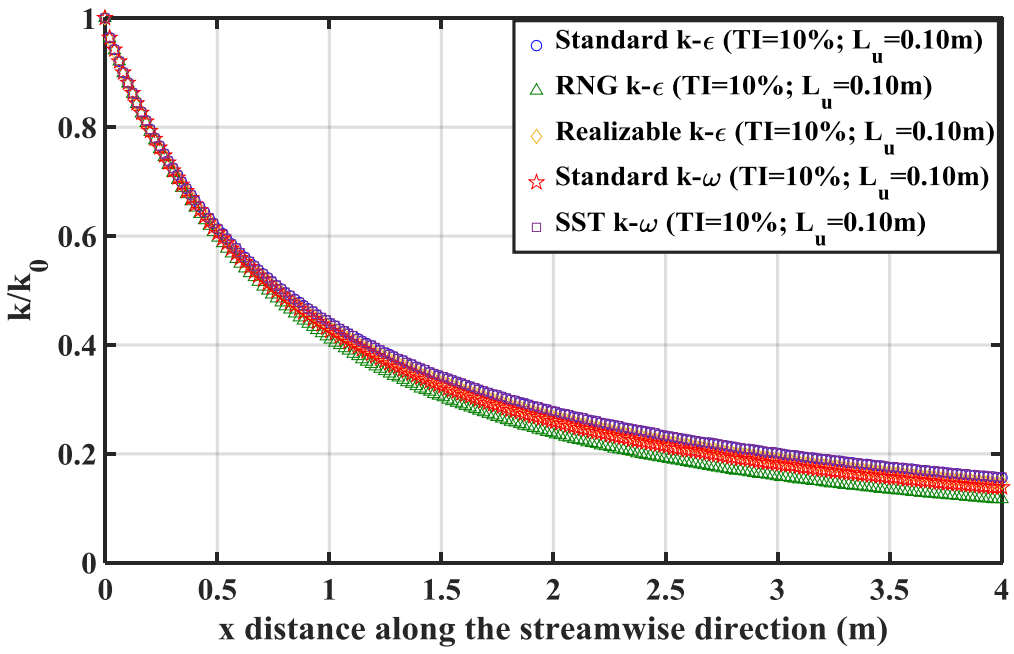

Figure 2.3 Comparisons between different RANS turbulence models showing the decay of TKE in the streamwise direction (FLUENT simulations).

Henceforth, only the shear stress transport k-ω and LES models will be discussed in the subsequent sections, since these turbulence models are being employed in the current study. The LES model offers unsteady simulation methods with better grid resolution that is expected to give instantaneous information about the flow variables influenced by the larger scales of turbulence, whilst the effect of the small scales of turbulence is computed through sub-grid models of which many styles are available. More details about the chosen turbulence models are presented in the following section. All the transport equations in the following section are written for compressible flows. They can be modelled for any incompressible flow by treating density as a constant variable.

2.5.4 Shear Stress Transport k-ω model

The shear stress transport k-ω model (SST k-ω) is a two-equation eddy viscosity model developed by Menter (1994) which more accurately predicts boundary layer flows with separation and reattachment, when compared to the k-ε (Launder and Spalding, 1974) and standard k-ω model (Wilcox, 1998). The model consists of blending of the equations of

the k-ε and standard k-ω model, such that the model retains the robustness and accuracy in the inner parts of the boundary layer all the way down to the wall through the viscous sub-layer. Hence, the SST k-ω model can be used as a Low-Re turbulence model without any damping functions. The SST formulation also switches to a k-ε behaviour in the free stream and thereby, avoids the common k-ω problem of high sensitivity to the inlet free stream properties. Besides this, the SST k-ω model incorporates a damped cross-diffusion derivative term in the equation for the specific dissipation rate, ω. The definition of the turbulent viscosity is modified to account for the transport of the turbulent shear stress and the modelling constants are different in this case.

Transport equations for k and ω for this model are given as follows

$$\frac{\partial}{\partial t}(\rho k)+\frac{\partial}{\partial x_i}(\rho k u_i)=\frac{\partial}{\partial x_j}[(\mu+\frac{\mu_t}{\sigma_k})\frac{\partial k}{\partial x_j}]+G_k-Y_k+S_k \tag{2.8}$$

And

$$\frac{\partial}{\partial t}(\rho \omega)+\frac{\partial}{\partial x_i}(\rho \omega u_i)=\frac{\partial}{\partial x_j}[(\mu+\frac{\mu_t}{\sigma_\omega})\frac{\partial \omega}{\partial x_j}]+G_\omega-Y_\omega+D_\omega+S_\omega \tag{2.9}$$

In equation (2.8) and (2.9), G_k represents the generation of turbulence kinetic energy due to the mean velocity gradients, G_ω is the generation of ω, Y_k and Y_ω represent the dissipation of k and ω due to turbulence respectively, D_ω represents the cross diffusion term. S_k and S_ω are user-defined source terms. σ_k and σ_ω are the turbulent Prandtl numbers for k and ω, respectively, and are defined as

$$\sigma_k=\frac{1}{\frac{F_1}{\sigma_{k,1}}+\frac{1-F_1}{\sigma_{k,2}}} \tag{2.10}$$

$$\sigma_\omega=\frac{1}{\frac{F_1}{\sigma_{\omega,1}}+\frac{1-F_1}{\sigma_{\omega,2}}} \tag{2.11}$$

The turbulent viscosity for this model is computed as follows

$$\mu_t = \frac{\rho k}{\omega} \frac{1}{\max[\frac{1}{\alpha^*}, \frac{SF_2}{a_1 \omega}]} \tag{2.12}$$

The coefficient α^* damps the turbulent viscosity causing a low-Re correction and is defined as

$$\alpha^* = \alpha^*_\infty (\frac{\alpha^*_0 + \frac{Re_t}{R_k}}{1 + \frac{Re_t}{R_k}}) \tag{2.13}$$

where

$$Re_t = \frac{\rho k}{\mu \omega} \tag{2.14}$$

$$\alpha^*_0 = \frac{\beta_i}{3} \tag{2.15}$$

F_1 and F_2 are the blending functions and are given by

$$F_1 = \tanh(\phi_1^4) \tag{2.16}$$

where

$$\phi_1 = \min[\max(\frac{\sqrt{k}}{0.09 \omega y}, \frac{500 \mu}{\rho y^2 \omega}), \frac{4 \rho k}{\sigma_{\omega,2} D^+_\omega y^2}] \tag{2.17}$$

$$D^+_\omega = \max[2 \rho \frac{1}{\sigma_{\omega,2}} \frac{1}{\omega} \frac{\partial k}{\partial x_j} \frac{\partial \omega}{\partial x_j}, 10^{-10}] \tag{2.18}$$

and

$$F_2 = \tanh(\phi_2^2) \tag{2.19}$$

where

$$\phi_2 = \max[2\frac{\sqrt{\mathrm{k}}}{0.09\omega \mathrm{y}}, \frac{500\mu}{\rho \mathrm{y}^2 \omega}] \tag{2.20}$$

The model constants have the following values for the SST k-ω model

$\sigma_{\mathrm{k},1} = 1.176$ $\sigma_{\omega,1} = 2.0$ $\sigma_{\mathrm{k},2} = 1.0$ $\sigma_{\omega,2} = 1.168$

$\mathrm{a}_1 = 0.31$ $\beta_{\mathrm{i},1} = 0.075$ $\beta_{i,2} = 0.0828$

All other model constants are similar to those of the k-ω model and are given by

$a_\infty^* = 1.0$ $a_\infty = 0.52$ $a_0 = \frac{1}{9}$ $\beta_\infty^* = 0.09$ $\beta_{\mathrm{i}} = 0.072$ $\mathrm{R}_\beta = 8$

$\mathrm{R}_{\mathrm{k}} = 6.0$ $\mathrm{R}_\omega = 2.95$ $\varsigma^* = 1.5$ $\mathrm{M}_{\tau,0} = 0.25$ $\sigma_{\mathrm{k}} = 2.0$ $\sigma_\omega = 2.0$

2.5.5 Large Eddy Simulation

Turbulent flow consists of a continuous spectrum of scales ranging from the largest to the smallest. Turbulent eddies of different sizes are often used to describe a turbulent flow across those scales. A turbulent eddy can be thought of as a local swirling motion whose characteristic dimension is the local turbulence scale. The primary idea behind LES is to simulate only the larger scales of turbulence, that are set by geometry or specific flow conditions, and to account for the influence of the neglected smaller scales on the mean flow by the use of a model. This is due to the fact that mass, momentum and energy and any other passive scalars are transported mostly by the large eddies in the motion whilst the small scales vary less with the dimensional constraints and are isotropic and more universal in nature.

The large eddy simulation technique is based on a spatial scale separation between the large scales and the small scales. In order to define the two categories, a reference cut-off length or cut-off frequency has to be determined. The scales that are of characteristic length greater than the cut-off length are called large scales or resolved scales and the

others are called small or sub-grid scales. The influence of the small scales on the large scales of motion is included through sub-grid scale modelling. The separation between the different scales is not associated with a statistical averaging operation and therefore defining the cut-off length or the scale-separation operator is a very difficult task. The difficulty comes from the fact that many parameters contribute to the definition of the effective scale-separation operator observed in practical simulations.

To obtain the governing equations for LES, the Navier-Stokes equations are spatially filtered which effectively filters out those eddies whose scales are smaller than the filter width or grid spacings used in the computations. Filtering the Navier-Stokes equations gives,

$$\frac{\partial \rho}{\partial t} + \frac{\partial}{\partial x_i}(\rho \overline{u_i}) = 0 \tag{2.21}$$

$$\frac{\partial}{\partial t}(\rho \overline{u_i}) + \frac{\partial}{\partial x_j}(\rho \overline{u_i}\,\overline{u_j}) = \frac{\partial}{\partial x_j}(\mu \frac{\partial \sigma_{ij}}{\partial x_j}) - \frac{\partial \overline{p}}{\partial x_i} - \frac{\partial \tau_{ij}}{\partial x_j} \tag{2.22}$$

where the overbar in equations (2.21) and (2.22) represents the filtered or resolved components of pressure, velocity and strain.

The stress tensor due to molecular viscosity, σ_{ij} is defined by

$$\sigma_{ij} \equiv [\mu(\frac{\partial \overline{u_i}}{\partial x_j} + \frac{\partial \overline{u_j}}{\partial x_i})] - \frac{2}{3}\mu \frac{\partial \overline{u_i}}{\partial x_i}\delta_{ij} \tag{2.23}$$

The Sub-grid scale stresses are computed from

$$\tau_{ij} - \frac{1}{3}\tau_{kk}\delta_{ij} = -2\mu_t \overline{S_{ij}} \tag{2.24}$$

where, τ_{ij} is the sub-grid Reynolds stress (analogous to the turbulent stresses that result from Reynolds-averaging of the Navier-Stokes equations), μ_t is the sub-grid scale turbulent viscosity, τ_{kk} is the isotropic part of the sub-grid scale stresses added to the

filtered static pressure term and $\overline{S_{ij}}$ is the rate of strain tensor for the resolved scale, defined by

$$\overline{S_{ij}} \equiv \frac{1}{2}\left(\frac{\partial \overline{u_i}}{\partial x_j} + \frac{\partial \overline{u_j}}{\partial x_i}\right) \tag{2.25}$$

It is the purpose of the sub-grid models to resolve the influence of these additional unknown sub-grid scale stresses that result from the filtering process through the computation of turbulent viscosity. Sub-grid scale models are similar to the turbulence model used in RANS calculations, and their primary purpose is to provide the influence of the small scales, usually based on some gradient diffusion hypothesis. The role of the small eddies is predominantly to accept energy from the larger scales and dissipate it, and that this net transfer of energy is considered as a one-way process. This influence acts primarily as a sink for the energy of the large scales to ensure that the statistics of the large scales are correct in that they continually dissipate their energy.

Currently three sub-grid scale models are available in Star-CCM+ that model the sub-grid scale viscosity μ_t, which are: Smagorinsky-Lilly sub-grid scale model (Smagorinsky, 1963),(Lilly, 1992), Dynamic Smagorinsky sub-grid scale model (Germano *et al.*, 1991), (Lilly, 1992) and the Wall-Adaptive Local Eddy viscosity (WALE) sub-grid model (Nicoud and Ducros, 1999). Only the Dynamic Smagorinsky model is discussed here as that model is used in the current study and has the correct limiting behaviour in laminar flows and wall bounded turbulent flows (Lévêque *et al.* (2007)).

2.5.6 Dynamic Smagorinsky-Lilly Model

The Smagorinsky-Lilly model was proposed by Smagorinsky (1963) and is the basic sub-grid scale model. The dynamic Smagorinsky model was developed after few shortcomings of the simple Smagorinsky-Lilly model which didn't accurately model large-scale fluctuations in the presence of mean shear and transitional flows near solid boundaries.

In this model, the eddy viscosity is modeled by

$$\mu_t = \rho L_s^2 \left|\bar{S}\right| \tag{2.26}$$

where L_s is the mixing length for the sub-grid scales and

$$\left|\bar{S}\right| = \sqrt{2\bar{S}_{ij}\bar{S}_{ij}} \tag{2.27}$$

L_s is computed using $L_s = \min(\kappa d, C_s \Delta)$

where κ is the von-Kármán constant, *d* is the distance to the closest wall, C_s is the Smagorinsky constant and Δ is the local grid-scale. If Δx, Δy and Δz are the grid-spacings of a computational volume in X, Y and Z directions, then, empirically, Δ is computed using the volume of the computational cell V by

$$\Delta = \sqrt[3]{\Delta x \Delta y \Delta z} = V^{\frac{1}{3}} \tag{2.28}$$

Lilly derived a value of 0.23 for C_s in the case of homogeneous isotropic turbulence in the inertial range which didn't accurately model large-scale fluctuations in the presence of mean shear and transitional flows near solid boundaries. Henceforth, Germano *et al.*, (1991) and subsequently Lilly (1992) tried to overcome the limitations and come up with a Smagorinsky-Lilly constant C_s that is dynamically computed based on the information provided by the resolved scales of motion. The dynamic procedure, therefore, obviates the need for users to specify the model constant C_s in advance.

The concept of the dynamic procedure is to apply a second filter (called the test filter) to the equations of motion. The new filter width $\hat{\Delta}$ is equal to twice the grid filter width Δ. Both filters produce a resolved flow field. The difference between the two resolved flow fields is the contribution of the small scales whose size is in between the grid filter and the test filter. The information related to these scales is used to compute the model constant.

At the test filtered field level, the SGS tensor can be expressed as:

$$T_{ij} = \overline{\hat{\rho} u_i u_j} - (\overline{\hat{\rho} u_i}\,\overline{\hat{\rho} u_j} / \overline{\hat{\rho}}) \tag{2.29}$$

Both T_{ij} and τ_{ij} are modelled in the same way with the Smagorinsky-Lilly model, assuming scale similarity:

$$\tau_{ij} = -2C\overline{\rho}\Delta^2 S \left| (S_{ij} - \frac{1}{3} S_{kk}\delta_{ij}) \right. \tag{2.30}$$

$$T_{ij} = -2C\overline{\hat{\rho}}\hat{\Delta}^2 \left| \hat{S} \right| (\hat{S}_{ij} - \frac{1}{3}\hat{S}_{kk}\delta_{ij}) \tag{2.31}$$

In equations number (2.30) and (2.31), the coefficient C is assumed to be the same and independent of the filtering process. The grid filtered SGS and the test filtered SGS are related by the Germano identity (Germano *et al.*, 1991) such that

$$L_{ij} = T_{ij} - \tau_{ij} \tag{2.32}$$

Substituting the grid-filter Smagorinsky-Lilly model, the following expressions can be derived to solve for C with the contraction obtained from the least square analysis of Lilly (1992).

$$C = \frac{(L_{ij} - L_{kk}\delta_{ij}/3)}{M_{ij}M_{ij}} \tag{2.33}$$

The $C_S = \sqrt{C}$ obtained using the Dynamic-Smagorinsky Lilly model varies in time and space over wide range. To avoid numerical instability, both the numerator and the denominator in the equation are locally-averaged or filtered using the test filter. The dynamic variation of the constant allows the model to obtain correct results for wall bounded flows without the use of damping functions.

2.5.7 Solution Parameters

For the steady RANS modelling (SST k-ω) of the decay of turbulent kinetic energy the second order upwind discretization for momentum and first order upwind discretization

scheme for turbulence parameters (turbulent kinetic energy and specific dissipation rate) was used while the pressure interpolation was second order. As the flow is aligned with the grid in the present study, the first order upwind discretization schemes for the turbulence parameters will yield results of the same degree of accuracy (less than 1% difference) as of the second order with low numerical diffusion and better convergence. This is verified from the results shown in figure (2.4) where a relative comparison between the first order upwind and second order upwind discretization schemes are presented, used for the computation of turbulence parameters using SST k-ω model. As expected, the second order scheme in the present case provides no improvement in the accuracy of the solution field pertaining to the decay of TKE along the streamwise distance.

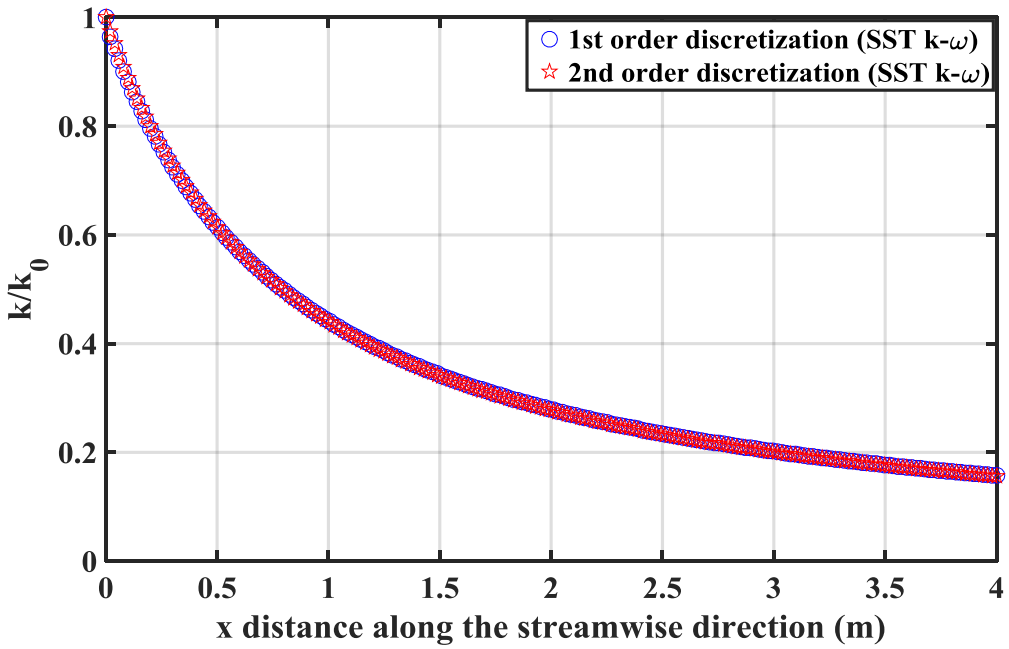

Figure 2.4 Comparison between the 1st order and 2nd order discretization schemes of the SST k-ω model with respect to the spatial decay of TKE ($\bar{U}$ = 4m/s, TI = 10% and L_u = 0.10m)

However, it should be kept in mind that, for near wall bounded turbulent flows, the second order discretization schemes provide higher solution accuracy and numerical

stability in the solution than the first order schemes because of less numerical diffusion and increased damping in the vicinity of the wall solid-boundary.

For the pressure velocity coupling, the Semi-Implicit method for Pressure Linked Equations (SIMPLE) algorithm (Patankar *et al.* 1972) was used for the steady RANS as it is more suitable for steady state flows. For the evaluation of gradients and derivatives, the Least-square cell based gradient method is employed as it is more accurate and less expensive than other gradient methods on a structured hexahedral mesh.

For LES, a bounded central-differencing discretization scheme was used for the convective terms in the momentum equations. This scheme provides improved accuracy for LES calculations. The segregated flow model according to the SIMPLE algorithm was used to solve for the solution updates for the pressure and velocity field along the domain. The Hybrid Gauss-Least squares method was used for the gradient computation for the pressure terms and the secondary gradients for the diffusion terms with the Venkatakrishnan method (Venkatakrishnan, 1993) for limiting the reconstruction gradients and therefore more accurate than the Green-Gauss method. The limited reconstruction gradients are used to determine the scalar values at the cell faces. These scalar values are used in computing the flux integrals. The second-order upwind convection schemes were used for all the other transport equation terms and the implicit unsteady method for time-step marching was used for better stability with no restrictions on the choice of the time-step size. Based on the cut-off frequency and the percentage of the turbulent kinetic energy resolved in this study a time step size of 0.002s was used. The simulations were run for 40s of flow time that would yield 20000 samples of the time-histories of the velocity fields, large enough (in this case) to adequately describe the statistical properties of turbulence decay. The statistical average of the last 30s of flow time with 15000 samples was performed to evaluate the descriptive properties of the flow field throughout the domain. The convergence criteria were kept at 10^{-4} for all the momentum terms in the simulations for this study. A maximum no. of 200 inner loop iterations were specified to fully ensure the residual convergence of continuity, X-momentum, Y- momentum and Z-momentum to 10^{-4} for each unsteady physical time-step of the implicit solver and then the solution marched onto the next time-step.

2.6 Boundary Conditions

The proper of choice of boundary conditions for any CFD based problem is very important, as the boundary conditions would drive the flow field to be solved inside the computational domain. The boundary conditions should also be as close to the physical reality that would represent the influence of the surroundings which have been cut-off by the boundaries of the computational domain. The inlet boundary condition is of extreme importance in this regard as, in many cases, the fluid behaviour within the domain is determined in large part by the inlet behaviour.

2.6.1 Boundary conditions for steady Reynolds Averaged Navier-Stokes Model (RANS)

For the steady RANS study, a well-specified velocity boundary condition was defined at the inlet to construct the flow velocity along with the turbulent parameters i.e. turbulence intensity in percentage (TI) and turbulence length scale (L_u) for turbulent calculations. The pressure outlet boundary condition is specified with a gauge pressure of zero Pascals which physically relates to the atmospheric pressure to which the flow exits. The slip boundary condition was specified at all the other boundaries where the shear stress is assumed to be zero so that it had negligible effect on the decay of TKE inside the domain.

2.6.2 Inflow and Boundary conditions for Large Eddy Simulation (LES)

For LES calculations, generating the inlet conditions is considerably more difficult than for RANS modelling. Ideally, the proper inlet boundary condition should represent physical turbulent motions of stochastically varying nature that would have the structure of turbulence, of coherent eddies across a range of spatial scales starting from integral length scale to the Kolmogorov length scale. For free stream turbulence, it is important to recreate the overall energy contained in the turbulent fluctuations and the distribution of energy along the length scales having proper coherent energy spectra. The importance of defining proper inflow boundary conditions while using LES was extensively discussed by various researchers (Sagaut *et al.*, (2003); Tutar and Celik, (2007) ; Xie and Castro, (2008) **;** Dagnew and Bitsuamlak, (2013)). According to Keating *et al.* (2004) inlet

boundary conditions can be generated by using three methods: precursor database, recycling method, and synthesizing the turbulence. A review of two different methods to define inlet conditions for LES is done by Tabor and Baba-Ahmadi (2010). They classified the inlet conditions into two different categories namely synthesis inlets and precursor simulation methods and discussed the advantages of one method over the other. Their study revealed that, although synthesis methods are easy for specifying parameters of the turbulence, such as length scales or turbulent energy levels; they can be inaccurate and may require provision of an inlet development section before turbulence can develop fully. On the other hand, precursor simulation methods have the advantage of generating true turbulence with required characteristics but are cumbersome to modify the required state of turbulence. Recently, Aboshosha *et al.* (2015) have developed an efficient inflow generator technique for LES modelling based on synthesizing random divergent-free-turbulent velocities, which is named the Consistent Discrete Random Flow Generation technique (CDRFG). This method is able to model properly the statistical properties of the inflow turbulence represented in the turbulent spectra that generates consistent coherency in the velocity field matched with the available atmospheric boundary layer flow statistics (Aboshosha *et al.*, 2015). The technique is based on discretizing the power spectrum of velocities into a number of segments using the original random flow generation (RFG) technique (Kraichnan, (1970); Smirnov *et al.*, (2001)), but with some modifications to allow modelling of a spectrum with an arbitrary distribution. This technique has been used in the present study to generate isotropic and spatially homogeneous velocity fields at the inlet based on the von-Kármán turbulent spectra which was later used in defining the inlet boundary conditions for all the simulations. Details of the technique including a matlab source code, are also provided in Aboshosha *et al.* (2015). A pressure outlet boundary condition was specified at the outlet where the flow issues into a zero-gauge pressure surroundings with all the other boundaries treated as slip walls.

2.7 Flow Characteristics at the Inlet

In the present section the flow behaviour at the inlet is assessed in terms of isotropy and homogeneity of the turbulent velocity fields. One might argue that no real turbulent flow

is isotropic or even homogeneous at large scales and questionable at small scales. But it is emphasized here that the assumptions of isotropy and homogeneity only allow one to analyze turbulence in a more simplified manner in terms of the varying dynamics of the 3D scales of turbulence.

2.7.1 Isotropy

The turbulent flow characteristics at the inlet are gauged in terms of isotropy of the velocity fields. For an isotropic flow, skewness of the streamwise velocity fluctuation component $S(u) = \overline{u'^3} / \overline{u'^2}^{\frac{3}{2}}$, must be zero and this needs to be true for all directions of isotropy (Mohamed and Larue, 1990). Figure (2.5) shows an example of the statistics of skewness coefficient of the velocity fluctuations at the inlet (0,0,0), over 20,000 samples, with an initial transience until 3000 samples (fig. 2.5) which corresponds to 6s of flow time that is ignored for the computation of the averaged statistics from the data. The convergence criteria for the statistical sampling was chosen based on the statistics of the mean flow velocity ($\overline{U}$) and the mean of the turbulent velocity fluctuations ($\overline{u'^2}$) which are the first and the second-order statistics. From the figure it is clearly seen that the values of isotropy fluctuate around 0 with a statistical averaged magnitude of 0.0092 averaged over 17000 samples obtained from the LES simulations. The statistics for the other two skewness coefficients of the spanwise velocity component (v) and the normal velocity component (w) are also plotted in the same figure (2.5) to confirm the isotropy of the flow at the inlet in all directions. All the data show near converged statistics after initial transience of 3000 samples.

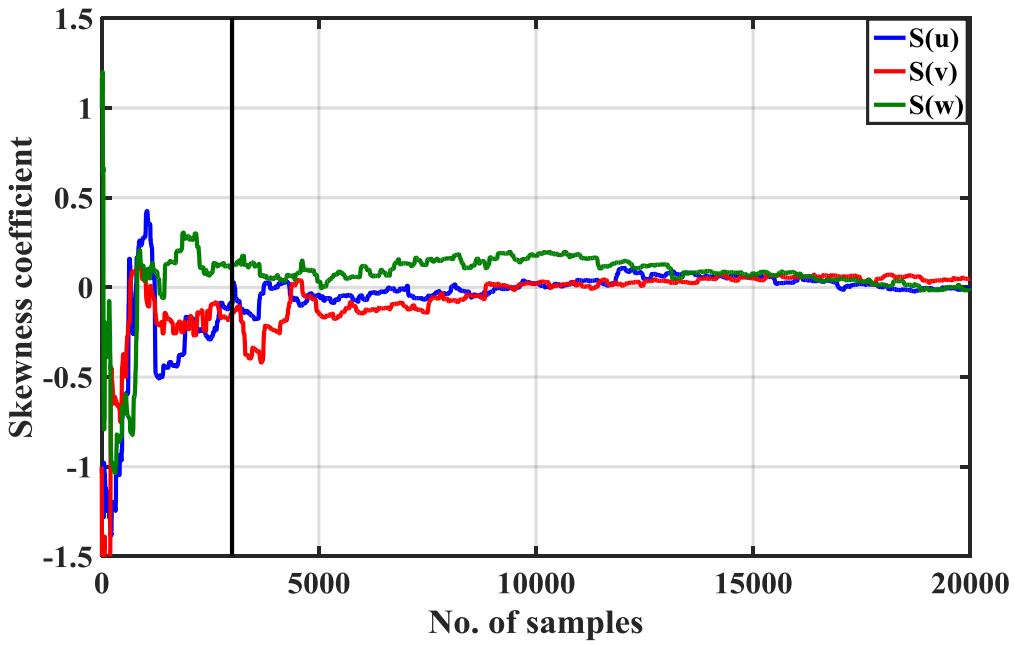

Figure 2.5 Skewness coefficient of the different velocity components obtained from LES simulations with an initial condition of $\bar{U}$ = 4m/s, TI = 10% and L_u = 0.10m

2.7.1.1 Spatial Homogeneity

The transverse and normal variation of the root-mean squares of the u, v and w velocity fields (denoted by u', v' and w') at thirteen different points at the inlet are presented in table (2.1) and they all vary within 2% of the mean value (Table 2.2) which confirms the homogeneity of the flow field at the inlet plane. Figure (2.6) and figure (2.7) shows the transverse and the normal distribution of the turbulence intensity (TI in %) along the inlet plane which gives another measure of the spatial homogeneity. The peak to peak variation of the turbulence intensity in the transverse direction is about 1.39% and in the normal direction is about 2.6%.

Table 2.1 Spanwise and normal variation of the root-mean square of the velocity fields at the Inlet with initial condition of $\bar{U}$ = 4m/s, TI = 10% and L_u = 0.10m

x(m)	y(m)	z(m)	(u') (m/s)	(v') (m/s)	(w') (m/s)	TI (%)
0	0	-0.4	0.38	0.38	0.40	9.66
0	0	-0.2	0.39	0.39	0.39	9.70
0	0	-0.1	0.39	0.39	0.39	9.76
0	0	0	0.39	0.39	0.40	9.75
0	0	0.1	0.38	0.38	0.39	9.67
0	0	0.2	0.37	0.38	0.38	9.52
0	0	0.4	0.38	0.38	0.40	9.75
0	-0.4	0	0.38	0.40	0.38	9.62
0	-0.2	0	0.38	0.39	0.38	9.58
0	-0.1	0	0.38	0.39	0.39	9.64
0	0.1	0	0.37	0.39	0.40	9.58
0	0.2	0	0.39	0.40	0.38	9.61
0	0.4	0	0.38	0.39	0.39	9.71

Table 2.2 Percentage variation of root-mean square velocities at the inlet plane

	Components	Percentage
Standard deviation of u', v', w' and turbulence intensity as a percentage of its mean value	$(\mathbf{u'})$	1.68%
	$(\mathbf{v'})$	1.30%
	$(\mathbf{w'})$	1.81%
	$TI = \frac{\sqrt{\frac{1}{3}(\overline{u'^2})+(\overline{v'^2})+(\overline{w'^2})}}{\bar{U}} \times 100$	0.80%

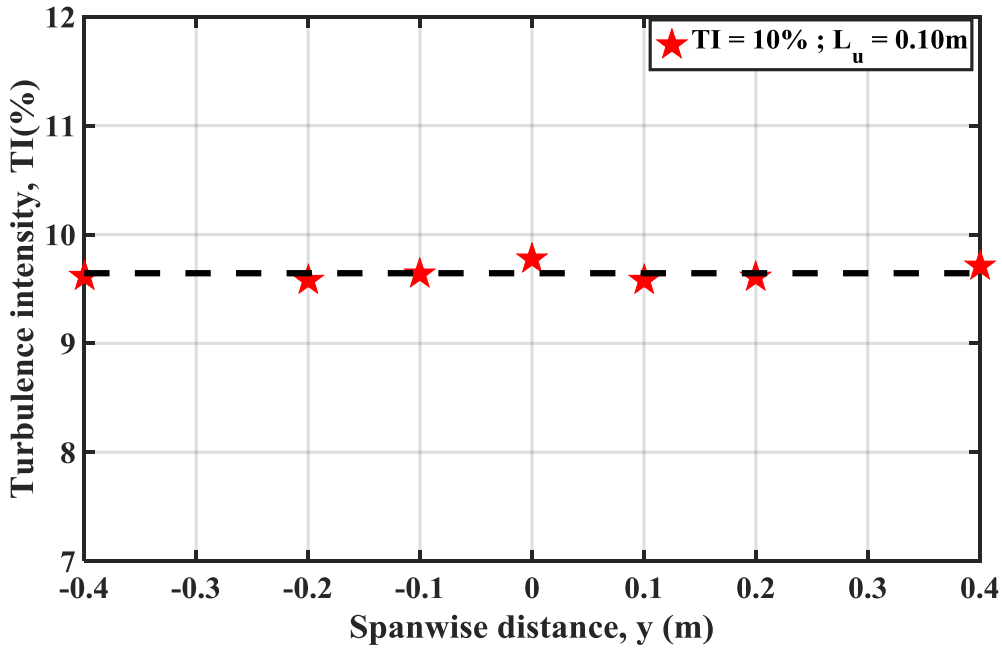

Figure 2.6 Transverse distribution of turbulence intensity laterally across the inlet plane obtained from LES simulations with an initial condition of $\bar{U}$ = 4m/s, TI = 10% and L_u = 0.10m

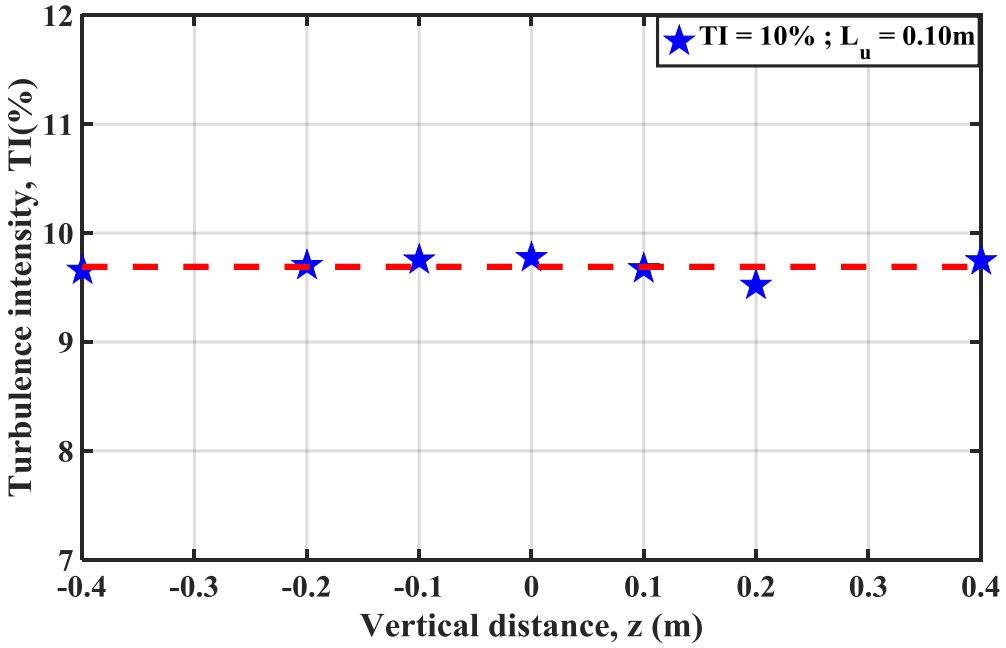

Figure 2.7 Normal distribution of turbulence intensity vertically across the inlet plane obtained from LES simulations with an initial condition of $\bar{U}$ = 4m/s, TI = 10% and L_u = 0.10m

2.7.2 Probability Density Function

The probability density function (PDF) gives a measure of the distribution of the random data about the mean. The equation of the probability density function is given by $B(u) = \frac{N_x}{N\Delta u}$ where, N_x is the number of data samples per bin, N is the total number of data points (17000 in the present case); and Δu is the interval size which is taken as 0.05m/s. The PDF is compared to the Gaussian distribution calculated using the following equation.

$$B(u)_{Gaussian} = \frac{1}{\sigma\sqrt{2\pi}} e^{-\frac{(u_i-\bar{U})^2}{2\sigma^2}} \tag{2.34}$$

where σ is the standard deviation of the velocity fluctuations, u_i is the instantaneous velocity component and $\bar{U}$ is the statistical mean of the instantaneous velocity values. Table (2.3) shows a simple comparison between the PDF and the Gaussian distribution.

The comparison shows that there is a slight deviation from the normal distribution which is given by a slight positive value of the skewness measurement and a slightly lower value of the kurtosis function. The kurtosis function is given by $K(u) = \overline{u'^4} / \overline{u'^2}^2$ where u' is the streamwise velocity fluctuation value. The statistical sampling of the kurtosis magnitudes is shown in figure (2.8) with an initial transient period extending up to 3000 samples, corresponding to 6s of flow time. Figure (2.8) also reveals that the turbulent velocity flow fields are consistent with the normal distribution of the data. Figure (2.9) shows the plot for both the probability density function along with the normal distribution normalized by the mean velocity. The difference in skewness is shown by small shift of data from the normal distribution and slight increase in the tails is attributed to the small difference in the kurtosis values.

Table 2.3 Comparison between Probability Density Function and Normal Distribution

Quantity	B(u)	Normal Distribution	Deviation
Skewness	0.01	0	0.01
Kurtosis	2.92	3	-0.08

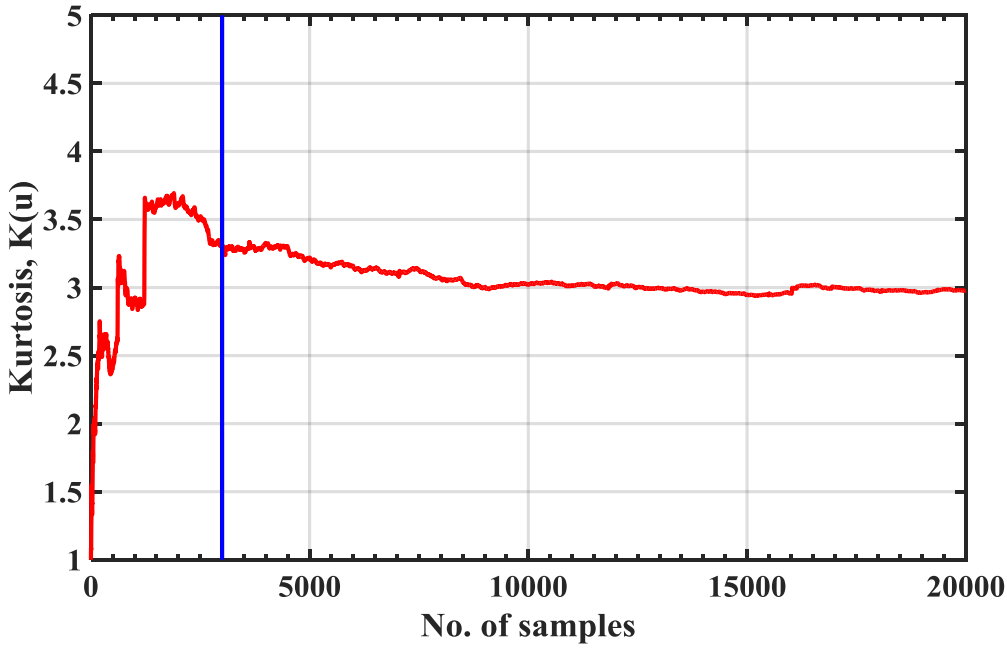

Figure 2.8 Kurtosis function of the streamwise velocity component obtained from LES simulations with an initial condition of $\bar{U}$ = 4m/s, TI = 10% and L_u = 0.10m

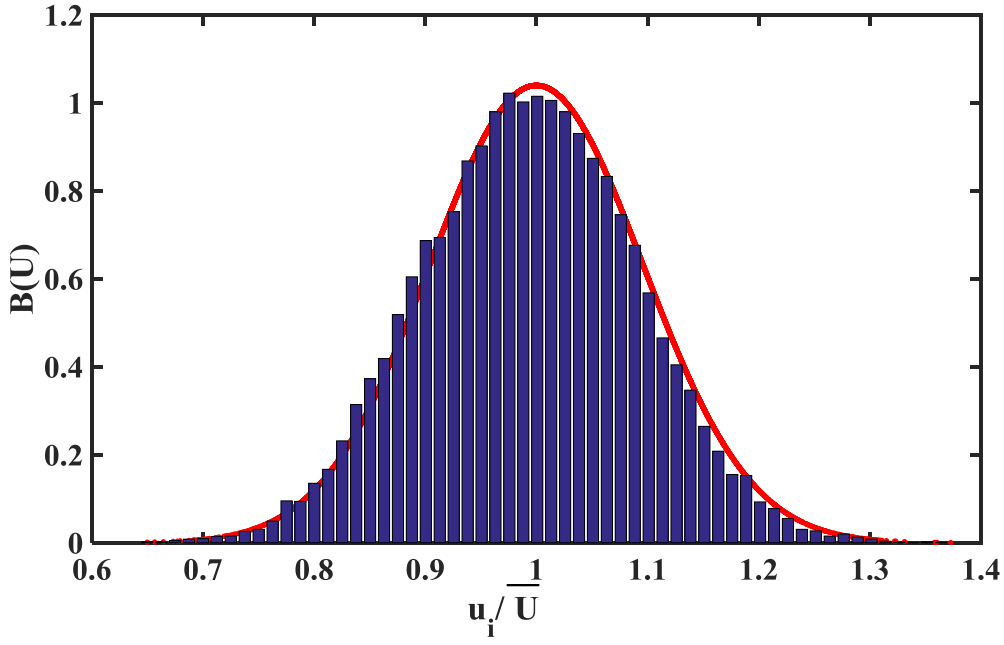

Figure 2.9 Probability density function plotted against the normal Gaussian distribution normalized by mean velocity ($\bar{U}$ = 4m/s, TI = 10% and L_u = 0.10m)

2.7.3 Inertial sub-range of Spectral Energy Transfer

The inertial sub-range in a wavenumber space is the region where turbulent kinetic energy from the larger eddies is being transferred per unit time to the small scale dissipative range of the eddies. The existence of this region requires that the Reynolds number is high enough so that the flow is fully turbulent in nature. The transport of energy in the wavenumber space is called spectral energy transfer and is given by the assumption of the cascade process, i.e. the energy transfer per unit time from eddy-size-to-eddy size is the same for all the eddy sizes and is given by ε. The turbulent kinetic energy, k, of an eddy of size (length scale), $\frac{1}{\kappa}$ (where κ is the wave-number proportional to the inverse of the length scale of an turbulent eddy), represents the kinetic energy of all the eddies of this size. The eddies in this region are independent of both the large, energy containing eddies and the eddies in the dissipation range and, hence, one can argue that the eddies in this region should be characterised by the spectral transfer of energy per unit time (ε) and the size of the eddies, $\frac{1}{\kappa}$. (Versteeg and Malalasekera, (2007), Davidson, (2015). Dimensional analysis gives

$$\mathrm{E}(\kappa) = \mathrm{C}\varepsilon^{\frac{2}{3}}\kappa^{-\frac{5}{3}} \tag{2.35}$$

This is the important Kolmogorov spectrum law (Kolmogorov, 1941a, 1941b) or the -5/3 decay law which states that, if the flow is fully turbulent in nature, the energy spectra should exhibit a -5/3 decay in the inertial region of the flow. Figure (2.10) shows the spectral energy density measured at the centre of the inlet plane at point (0,0,0) that has a universal slope of -1.66 i.e. -5/3 which indicates that the rate of energy transfer is evenly distributed between the larger eddies and the smaller scales of turbulence and that the CDRFG technique succeeds well in accurately developing the random fluctuations of turbulence.

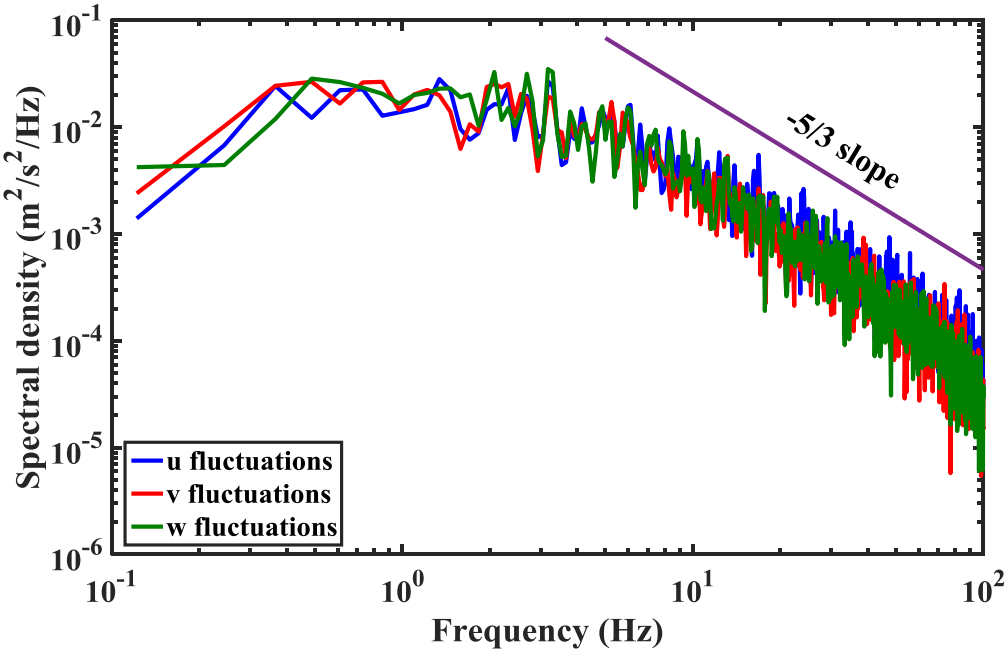

Figure 2.10 Turbulent kinetic energy spectra at the inlet plane plotted with a reference line of slope (-5/3) representing Kolmogorov decay ($\bar{U}$ = 4m/s, TI = 10% and L_u = 0.10m)

2.8 Model Convergence

2.8.1 Grid-Independence Test

A grid-convergence study was carried out to reduce the discretization errors from the computation of the flow variables within the domain. The grid independence study was carried out for both RANS and LES simulations to ensure an acceptable magnitude of convergence error within the results. The evolution of length scales (L_u) along the streamwise direction and the decay of TKE in the streamwise direction were used as an indicative parameter to assess the relative magnitude of variability of those variables going from one grid-resolution to the other. According to the COST guidelines (Franke *et al.*, 2007), at least three systematically and substantially refined grids should be used for a grid-independence study so that the ratio of the cells for two consecutive grids should be at least 1.5 in each dimension. Three different grid resolutions M1, M2 and M3 were created and used for the present grid-independence tests. The mesh refinement ratio

between M1 and M2 and between M2 and M3 was 2 times in the streamwise direction. The inlet mesh nodes were fixed in each of the three grids as the inlet velocity fields generated at those node points were intended to keep constant for all the three meshes used here. The properties of the three grids are summarized in table (2.4). The grid-independence study for both RANS and LES was carried out for a mean inlet velocity $(\overline{U})$ of 4m/s, inlet turbulence intensity (TI) of 10% (TKE = 0.24 m^2/s^2) and inlet integral length scale (L_u) of 0.1m.

Table 2.4 Properties of the different grids used in the current study

Grid	Element size (Δx)	Element size (Δy)	Element size (Δz)	No. of cells
M1 (Coarse)	40mm	20mm	20mm	250,000
M2 (Medium)	20mm	20mm	20mm	500,000
M3 (Fine)	10mm	20mm	20mm	1,000,000

For steady RANS simulation, the turbulent properties for free stream flow i.e. the integral length scales and non-dimensional TKE i.e. $(k' = k/\overline{U^2})$ along the streamwise direction were compared for the three meshes. For LES, the integral length scale values and non-dimensional TKE (k') values, statistically averaged over 17000 samples were compared in relative to each other to check the grid-independence. The variability of non-dimensional TKE and the integral length scales for all the three different grid results are presented here in the graphical form. Figure (2.11) and figure (2.12) shows the streamwise variation of the non-dimensional turbulent kinetic energy (k') and the length scales (L_u) for three different grids for the steady RANS simulation whereas, figure (2.13) and figure (2.14) shows the streamwise evolution of non-dimensional turbulent kinetic energy (k') and the length scales (L_u) for three different grids obtained from the LES simulations.

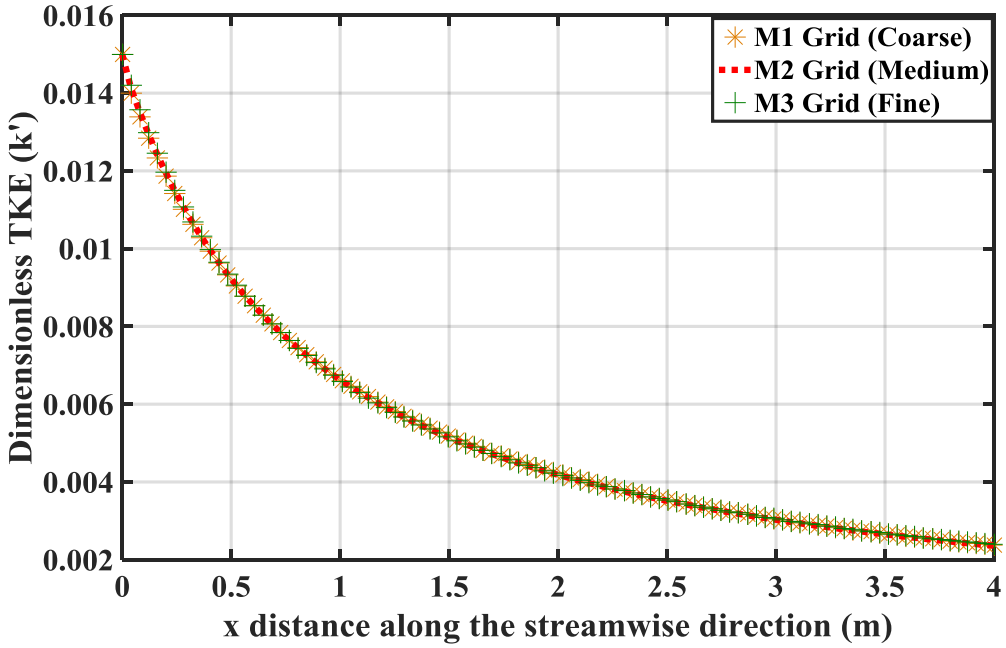

Figure 2.11 Comparison of streamwise decay of non-dimensional TKE for coarse, medium and finer mesh (Steady RANS) ($\bar{U}$ = 4m/s, TI = 10% and L_u = 0.10m)

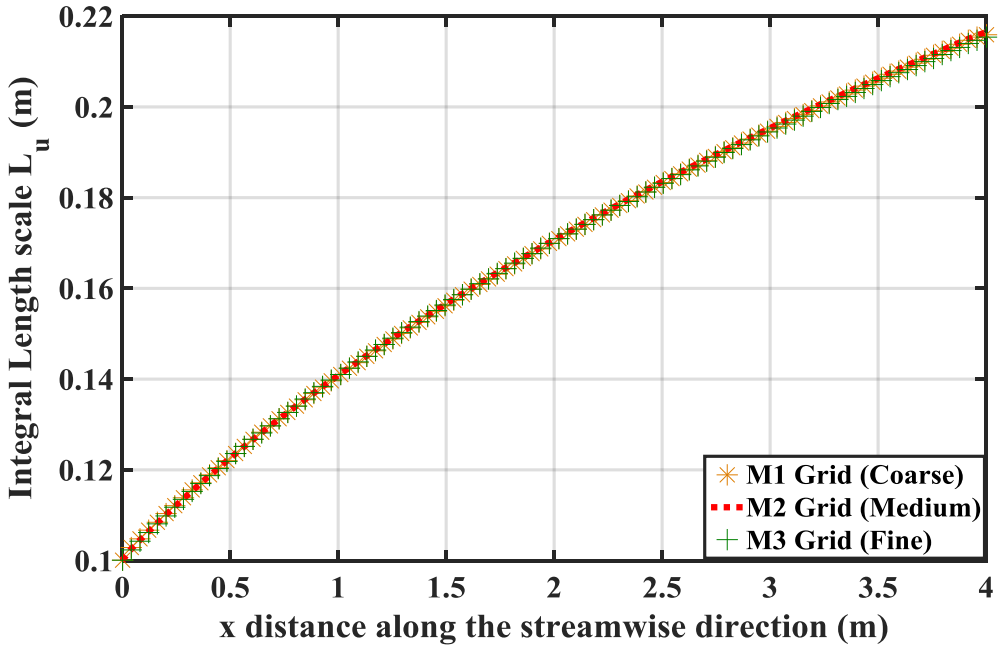

Figure 2.12 Comparison of streamwise evolution of length scales for coarse, medium and finer grids (Steady RANS) ($\bar{U}$ = 4m/s, TI = 10% and L_u = 0.10m)

For RANS simulations, the variability in non-dimensional TKE going from the M1 grid to M2 in proportion to its average value over the constant region where the TKE is fairly uniform (i.e. x = 2m to x = 4m) is 0.97% whereas the variability of the same variable going from the M2 grid to the M3 is 0.64%. Also, the variation of the magnitude of the L_u in proportion to its average value over the constant region from the M1 grid to M2 is 0.25 % and from the M2 grid to M3 grid is 0.15%. Hence, the medium grid M2 is chosen for the present RANS study and for further simulations as the variability of non-dimensional TKE and L_u values for M2 grid relative to M1 grid is below 1% which is accepted as a very good grid convergence (Franke *et al.*, 2004). The results of the grid-independence studies are also presented in tabular form in table (2.5) and table (2.6) for completeness.

Table 2.5 Grid independence study on three different grids for steady RANS predicting the turbulent kinetic energy decay along the streamwise distance

Grid	RMS difference of dimensionless TKE	Average value of dimensionless TKE	% Difference
Coarse (M1)	-	-	-
Medium (M2)	3×10^{-5}	0.00312	0.97
Fine (M3)	2×10^{-5}	0.00311	0.64

Table 2.6 Grid independence study on three different grids for steady RANS predicting the growth of integral length scales along the streamwise centreline

Grid	RMS difference of the integral length scales	Average value of integral length scale	% Difference
Coarse (M1)	-	-	-
Medium (M2)	4.94×10^{-4}	0.1946	0.25
Fine (M3)	2.94×10^{-4}	0.1948	0.15

2.8.1.1 Grid-Resolution for LES

For steady state RANS simulations, insensitivity of the solution field towards further grid refinement is an essential criterion to establish the accuracy of the solution in terms of discretization error. However, such grid convergence is not possible in LES. As a finer grid is utilized, a greater fraction of the turbulence spectrum is directly computed as opposed to directly modeled by an explicit or implicit sub-grid model. It was pointed out by both Speziale, (1998) and Celik *et al.*, (2005) that 'a good LES is almost a Direct Numerical Simulation (DNS)' where the flow field is solved for the smallest Kolmogorov scales. As a consequence, a grid-independence study cannot really exist in LES, since systematic grid-independent LES is actually a DNS, which offers no great benefit while considering economical computational solutions. It is generally agreed that an important requirement for constructing an appropriate grid is to ensure that the cut-off wavenumber or the cut-off frequency is in the inertial sub-range, especially in the primary regions of interest in the simulations.

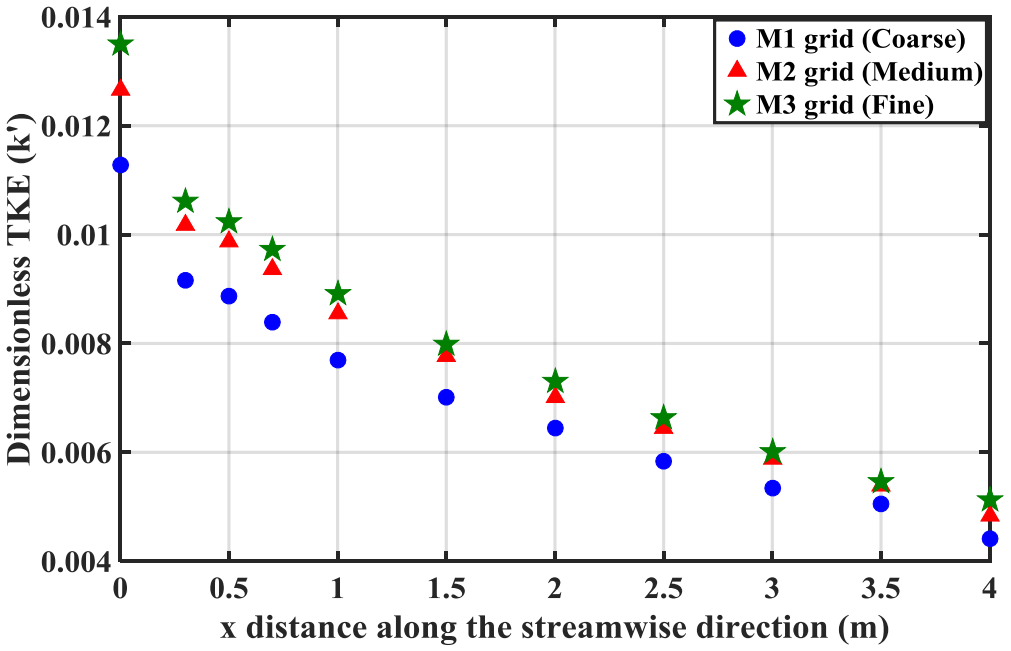

Figure 2.13 Comparison of streamwise decay of non-dimensional TKE for coarse, medium and fine grids (LES) ($\bar{U}$ = 4m/s, TI = 10% and L_u = 0.10m)

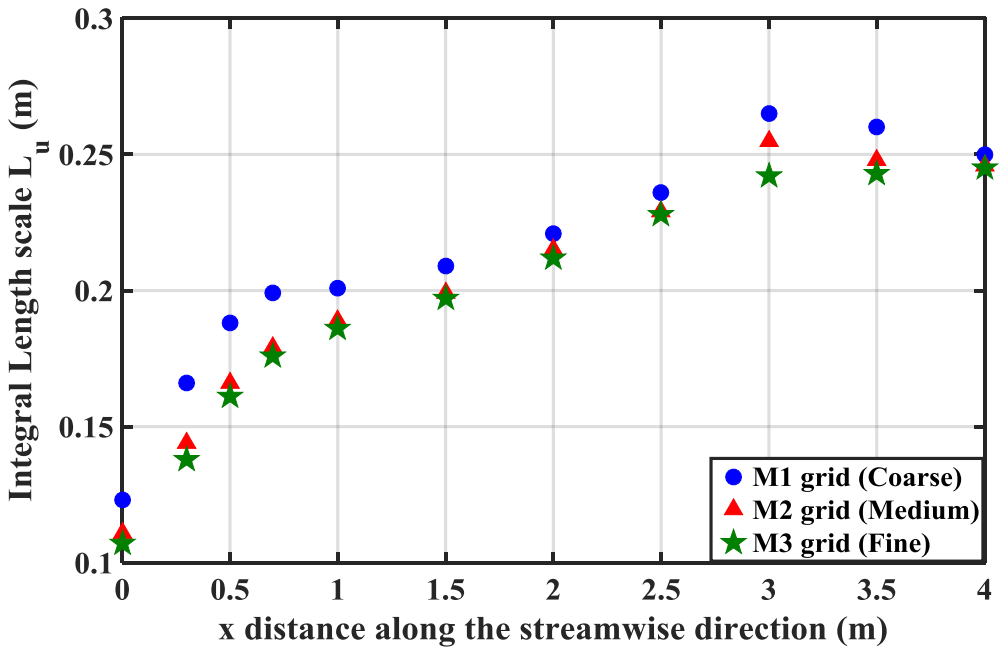

Figure 2.14 Comparison of streamwise evolution of length scales for coarse, medium and finer grids (LES) ($\bar{U}$ = 4m/s, TI =10% and L_u =0.10m)

For LES, the variability in non-dimensional TKE going from the M1 grid to M2 in proportion to its average value over the constant region where the TKE is fairly uniform (i.e. x=2m to x=4m) is 13.15% whereas the variability of the same variable going from the M2 grid to M3 is 4.81%. Again, the variation of the magnitude of the L_u in proportion to its average value over the constant region from the M1 grid to M2 grid is 5.93% and from M2 grid to M3 grid is 2.29%. Hence the fine grid M3 is chosen for the present study and for further simulations as the variability of non-dimensional TKE and L_u for grid M3 relative to grid M2 is below 5% which is within an acceptable value of convergence (Georgiadis *et al.* 2009). The present grid M3 with 1,000,000 cells also corresponds to the least relative discretization error and resolves the most energy containing eddies (resolving 80% of TKE in the present case) (Gerasimov, 2016) that regulate the essential flow properties along the domain. The results of the grid-independence study for the LES simulations are presented in tabular form in table (2.7) and table (2.8) for completeness in discussion.

Table 2.7 Grid independence study on three different grids for LES simulations predicting the turbulence kinetic energy decay at 11 points along the streamwise centreline

Grid	RMS difference of dimensionless TKE	Average value of dimensionless TKE	% Difference
Coarse (M1)	-	-	-
Medium (M2)	0.00074	0.0057	13.15
Fine (M3)	0.00029	0.0060	4.81

Table 2.8 Grid independence study on three different grids for LES predicting the growth of integral length scales at 11 points along the streamwise centreline

Grid	RMS difference of integral length scale	Average value of integral length scale	% Difference
Coarse (M1)	-	-	-
Medium (M2)	0.0138	0.233	5.93
Fine (M3)	0.0052	0.236	2.29

2.8.2 Homogeneity and Isotropy of the velocity fields (LES)

In this section, the spatial homogeneity of the velocity fields, both in the spanwise and normal direction at x = 2m location is first assessed and discussed. Then the isotropy of the flow in the mean flow direction are discussed.

In the following section, the streamwise variation of the mean velocity ($\overline{U}$), along with the turbulence Reynolds number (Re_λ) based on the Taylor microscale (λ), is examined and discussed. All the data were extracted and plotted after the flow statistics converged with respect to the number of samples. Figure (2.15) shows the streamwise variation of

the time-averaged centreline mean velocity $\overline{U}$, normalized with the velocity magnitude specified at the inlet i.e. $\overline{U}_0$, as a function of x. The time-averaged streamwise mean velocity $\overline{U}$ at different x locations downstream was found to be constant within -0.46%/+0.24% of the spatial mean velocity $\overline{U}_0$ specified at the inlet. The velocity profiles also certify that there is no mean shear present in the flow throughout the domain except a very weak acceleration/ deceleration observed in the region 0<x<1m.

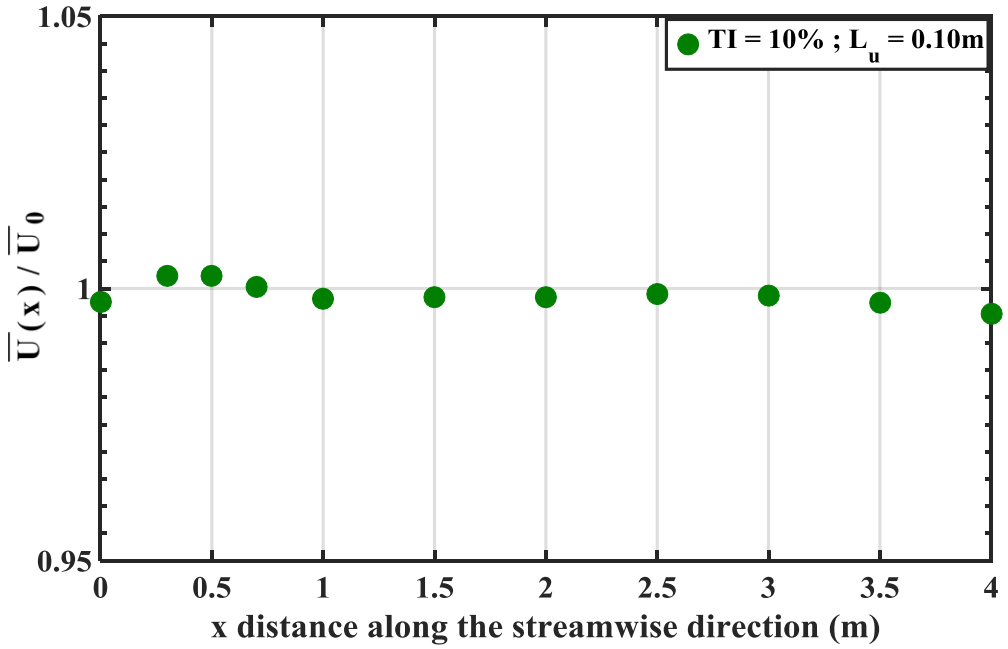

Figure 2.15 Streamwise distribution of $\overline{U}$ along the centreline normalized by the mean velocity at the inlet i.e. $\overline{U}_0$ ($\overline{U}$ = 4m/s, TI = 10% and L_u = 0.10m)

This is illustrated by the development of turbulent Reynolds number, $Re_\lambda = \overline{u'}\lambda / \nu$ (where λ is longitudinal Taylor microscale; ν is the kinematic viscosity) along the centreline in the streamwise direction (fig. 2.16), which shows a weak transient behaviour in the region (0m < x < 1m), followed by a much more gradual slope of the decay of turbulent Reynolds number (Re_λ) downstream where $\overline{U} \approx$ constant. The Taylor longitudinal micro length scale (λ), is computed based on the effect of molecular viscosity and is given by the expression

$$\lambda^2 = 15\nu\frac{\overline{u'^2}}{\varepsilon} \tag{2.36}$$

where ν is taken as 1.57×10^{-5} m^2/s and ε is the turbulent kinetic energy dissipation rate expressed as:

$$\varepsilon = \frac{dk}{dt} \tag{2.37}$$

Invoking Taylor's hypothesis of frozen turbulence (Taylor, 1938b), and replacing the turbulent kinetic energy $k = \frac{1}{2}(\overline{u'^2} + \overline{v'^2} + \overline{w'^2})$ in equation (2.37) one obtains (ε) in the form of

$$\varepsilon = \frac{1}{2}\overline{U}\frac{\overline{dq^2}}{dx} \tag{2.38}$$

where $\overline{q^2} = (\overline{u'^2} + \overline{v'^2} + \overline{w'^2})$. Substituting ($\varepsilon$) from equation (2.38) into equation (2.36) gives the expression of the Taylor micro length scale (λ) in the form of

$$\lambda^2 = \frac{30\nu\overline{u'^2}}{(\overline{U}\frac{\overline{dq^2}}{dx})} \tag{2.39}$$

The turbulent Reynolds number (Re_λ) is then computed from λ which is computed from corresponding values of ν, $\overline{u'^2}$, $\overline{U}$ and $\frac{\overline{dq^2}}{dx}$ at each x location downstream from the inlet. The decay of the turbulent Reynolds number (Re_λ) shown in the figure (2.16) is an indicative of the fact that, as the small-scale turbulence decays with time, the size of the smallest scales becomes larger, which would manifest itself in the size of the average eddy (L_u) increasing.

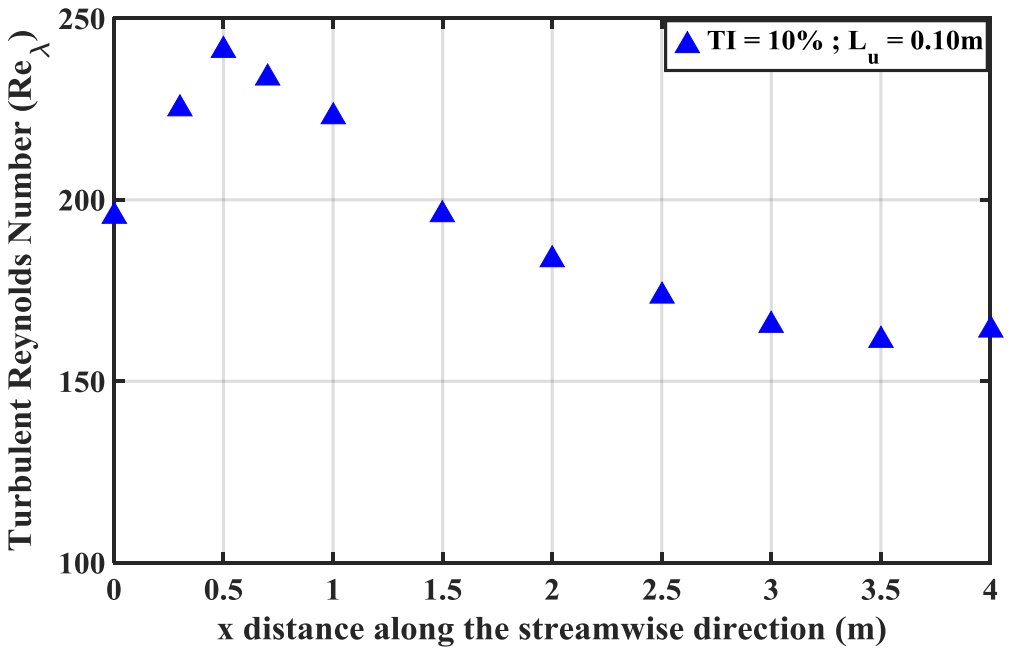

Figure 2.16 Streamwise distribution of turbulent Reynolds number (Re_λ) based on Taylor microscale along the centreline ($\bar{U}$ = 4m/s, TI = 10% and L_u = 0.10m)

The streamwise variation of turbulent Reynolds number (Re_λ) could also cause a slow evolution of the dimensionless decay coefficient (D), as will be seen in the upcoming discussion.

2.8.2.1 Test for Homogeneity

The variation of the root-mean-square of the streamwise velocity fluctuations in both the spanwise and normal directions along 13 points at the mid-section plane (x=2m), of the computational domain is shown in the table (2.9). All the data presented here are statistically averaged over 17000 samples which represents 34 seconds of flow time. It is clearly seen that the variation in the standard deviation of the observed velocity fluctuations, in both span-wise and normal directions, is less than 3% (2.98%) of its average value, which affirms the spatial homogeneity of the turbulent flow field at mid-section downstream from the inlet. This is an indication of the fact that the flow associated with the free stream turbulence is almost homogenous throughout the computational domain.

Table 2.9 Spanwise and normal variation of the root-mean square of the streamwise velocity fields at the centre plane ($\bar{U}$ = 4m/s, TI = 10% and L_u = 0.10m)

x(m)	y(m)	z(m)	u'
2	0	-0.4	0.30
2	0	-0.2	0.30
2	0	-0.1	0.28
2	0	0	0.28
2	0	0.1	0.30
2	0	0.2	0.30
2	0	0.4	0.31
2	-0.4	0	0.31
2	-0.2	0	0.30
2	-0.1	0	0.29
2	0.1	0	0.29
2	0.2	0	0.30
2	0.4	0	0.30

2.8.2.2 Test for Isotropy

For an isotropic flow field, the skewness of the streamwise velocity fluctuations, i.e. $S(u) = \overline{u'^3} / \overline{u'^2}^{\frac{3}{2}}$ should be of zero magnitude. The isotropy of the flow S(u), as a function of streamwise distance at 11 distinct points is shown in figure (2.17), which provides one means of assessing whether the flow reaches isotropy in the domain. Along the centreline

of the domain, where the boundary effects and the mean shear levels are negligible, the flow remains nearly isotropic and the skewness values approach an asymptotic magnitude of zero since there is no source of anisotropy introduced into the flow.

The isotropy ratio $\frac{3\overline{u'^2}}{\overline{q^2}}$ was also checked along the centreline in the streamwise direction and it ranges between 1.02 to 1.15. Similarly, $\frac{3\overline{v'^2}}{\overline{q^2}}$ was found to be in the range of 0.84 and 1.01 and $\frac{3\overline{w'^2}}{\overline{q^2}}$ lies between 0.86 and 1.01, where $\overline{q^2} = \overline{u'^2} + \overline{v'^2} + \overline{w'^2}$.

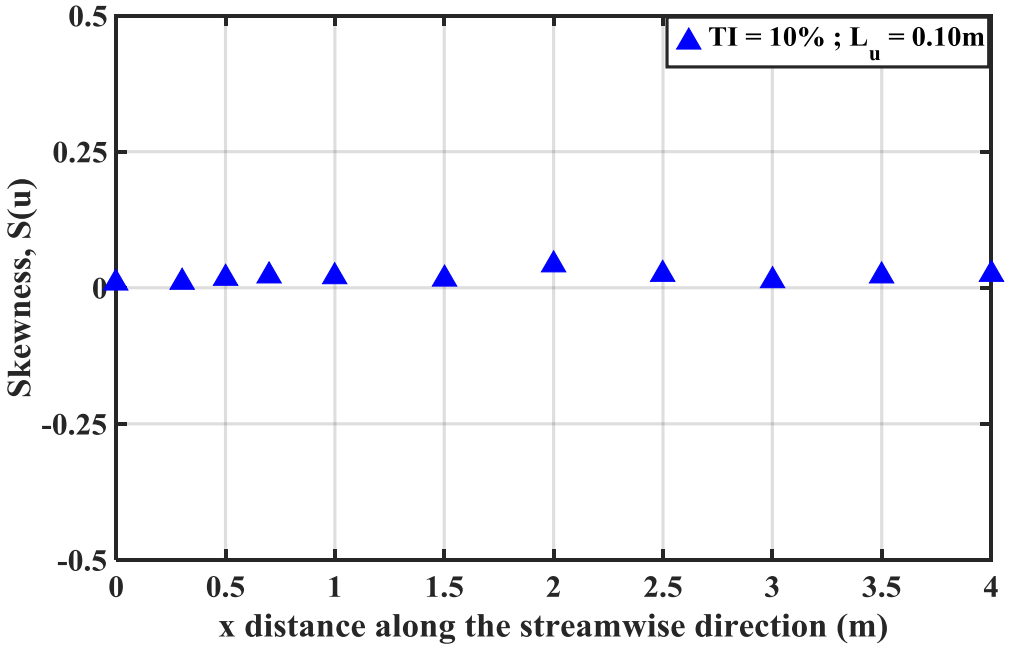

Figure 2.17 Downstream variation of velocity skewness S(u) along the centreline of the domain ($\bar{U}$ = 4m/s, TI = 10% and L_u = 0.10m)

Figure (2.18) shows the downstream variation of the Kurtosis coefficient, $K(u) = \overline{u'^4} / \overline{u'^2}^2$ at 11 points along the centreline through the domain. The kurtosis for a standard normal distribution is 3. The maxima and minima profiles of the kurtosis values at any downstream location varies within 2% of its average value of 3 which confirms that the distribution of data is consistent about its mean.

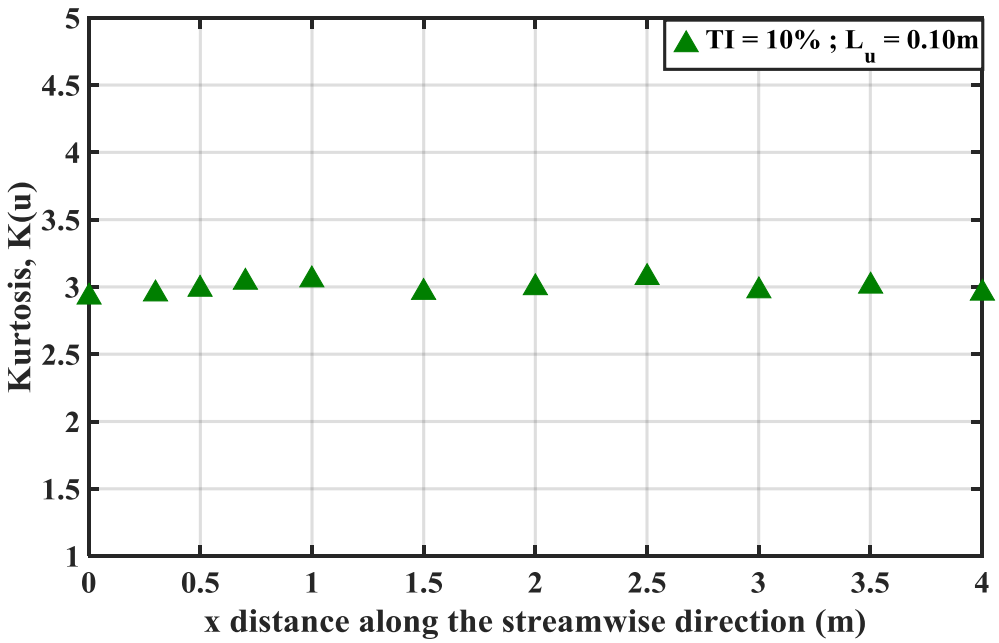

Figure 2.18 Downstream variation of Kurtosis coefficient, K(u) along the centreline of the domain ($\bar{U}$ = 4m/s, TI = 10% and L_u = 0.10m)

2.8.3 Batchelor Turbulence or Saffman Turbulence?

It has been debated over the years among researchers, as to whether the large scales of turbulence, responsible for convecting heat and mass transfer, should be classified as Batchelor Turbulence (Batchelor, 1953) or Saffman Turbulence (Saffman, 1967). In the former, the large scale statistical properties of turbulence u' and L_u, satisfy $\overline{u'^2}L_u^5 \approx$ constant, whereas in the latter $\overline{u'^2}L_u^3 \approx$ constant. This contrasting behaviour of the large-scale properties is manifested through different rates of temporal decay of the turbulent kinetic energy. For turbulence of Batchelor type the temporal energy decay rate is given by $\overline{u'^2} \sim t^{-10/7}$ whereas, for Saffman type the temporal decay rate formulates according to $\overline{u'^2} \sim t^{-6/5}$. Both types of turbulence may be generated, at least approximately, in computer simulations as shown in Ishida *et al.* (2006). This section examines the nature of turbulence generated downstream by well-defined, specified inlet conditions in a commercial CFD code and classifies it according to the nature of its self-preserving state. Figure (2.19) represents $\overline{u'^2}L_u^5$ plotted along the centreline in the streamwise direction,

downstream of an inlet, for an initial specified turbulence intensity of 10% and integral length scale (L_u) of 0.1m. It is evident from figure (2.19) that $\overline{u'^2}L_u^{\,5}$ increases exponentially along x which gives a notion that turbulence generated from the computer simulations (in the present case) is certainly not of Batchelor type. Figure (2.20) shows $\overline{u'^2}L_u^{\,3}$ along the centreline versus streamwise distance x with same specified initial conditions. It is clear from figure (2.20) that, apart from an initial transient in the region of (0m<x<0.7m), $\overline{u'^2}L_u^{\,3}$ is indeed more or less constant throughout the domain, which suggests that the predicted homogeneous and isotropic turbulence generated using the commercial CFD simulations is predominantly of Saffman type. The slight scatter of the data observed in the upstream region at x<1m (fig. 2.20) might be mostly due to the consequence of the difficulty associated with the estimation of L_u which is computed using the auto-correlation function represented as**:**

$$R(\tau) = R(r\Delta t) = \frac{1}{\overline{u'^2}} \frac{1}{N-r} \int_{n=1}^{N-r} u'_n u'_{n+r} \tag{2.40}$$

where, $R(\tau)$ is the auto-correlation function that relates the velocity at a certain location at time t to the same velocity at a later time $t + \Delta t$, $\tau = r\Delta t$ is the lag-time in seconds, N is the number of the velocity samples, r = 0,1,2,3…….m; and m is the maximum lag number given by $\frac{\tau}{\Delta t}$. The lag number is suitably adjusted to demonstrate the behaviour of the auto-correlation at different lag times The integral time scale T_E is computed by integrating the area under the auto-correlation curve bounded by time (τ) equals zero and the time at which the first zero crossing of the auto-correlation $R(\tau)$ takes place which introduces a small systematic error, since the evaluation of $\int_{n=1}^{N-r} u'_n u'_{n+r}$ (recall eq. (2.40)) depends on where the integral is terminated. The integral length L_u is then computed from the integral time scale invoking Taylor's hypothesis (Taylor, 1938b) by $L_u \approx \overline{U} T_E$, which introduces some uncertainty in the computed values of L_u since it is not extremely accurate in nature (Moin, 2009).

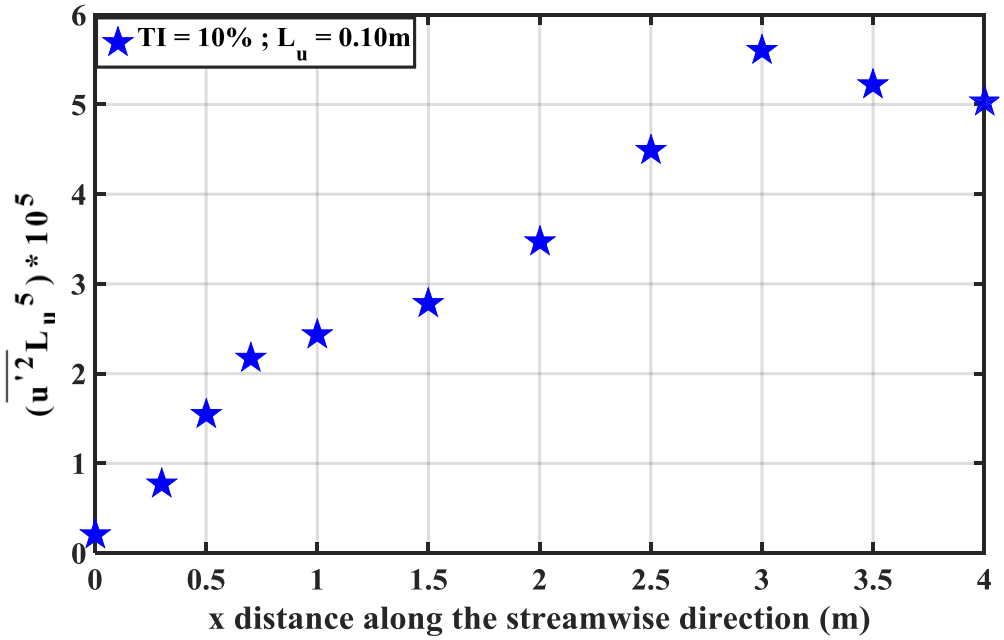

Figure 2.19 Downstream variation of $\overline{u'^2}L_u^5$ along the centreline of the domain ($\bar{U}$ = 4m/s, TI = 10% and L_u = 0.10m)

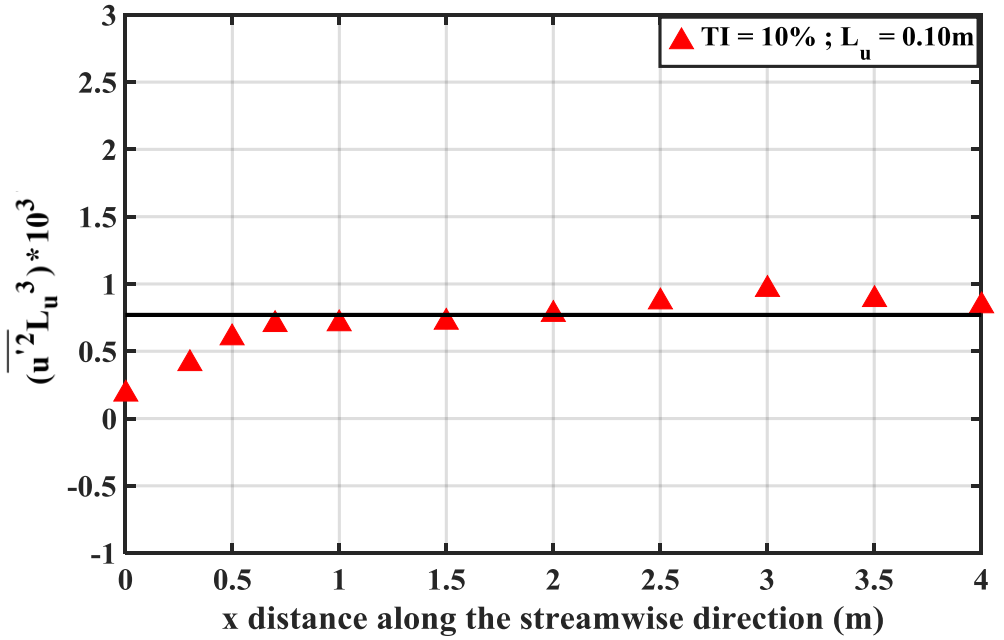

Figure 2.20 Downstream variation of $\overline{u'^2}L_u^3$ along the centreline of the domain ($\bar{U}$ = 4m/s, TI = 10% and L_u = 0.10m)

2.8.4 Influence of the Time-Step Size

The (Courant-Friedrichs-Lewy) or CFL condition is a necessary condition to ensure stability of the numerical methods used to solve certain partial differential equations. In CFD, the CFL condition states that any information convected through the time-step length within the mesh must be lower than the distance between the mesh elements. In other words, the CFL condition must always satisfy $\frac{u\Delta t}{\Delta x} \leq 1$ to ensure stability i.e. the flow Courant number should be always less than 1. The use of an implicit time discretization scheme in the present formulation allows the use of time step sizes with corresponding CFL (Courant-Friedrichs-Lewy) greater than 1. However, in the present study Δx and Δt have been chosen in such a way that they always satisfy a maximum CFL number of 1.

To gain information on whether the choice of time-step size affects the results of the simulations, computations with two different time-step sizes corresponding to the maximum CFL numbers of 0.4 and 0.8 were carried out. Statistical averaging was performed over 17000 samples for both cases which gives flow times of 34 seconds and 17 seconds, respectively, to restrict the effect of the initial transience of the flow field into the data sets. Table (2.10) gives an overview of the performed simulations on the time-step independence.

Table 2.10 Overview of performed simulations on the time-step independence

Δt	0.002s	0.001s
Courant number	0.8	0.4

Figure (2.21) shows the profiles of the normalized mean streamwise velocity component along the centreline, for two different time-step sizes corresponding to CFL numbers of approximately 0.4 and 0.8 with a convergence criterion of 0.001. At all considered locations the profiles are in very good agreement with reference to the specified velocity at the inlet. It is noticeable that there are no significant differences between the results for

averaged mean velocities for different time step sizes and variation of the time-step size shows a very small effect (less than 1%) on the computational results.

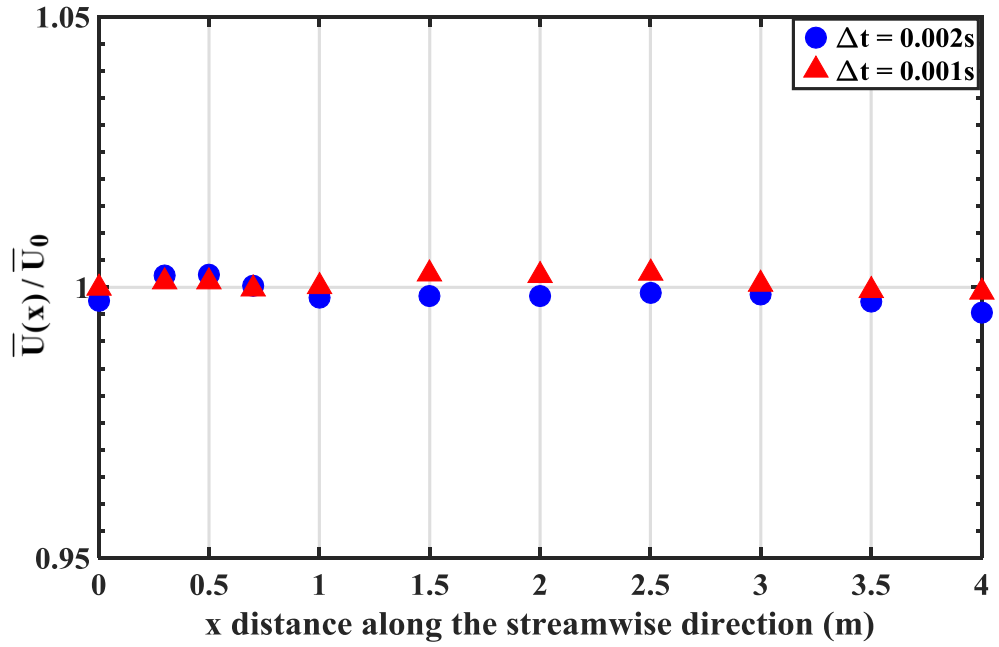

Figure 2.21 Influence of the time-step size on the profiles of normalized mean velocity component at different locations along the centreline ($\overline{U}$ = 4m/s, TI = 10% and L_u = 0.10m)

Figure (2.22) shows the comparisons of the turbulent kinetic energy spectra taken at the point located at the centre of the inlet plane i.e. at (0,0,0). The spectra show the same behaviour for both time-step sizes within the cut-off frequency of 100 Hz (frequency until which the spectra are modeled). The higher frequencies are not plotted since they correspond to the small amount of energy (less than 15%) contained by the small scales. The following figure also reveals that the time-step size (at least in the considered range) has a negligible effect on the modeled part of the energy spectrum, so it can be concluded that both the time scale sizes are small enough to resolve the relevant scales in the spectrum (in the present case). Figure (2.22) also shows that, irrespective of the choice of the time-step size, the spectrum satisfies the classical Kolmogorov prediction for the energy cascade in the inertial sub-range of the spectrum which is plotted as a reference line with (-5/3) slope.

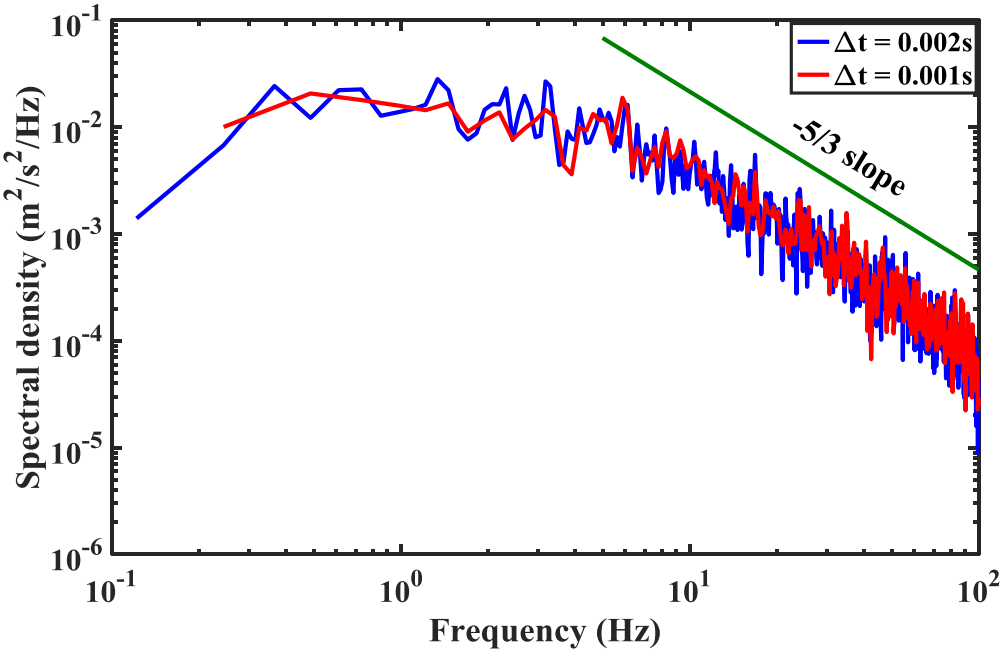

Figure 2.22 Influence of the time step size on the streamwise turbulent kinetic energy spectrum at the inlet ($\bar{U}$ = 4m/s, TI = 10% and L_u = 0.10m)

Figure (2.23) displays the evolution of the integral length scales (L_u) monitored at 11 different locations along the centreline of the domain for the two-different time-step sizes. It can be clearly seen that at the considered locations, the choice of time-step size has least effect (less than 1%) on the growth of the average eddy size which are then comparable to each other.

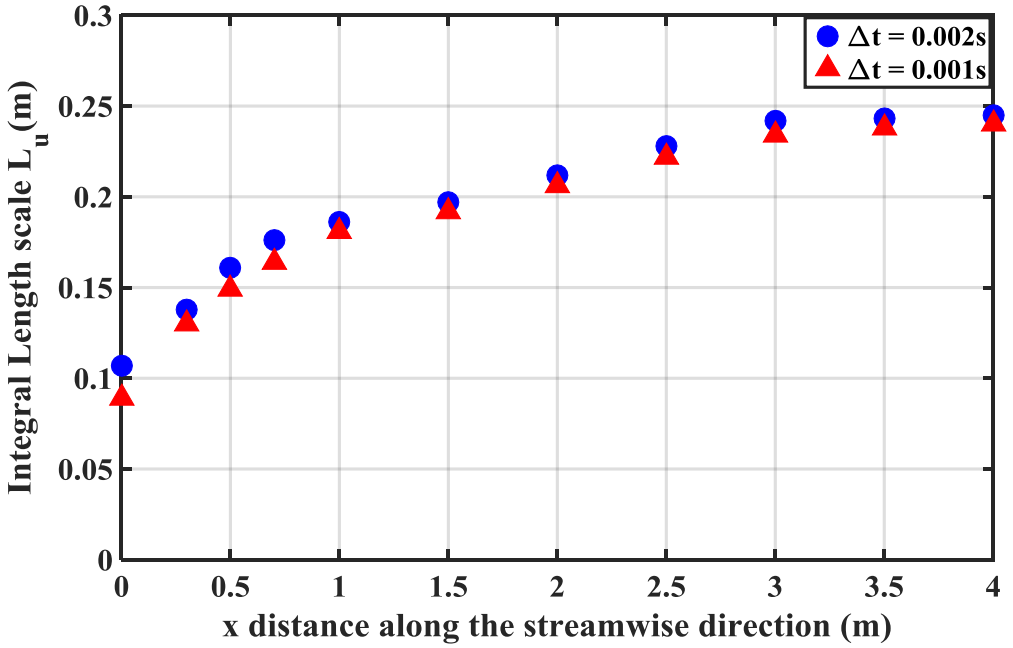

Figure 2.23 Influence of the time-step size on the profiles of integral length scales at different locations along the centreline ($\bar{U}$ = 4m/s, TI = 10% and L_u = 0.10m)

Figure (2.24) presents the streamwise decay of dimensionless normalized turbulent kinetic energy (TKE) in the longitudinal direction. For the considered test cases the differences of the turbulent kinetic energy are negligible (less than 2%) for the chosen different time-step sizes.

So, it can be stated that the simulations with CFL ≈ 0.8 with time-step size equals to 0.002s is more efficient, since it captures enough statistical information carried by large scales of turbulence, whilst having a larger flow time but a slower rate of convergence per time step. The turbulent flow traverses 40 times through the domain in the flow time which ensures that the domain is entirely populated with a sufficient number of eddies to allow extraction of relevant statistics from the flow.

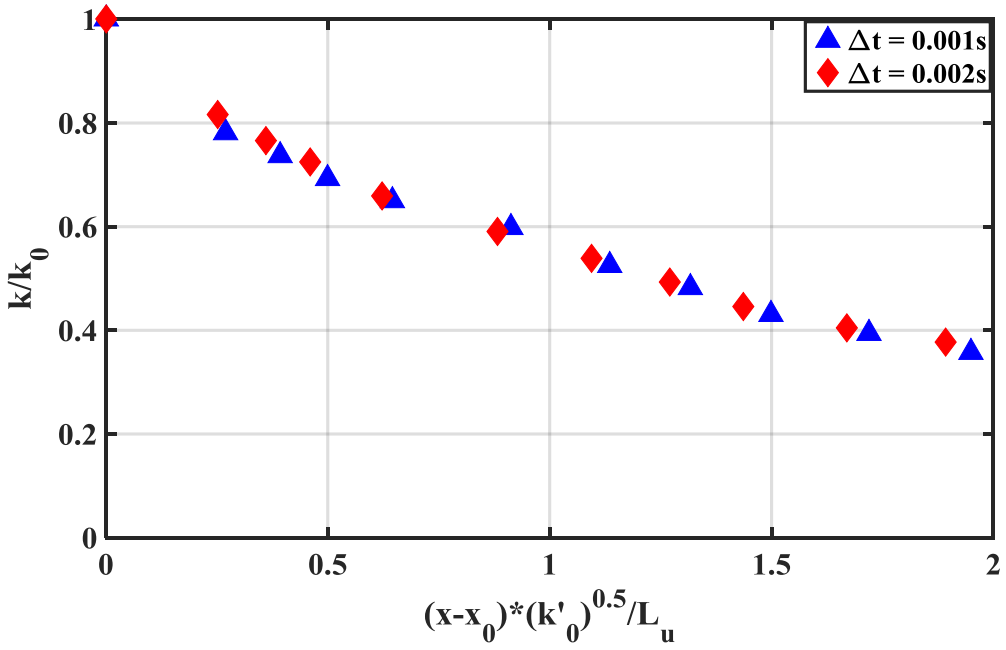

Figure 2.24 Influence of the time-step size on the TKE decay along the centreline in the streamwise direction ($\bar{U}$ = 4m/s, TI =10% and L_u =0.10m)

Having documented the first and second-order statistics along with the test for homogeneity and isotropy for the computer-generated turbulence, in the next section statistical LES results are compared with the earlier relevant experiments performed in the field of decaying isotropic homogeneous turbulence.

2.9 Comparison with previous studies (Validation of the CFD model)

In the following section, the spatial TKE profiles obtained from the numerical simulations employing both steady RANS and LES models, using commercial CFD codes are compared and validated with earlier relevant experimental and numerical studies. Both qualitative and quantitative comparisons are drawn to examine the differences observed with the previous studies. Additionally, a predictive methodology has been formulated using the numerical results to provide a unifying framework to the existing experimental decay laws that can estimate both local and the initial TKE and integral length scale values which will help one achieve distinct magnitudes of turbulence

scales at a location of choice, whilst relating it to a particular type of grid, which can then generate similar scales of turbulence. The latter can be then used to generate known turbulence in a typical wind-tunnel experiment.

Since, the true isotropy condition is very difficult to generate, both experimentally and numerically, one may argue that instead of studying the decay of the stream-wise velocity fluctuations $\overline{u'^2}$ along the domain, it would make more sense to study the decay of the turbulent kinetic energy (TKE) which includes the influence of the decay rates of $\overline{u'^2}$, $\overline{v'^2}$ and $\overline{w'^2}$ embedded into the expression of TKE, since $TKE = \frac{1}{2}(\overline{u'^2} + \overline{v'^2} + \overline{w'^2})$. The isotropy levels in the streamwise direction given by $\frac{3\overline{u'^2}}{\overline{q^2}}$ range between 1.02 to 1.15 respectively. Similarly, $\frac{3\overline{v'^2}}{\overline{q^2}}$ lies between 0.84 and 1.01, whilst $\frac{3\overline{w'^2}}{\overline{q^2}}$ lies between 0.86 to 1.01, where $\overline{q^2} = (\overline{u'^2} + \overline{v'^2} + \overline{w'^2})$. Hence, in the following sub-sections the spatial decay of TKE is discussed in relation to its decay mechanism.

The time-averaged, non-dimensional TKE profiles along the centreline of the domain in the streamwise direction obtained using the Dynamic-Smagorinsky LES model are compared with the previous existing experimental and numerical data of Kang *et al.* (2003), which is an update to the classical Comte-Bellot and Corrsin (1971) experiments as high turbulent Reynolds number flows (Re_λ = 720) (fig 2.25). The results from Kang *et. al.* (2003) have been scanned and reproduced in the figure (2.25) for comparisons. The experimental grid used in Kang *et al.* (2003) comprised of horizontal and vertical rotating shafts having eight and six winglets, respectively, with the grid size, M = 0.152m. These types of grids are termed as active grids as it is an active method of turbulence generation. A pseudo-spectral code had been used in their study to perform the LES simulations. It is clear from figure (2.25) that the quantitative agreement between LES and different sets of data presented from that study (Kang e*t al.* 2003) is remarkably good with a proper choice of the virtual origin (x_0) value (which refers to the distance

downstream of an experimental grid origin, where the wake vortices from the grid (active) have coalesced sufficiently and the turbulence has started to become well-developed and be nearly isotropic and homogeneous in nature). Crucially, their experiments were carried out in a large working section of 10m to allow sufficient streamwise distance for re-organization of turbulence. It should be noted that the decay rate of TKE is sensitive to the choice of the virtual origin (x_0) and, in this comparison, the virtual origin of the experiments was typically taken at 20 mesh widths i.e. x_0 =20M, downstream from the experimental test-section origin where the flow has effectively become homogeneous and isotropic. As x_0 is an important parameter to this fitting, a summary of its magnitude, obtained with respect to the origin of the physical grid location is presented in table (2.11) which also includes the virtual origin for the present numerical simulations.

Table 2.11 Summary of the virtual origin location (x_0) with respect to the physical grid location for both experimental results of Kang *et al.* (2003) and LES

Comparison between the study by Kang *et al.* (2003) and the present numerical study	Virtual Origin (x_0)	Physical location of the virtual origin (x_0) with respect to the origin of active grid location (experiments)/inlet (CFD)
Kang *et al.* (2003)	20M	3.04m
LES study	0	0m

The agreement between these two studies shows that, in absence of mean shear and boundary layer wall effects, well-developed turbulent flow decays at a similar rate and there exists a universal decay mechanism of turbulence that would fit the same non-dimensional curve. However, the similar rate of decay curves observed between the study by Kang *et al.* (2003) and the present study (fig. 2.25) is not surprising, yet it calls for a deeper analysis, since the prescribed initial turbulent characteristics of the flow (turbulent kinetic energy and length scales) are different in magnitude for both the cases. The initial

non-dimensional TKE magnitude and the integral length scales values at the location $x\text{-}x_0 = 0$m, for both the studies are summarized in table (2.12) for completeness.

Table 2.12 Initial TKE and length scale magnitudes for experimental data of Kang *et al.* (2003) and the present LES study

Comparison between the study by Kang *et al.* (2003) and the present numerical study	Non-dimensional initial TKE value	Integral length scale (L_u)
Kang *et al.* (2003)	0.035	0.25
LES study	0.015	0.10

Starting from the inviscid estimation of the kinetic energy dissipation rate (ε) given by

$$\varepsilon = \frac{dk}{dt} \approx -\frac{u'^3}{L_u} \tag{2.41}$$

and invoking Taylor's hypothesis, it is possible to deduce the decay of energy dissipation in the form of

$$\varepsilon = U\frac{dk}{dx} \approx -\frac{u'^3}{L_u} \tag{2.42}$$

Re-arranging and simplifying the equation (2.42) with a constant of proportionality D, a simpler empirical relation between the spatial gradient of non-dimensional TKE (k') and the global turbulence parameters (turbulent velocity fluctuation and length scale) is obtained which takes the form of

$$\frac{dk'}{dx} \approx -D\frac{\frac{(u')^3}{\overline{U}^3}}{L_u} \tag{2.43}$$

A more detailed description about the constant of proportionality D and its deduction is presented in the upcoming section which is discussed purely based on dimensional considerations. Thus ,the magnitude of the $\frac{dk'}{dx}$ computed from the values of D, u', $\overline{U}$ and L_u at $x\text{-}x_0$ = 0m gives an approximate value of 0.014 for Kang *et al.* (2003) and a value of 0.010 for present LES study which are in close proximity to each other. Since the initial spatial TKE gradient rate controls the downstream decay of the turbulent kinetic energy there is a similar tendency in the nearly isotropic and homogeneous region of turbulence. Moreover, the corresponding local TKE gradient rates in the streamwise direction (i.e. $\frac{(\frac{dk'}{dx})}{\frac{dk'_0}{dx}}$) are very close to each other (within ±2%) at each considered measurement locations (including $x\text{-}x_0$ = 0m) which explains the identical nature of the loss of kinetic energy observed in both the studies.

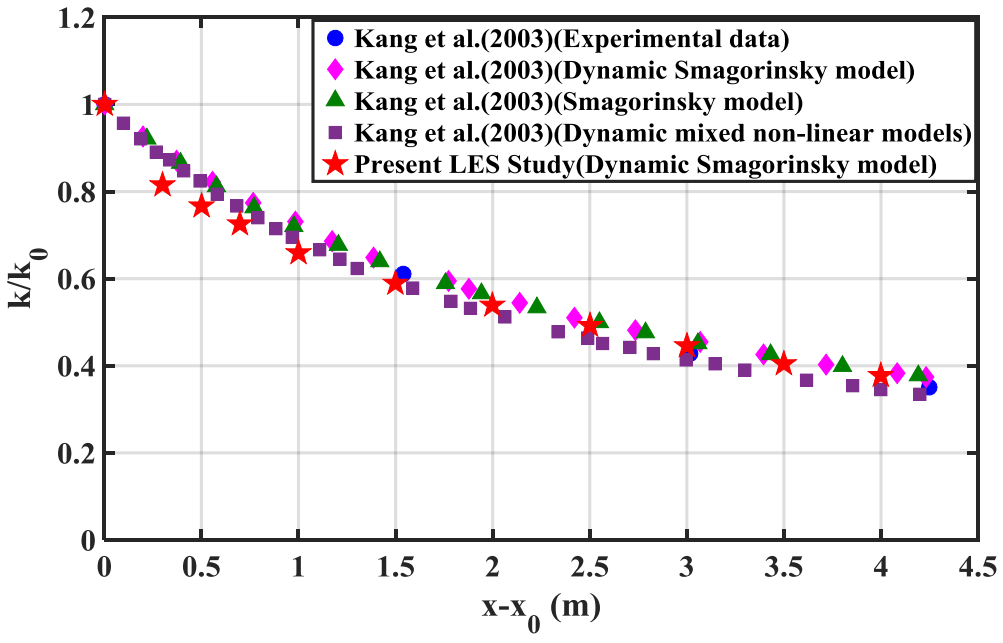

Figure 2.25 Comparison of decay of TKE in the streamwise direction between the studies of Kang *et al.* (2003) and the present LES results.

2.9.1 Predictive methods for spatial decay of turbulent kinetic energy (TKE)

A new predictive algorithm based on the current methodology has been formulated in the present study which is used to identify a region of nearly constant turbulence (TKE and L_u) scale and to provide an estimate of the local and the initial turbulence levels of the fluid flow approaching the leading edge of a bluff body. The predictive algorithm is based on the simple inviscid estimation of the turbulence dissipation rate ε at a given length scale, represented by $\varepsilon = \frac{dk}{dt}$.

The prediction method in the current study has been cast into a single correlation equation derived in the current section assuming that the turbulence is strictly isotropic in nature, the length scales (L_u) do not vary with the streamwise distance x, the dimensionless constant D is of the order of magnitude 1 (Sreenivasan, 1998), the temporal rate of decay is approximated by Taylor's hypothesis of frozen turbulence $Udt = dx$, and the kinetic energy dissipation rate $\varepsilon = \frac{dk}{dt}$ is computed through the inviscid estimate given by $-\frac{u'^3}{L_u}$.

The mean turbulent kinetic energy k is directly related to the fluctuating velocity components in the three directions u' , v' and w' is represented as follows

$$k = \frac{1}{2}(\overline{u'^2} + \overline{v'^2} + \overline{w'^2}) \tag{2.44}$$

If the perfect isotropic condition is satisfied, then $\overline{u'^2} = \overline{v'^2} = \overline{w'^2}$ and then the turbulent kinetic energy k is

$$k = \frac{3}{2}\overline{u'^2} \tag{2.45}$$

Normalizing both the sides of the equation (2.45) with $\overline{U}^2$ gives

$$k' = \frac{k}{\overline{U}^2} = \frac{3}{2}\left(\frac{\overline{u'^2}}{\overline{U}^2}\right) = \frac{3}{2}(Tu)^2 \tag{2.46}$$

where k' is the dimensionless TKE and Tu is the turbulence intensity in fraction given by $Tu = \frac{u_{rms}}{\overline{U}} = \frac{u'}{\overline{U}}$ and $u_{rms} = \sqrt{\overline{u'^2}}$

Restating equation (2.43) given by $\frac{dk'}{dx} = -D\frac{\frac{(u')^3}{\overline{U}^3}}{L_u}$ and substituting $\left(\frac{u'^3}{\overline{U}^3}\right)$ with appropriate form of k' we get

$$\frac{dk'}{dx} = -\left(\frac{2}{3}\right)^{1.5} D\frac{(k')^{1.5}}{L_u} \tag{2.47}$$

where D is the dimensionless dissipation constant taken as unity for simplicity. A more rigorous discussion on the dimensionless dissipation constant D is carried out later in the present section. Integrating both sides with respect to x, gives the spatial variation of non-dimensional TKE with the streamwise distance presented in the form of a power decay law as

$$\frac{k}{k_0} = \frac{k'}{k_0'} = \left(\frac{A(k_0')^{0.5}x}{L_u} + 1\right)^{-n} \tag{2.48}$$

where k and k_0 are the local and initial TKE (at x = 0) , k' and k_0' are the dimensionless local and initial TKE (at x = 0), A is a dimensionless constant having a magnitude of 0.272 (where A =0.272×D; D=1) , n is the decay exponent of magnitude 2, x (m) is the streamwise distance starting from the origin of the physical grid and L_u is the integral length scale (m) which is taken as a constant in this derivation for simplicity. However, in reality, the integral length scale (L_u) grows in the streamwise direction as turbulence decays (Dryden, 1943) and cannot be treated as a constant which then alters the magnitude of the power law exponent n obtained in the correlation presented in equation

(2.48). Hence, to incorporate the effects of the spatial evolution of the length scale (L_u), the correlation equation (2.48) is rewritten in a general form as

$$\frac{k}{k_0} = \frac{k'}{k_0'} = \left(\frac{A_1 (k_0')^{0.5} (x - x_0)}{L_u} + 1\right)^{-n_1} \tag{2.49}$$

where x_0 is the virtual origin, and A_1, n_1 gives general decay coefficient and decay exponent for the above correlation (eq. 2.49)

Replacing L_u with L_{u0} in the equation (2.49) yields

$$\frac{k}{k_0} = \frac{k'}{k_0'} = \left(\frac{A_2 (k_0')^{0.5} (x - x_0)}{L_{u0}} + 1\right)^{-n_2} \tag{2.50}$$

where L_{u0} is the initial value of the integral length scale (at x = 0), A_2 and n_2 are the new decay coefficient and the decay exponent for the above correlation equation (2.50).

The correlations presented in equations (2.49, 2.50) clearly depicts a power law form analogous to the grid-generated turbulence decay given by Pope (2000) in the form of

$$\frac{k}{\overline{U^2}} = D\left(\frac{x - x_0}{M}\right)^{-n} \tag{2.51}$$

$$\frac{L_u}{M} = D'\left(\frac{x - x_0}{M}\right)^{n'} \tag{2.52}$$

where M is the mesh spacing of the grid. A schematic representation of the typical turbulence generating grid was shown previously in figure (1.1), where the grid is typically made of cylindrical bars of diameter d.

The correlation equation obtained in equation (2.49) is tailored specifically to include the effects of the turbulent velocity fluctuation (in the form of TKE) and integral length scale (L_u) into a single correlation equation, since the evolution of length scales have an influential effect on the decay rate of the turbulent velocity fluctuations (Dryden,(1943), Krogstad & Davidson, (2010), irrespective of whether the large turbulent scales belongs

to Batchelor (Batchelor, 1953) or Saffman type (Saffman, 1967). Characterizing the decay of turbulence by equations (2.49, 2.50) allows extraction of the relevant global characteristics of the turbulent flow at any downstream location from the turbulent flow inlet. There has been a longstanding debate by previous researchers on the range of decay exponent (n) obtained for different types of grids and numerical simulations since its magnitude is said to depend on the initial conditions of the flow, the physical characteristics of the experimental grids (shape, size, width and porosity) and the choice of the virtual origin (x_0) (Mohamed and Larue (1990), Lavoie *et al.* (2005)). A faster or slower rate of decay of turbulent kinetic energy (TKE) is also possible depending upon the solidity of the grids which depends on the porosity (β), which itself is a function of the rod or wire dimeter used and the mesh width (M), as reported by Tan-atichat *et al.* (1982).

Hence, the present work does not aim to address the question of determining definitive and precise values of the decay exponent (n) exhibited in eq. (2.49), but, rather, to come up with a global decay exponent (n) and dimensionless constant (A), that best fits the correlation function when using all the relevant previous experimental studies and the present numerical simulations, within an acceptable degree of accuracy, in the well-developed region of homogeneous and isotropic turbulence.

The final goal is to use steady RANS or LES simulations as a predictive tool to identify a region of fairly-constant TKE conditions and the maximum achievable value for such conditions. The correlations (equations 2.49 and 2.50) can also be used to estimate the local statistical turbulence parameters (k and L_u) at any location downstream of a grid based on the specified initial turbulence levels (k_0 and L_{u0}) at the inlet. Similarly, the same set of prediction equations (2.49 and 2.50) also helps one to recover the initial freestream turbulence levels relevant to any bluff-body aerodynamics problem knowing the local magnitudes of turbulence scales, thus making this prediction method a complete closure solution to the choice of experimental turbulence generating grids required to achieve a particular level of turbulence.

While comparing with earlier experimental studies, it must be acknowledged that, for any experiment, that there is no *a priori* origin for x, where the turbulence is generated by a grid. The origin is not at the centre of the physical location of the grid elements and probably is the point where $(\frac{dk}{dx})$ is a local maxima. Hence, while comparing the present numerical results to the experimental studies, the experimental data are shifted downstream, where the turbulence is well developed and nearly isotropic, homogeneous in nature, so that the origin for x for the experimental studies lines up with the CFD origin on a consistent metric. In the CFD it is at x = 0 but in the experiments, it is going to be at some location x downstream from the centre of the grid elements which would then become the effective origin for x which is $(x - x_0)$. Table (2.13) summarizes the shift of all the different experimental data (considered in the present study) downstream to the location of the virtual origin x_0 which is consistently related to the grid geometry. From table (2.13) it is clear that the prediction of actual (x_0) location downstream depends on the ratio between the physical grid-element size (M) and the diameter of the physical grid element (d) given as M/d. From the same table it is also noticed that, as the ratio M/d increases, the physical location of the virtual origin (x_0) with respect to the actual grid location decreases. Figure (2.26) shows a plot of M/d versus the physical location of the virtual origin (x_0), with the best fit curve. The variables show a direct linear dependency with each other having $R^2 = 0.999$, intercept on y axis equals 6.10 and the magnitude of the slope being 1.02. It follows that the actual location of the virtual origin (x_0) can be predicted in a typical wind-tunnel set up, to a certain degree, based on the physical grid element sizes. The corresponding equation of the prediction comes out to be as $M/d = -1.02 \times x_0 + 6.10$. However, it is being pointed out here that the analysis of (x_0) is incomplete here because of the fact that M/d is dimensionless parameter and x_0 has dimensions of length so the constant -1.02 is not a just constant number with dimension of (1/length). The equation is dimensionally inconsistent and therefore must be used with care. The choice of the mesh width M also dictates the magnitude of the turbulent Reynolds number (Re_λ) that is generated downstream in the well-developed region of turbulence. Higher turbulent Reynolds number (Re_λ) requires the grid-element sizes (M) to be large enough and, therefore, (Re_λ) can be said to be directly proportional to the

mesh width (M). Nevertheless, the accurate prediction of the virtual origin (x_0) requires measurements carried out in a larger test-section over much longer range of downstream distances to limit the influence of the virtual origin (x_0) on the decay exponent (n) as shown by Krogstad & Davidson, (2010).

Table 2.13 Summary of the virtual origin location (x_0) with respect to the physical grid location obtained from earlier relevant experimental data

Source	Type of Grid Geometry	Mesh Width (M)	Bar-width of the grid element	M/d	Virtual origin (x_0)	Physical location of the virtual origin (x_0) w.r.t. physical grid location	Turbulence Reynolds number (Re_λ)
Kang *et. al* (2003)	Active Square grid (Aluminum Plates)	0.15m	0.05m	3.04	20M	3m	750
Krogstad & Davidson (2011)	Passive Square grid (Sheet metal)	0.04m	0.01m	4	50M	2m	90
Torrano *et al.* (2015)	Passive Square grid (Sheet metal)	0.05m	0.01m	5	20M	1m	100

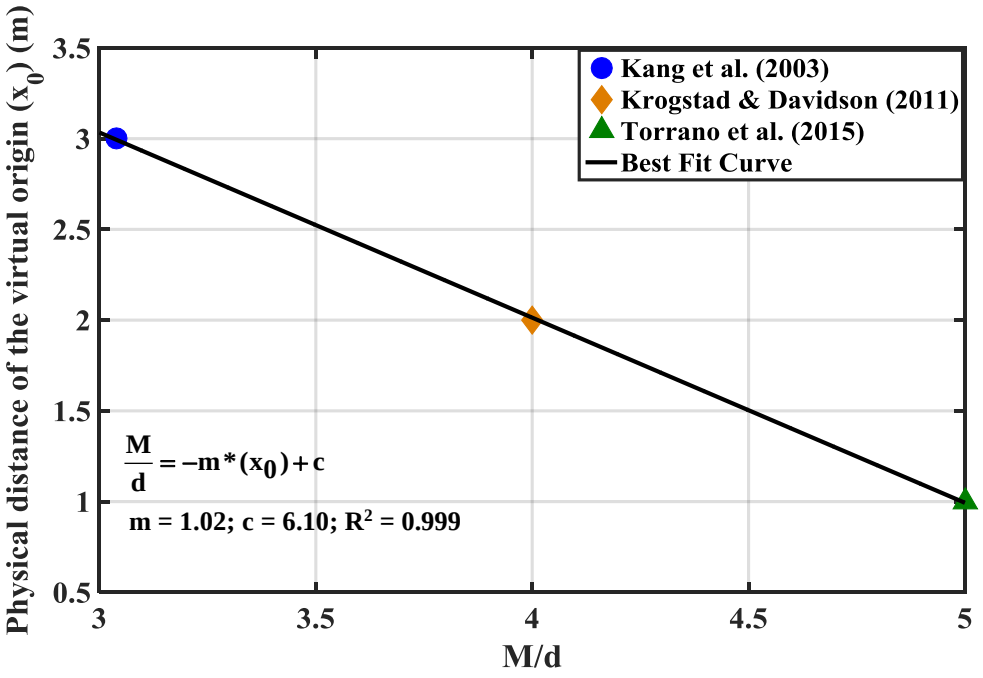

Figure 2.26 Physical distances of the virtual origin(x_0) with respect to the physical grid location plotted against the ratio of physical grid element size (M/d), for all the experimental studies (Kang *et al.* (2003); Krogstad & Davidson (2011); Torrano *et al.* (2015))

2.9.1.1 Prediction equation based on the local value of the integral length scale (L_u)

Figure (2.27) shows the direct comparisons of the normalized TKE profiles between the earlier experimental studies of Kang *et al*. (2003), Krogstad and Davidson (2011), Torrano *et al.* (2015) and the present numerical study (RANS and LES) where the dimensionless TKE profiles $(\frac{k}{k_0})$ are plotted against a non-dimensional parameter $(x-x_0)*(k_0')^{0.5}/L_u$ where $(x-x_0)$ is the effective origin, (k_0') is the non-dimensional initial TKE value and (L_u) is the local value of the integral length scale. The magnitude of the initial normalized TKE and integral length scale values are digitized, extracted and reproduced from the previous experimental studies to achieve a direct comparison between the variables used in the plots by using the above scaling, even though the initial

conditions of the different experiments and the CFD are different. Figure (2.27) also reveals that the numerical results (except the RANS results) are fairly consistent (±3%) with the overall experimental data (except few data from Torrano *et al.* (2015) which display larger deviation) and both the studies reproduce a similar tendency of the predicted turbulent kinetic energy decay. The deviation of the results obtained from the RANS modelling is due to the fact that the flow field is entirely modelled in a steady RANS simulation which entirely depends on the way the model constants are treated in the commercial CFD formulation. A more meticulous discussion on the standard RANS models and their shortcomings and possible improvements are discussed in the next chapter. The LES model computes most of the stochastic flow field directly and, therefore, has a better match with the experiments.

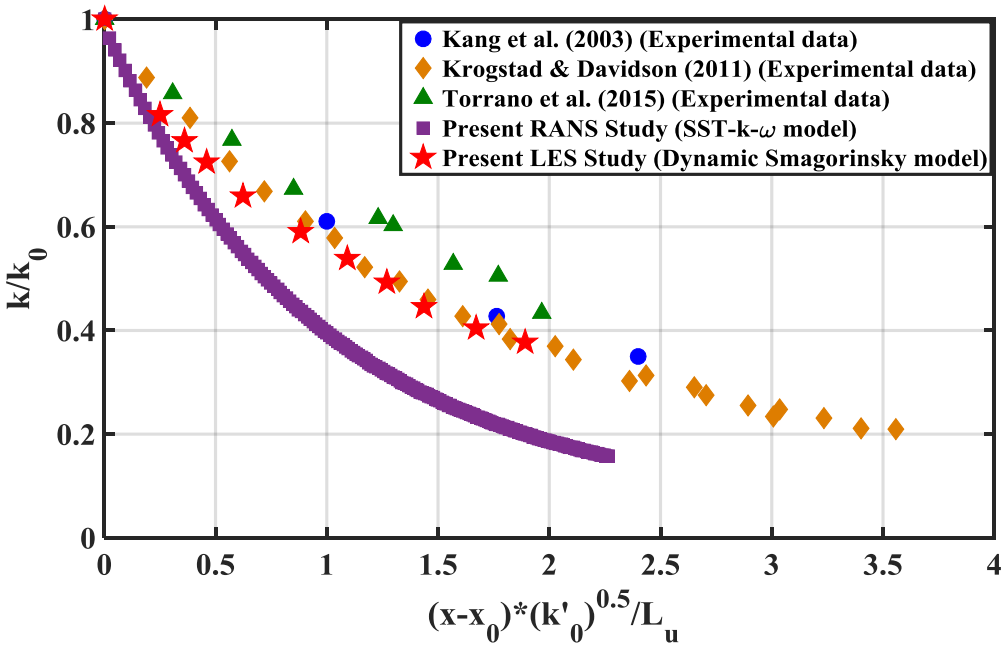

Figure 2.27 Quantitative comparisons of the spatial decay of TKE profiles between earlier experimental studies and the present LES study

Figure (2.28) shows the best-fit for the correlation function to all of the experimental and numerical data (TKE profiles), given by equation (2.49). The fitted coefficient values of A_1 and n_1 estimated from the best-fitted plots are (A_1 = 0.27 and n_1 = 2.38) with a 95% confidence interval that indicates the uncertainty of the above estimate. The robust Bi-

square method has been used for the current regression fit because the curve-fitting procedure fits the bulk of the data using the method of least squares. The goodness of the fit is excellent at $R^2 = 0.992$.

Here, the CFD data have well-specified initial conditions and the experimental data have a (consistent) virtual origin for x (i.e. $x_0 = x/M = 20$). In practice, this re-organization length will probably be a bit different for different grid types and so the data could all be shifted along the x axis by a small amount. In addition, there is the influence of L_u in shifting the data along the x-axis. This is probably not measured accurately in any of the experiments (since spatial correlations are needed for this and all the data that have been used are obtained from temporal correlations where Taylor's hypothesis has been invoked which is not as accurate). This contributes to the slight variation between the data sets obtained from different experiments.

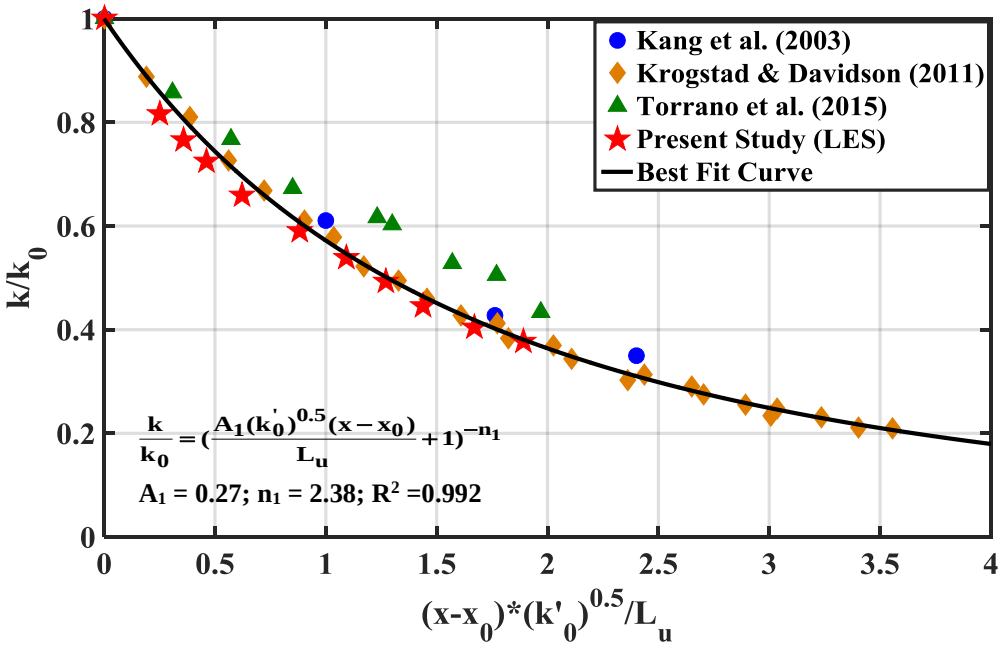

Figure 2.28 Spatial decay of TKE profiles of earlier experimental studies and present LES study, scaled with local integral length scale (L_u) plotted with a solid line that shows the best fit power law

2.9.1.2 Prediction equation based on the initial value of the integral length scale (L_{u0})

Figure (2.29) shows the comparison of the spatial decay of the TKE profiles for the different experiments stated earlier and the LES study, with the x axis variable $(x-x_0)*(k_0^{'})^{0.5}/L_{u0}$ now scaled with the initial constant value of L_u i.e. (L_{u0}) instead of local values of L_u. The scaling parameter has been changed to see its effect on the quantitative agreement between the LES and the experimental studies. Here R^2 = 0.971, which is not as good as the previous scaling, whilst the values of A_2 and n_2 are 0.44 and 1.16, respectively. A confidence level of 95% is used for the above estimate. It turns out that the A_2 and n_2 values obtained from the regression fit (eq. 2.50) have values of different magnitudes compared to the A and n values obtained while deriving equation (2.48), even though both the correlation equation assumes a constant L_u in its scaling. The values of the decay coefficient (A) and the decay exponent (n) obtained from equation (2.48) are 0.27 and 2 respectively.

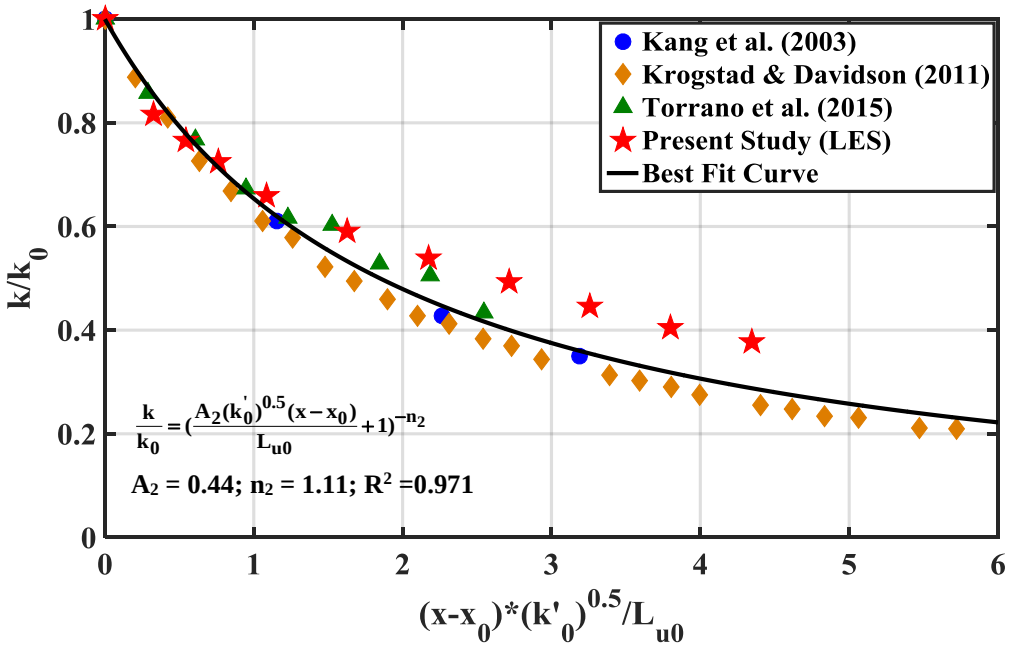

Figure 2.29 Spatial decay of TKE profiles for different experiments and the present LES study scaled with initial integral length scale (L_{u0}) plotted with a solid line that shows the best fit power law

There are reasons for this observed variation, between the decay coefficients (A) and decay exponents (n), obtained in the derivation using the simple inviscid estimation of ε (eq. 2.48), and that obtained from the best fit curve over all the experimental data and LES results (eq. 2.50).

Firstly, strictly isotropic turbulence has been assumed while deriving the correlation (eq. 2.48), which in reality is difficult to achieve in turbulence generated in computer simulations (Ishida *et al.* 2006). In the present study, the isotropy ratio $\overline{u'^2}/\overline{v'^2}$ varies from 1.02 to 1.18 while $\overline{u'^2}/\overline{w'^2}$ varies between 1.01 to 1.15 at 11 different considered measurement locations, which confirms that there is, at least, some amount of bias involved with the velocity fluctuations in each of the three directions. It is evident from the isotropy ratio's that $\overline{v'^2}$ and $\overline{w'^2}$ decreases more rapidly than $\overline{u'^2}$ which might be the consequence of the mean flow being in the streamwise direction. However, this phenomenon is not surprising as such anisotropy of the flow has already been observed in the earlier experiments of Bennett and Corrsin (1978) and Lavoie *et al.* (2007). Secondly, while deriving the correlations presented in equations (2.47), (2.49) and (2.50) , it was assumed that D is a non-dimensional constant of magnitude unity, having no temporal or spatial dependency in the streamwise direction, since in developed isotropic and homogeneous turbulence, dissipation ε relates to the kinetic energy transferred per unit time from the large scales to small scales which is same for all scales, and is a function of only large-scale quantities u'^3 and L_u only. But D is seen to have spatial dependency in the studies reported by Krogstad & Davidson, (2010). Hence, it is possible that the estimate of A_2 and n_2 obtained from the best fit curve shown in the figure (2.29) inherently incorporates the variability of D, if any, present in the current simulations.

However, a closer look at the dimensional identity of the inviscid estimate of (ε) demands $\varepsilon L_u / \overline{u'^2}^{(\frac{3}{2})} \approx D =$ constant. But, in both experiments and computer simulations, the ideal homogeneous condition is not achieved which is manifest through the streamwise decay of $\frac{d(\overline{u'^2})}{dx}$. Hence, ε may now be a function of $\overline{u'^2}$, L_u and $\frac{d(\overline{u'^2})}{dx}$.

Thus, there is a strong probability of D having a weak dependency on streamwise distance x, or t in both grid generated turbulence and turbulence generated through numerical simulations (Krogstad and Davidson, 2010). Besides this, Sreenivasan in his study (Sreenivasan, 1998) highlighted the fact that the variation of D is not only a function of the large scale turbulent properties (turbulence intensity and integral length scale), but also depends on the turbulence generation methods (active or passive) by the grid itself which, again, depends on the geometrical configuration of the grid. Hence, to explore the dependency of D with the streamwise distance x, it is imperative to accurately determine the rate of dissipation (ε) which is an independent estimate based on the turbulent kinetic energy equation.

2.9.1.2.1 Estimate of the turbulent kinetic energy dissipation rate *(ε)*

The present data (time-history of the measured velocity values) obtained from the LES solution offers two different methodologies to compute the turbulent kinetic energy dissipation rate (ε). First, (ε) maybe directly computed from the dissipation of the turbulence kinetic energy equation given by $\varepsilon = \frac{dk}{dt}$. Substituting k as $k = \frac{1}{2}(\overline{u'^2} + \overline{v'^2} + \overline{w'^2})$ and invoking Taylor hypothesis (i.e. $\overline{U}dt = dx$) and representing ε as ε_q one obtains

$$\varepsilon_q = \frac{1}{2}\overline{U}\frac{d\overline{q^2}}{dx} \tag{2.52}$$

where, $\overline{q^2} = (\overline{u'^2} + \overline{v'^2} + \overline{w'^2})$. The value of $\frac{d\overline{q^2}}{dx}$ can be computed directly from the data for $\overline{q^2}$ vs x. A second and independent estimate of the viscous dissipation rate ε, (referred to as ε_{iso}), is obtained using the measured spatial derivative of the downstream velocity using Taylor's hypothesis (Taylor, 1938b) and the assumption of local isotropy of the small scales. The corresponding expression of (ε_{iso}) is as follows

$$\varepsilon_{iso} = 15\nu\overline{(\frac{du'}{dx})^2} \tag{2.53}$$

where, ν is the kinematic viscosity of the fluid. Defining the Taylor microscale λ in the form of $\lambda^2 = \frac{\overline{u'^2}}{\overline{(\frac{du'}{dx})^2}}$, for isotropic turbulence and substituting $\overline{(\frac{du'}{dx})^2}$ with $\frac{\overline{u'^2}}{\lambda^2}$ in the equation (2.53) , ε_{iso} may be then written as

$$\varepsilon_{iso} = 15\nu(\frac{\overline{u'^2}}{\lambda^2}) \tag{2.54}$$

The expression ε_q in eq. (2.52) is based on the gradient of turbulent kinetic energy distribution, whereas the expression in the eq. (2.54) is based on the assumption of the local isotropy. Ideally, in a perfect isotropic and homogeneous turbulent flow, $\varepsilon_q / \varepsilon_{iso}$ should yield a magnitude close to unity. The results shown in figure (2.30) gives a comparison of the turbulent kinetic energy dissipation rate (ε) plotted against the streamwise distance x, computed based on the assumptions of homogeneity and isotropy (ε_q), and on the assumption of local isotropy (ε_{iso}). These results show that, at downstream locations further from inlet (i.e. at x >1m) the dissipation rate (ε) decays slowly compared to the region adjacent to the inlet which establish that, after a rapid decay in the initial regime, the turbulent kinetic energy (TKE) may nearly approach an asymptotic constant magnitude.

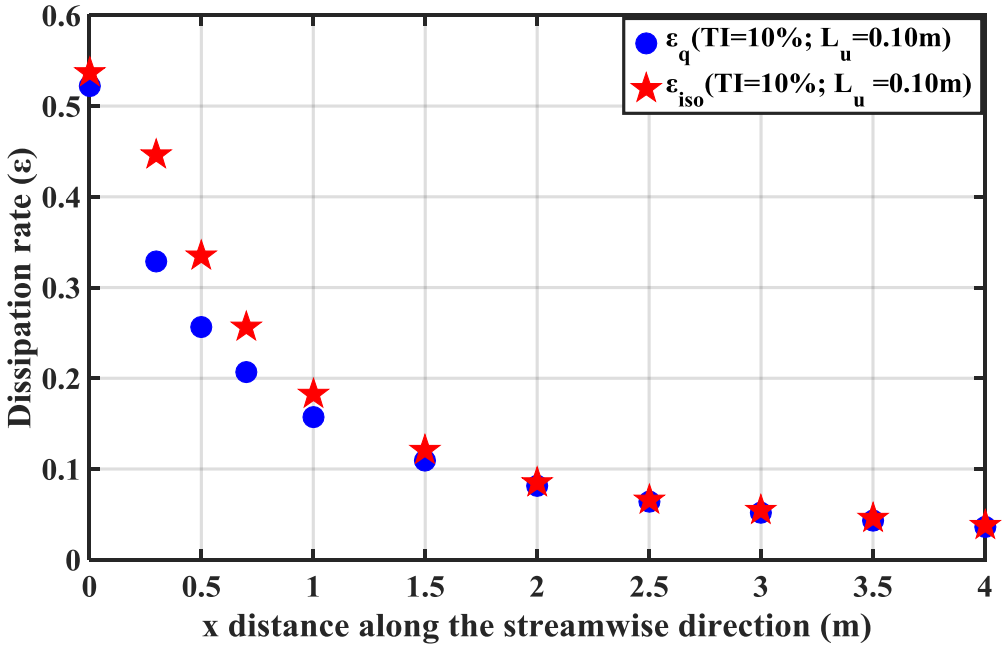

Figure 2.30 Comparison of the dissipation rate of turbulent kinetic energy computed as: $\varepsilon_q=\frac{1}{2}\bar{U}(\frac{\overline{du'^2}}{dX})$; $\varepsilon_{iso}=15\nu(\frac{\overline{u'^2}}{\lambda^2})$ ($\bar{U}$ = 4m/s, TI = 10% and L_u = 0.10m)

Figure (2.31) shows the ratio, $\frac{\varepsilon_q}{\varepsilon_{iso}}$ obtained for the present results. The deviation of the ratio, $\frac{\varepsilon_q}{\varepsilon_{iso}}$ from unity in the initial regime highlights the fact that, even though a perfect isotropic condition can be achieved at the inlet based on the prescribed boundary conditions, a certain degree of inhomogeneity and anisotropy still exists until x ≈ 1m, after which the turbulence begins to achieve near isotropy levels. This phenomenon is verified by the similar trend of results observed in the study by Ishida *et al.* (2006) where the turbulence was generated using computer simulations by using an in-house spectral code.

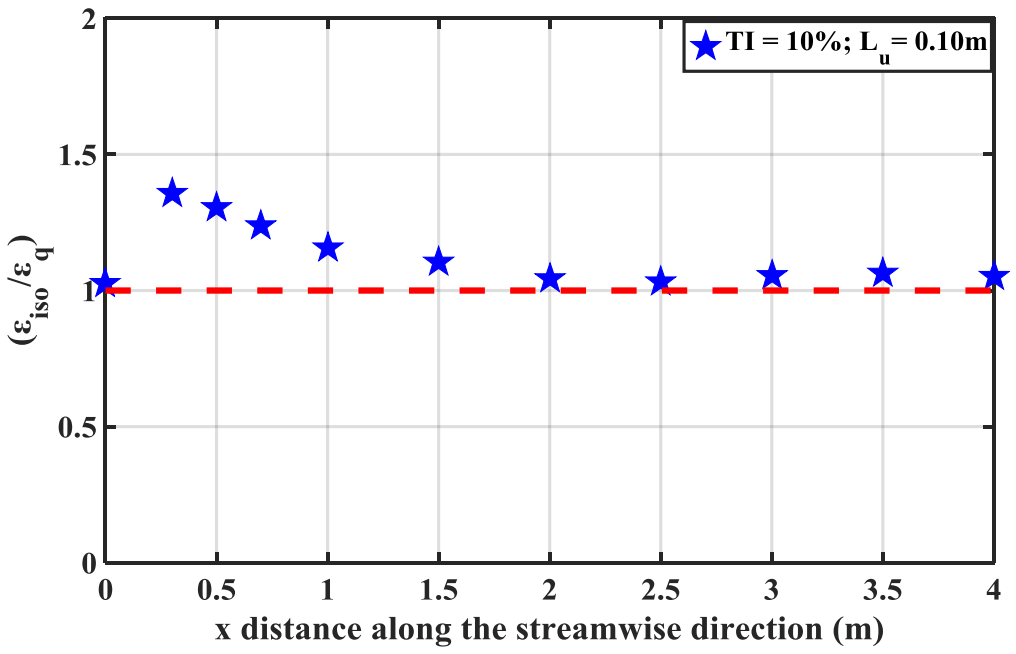

Figure 2.31 Ratio of the dissipation rate of turbulent kinetic energy, $\frac{\varepsilon_{iso}}{\varepsilon_q}$ ($\bar{U}$ = 4m/s, TI = 10% and L_u = 0.10m)

2.9.1.2.2 Estimation of the dimensionless dissipation coefficient D

It has already been mentioned in the previous section that, in order to report the spatial variability of the dimensionless dissipation constant D, an accurate estimation of the dissipation rate (ε) is required. Two different estimates of (ε) presented in the previous section, gives two choices to measure the variation of D spatially in the streamwise direction along the domain. The value of D computed using (ε_q) shall be denoted by D_q and that computed using (ε_{iso}) is denoted by D_{iso}. The expected form of the two variants of D may then written as

$$D_q \approx \frac{\varepsilon_q}{\frac{(u')^3}{L_u}} \tag{2.55}$$

$$D_{iso} \approx \frac{\varepsilon_{iso}}{\frac{(u')^3}{L_u}} \tag{2.56}$$

Both D_q and D_{iso} are computed using the local measurements of $\varepsilon_q, \varepsilon_{iso}$, u'^3 and L_u at each x location along the domain. The corresponding values of D_q and D_{iso} are plotted in figure (2.32) as a function of the streamwise distance x. The figure reveals a slow but steady decline of D along the centreline in the streamwise direction, consistent across both the variants of D plotted, a trend which was previously observed by Batchelor, (1953), Krogstad and Davidson (2010) and (Krogstad and Davidson, 2011). The scatter observed in the magnitudes of D in figure (2.32) is mostly due to the difficulty associated with the estimate of L_u, as discussed previously in section (2.8.3).

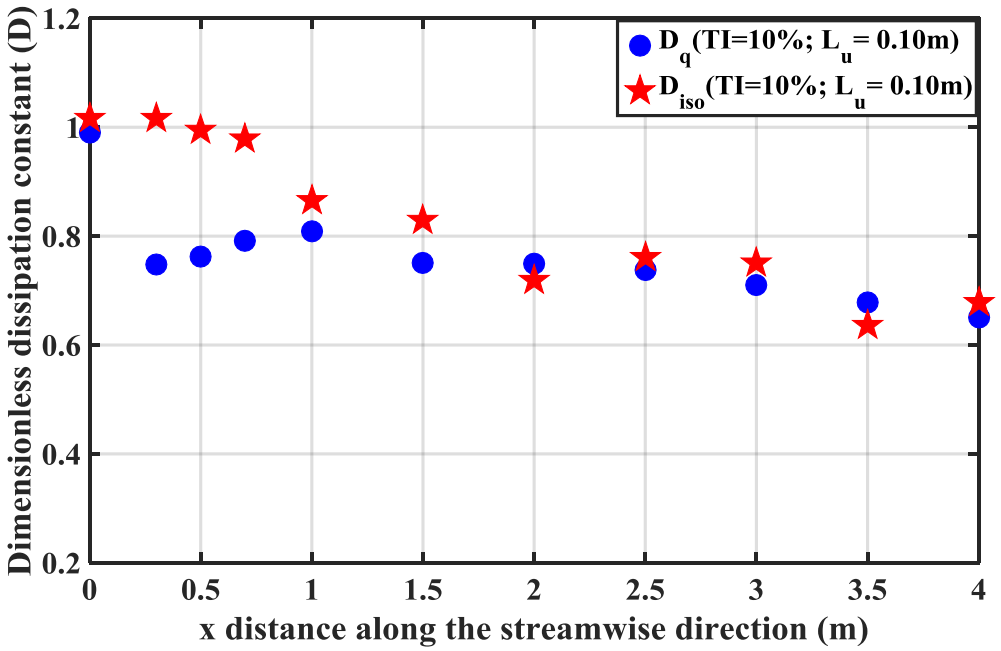

Figure 2.32 Streamwise distribution of D along the centreline of the domain obtained from $D_q = \frac{\varepsilon_q}{\frac{(u')^3}{L_u}}$ and $D_{iso} = \frac{\varepsilon_{iso}}{\frac{(u')^3}{L_u}}$

There can be numerous reasons for this variability, of which the most important is the dependency of the quantity $D = \varepsilon \frac{L_u}{u'^3}$ on the microscale turbulent Reynolds number (Re_λ) in the domain. The origin of this sensitivity of the dissipation constant D on the microscale Reynolds number (Re_λ) is a subject of extensive analysis and will be not be discussed here. The significance of this premise has been emphasized at various times in the past ((Saffman, (1968); Lumley, (1992); Frisch, (1995)). Attempts have also been made to test its credibility for different class of grid-generated flows (Jimenez *et al.*, (1993); Wang *et al.*, (1996); Wang *et al.*, (1999); Yeung and Zhou, (1997); Cao *et al.*, (1999)). Sreenivasan (1984), (1998) presented a critical discussion and a suitable tabulation of all the relevant experimental and numerical studies, on the mutual dependence of D on (Re_λ) and showed that, irrespective of the grid configurations, an asymptotic constant magnitude of D is never achieved in both high and low turbulence Reynolds number flows. To support this fact in the current study, a figure (2.33) showing the variation of the quantity ($D = \varepsilon \frac{L_u}{u'^3}$) with respect to the Taylor microscale Reynolds number (Re_λ) is presented, which clearly shows that both variants of D (D_q and D_{iso}) vary with Re_λ downstream from the inlet. The dimensionless dissipation constant D decreases when Re_λ becomes smaller and vice versa. These results are also supported with the similar trend of D observed with respect to the turbulent Reynolds number (Re_λ) reported in Krogstad and Davidson (2010) and Krogstad and Davidon (2011). The underlying premise from the present discussion acknowledge that the variation in the microscale turbulent Reynolds number (Re_λ) in the streamwise direction could have possibly manifested itself in the slow evolution of D seen in figure (2.33).

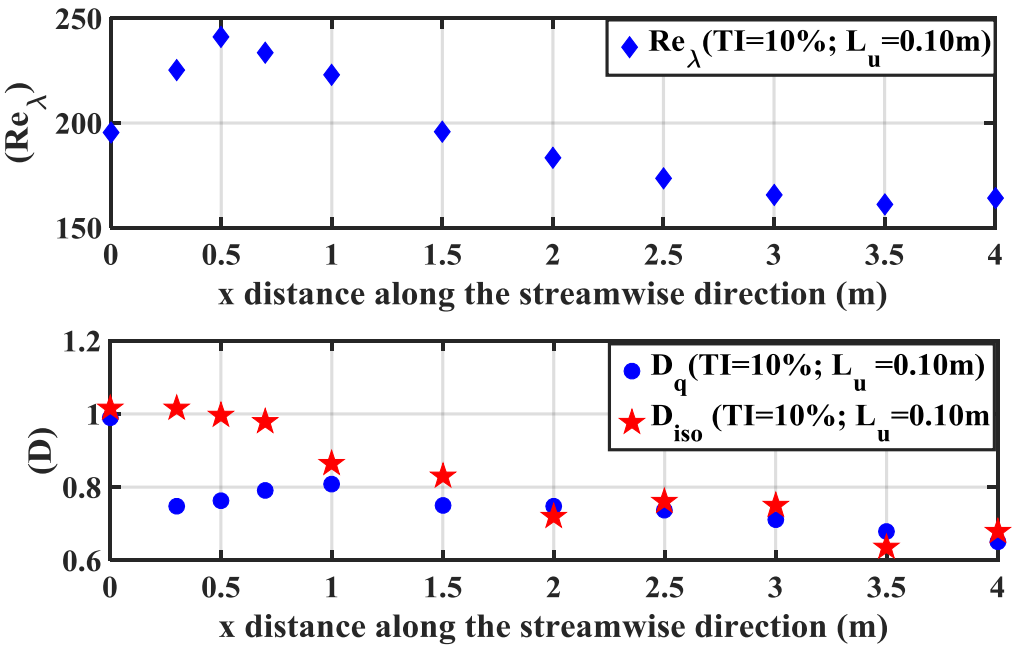

Figure 2.33 Variation of the dimensionless dissipation constant D along the streamwise distance of the domain plotted to compare with the variation of the turbulent Reynolds number (R_λ) along the same direction

2.9.1.3 Prediction equation based on the local magnitude of TKE (k) and the local magnitude of the integral length scale (L_u)

Figure (2.34) shows another form of spatial decay of the TKE profiles from both the experiments and LES data, but with the x ordinate scaled with local non-dimensional turbulent kinetic energy value $k^{'}$ and local magnitude of the integral length scale (L_u). The figure (2.34) reveals an approximate linear relationship between the variables (k/k_0) and $(x-x_0)*(k^{'})^{0.5}/L_u$ which implies that

$$\frac{\frac{d}{dx}(k/k_0)}{\frac{d}{dx}(x-x_0)*(k^{'})^{0.5}/L_u} \approx \text{constant} \qquad (2.57)$$

This holds true and is manifest through the power law dependencies of k and L_u in the streamwise direction which are given by the following two equations:

$$\frac{k}{k_0} = \frac{k'}{k_0'} = (a_1 x + 1)^{-p} \tag{2.58}$$

$$\frac{L_u}{L_{u0}} = (a_2 x + 1)^{q} \tag{2.59}$$

In order to arrive at linearity; $a_1 \approx a_2$ and a slight deviation from the numbers (a_1 and a_2) can affect the linearity of the experimental data sets and the LES results seen in figure (2.34), which is simply a consequence of the curve fitting performed for the best fit for equations (2.58) and (2.59). Similarly, p and q are closely related to each other in the form of $\frac{q}{2} - p = 1$ for the LES results, which is verified by the exponents derived in Krogstad and Davidson (2010). The left-hand side of equation (2.57) can be solved to arrive at a constant value and the solution method is shown in the Appendix A. The best linear fit line is drawn in the figure (2.37) which gives R^2 = 0.953 with the slope m = -0.51 and the intercept C=1 having 95% confidence bounds in the intervals. Hence, the final equation of the spatial decay of TKE is

$$(\frac{k}{k_0}) = (\frac{k'}{k_0'}) = m(\frac{(x - x_0) * (k')^{0.5}}{L_u}) + C \tag{2.60}$$

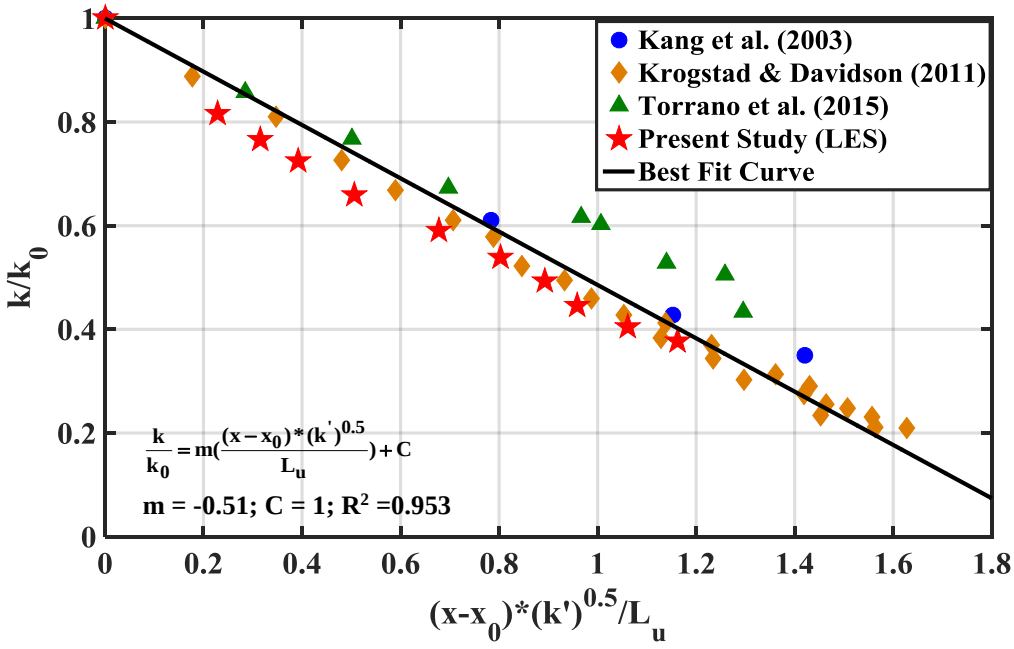

Figure 2.34 Spatial decay of TKE profiles for different experiments and the present LES data with the x abscissa scaled with local k and L_u plotted with a sold line that shows the best fit linear curve

Equation (2.50) along with equation (2.60) also helps one predict the initial TKE (k_0) and length scale values (L_{u0}), provided one knows the local values of TKE (k) and length scale (L_u) which gives another method of estimating the statistical turbulence parameters in the domain.

However, it is worth mentioning that, within computational accuracy, the turbulent kinetic energy (TKE) decay curves obtained from the experiments and the LES plotted in figures (2.28, 2.29 and 2.34) all collapse onto a universal decay curve, as expected from the model equations (2.49, 2.50 and 2.60).

2.9.2 Set of prediction correlation equations

There are, altogether, 3 sets of data, which have been used here for the predictive methodology, in accordance with the previous experimental studies, to estimate the magnitude of the local and initial TKE and L_u values. The values of the fitted coefficients for all sets of data are summarized in table (2.14) and (2.15).

Table 2.14 Constants obtained from best regression curve fitting procedure to equations 2.49 and 2.50 using the method of Non-linear least squares

Normalization parameter of the x ordinate	Decay exponent (n)	Decay coefficient (A)	R^2
$k_0^{'}$ and L_u	2.38	0.27	0.992
$k_0^{'}$ and L_{u0}	1.16	0.44	0.971

Table 2.15 Constants obtained from best regression curve fitting procedure to equation 2.60 using the method of Non-linear least squares

Normalization parameter of the x ordinate	m (slope)	C (intercept on the y ordinate)	R^2
$k^{'}$ and L_u	-0.51	1	0.953

Since, the primary objective from the current study was to formulate a simple predictive method for establishing particular leading edge TKE and L_u values for bluff body studies based on specifying upstream inlet conditions, equations (2.49), (2.50) are re-written in logarithmic form to arrive at a system of linear equations consistent with the form of equation (2.60). The new system of equations is presented below:

$$\log(k^{'}) = \log(k_0^{'}) - n_1 \log(\frac{A_1 (k_0^{'})^{0.5} (x - x_0)}{L_u} + 1) \qquad (2.61)$$

where $n_1 = 2.38$ $A_1 = 0.27$, $x_0 = 20M$ (for bi-planar square grids)

$$\log(k^{'}) = \log(k_0^{'}) - n_2 \log(\frac{A_2 (k_0^{'})^{0.5} (x - x_0)}{L_{u0}} + 1) \qquad (2.62)$$

where $n_2 = 1.16$, $A_2 = 0.44$, $x_0 = 20M$ (for bi-planar square grids)

$$\frac{k}{k_0} = \frac{k'}{k_0'} = m\left(\frac{(x - x_0) * (k')^{0.5}}{L_u}\right) + C \tag{2.63}$$

where m = -0.51, C = 1, $x_0 = 20M$ (for bi-planar square grids)

All the equations presented here show several variants of the same phenomenological model obtained using the relation between the inviscid estimate of ε and the decay of turbulent kinetic energy (TKE), that in turn quantifies the spatial decay of turbulent kinetic energy downstream from the point of inlet turbulence generation.

Sample calculations are shown in Appendix B, where both initial and local values of the turbulent parameters (TKE and L_u) have been estimated to make the use of the equations clearer to the reader.

2.9.3 Sensitivity of the virtual origin (x_0)

The sensitivity to the choice of virtual origin x_0 on the goodness of the fit for the experimental data sets with each other and to the LES data, based on the different correlations (eq. 2.49, 2.50, 2.60) are explored in the current section. The sensitivity check was performed to see whether a change in the choice of the virtual origin (x_0) value, yields a better fit of the LES results to the experimental data or not. The virtual origin was shifted further downstream for all the experimental data (x_0 = 30M for Kang *et al.* (2003), x_0 = 60M for Krogstad and Davidson (2011), x_0 =30M for Torrano *et al.* (2015)) on a consistent metric (shifting 10M for each), while comparing both sets of data, in the homogeneous region of turbulence. Three sets of figures (fig. 2.35, fig. 2.36 and fig.2.37) are presented in the following section where the x abscissa have been scaled differently in each of the figures.

2.9.3.1 Scaling with the local magnitudes of integral length scale (L_u)

Figure (2.35) represents the spatial decay of non-dimensional TKE profiles scaled with the non-dimensional parameter $(x - x_0) * (k_0')^{0.5} / L_u$ with local L_u as a variable, plotted

for all the relevant experimental studies and the current LES study. The A_1 and n_1 values obtained from the best fit curve shown are 0.27 and 2.35 with R^2 = 0.996 respectively with 95% confidence bounds of the estimate. As expected, the values of the decay coefficient (A_1) and the decay exponent (n_1) obtained from the best fit curve in the figure (2.35) are in close proximity (less than 2%) to those obtained from the earlier plot (fig. 2.28) with the same scaling parameter. This concludes that after turbulence becomes fully developed to isotropic and homogeneous condition, a shift in the virtual origin (x_0) of the experimental data has negligible effect on the goodness of the fit between the LES and the experimental results when scaled with the local values of the integral length scale (L_u).

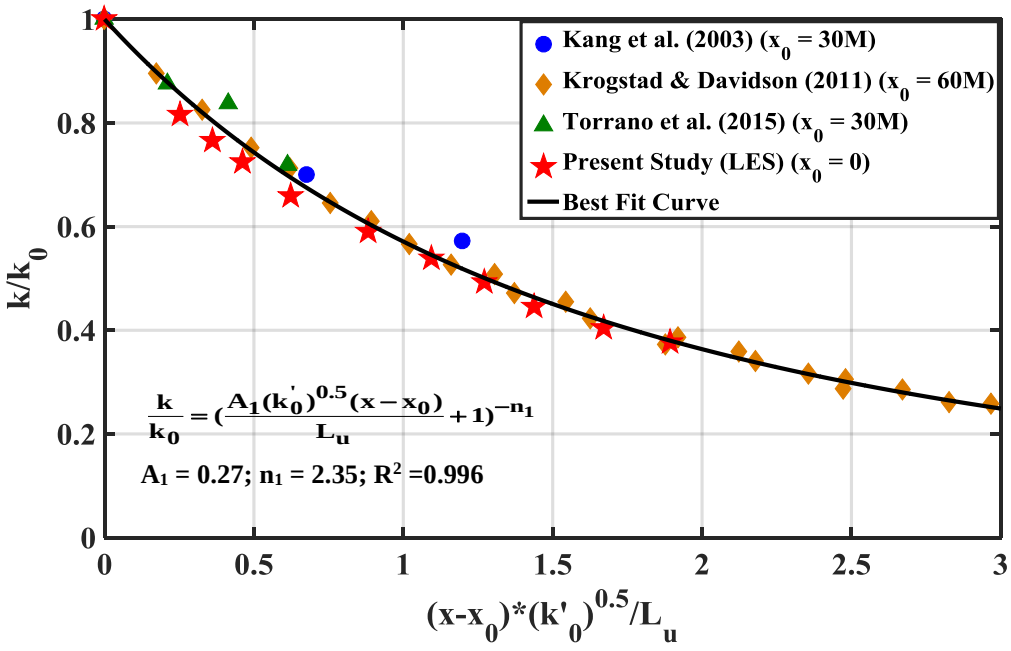

Figure 2.35 Spatial decay of TKE profiles for different experiments and the present LES study scaled with local integral length scale (L_u) with a different choice of virtual origin (x_0) plotted with a solid line that shows the best fit power law

2.9.3.2 Scaling with the initial magnitude of integral length scale (L_{u0})

Figure (2.36) shows the non-dimensional TKE profiles now plotted with the different scaling parameter, $(x-x_0)*(k_0')^{0.5}/L_{u0}$, scaled with an initial value of integral length

scale (L_{u0}). The values of A_2 and n_2 obtained from the best fit performed, after shifting the virtual origin (x_0), further downstream for the experimental data are, are 0.91, 0.64 respectively with the fitted R^2 = 0.967. However, from figure (2.36), it is revealed that, although the experimental data lie up much closely with each other, the current fit between the experimental data and the LES results does not improve as compared to the previous fit presented in figure (2.29). This is evident from the R^2 value of 0.971 obtained for the figure (2.29) which shows less than 0.5% difference when compared to the R^2 = 0.967 obtained with a shift in the virtual origin in the current plot. (fig 2.36). This verifies the earlier observation made in the previous section that a shift in the virtual origin (x_0) has negligible influence on the goodness of the fit between the earlier experimental studies and the current LES data.

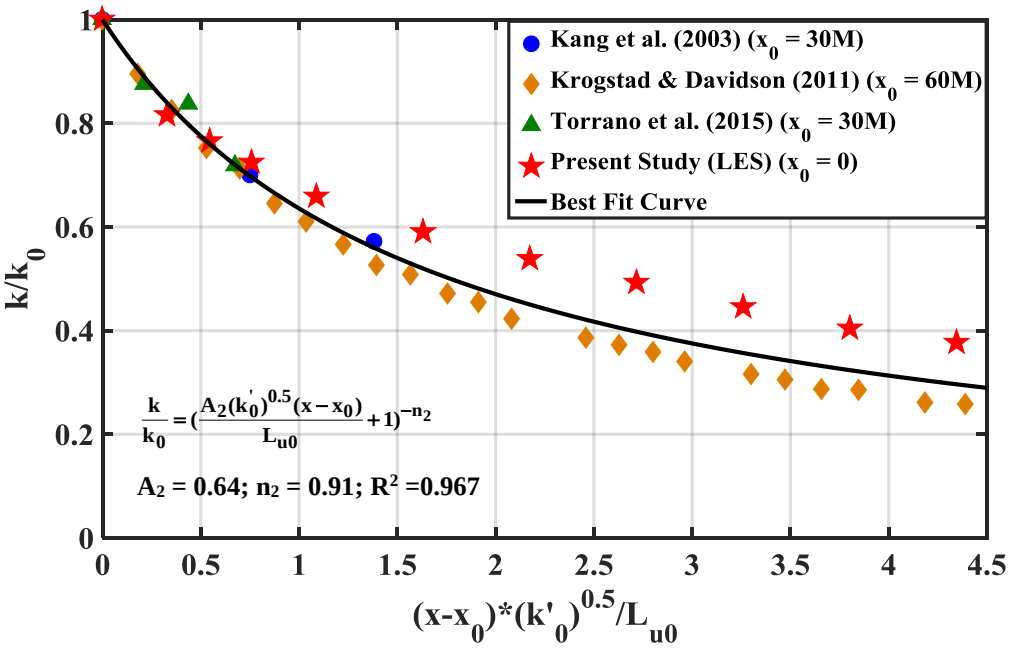

Figure 2.36 Spatial decay of TKE profiles for different experiments and the present LES study scaled with initial integral length scale (L_{u0}) with a different choice of virtual origin(x_0) plotted with a solid line that shows the best fit power law

2.9.3.3 Scaling with the local magnitude of TKE (k) and local magnitude of the integral length scale (L_u)

The spatial decay of TKE profiles is shown in figure (2.37) as a function of dimensionless parameter $(x-x_0)*(k')^{0.5}/L_u$, scaled with the local values of TKE (k) and the integral length scale (L_u). The best fit linear curve in the figure (2.37) yields a slope m = -0.53 and C = 1, having R^2 = 0.978. As expected, the slope of the function obtained from the current fit (fig. 2.37) is close to that obtained previously from the fit in figure. (2.34). However, an improvement in the magnitude of R^2 coefficient is observed in the current fit (R^2 = 0.978) in compare to the previous fit (R^2 = 0.953), which is mostly due to less scatter in the data sets obtained from the data of Torrano *et al.* (2015), at further downstream positions. This hints at the possibility that, if the virtual origin (x_0) is shifted downstream for the experiments, a better match between the different experiments and the LES results may be obtained provided the shift in the virtual origin is performed in an objective and consistent manner.

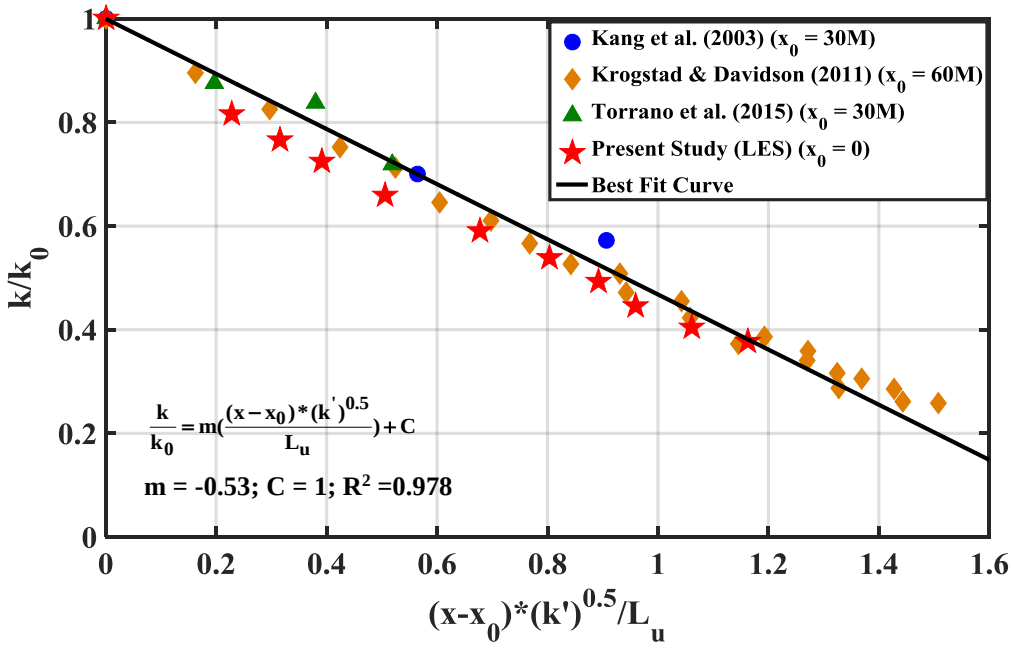

Figure 2.37 Spatial decay of TKE profiles for different experiments and the present LES study scaled with local TKE (k) and local integral length scale (L_u), with a different choice of virtual origin(x_0) plotted with a solid line that shows the best fit power law

All the fitted coefficient and exponent values obtained from the above best fitting curve procedure, with and without the shift in the virtual origin (x_0) are summarized in table (2.16) and table (2.17) for relative comparisons with each other.

Table 2.16 Constants obtained from best regression fit curve procedure using the method of Non-linear Least Squares (with a shift in virtual origin)

	Without a shift in the virtual origin (x_0)			With a shift in the virtual origin (x_0)		
Normalization parameter of the x ordinate	Decay exponent (n)	Decay coefficient (A)	R^2	Decay exponent (n)	Decay coefficient (A)	R^2
k_0' and L_u	2.38	0.27	0.99	2.35	0.27	0.996
k_0' and L_{u0}	1.16	0.44	0.97	0.91	0.64	0.967

Table 2.17 Constants obtained from best regression fit curve procedure using the method of Non-linear Least Squares (with a shift in virtual origin)

	Without a shift in the virtual origin (x_0)			With a shift in the virtual origin (x_0)		
Normalization parameter of the x ordinate	m (slope)	C (intercept on the y ordinate)	R^2	m (slope)	C (intercept on the y ordinate)	R^2
k' and L_u	-0.51	1	0.95	-0.53	1	0.978

2.9.4 Identification of nearly constant TKE conditions

It is worth mentioning that the correlations presented in equations (2.61, 2.62, 2.63) each represent a simplistic linear equation involving one unknown variable which can be used to estimate either the local turbulence parameters (TKE and L_u) at any downstream location or predict the initial turbulent parameters for decaying freestream turbulent flow. Thus, the equations (2.61), (2.62) and (2.63) completes the prediction tool for designing turbulence generating grids.

In order to support the previous statement, a few sample calculations have been done, where the known inlet turbulent parameters have been used to predict the unknown turbulent parameters at any location x downstream in the computational domain (for e.g. the values of TKE (k) and integral length scale (L_u), at x = 2m, 3m and 4m have been estimated using the inlet values of TKE and L_u). Similarly, additional calculations have been shown to estimate the unknown turbulent variables at the inlet for all the relevant experimental data sets available, with known local turbulent levels, in order to verify the applicability of the prediction tool to the experiments on decaying turbulence. All the computed values of TKE and L_u using the above prediction tool lie approximately within ±5% in accordance with the actual known values of those parameters. All the sample calculations are presented in the Appendix B for completeness in the discussion.

The other main objective from the present study was to identify a region of nearly constant incident TKE, where the spatial decay rates of TKE would be substantially smaller than in the other regions. This region of uniform TKE holds primary importance in experimental investigations carried out in wind tunnels for turbulent flow measurement, since in such case, the effect of free stream turbulence can be quantified accurately (as it will not vary monotonically over that regime), with relevance to the dynamics of boundary layer heat and mass transfer from a bluff body placed in a turbulent free stream. Determining the near constant TKE conditions in experimental surroundings is an arduous task and, hence, the CFD model prediction is aimed at specifying a grid to achieve acceptable levels of target TKE over a constant region. Figure (2.38) shows the variation of the TKE profiles as a function of the streamwise distance x. It is clearly identified from figure (2.38) that, in the region that extends from

x=2m to x=4m, the rate of decay of non-dimensional TKE is small with reference to the rates of change of TKE in the upstream section. The percentage variation of non-dimensional TKE in proportion to its specified initial TKE value over that near constant region (i.e. from x = 2m to x = 4m) is 14.41% which is relatively very small compared to the percentage variation of TKE over x= 0m to x=2m, which is 41.33%. The observation is more pronounced in the next figure (2.39), where the spatial gradient of TKE $\frac{d(\frac{k}{k_0})}{dx}$ has been plotted against the distance x in the streamwise direction. As can be seen from the plot in figure (2.39) the rate of change of non-dimensional TKE is of the order of magnitude -2 over the region extending from x = 2m to x = 4m. This establishes the premise that the turbulent kinetic energy (TKE) asymptotically decays spatially in the streamwise direction to achieve a fairly constant magnitude over a region located downstream starting at x = 2m. Figure (2.40) shows the variation of spatial rate of decay of TKE in the form of $\frac{d(\frac{k}{k_0})}{d((x-x_0)*(k_0')^{0.5}/L_u)}$ plotted against the non-dimensional variable $(x-x_0)*(k_0')^{0.5}/L_u$ for all the experimental data and the LES results. The comparisons between the experimental results and the LES data display very good quantitative agreement over the entire range of data and suggests very little change in the decay rate of TKE over the x-ordinate dimension ranging from 1 to 3.5. Therefore, the quantitative agreement presented in figure (2.40) can act as a validation case towards specifying a grid to achieve similar levels of turbulence as generated in numerical simulations. The grid that has the closest match to the aforementioned CFD prediction model and can be used as the turbulence generator in wind-tunnel experiments is *"Conventional Bi-Planar square grid*" which can be made up of any thin sheet metal (e.g. aluminum). The grid must have square holes of uniform cross-sectional area with the mesh spacings (M) chosen in accordance to the range of turbulent Reynolds number (low, medium or high) one wishes to generate downstream from the grid-section.

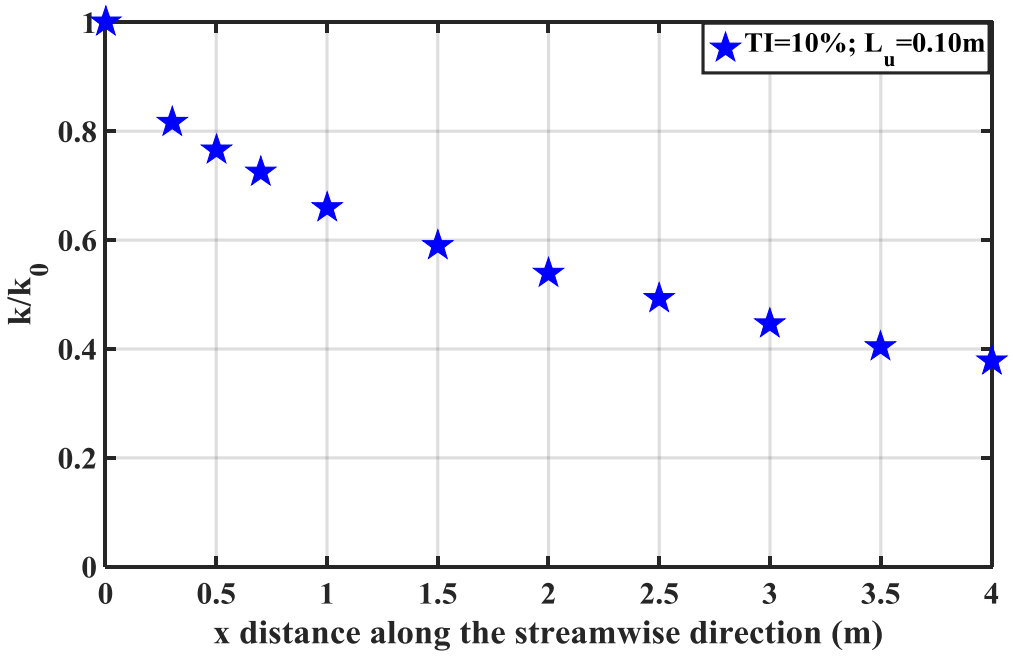

Figure 2.38 Spatial decay of TKE profile (LES) plotted against the streamwise distance x ($\bar{U}$ = 4m/s, TI = 10% and L_u = 0.10m)

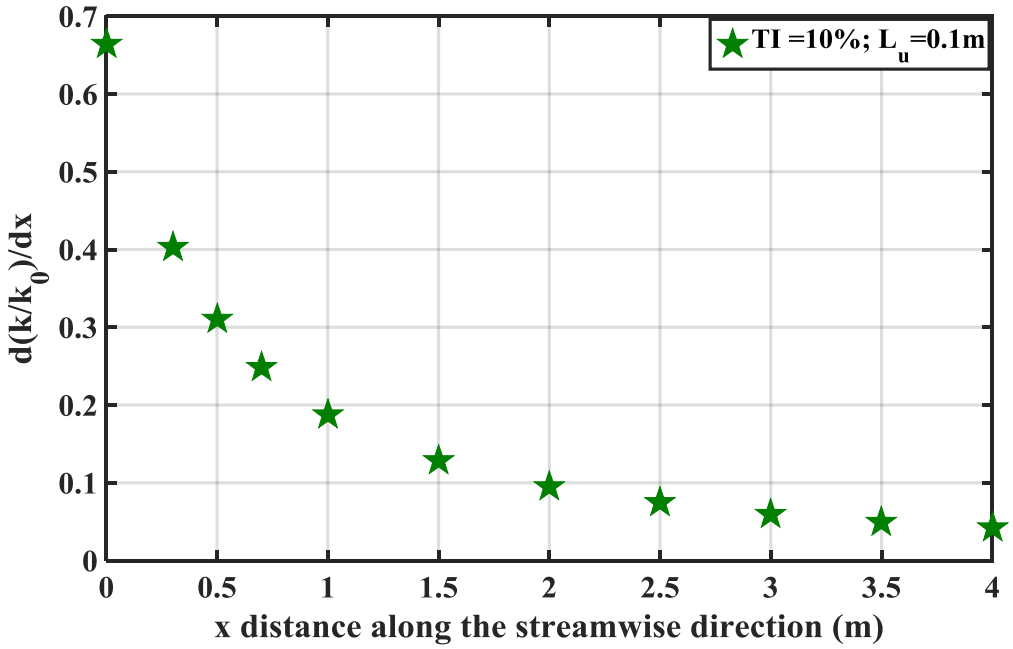

Figure 2.39 Rate of spatial decay of TKE profile (LES) along the streamwise distance x ($\bar{U}$ = 4m/s, TI = 10% and L_u = 0.10m)

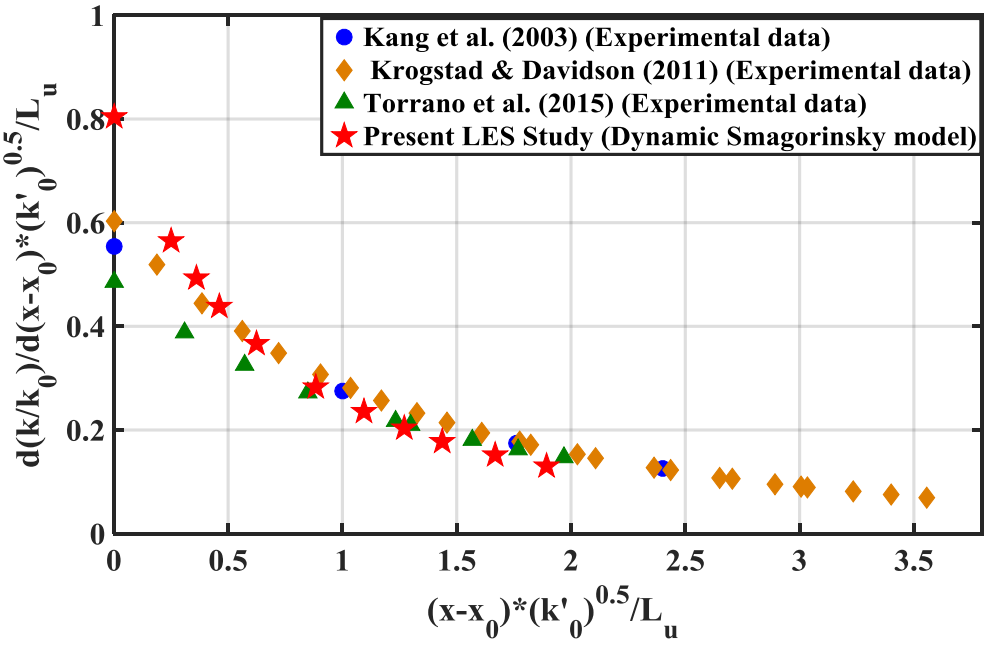

Figure 2.40 Rate of spatial decay of TKE profile in the form of $d(k/k_0)/d((x-x_0)*(k_0')^{0.5}/L_u$ plotted against $(x-x_0)*(k_0')^{0.5}/L_u$ for all the experimental data and the LES results ($\bar{U}$ = 4m/s, TI = 10% and L_u = 0.10m)

2.9.5 Influence of the different Reynolds number, integral length scales and turbulence intensities on the spatial decay rate of TKE

In this section the effect of initial turbulent flow parameters on the spatial decay rate of TKE has been examined, to find out whether the decay downstream has a universal self-similar behaviour. This effect is determined in terms of data obtained as a part of the present numerical study performed for both RANS and LES simulations. The studies cover a range of flow Reynolds number corresponding to velocities ranging from 4m/s to 40m/s, initial turbulence intensity (TI) varying from 10% to 30%, and the initial integral length scales (L_u) varying from 0.02m to 0.1m.

2.9.5.1 Effect of initial conditions on the decay power law exponent and coefficient based on RANS studies

In this section, the influence of the initial conditions such as Reynolds number (Re), turbulence intensity (TI) and integral length scales (L_u) on the spatial decay rate of TKE is assessed and its consequence on the values of decay coefficient and decay exponent are explored. This assessment is done for the 3D steady RANS simulations carried out in the present work. For all the numerical simulations, the virtual origin (x_0) is taken to be zero and the decay exponent (n) and coefficient (A) are found using the method of best fit curve to the equations; presented in (eq. 2.49 and 2.50), as discussed previously.

The spatial decay of the TKE profiles as a function of turbulent Reynolds number (Re_{Lu}) at the inlet is shown on figure (2.41) for steady RANS simulations. The turbulent Reynolds Number (Re_{Lu}) is based on the integral length scale value at the inlet (L_{u0}) and the streamwise r.m.s velocity fluctuation u', given by $Re_{Lu0} = u' L_{u0} / \nu$, where ν is the kinematic viscosity of the fluid (1.57×10^{-5} m^2/s^2) and it varies from 2.55×10^3 to 2.55×10^4. The turbulence intensity (TI) and the integral length scales were maintained at 10% and 0.1m respectively at the inlet, to make the parameters consistent across all cases. It is obvious from the plot that the global turbulent Reynolds number (Re) based on the inlet integral length scale (L_{u0}) (i.e. Re_{Lu0}) has no effect on the decay rate of TKE downstream of an inlet. This can be attributed to the fact that the turbulent kinetic energy dissipation rate ε does not depend on the mean streamwise flow velocity $\overline{U}$, rather it depends on the local velocity fluctuations and the length scales at a prescribed location, since $\varepsilon = -\frac{u'^3}{L_u}$. Hence, all the turbulent Reynolds numbers studied in the following range present the same decay curve. A best fit curve is plotted according to equation (2.49), yielding R^2 = 0.999. The corresponding values of decay coefficient (A_1) and the decay exponent (n_1) are 0.25 and 4.09, respectively. Here, the exact values of the decay coefficient (A_1) and the decay exponent (n_1) are not important, rather the aim is to observe whether the difference in the flow velocity at the inlet has an effect on the spatial decay of TKE.

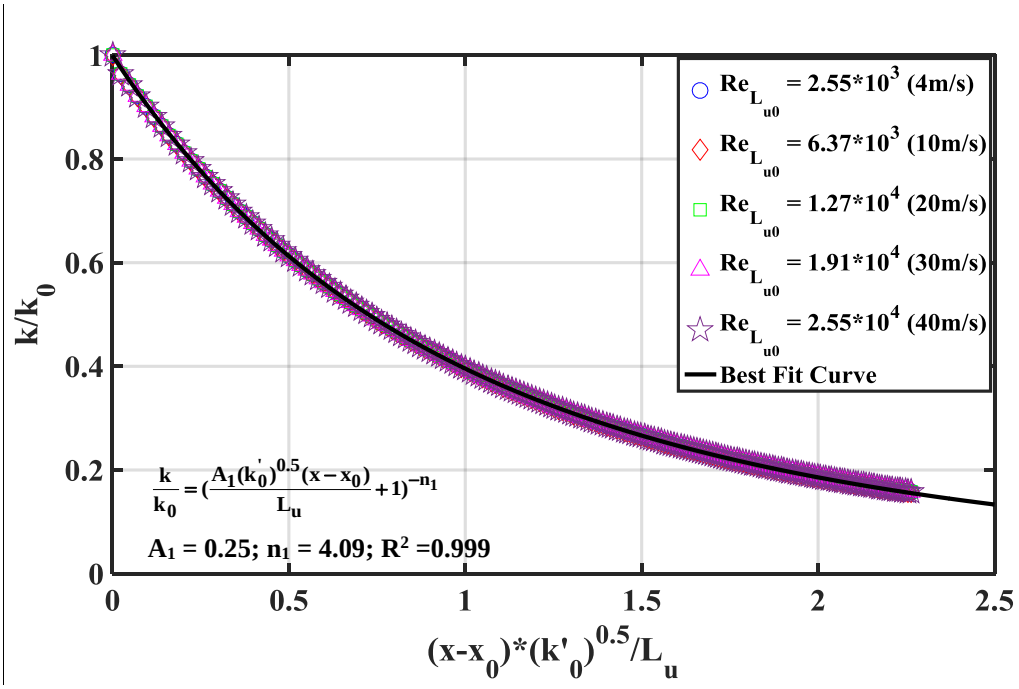

Figure 2.41 Spatial decay of TKE profiles for different Reynolds number (Re) prescribed at the inlet (RANS)

A parametric study is carried out in the following section, where figure (2.42) and (2.43) shows the influence of different magnitudes of turbulence intensities (TI) and integral length scales (L_u) prescribed at the inlet, on the streamwise decay of TKE. The specified inlet length scale value has been varied from 0.02m to 0.10m, at a fixed turbulence intensity (TI) of 10% at the inlet, which then corresponds to the turbulent Reynolds number (Re_{Lu0}) varying from 509.5 to 2.55×10^3. Similarly, the inlet turbulence intensity (TI) has been varied from 10% to 30% keeping the inlet length scale (L_{u0}) fixed at 0.1m, that corresponds to a turbulent Reynolds number (Re_{Lu0}) varying from 2.55×10^3 to 7.69×10^3. It is clear from figure (2.42) that, for a fixed turbulence intensity, a smaller length scales facilitates a higher rate of decay of the velocity fluctuations. This is already predicted from the inviscid estimation of ε where, $\varepsilon \propto \frac{1}{L_u}$, for fixed u' value. Similarly, $\varepsilon \propto u'^3$ for a fixed length scale value, which is why a higher velocity fluctuation u' aids higher rate of decay of the TKE, since the dissipation rate is higher. This is also verified from the plot shown in figure (2.43) where the highest turbulence intensity curve has the steepest slope.

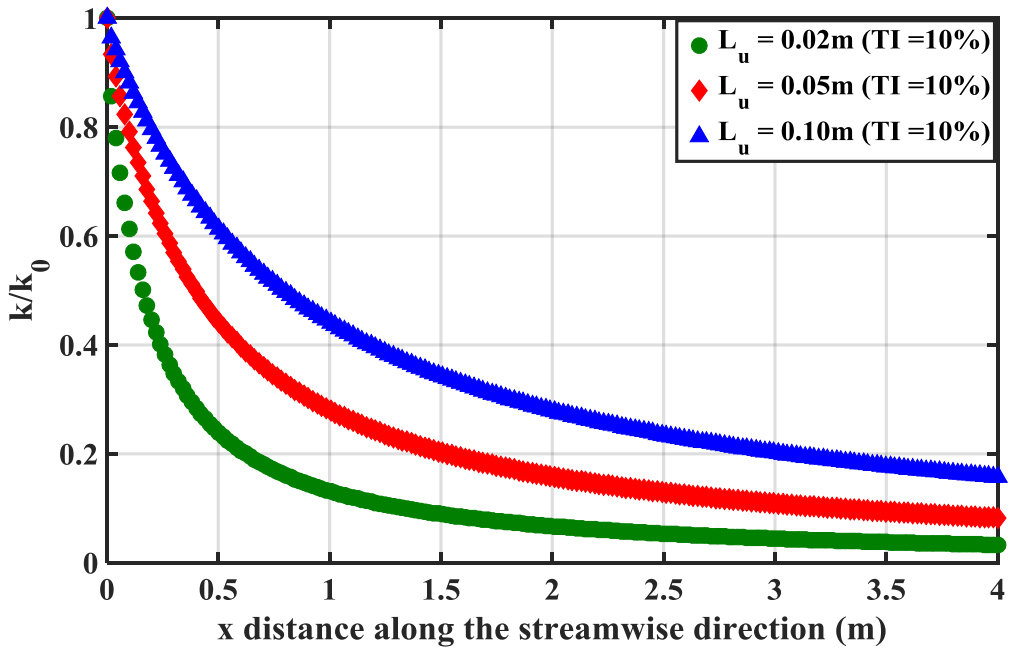

Figure 2.42 Spatial decay of TKE profiles (RANS) for different integral length scales (L_u) prescribed at the Inlet

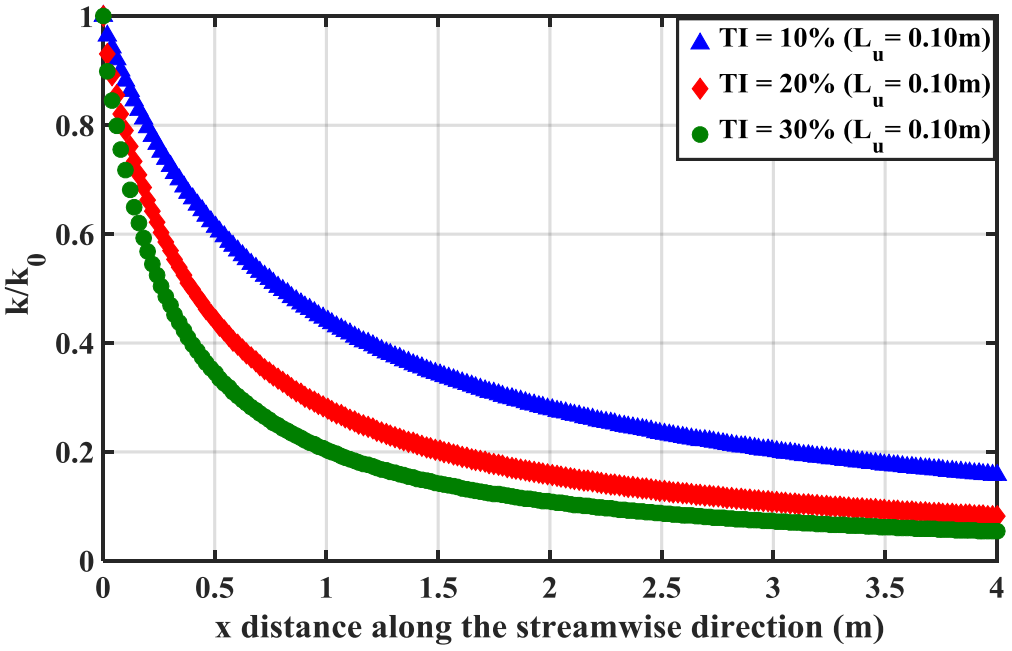

Figure 2.43 Spatial Decay of TKE profiles (RANS) for different Turbulence Intensities prescribed at the Inlet

However, as discussed before, the decay of turbulence is universally self-similar in nature and, as expected, is not a function of the initial conditions. Hence, when the TKE equations are suitably normalized according to equation (2.49), a single best fit decay curve is obtained, for all values of turbulence intensity (TI) and length scale (L_u) prescribed at the inlet. Figure (2.44) shows the best fit curve plotted against the spatial variation of TKE for different turbulence intensities and integral length scales, where R^2 = 0.999. The corresponding values of the fitted decay coefficient (A_1) and the decay exponent (n_1) values are equal to 0.31 and 3.40, respectively.

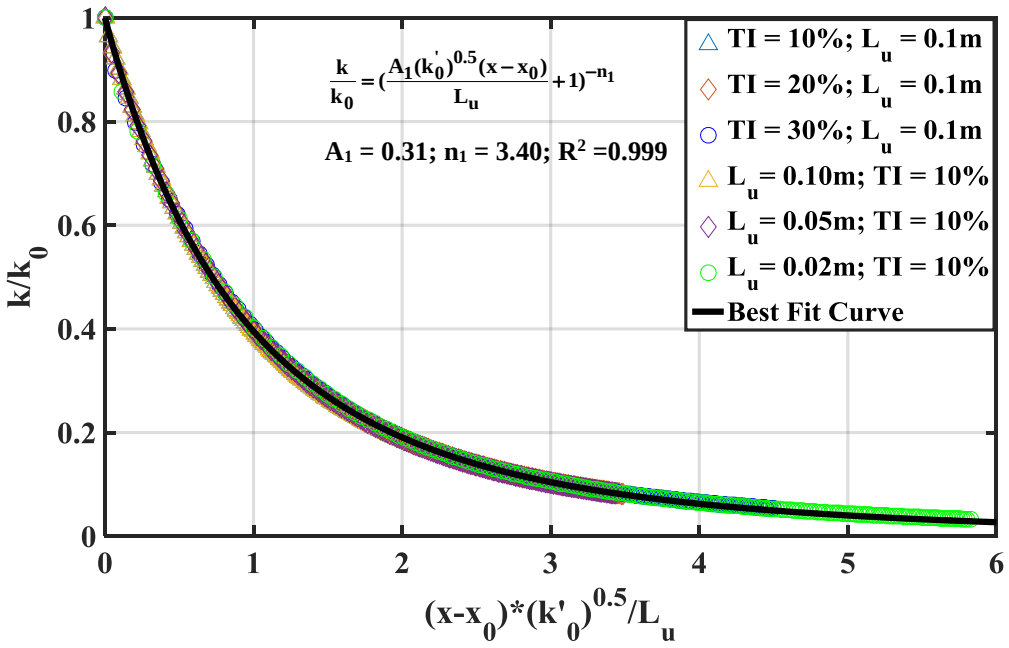

Figure 2.44 Spatial decay of TKE profiles (RANS) for different turbulence intensities and Integral length scales plotted with a solid line that shows the best fit power law

2.9.5.2 Effect of initial conditions on the decay power law exponent and coefficient based on LES studies

In the present section, a parametric analysis obtained from the LES simulations are presented. The integral length scales have been varied from 0.02m to 0.10m, at a fixed turbulence intensity (TI) of 10%, which corresponds to the flow turbulent Reynolds number (Re_{Lu0}) varying from 509.5 to 2.55×10^3. Similarly, the turbulence intensities (TI)

have been varied between 10% and 30%, at a fixed length scale value of 0.1m. The turbulent Reynolds number of the flow varies from 2.55×10^3 to 7.64×10^3. The simulations with different mean flow velocities at the inlet was not carried out for LES, since the RANS simulations already predicted that the rate of turbulence decay is insensitive to the variation of flow velocities at the inlet. A similar behaviour of the spatial decay of the TKE profiles was observed when the integral length scales and turbulence intensities were varied at the inlet, the reasons for which have been already discussed in the previous section.

As expected, when the length scale becomes smaller the decay rate is higher and, similarly, higher turbulence intensity gives a higher decay rate, as evident from figures (2.45) and (2.46), which shows the spatial decay of TKE profiles for different turbulence intensities and length scales, the reasons for which has been discussed previously. Figure (2.47) is another indicative measure of the nature of turbulence encountered in numerical simulations, which is mostly of Saffman type where the streamwise velocity fluctuations and the length scale satisfies the relation $\overline{u'^2}L_u^{\,3} \approx$ constant.

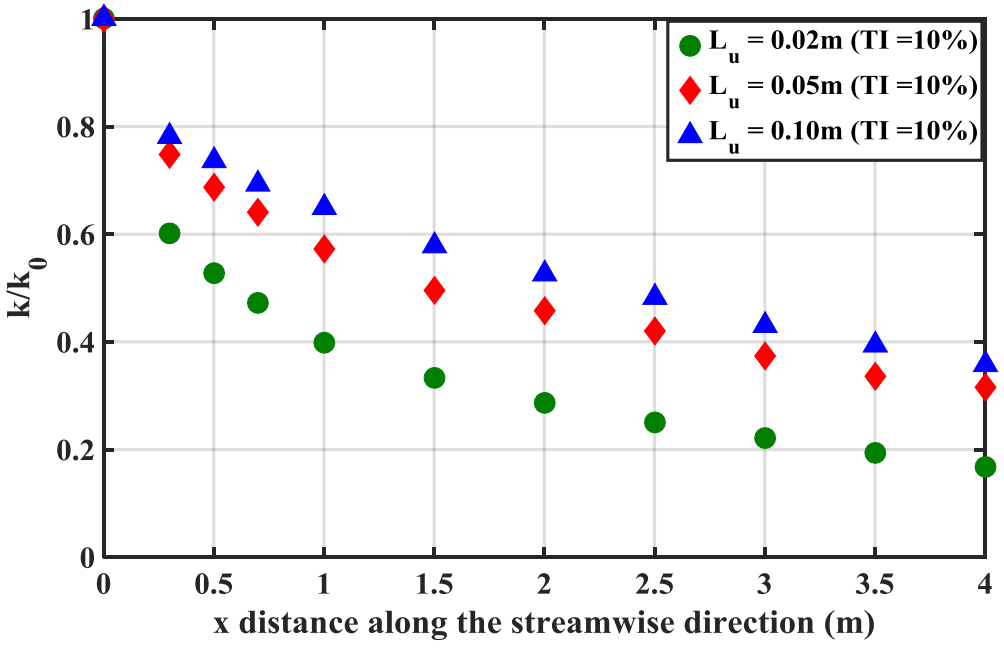

Figure 2.45 Spatial decay of TKE profiles for different integral length scales (L_u) prescribed at the inlet (LES)

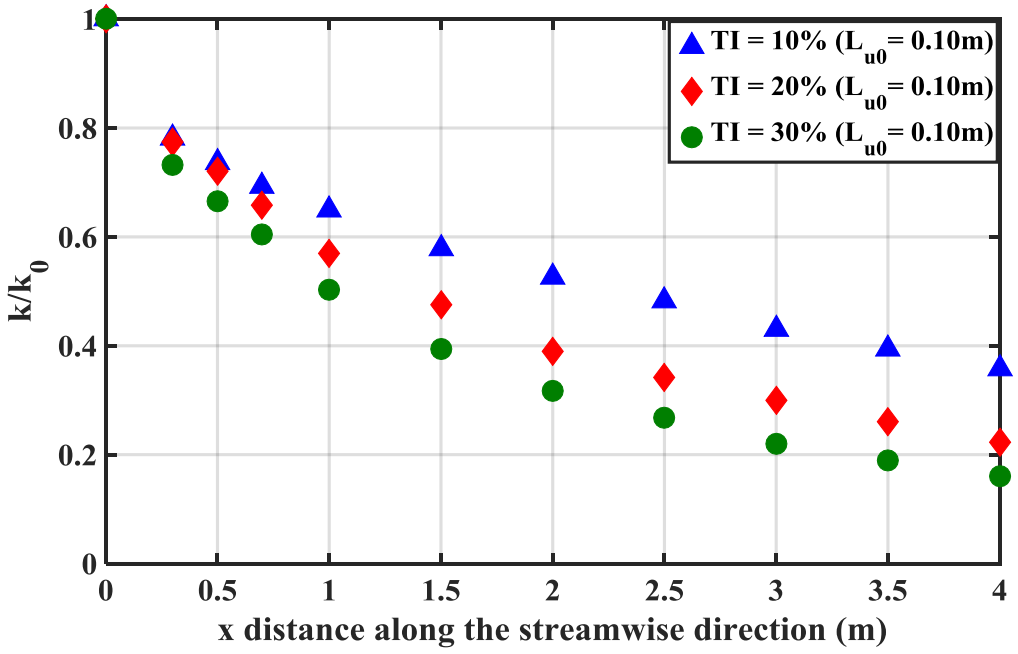

Figure 2.46 Spatial decay of TKE profiles for different turbulence intensities at the inlet (LES)

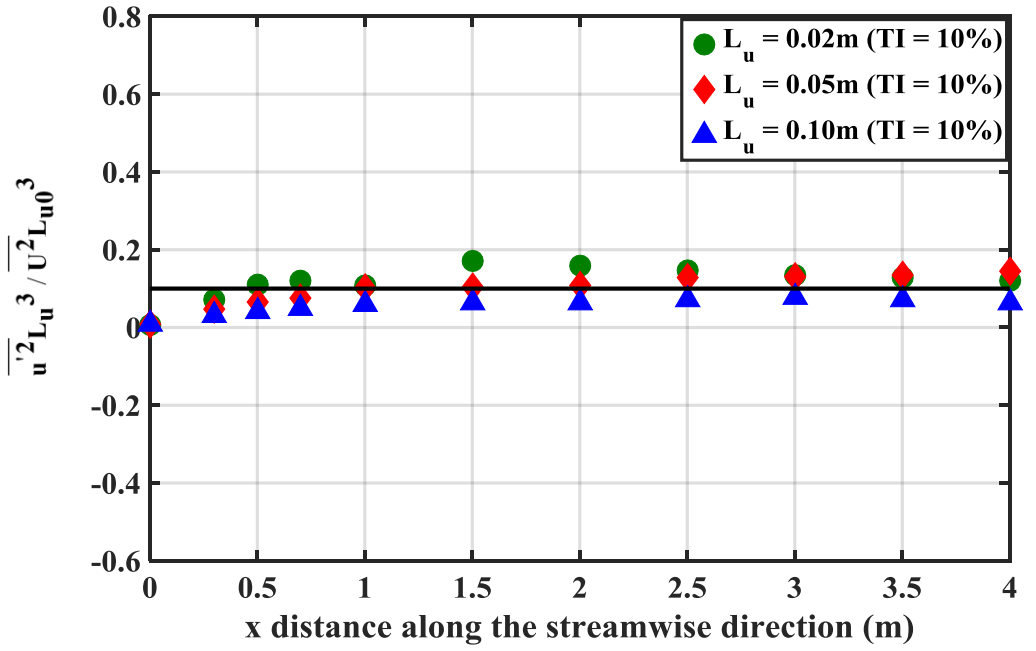

Figure 2.47 Downstream variation of $\overline{u'^2}L_u^3 / \overline{U^2}L_{u0}^3$ along the centreline of the domain (LES)

Figure (2.48) shows the spatial decay of TKE profiles for all values of turbulence intensity and length scales considered in the study, put into a single regression equation fit (eq. 2.49) to find a single value of the estimated coefficients from the curve fit. As anticipated, the decay characteristics of the turbulent flow shows similar behaviour for all length scales and turbulence intensity values, which depicts a unifying nature of the turbulence decay in the nearly isotropic and the homogeneous region. R^2 = 0.977, which is convincing for a good fit. The decay coefficient (A_1) and the decay exponent (n_1) obtained from the fit are 0.30 and 2.43, respectively. These values are very close and are comparable to those obtained from the experimental validation of the LES results with the curve fit (eq. 2.49) shown in figure (2.28). The difference in the fitted coefficients is due to the fact that, in the former case the aim was to bring the LES results and experimental data together, whereas in the latter, only the LES results are compiled together and plotted for different length scale and turbulence intensity values.

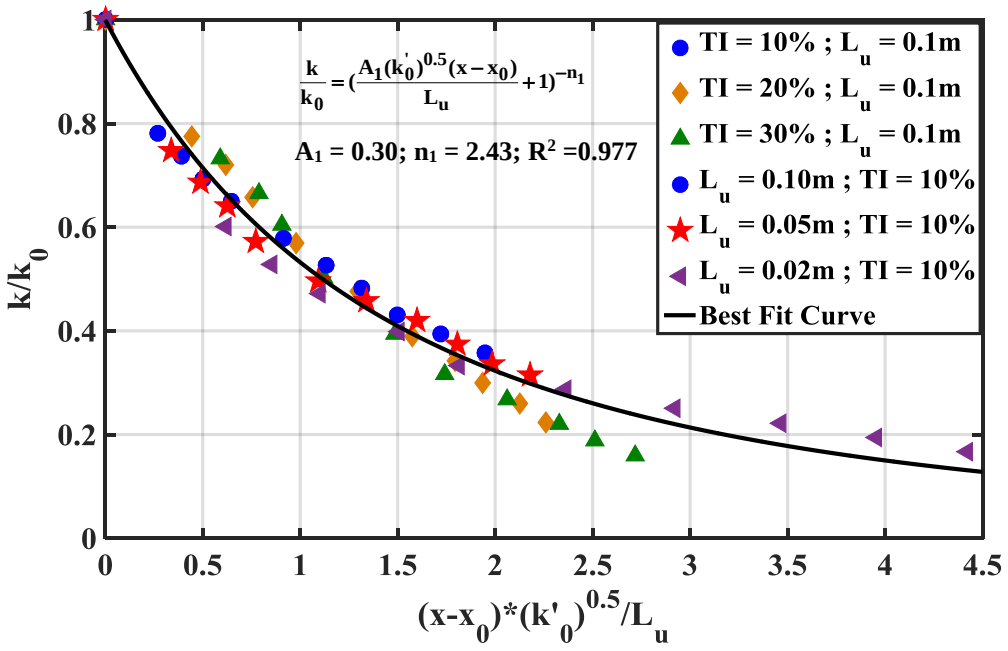

Figure 2.48 Spatial decay of TKE profiles for different Turbulence Intensities and Integral length scales plotted with a solid line that shows the best fit power law

On a similar note, all the LES results obtained for different values of inlet turbulence intensities (10%, 20% and 30%) and integral length scale values are plotted with all the

experimental data together with its fit in figure (2.49). The best fit curve obtained with 95% confidence bounds estimates the decay coefficient (A_1) and the decay exponent (n_1) values as 0.29 and 2.32 which have less than 2% variation compared to those obtained while plotting the best fit curve in figure (2.28). An $R^2 = 0.973$ is obtained which reflects the goodness of the curve fit in the following figure for all the data. This concludes the fact that that, irrespective of the different magnitudes of the turbulent parameters specified at the inlet, a reasonable fit with a single power law can be obtained that best represents all the data. However, a slight deviation of the data observed for the 20% and 30% turbulence intensity cases (refer to fig. 2.48), reflects that, an increase in the turbulence levels at the inlet increases the anisotropy of the turbulent fluctuations to some extent in the computational domain, the levels of which are not very excessive (isotropy ratio around 1.3-1.5) and are comparable to, if not better, than in most experiments where 10%-30% difference in the streamwise and the span wise velocity variance have been reported (Skrbek and Stalp, 2000). The other possible reason for the deviation observed could be the uncertainty error associated with the estimate of the local integral length scale (L_u) used in the scaling factor for the x abscissa variable. The well-known Taylor hypothesis (Taylor, 1935) has been used while determining the integral length scale values from the integral time-scale estimation using the auto-correlation function discussed in section (2.8.3). However, according to (Batchelor, 1967), this hypothesis is only valid for turbulence intensity up to 15%, whereas in the current study simulations were carried out for turbulence intensities of 20% and 30% and, thus, the integral length scale estimation for these turbulent intensity cases may not be very accurate in nature.

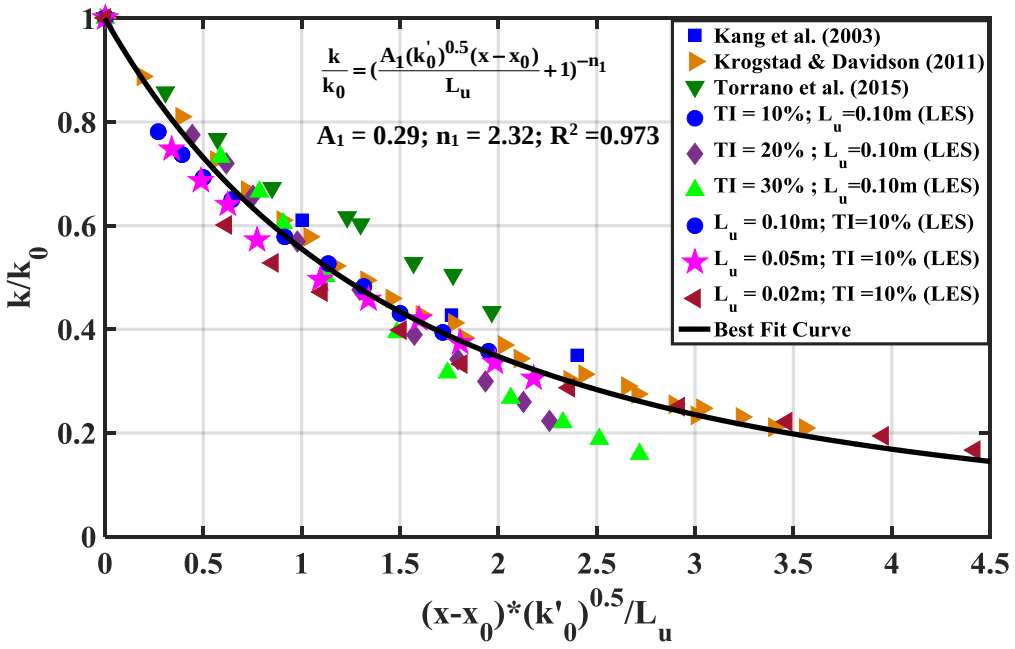

Figure 2.49 Spatial decay of TKE profiles for different turbulence intensities and integral length scales compared with the relevant experimental results plotted with a solid line that shows the best fit power law

2.9.5.3 Identification of near constant turbulent conditions for different inlet turbulence conditions

In this section, re-assessment of the CFD predictive model with different inlet turbulence intensities and integral length scales have been carried out to identify the near constant turbulent conditions downstream from the inlet. Figure (2.50) illustrates the results of the investigation where the spatial decay of non-dimensional TKE profiles for different prescribed turbulence intensities and length scales are plotted against the streamwise distance. The figure clearly reflects that, between x=2m and x=4m, the variation in the magnitude of TKE is relatively smaller than in the upstream section ranging from x=0m to x=2m. The present results are consistent with the results already shown (fig. 2.38) and discussed in section (2.8.6), which demonstrates that, irrespective of the different magnitudes of turbulence intensities and integral length scales specified at the inlet, a near uniform region extending between the x=2m to x=4m can be achieved, over which

the TKE does not change more than 15% in proportion to the specified turbulence intensity at the inlet.

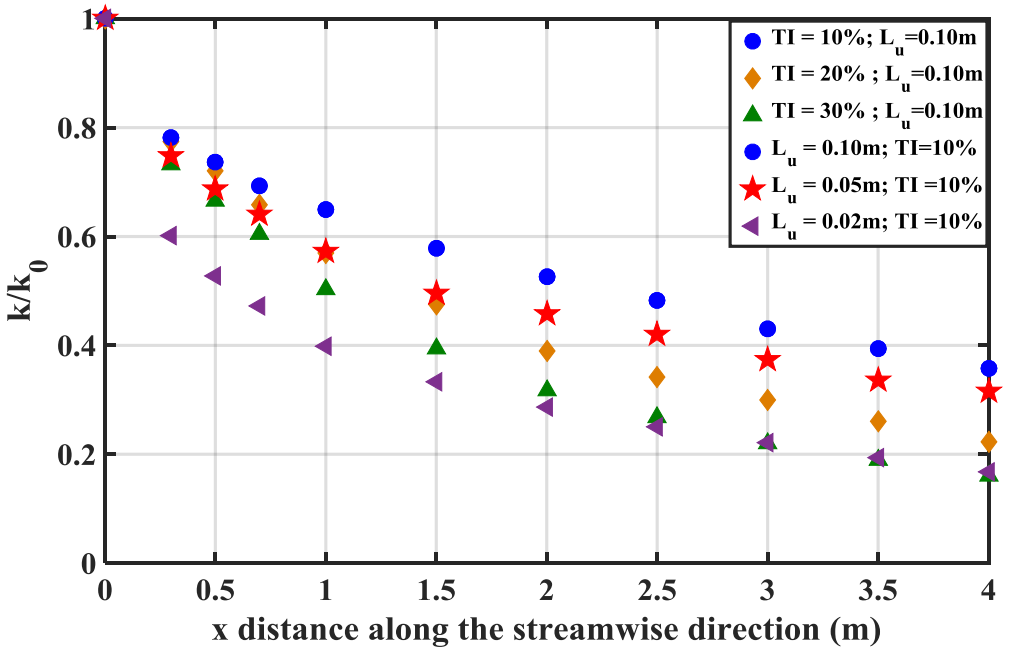

Figure 2.50 Spatial decay of TKE profiles for different inlet turbulence intensities (TI) and integral length scales (L_u) along the streamwise distance x

These results are also justified from the plot shown in the figure (2.51) where the streamwise spatial gradient of the dimensionless TKE is plotted against the streamwise distance x to identify regions where the rate of change of TKE is small. The slope of the gradient is of the order of magnitude -2 in the region from the mid-section until the end which re-asserts the validity of the current prediction method in determining the nearly constant region of uniform TKE that roughly extends from x=2m to x=4m consistent with figure (2.39).

Having thoroughly examined the different aspects of spatially decaying freestream turbulence in the previous discussions, the next section summarizes the key findings from the research.

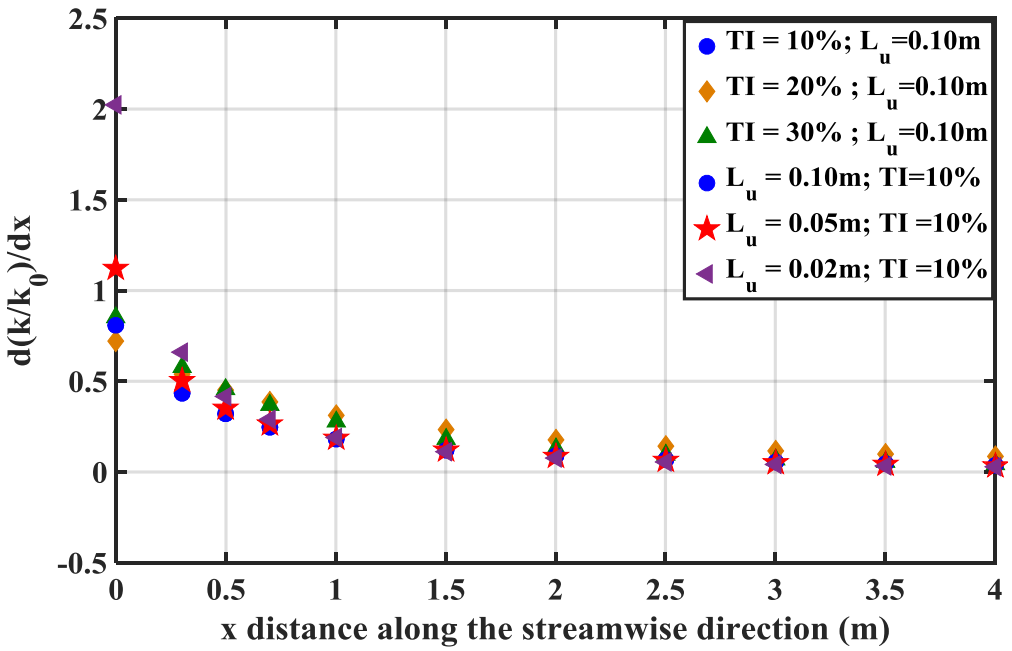

Figure 2.51 Rate of spatial decay of TKE profiles for different inlet turbulence intensities (TI) and integral length scales (L_u) along the streamwise distance x

2.10 Summary

This section discusses key points and summarizes the results obtained from the current numerical simulations carried out in this study.

- With proper choice of inlet turbulence generator algorithm, an approximate isotropic and homogeneous condition can be achieved in turbulence generated by computer simulations. The skewness of the velocity fluctuations exhibits near isotropic conditions with the isotropy ratio varying between 1.01 to 1.15, which is well in accordance with the nature of the turbulence generated in most wind tunnel experiments.

- Turbulence generated in numerical simulations highly suggests its nature to be of Saffman type (Saffman, 1967), ($\overline{u'^2}L_u^3 \approx$ constant), irrespective of the integral length scale (L_u) value specified at the inlet.

- The laws of similarity suggested by Saffman (Saffman, 1967) point out that a decrease in the velocity fluctuations in the streamwise direction would manifest itself in growth of the integral length scale (L_u) along the domain, a trend that is verified in the current study. Therefore, both turbulent velocity fluctuations and integral length scale are inter-linked with each other and both contribute to the decay of TKE downstream from the inlet. Therefore, one should consider both the factors before invoking any prediction on the decay rate of the TKE.

- The current LES results (though not the RANS model) show very good qualitative and quantitative agreement with the earlier relevant experimental studies of Kang *et al.*, (2003), Krogstad and Davidson (2011) and Torrano *et al.* (2015) and, thus, the CFD model prediction results are expected to be reliable.

- Irrespective of the magnitude of the turbulence scales specified at the inlet (initial TKE (k_0) and inlet integral length scale (L_{u0})), it was found that the decay of turbulence exhibits a near universal behaviour throughout the domain and, therefore, all the decay curves collapse onto a single power law curve, when scaled appropriately with the TKE and the integral length scale values. Thus, the decay of turbulent kinetic energy (TKE) is universally self-similar in nature.

- A predictive methodology has been proposed in the current study with estimates of the decay coefficient (A) and the decay exponent (n) based on all the LES and the earlier experimental results, that can be used to estimate unknown values of turbulent parameters (TKE or length scales) at different locations in the domain (at the inlet or any downstream position from the inlet). These predictions can be then extended to the type of turbulence generated in typical wind-tunnel experiment using a bi-planar square grid. The predictive tool is shown to replicate values within a difference of ±5% from the actual known values of those parameters.

- The sensitivity of the choice of virtual origin (x_0) on the goodness of the fit was examined and it was found that the shift in the virtual origin downstream of the grid in near isotropic and homogeneous regime had least effect on the goodness of the fit

provided that the shift in the virtual origin is performed in a consistent and objective manner.

- A near constant region of uniform incident TKE has been identified in the computational domain using the aforesaid predictive method and it ranges roughly between x=2m to x=4m. The region is same for all different values of prescribed inlet TKE and length scales and is insensitive to the choice of the inlet parameters.

2.11 Conclusion

The present work attempted to simulate freely decaying isotropic homogenous turbulence using numerical LES and RANS methodologies. The simulation results are compared qualitatively and quantitively to the earlier experimental data to justify the choice of the present numerical technique. The present LES results (but not the RANS model) demonstrate very good agreement with the earlier experimental studies and presents fairly accurate statistically averaged statistics (spectra, skewness, kurtosis) of quasi-homogeneous freestream turbulence. The Dynamic-Smagorinsky LES sub-grid model can be used to evaluate the correct rate of turbulence decay when compared with the decay characteristics of the earlier experimental results. Three different correlation equations, based on different scaling parameters, were presented in a simple linear form, which can be useful for estimating the local and initial values of turbulent parameters (i.e. TKE and L_u) which can then be extended to assist in the design of experiments carried out in wind tunnels for heat transfer and aerodynamic applications. However, such experimental techniques demand a uniform region of incident turbulent conditions for accurate quantification of relevant variables (Stanton number, Prandtl number, force-coefficients) on any bluff body (such as a sphere or cylinder) based on the oncoming turbulence intensities and turbulent length scales. The current CFD model helps in identifying those region, that can be deemed useful for studies of uniform freestream turbulence on bluff-body boundary layer phenomena.

The next chapter investigates the ineffectiveness of the standard RANS models from three different commercial codes (FLUENT, STAR-CCM+, CFX) in the accurate prediction of the decay rate of TKE. Inter-comparison of the RANS models from these

three softwares have been made with the LES model to show the discrepancy and, finally, improvement to the standard SST-k-ω turbulence models, based on the model constant values have been recommended to produce realistic turbulent decay behaviour for those turbulence models.

REFERENCES

Aboshosha, H., Elshaer, A., Bitsuamlak, G. T. and El Damatty, A. (2015) 'Consistent inflow turbulence generator for LES evaluation of wind-induced responses for tall buildings', *Journal of Wind Engineering and Industrial Aerodynamics*. Elsevier, 142, pp. 198–216.

ANSYS Fluent Theory Guide (2013). pp. 1-814.

Baines, W. D. and Peterson, E. G. (1951) 'An investigation of flow through screens', *Trans. Am. Soc. Mech. Engrs.*, 73, pp. 467–480.

Batchelor, G. (1948) 'Energy decay and self-preserving correlation functions in isotropic turbulence', *Quarterly of Applied Mathematics*, 6(2), pp. 97–116.

Batchelor, G. K. (1953) 'The theory of homogeneous turbulence', *Quarterly Journal of the Royal Meteorological Society*. John Wiley & Sons, Ltd, 79(341), pp. 457–458.

Batchelor, G. K. (1967) *An introduction to fluid dynamics*. Cambridge University Press. pp. 1-631

Batchelor, G. K. and Townsend, A. A. (1947) 'Decay of vorticity in isotropic turbulence', *Proceedings of the Royal Society of London A: Mathematical, Physical and Engineering Sciences*, 190(1023), pp. 534–550.

Batchelor, G. K. and Townsend, A. A. (1948a) 'Decay of isotropic turbulence in the initial period', *Proceedings of the Royal Society of London, Series A, Mathematical and Physical Sciences*, 193(1035), pp. 539–558.

Batchelor, G. K. and Townsend, A. A. (1948b) 'Decay of turbulence in the final period', *Proceedings of the Royal Society of London A: Mathematical, Physical and Engineering Sciences*, 194(1039), pp. 527–543.

Bennett, J. C. and Corrsin, S. (1978) 'Small Reynolds number nearly isotropic turbulence in a straight duct and a contraction', *Physics of Fluids*, 21(12), pp. 2129–2140.

Blair, M. F. (1983a) ‘Influence of free-stream turbulence on turbulent boundary layer heat transfer and mean profile development, Part I—Experimental data’, *Journal of Heat Transfer*, 105(1), pp. 33–40.

Blair, M. F. (1983b) ‘Influence of free-stream turbulence on turbulent boundary layer heat transfer and mean profile development, Part II—Analysis of results’, *Journal of Heat Transfer*, 105(1), pp. 41–47.

Cao, N., Chen, S. and Doolen, G. D. (1999) ‘Statistics and structures of pressure in isotropic turbulence’, *Physics of Fluids*, 11(8), pp. 2235–2250.

Celik, I. B., Cehreli, Z. N. and Yavuz, I. (2005) ‘Index of resolution quality for large eddy simulations’, *Journal of Fluids Engineering*, 127(5), pp. 949–958.

Chorin, A. J. (1968) ‘Numerical solution of Navier-Stokes Equations’, *Mathematics of Computation*, 22(104), pp. 745–762.

Comte-Bellot, G. and Corrsin, S. (1966) ‘The use of a contraction to improve the isotropy of grid-generated turbulence’, *Journal of Fluid Mechanics*, 25(4), pp. 657–682.

Comte-Bellot, G. and Corrsin, S. (1971a) ‘Simple Eulerian time correlation of full-and narrow-band velocity signals in grid-generated, “isotropic” turbulence’, *Journal of Fluid Mechanics*, 48(2), pp. 273–337.

Corrsin, S. (1963) ‘Encyclopedia of physics’, *Springer*, 8(2), pp. 1- 568.

Dagnew, A. K. and Bitsuamlak, G. T. (2013) ‘Computational evaluation of wind loads on buildings: A review’, *Wind and Structures, An International Journal*, 16(6), pp. 629–660.

Davidson, L. (2015) Fluid mechanics, turbulent flow and turbulence modeling. *Available at: http://www.tfd.chalmers.se/˜lada/MoF/lecture notes.html.*

Dryden, H. L. (1943) ‘A review of the statistical theory of turbulence’, *Quarterly of Applied Mathematics*, 1(1), pp. 7–42.

Franke, J., Hellsten, A., Schlünzen, H. and Carissimo, B. (2007) Best practice guideline

for the CFD simulation of flows in the urban environment, *COST action 732;* Quality Assurance and Improvement of Microscale Meteorological Models. Hamburg, Germany.

Franke, J., Hirsch, C., Jensen, A. G., Krus, H. W., Schatzmann, M., Miles, P. S. W. and S. D., Wisse, J. A. and Wright, N. G. (2004) 'Recommendations on the Use of CFD in Wind Engineering', *Cost Action C*, 14(May), pp. 1–11.

Frisch, U. (1995) *Turbulence: the legacy of AN Kolmogorov*. Edited by Cambridge. University. Press. pp. 1-296

George, W. K. (1992) 'The decay of homogeneous isotropic turbulence', *Physics of Fluids A: Fluid Dynamics*, 4(7), pp. 1492–1509.

Georgiadis, N., Rizzetta, D. and Fureby, C. (2009) Large-Eddy Simulation: Current Capabilities, Recommended Practices, and Future Research, *47th AIAA Aerospace Sciences Meeting including The New Horizons Forum and Aerospace Exposition*. pp. 1772-1784.

Gerasimov, A. (2016) Quick Guide to Setting Up LES-type Simulations, *Ansys Customer Portal*. Available at: http://www.tfd.chalmers.se/~lada/comp_turb_model/postscript_files/Quick_Guide_to_Setting_Up_LES_version_1.4_for_Lars.pdf.

Germano, M., Piomelli, U., Moin, P. and Cabot, W. H. (1991) 'A dynamic subgrid-scale eddy viscosity model', *Physics of Fluids A: Fluid Dynamics*, 3(7), pp. 1760–1765.

Hall, A. A. (1938) 'Measurements of the intensity and scale of turbulence', *Aeronautical Research Committee*, 1842.

Hillier, R. and Cherry, N. J. (1981) 'The effects of stream turbulence on separation bubbles', *Journal of wind engineering and industrial aerodynamics*, 8(1–2), pp. 49–58.

Hinze, J. O. (1975) *Turbulence*. Tata Mc-Graw Hill. pp. 1-790

Ishida, T., Davidson, P. A. and Kaneda, Y. (2006) 'On the decay of isotropic turbulence',

Journal of Fluid Mechanics, 564, pp. 455–475.

Ishihara, T., Gotoh, T. and Kaneda, Y. (2009) 'Study of High–Reynolds number isotropic turbulence by Direct numerical simulation', *Annual Review of Fluid Mechanics*, 41(1), pp. 165–180.

Jimenez, J., Wray, A. A., Saffman, P. G. and Rogallo, R. S. (1993) 'The structure of intense vorticity in homogeneous isotropic turbulence', *Journal of Fluid Mechanics*, 255(65), pp. 21–45.

Kang, H. S., Chester, S. and Meneveau, C. (2003) 'Decaying turbulence in an active-grid-generated flow and comparisons with large-eddy simulation', *Journal of Fluid Mechanics*, 480, pp. 129–160.

Karava, P., Jubayer, C. M. and Savory, E. (2011) 'Numerical modelling of forced convective heat transfer from the inclined windward roof of an isolated low-rise building with application to photovoltaic/thermal systems systems', *Applied Thermal Engineering*, 31, pp. 1950–1963.

Kármán, T. V. and Howarth, L. (1938) 'On the statistical theory of isotropic turbulence', *Proceedings of the Royal Society of London A: Mathematical, Physical and Engineering Sciences*, 164(917), pp. 192–215.

Kármán, T. von (1930) 'Mechanische Ähnlichkeit und Turbulenz', in *3rd, Proceedings International Congress Applied Mechanics, Stockholm*, pp. 85–105.

Keating, A., Piomelli, U., Balaras, E. and Kaltenbach, H. J. (2004) 'A priori and a posteriori tests of inflow conditions for large-eddy simulation', *Physics of Fluids*, 16(12), pp. 4696–4712.

Kolmogorov, A. N. (1941a) 'Dissipation of energy in isotropic turbulence', *Doklady Akademii Nauk Sssr*, 32, pp. 325–327.

Kolmogorov, A. N. (1941b) 'The local structure of turbulence in incompressible viscous fluid for very large Reynolds numbers', *Doklady Akademii Nauk Sssr*, 30(4), pp. 299–

303.

Kolmogorov, A. N. (1942) ‘Equations of turbulent motion of an incompressible fluid’, *Izvestia Academy of Sciences, USSR, Physics*, 6(1 & 2), pp. 56–58.

Kraichnan, R. H. (1970) ‘Diffusion by a random velocity field’, *Physics of Fluids*, 13(1), pp. 22–31.

Krogstad, P.-Å. and Davidson, P. A. (2010) ‘Is grid turbulence Saffman turbulence?’, *Journal of Fluid Mechanics*, 642, pp. 373–394.

Krogstad, P. and Davidson, P. A. (2011) ‘Freely-decaying, homogeneous turbulence generated by multi-scale grids’, *Journal of Fluid Mechanics*, 32042(680), pp. 417–434.

L.D. Landau and Lifshitz, E. (1959) *Fluid Mechanics*. Permagon Press. pp.1-551

Launder, B. E. and Spalding, D. B. (1974) ‘The numerical computation of turbulent flows’, *Computer Methods in Applied Mechanics and Engineering*, 3(2), pp. 269–289.

Lavoie, P., Burattini, P., Djenidi, L. and Antonia, R. A. (2005) ‘Effect of initial conditions on decaying grid turbulence at low R_λ’, *Experiments in Fluids*, 39(5), pp. 865–874.

Lavoie, P., Djenidi, L. and Antonia, R. a. (2007) ‘Effects of initial conditions in decaying turbulence generated by passive grids’, *Journal of Fluid Mechanics*, 585, pp. 395-420.

Lilly, D. K. (1992) ‘A proposed modification of the Germano subgrid-scale closure method’, *Physics of Fluids A: Fluid Dynamics*, 4(3), pp. 633–635.

Llor, A. (2011) ‘Langevin equation of big structure dynamics in turbulence: Landau’s invariant in the decay of homogeneous isotropic turbulence’, *European Journal of Mechanics, B/Fluids*. Elsevier Masson SAS, 30(5), pp. 480–504.

Loitsyanskii, L. G. (1945) Some basic laws for isotropic turbulent flow, *(Central Aerohydrodynamic Inst) Zhukovsky*, pp. 1-37.

Lumley, J. L. (1992) ‘Some comments on turbulence’, *Physics of Fluids A: Fluid Dynamics*, 4(2), pp. 203–211.

Maciejewski, P. K. and Moffat, R. J. (1992) ‘Heat transfer with very high free-stream turbulence: Part I - Experimental data’, *Journal of Heat Transfer*, 114(4), pp. 827–833.

Medjroubi, W., Hochstein, H., Fuchs, A., Gülker, G. and Peinke, J. (2013) ‘Experimental and computational investigation of fractal grid wake’, in *14th European Turbulence Conference*. Lyon, France, pp. 5–6.

Menter, F. R. (1994) ‘Two-equation eddy-viscosity turbulence models for engineering applications’, *AIAA Journal*, 32(8), pp. 1598–1605.

Mizushina, T., Hiromasa, U. and Nobuyuki, U. (1972) ‘Effect of free-stream turbulence on mass transfer from a circular cylinder in cross flow’, *International Journal of Heat and Mass Transfer*, 15(4), pp. 769–780.

Mohamed, M. S. and Larue, J. C. (1990) ‘The decay power law in grid-generated turbulence’, *Journal of Fluid Mechanics*, 219, pp. 195–214.

Moin, P. (2009) ‘Revisiting Taylor’s hypothesis’, *Journal of Fluid Mechanics*, 640, pp. 1-4.

Nicoud, F. and Ducros, F. (1999) ‘Subgrid scale stress modelling based on the square of the velocity gradient tensor’, *Flow, Turbulence and Combustion*, 62, pp. 183–200.

Gartshore, I. G. (1973) The effects of freestream turbulence on the drag of rectangular two-dimensional prism, *Boundary Layer Wind Tunnel Laboratory Research Report, BLWT-4-73, Univ. of Western Ontario*, pp.1-12.

Patankar, S. V, Spalding, D. B. and Road, E. (1972) ‘A calculation procedure for heat, mass and momentum transfer in three-dimensional parabolic flows’, *International Journal of Heat and Mass Transfer*, 15(10), pp. 1787–1806.

Pope, S. B. (2000) Turbulent Flows, *Cambridge University Press.* pp. 1-810. Cambridge

University Press.

Portfors, E. A. and Keffer, J. F. (1969) ‘Isotropy in initial period grid turbulence’, *Physics of Fluids*, 12(7), pp. 1519–1521.

Prandtl, L. (1925) ‘Über die ausgebildete Turbulenz’, *ZAMM*, 5, pp. 136–139.

Prandtl, L. (1945) ‘Über ein neues Formelsystem für die ausgebildete Turbulenz’, *Nacr. Akad. Wiss. Göttingen, Math-Phys, Kl*, pp. 6–19.

Saathhoff, P. J. and Melbourne, W. H. (1989) ‘The generation of peak pressures in separated/reattaching flows’, *Journal of Wind Engineering and Industrial Aerodynamics*, 32(1–2), pp. 121–134.

Saathhoff, P. J. and Melbourne, W. H. (1997) ‘Effects of free-stream turbulence on surface pressure fluctuations in a separation bubble’, *Journal of Fluid Mechanics*. University of Western Ontario, 337, pp. 1–24.

Saffman, P. (1967) ‘The large-scale structure of homogeneous turbulence’, *Journal of Fluid Mechanics*, 27(3), pp. 581–593.

Saffman, P. G. (1968) *Lectures on homogeneous turbulence*, *Topics in non-linear physics*.pp. 485-614.

Sagaut, P., Garnier, E., Tromeur, E. and Larchevêque, L. (2003) ‘Turbulent inflow conditions for LES of supersonic and subsonic wall bounded flows’, *41st AIAA Aerospace Sciences Meeting & Exhibit*, (December 2014), pp. 1–11.

Simmons, L. F. . and Salter, C. (1934) ‘Experimental investigation and analysis of the velocity variations in turbulent flow’, *Proceedings of the Royal Society of London. Series A, Containing Papers of a Mathematical and Physical Character*, 145(854), pp. 212–234.

Simonich, J. C. and Bradshaw, P. (1978) ‘Effect of free-stream turbulence on heat transfer through a turbulent boundary layer’, *Journal of Heat Transfer*, 100(4), pp. 671–677.

Skrbek, L. and Stalp, S. R. (2000) ‘On the decay of homogeneous isotropic turbulence’, *Physics of Fluids*, 12(8), pp. 1997–2019.

Smagorinsky, J. (1963) ‘General circulation experiments with the primitive equations’, *Monthly Weather Review*, 91(3), pp. 99–164.

Smirnov, A., Shi, S. and Celik, I. (2001) ‘Random flow generation technique for large eddy simulations and particle-dynamics modeling’, ASME *Journal of Fluids Engineering*, 123(2), pp. 359-371.

Speziale, C. (1998) ‘Turbulence modeling for time-dependent RANS and VLES: A Review’, *AIAA Journal*, 36(2), pp. 173–184.

Sreenivasan, K. R. (1984) ‘On the Scaling of the turbulent energy dissipation rate’, *The Physics of FluidsPhys. Fluids*, 27(5), pp. 1048–1051.

Sreenivasan, K. R. (1998) ‘An update on the energy dissipation rate in isotropic turbulence’, *Physics Of Fluids*, 10(2), pp. 528–529.

Sreenivasan, R., Tavoulariss, S. and Henrys, R. (1980) ‘Temperature fluctuations and scales in grid-generated turbulence’, *Journal of Fluid Mechanics*, 100(3), pp. 597–621.

Stewart, R. W. and Townsend, A. A. (1951) ‘Similarity and self-preservation in isotropic turbulence’, *Philosophical Transactions of the Royal Society of London A: Mathematical, Physical and Engineering Sciences*, 243(867), pp. 359–386.

Tabor, G. R. and Baba-Ahmadi, M. H. (2010) ‘Inlet conditions for large eddy simulation: A review’, *Computers and Fluids*. Elsevier Ltd, 39(4), pp. 553–567.

Tan-atichat, J., Nagib, H. M. and Loehrke, R. I. (1982) ‘Interaction of free-stream turbulence with screens and grids : a balance between turbulence scales’, *Journal of Fluid Mechanics*, 114, pp. 501–528.

Taylor, G. I. (1935) ‘Statistical theory of turbulence’, *Proceedings of the Royal Society of London A: Mathematical, Physical and Engineering Sciences*, 151(873), pp. 421–444.

Taylor, G. I. (1938a) ‘Some recent developements in the study of turbulence’, in *Proceedings of the Fifth International Congress of Applied Mechanics*, pp. 294–310.

Taylor, G. I. (1938b) ‘The spectrum of turbulence’, *Proceedings of the Royal Society of London (Ser. A164)*, pp. 476–490.

Torrano, I., Tutar, M., Martinez-Agirre, M., Rouquier, A., Mordant, N. and Bourgoin, M. (2015) ‘Comparison of experimental and RANS-based numerical studies of the decay of grid-generated turbulence’, *Journal of Fluids Engineering*, 137(6), pp. 1–30.

Tutar, M. and Celik, I. (2007) ‘Large eddy simulation of a square cylinder flow: Modelling of inflow turbulence’, *Wind and Structures, An International Journal*, 10(6), pp. 511–532.

Uberoi, M. S. (1963) ‘Energy transfer in isotropic turbulence’, *Physics of Fluids*, 6(8), pp. 1048–1056.

Uberoi, M. S. and Wallis, S. (1967) ‘Effect of grid geometry on turbulence decay’, *Physics of Fluids*, 10(6), pp. 1216–1224.

Uberoi, M. S. and Wallis, S. (1969) ‘Spectra of grid turbulence’, *Physics of Fluids*, 12(7), pp. 1355–1358.

Venkatakrishnan, V. (1993) ‘On the accuracy of limiters and convergence to steady state solutions’, in *In 31st Aerospace Sciences Meeting*. Moffett Field, California, pp. 1–10.

Versteeg, H. K. and Malalasekera, W. (2007) An Introduction to Computational Fluid Dynamics - The Finite Volume Method, *Pearson Education*. pp. 1-267.

Wang, L.-P., Chen, S., Brasseur, J. G. and Wyngaard, J. C. (1996) ‘Examination of hypotheses in the Kolmogorov refined turbulence theory through high-resolution simulations. Part 1. Velocity field’, *Journal of Fluid Mechanics*, 309, pp. 113–156.

Wang, L.-P., Chen, S., Brasseur, J. G. and Wyngaard, J. C. (1999) ‘Examination of hypotheses in the Kolmogorov refined turbulence theory through high-resolution

simulations. Part 2. Passive scalar field', *Journal of Fluid Mechanics*, 400, pp. 163–197.

Wilcox, D. C. (1998) *Turbulence Modelling for CFD*. 1st edn. California: DCW Industries, Inc, pp.1-522.

Xie, Z. T. and Castro, I. P. (2008) 'Efficient generation of inflow conditions for large eddy simulation of street-scale flows', *Flow, Turbulence and Combustion*, 81(3), pp. 449–470.

Yeung, P. K. and Zhou, Y. (1997) 'Universality of the Kolmogorov constant in numerical simulations of turbulence', *Physical Review E - Statistical Physics, Plasmas, Fluids, and Related Interdisciplinary Topics*, 56(2), pp. 1746–1752.

Chapter 3

3 Comparison of RANS modelling against LES and experimental measurements of spatially decaying isotropic homogenous grid-generated turbulence

3.1 Introduction

The choice of any computational fluid dynamics (CFD) model is always based on a trade-off between the computational time required and the desired solution accuracy of a problem. Although, Large Eddy simulation (LES) and Direct numerical simulation (DNS) offer unsteady simulation methods to resolve length scales sufficiently**,** they are not practiced for small clock time runs because of the large memory requirements and high computational power that these numerical techniques (LES and DNS) are said to have required (Torrano *et al.*, 2015). On the other hand, in Reynolds Averaged Navier-Stokes based models (RANS), all the scales of turbulence are modelled using different turbulence models and therefore the cost of computation decreases exponentially compared to DNS and LES, but with the loss of instantaneous time related information associated with the turbulent scales of motion. Although, RANS simulations do not offer any relevant multi-scale information, they can handle complex geometries and, therefore, can be well-suited for initial investigations of a typical turbulent flow problem.

As previously discussed in Chapter 2, time averaging general Navier-Stokes (NS) equations yields Reynolds-averaged equations of motion that gives rise to an additional unknown stress tensor known as Reynolds stress tensor given by $-\rho\overline{u_i' u_j'}$. However, no additional equations are obtained to close the system of equations as a result of Reynolds-averaging. Therefore, the additional unknown terms must be modeled in order to close the system of equations. This is the well-known closure problem in RANS methodology and, hence a sufficient number of equations should be devised to solve the closure problem. Different turbulence models have been evolved over the years to solve this classical closure problem of Reynolds-averaging.

There are two different kinds of turbulence models that have been discussed widely among scientists, researchers and engineers in the CFD field. The simplest can be described as algebraic models, where the turbulent eddy viscosity is related algebraically to the length scales of the mean flow using the Boussinesq eddy-viscosity assumption. These models can also be termed zero equation models as they do not require the solution of any additional differential equations and can be computed directly from the mean flow variables. As a consequence, these models might not be helpful in estimating the convection, diffusion terms of TKE transport equation and cannot be extended to flows beyond the established data for which the models are calibrated (Wilcox (1998).

On the other hand, there are additional partial differential equation-based RANS models where the transport equations of turbulent kinetic energy and its dissipation are solved for the estimation of turbulent eddy-viscosity. These equations are complete in nature since the eddy viscosity automatically provides information about the turbulent length scale and not related to some typical flow dimension (Wilcox 1998).

All of the three commercial CFD codes used in the present work (FLUENT, STAR-CCM, CFX) offer several turbulence models; one-equation model, two-equation model, non-linear eddy viscosity model and Reynolds stress model. The choice of these models entirely depends on the user and is based on the type of turbulent flow problem and its application one wishes to study. For example, the Spalart-Allmaras model was designed specifically for aerospace applications involving wall-bounded flows and gives reliable results for boundary layer flows with adverse pressure gradients. However, the model performs poorly for industrial flows such as the free shear flow encountered in a round jet. Additionally, it cannot be relied upon completely to predict the decay of isotropic homogeneous turbulence in an accurate manner (Spalart and Allmaras, 1992) (ANSYS, 2013b).

As discussed earlier (in chapter 2), the Shear Stress Transport-k-ω model (SST-k-ω), a two-equation eddy viscosity model, is chosen over other model variants of RANS formulation to simulate and capture the global behaviour of the turbulence decay. Since, the current RANS model will be extended for flat plate heat transfer study in the future,

the choice of this model was rational in nature. Besides this, the SST k-ω model has also shown very good predictions of the velocity boundary layers, for a uniform boundary layer flow over an isothermal flat plate in the earlier studies by Karava *et al.* (2011). Comparison between the other RANS models in predicting the decay of turbulence have also been shown in figure (2.6) (refer to chapter 2), illustrating that the predicted rate of decay is similar (<1% difference) for all the other standard two equation models. The corresponding transport equations of the SST k-ω model were previously detailed in section (2.5.4) (refer Chapter 2).

In the subsequent sections, an investigation has been made to assess the capability of the SST-k-ω model from three different commercial software codes (FLUENT, STAR-CCM, CFX) to characterize the turbulent decay process and, thereby, provide an efficient numerical way to capture the main trends of grid generated turbulence. The results from the present numerical model (RANS) have been validated with the earlier relevant experimental studies and LES data to quantify the differences and point out limitations (if any) present in the SST-k-ω formulation.

The computational domain, boundary conditions, solver method, solution parameters and the grid-independence study of the current steady RANS problem have already been reported in the earlier chapter and so are not discussed here again.

3.2 Comparison between different commercial CFD codes against the spatial decay of isotropic homogeneous turbulence

In this section, relative comparisons between the results from three-available commercial CFD codes (FLUENT, STAR-CCM+, CFX) are drawn, to see whether the standard SST-k-ω model implemented in these three different codes is suitable for predicting the spatial decay of turbulence along the streamwise distance in a correct manner. The motivation for this comparative study has been inherited from the earlier discussion in chapter 2 (refer to figure 2.30), where the results from the SST-k-ω model simulated in FLUENT demonstrated a higher rate of turbulence decay in comparison to the experimental/LES results. Hence, it becomes necessary to investigate whether the commercial CFD codes

other than FLUENT, fare better or perform worse in reproducing turbulence decay comparable to the results of experimental grid-generated turbulence. Figure (3.1) shows the results of the spatial decay of TKE profiles obtained from FLUENT, STAR-CCM+ and CFX, in comparison to the LES study and the earlier experimental data. The x abscissa is scaled with the local magnitudes of integral length scale (L_u) whilst the y ordinate is represented by the non-dimensional TKE. From the figure, it is clearly observed that, although both FLUENT and CFX produce similar results, with a higher rate of decay, STAR-CCM+ on the other hand, displays a much slower rate of decay in comparison with the experimental and LES studies. The similar rates of decay observed in FLUENT and CFX may be explained by the fact that both the solvers belong to ANSYS and employ same formulation of the model, but the slower rate of turbulence decay observed from the results of STAR-CCM+ induces further investigation to quantify the differences between the FLUENT, CFX and STAR-CCM+ solvers. Also, the deviation in these results from the experimental/LES data needs to be addressed carefully to better understand the implementation of the SST-k-ω model in each of these solvers.

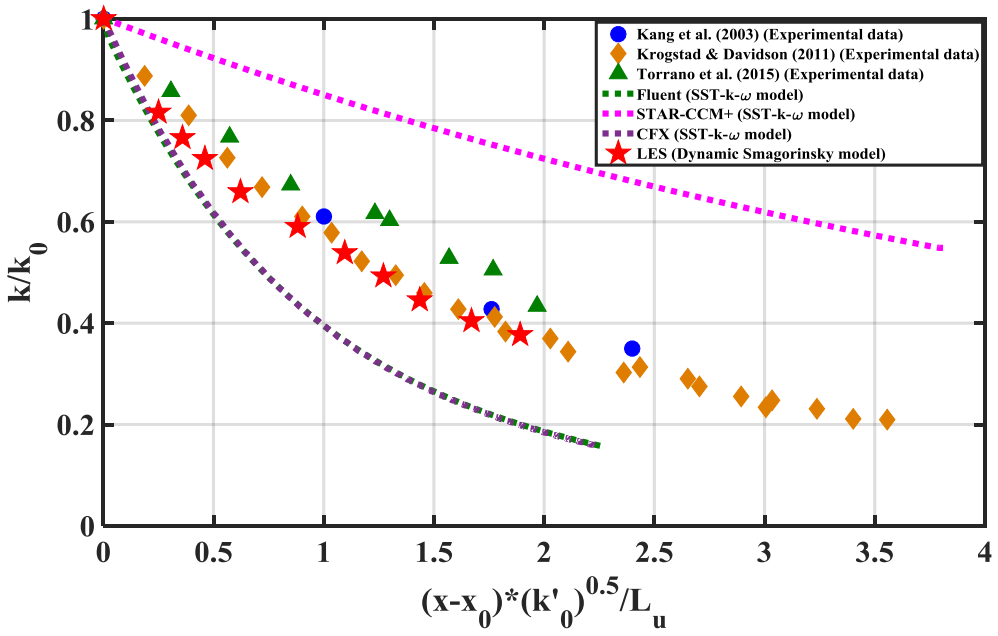

Figure 3.1 Spatial decay of TKE profiles obtained from three different commercial codes (FLUENT, STAR-CCM+ and CFX) compared with the LES and the previous experimental studies

Similar kinds of variation were also observed, even with the x axis scaled with the initial integral length scale (L_{u0}), while comparing the results from these three commercial codes and the previous LES, experimental results. The non-dimensional TKE profiles when plotted against the streamwise distance x also display a similar behaviour of decay from the commercial CFD codes against LES results. Those figures are not shown here in the current section but are presented in the appendix C (figures C.1 & C.2) for completeness.

The observed deviation in the RANS results obtained from three commercial CFD codes in comparison to the LES and experimental studies calls for a deeper analysis of the methodology of the turbulence models implemented in each of those CFD codes.

The next section briefly discusses the SST-k-ω model and its related model constants implemented in three different solvers viz. FLUENT, STAR-CCM+ and CFX, to answer the question whether or not there are any note-worthy differences between the ANSYS solvers FLUENT, CFX and the SIEMENS solver STAR-CCM+. If yes, how significant are the influence of those numerical differences on the solver results.

3.3 Investigation of the differences between the solver (FLUENT, STAR-CCM+ and CFX) results

In order to investigate the differences between the results obtained from three different CFD solvers, it is necessary to examine the ways in which the SST-k-ω model and its constants are implemented in those codes. The reader is suggested to examine the transport model equations of the SST-k-ω model very carefully, as already presented in section (2.5.4). While going through the model equations, one can easily realize the importance of the model constant (β^*_∞) which essentially controls the production of the turbulence specific dissipation rate (ω) and the dissipation of the turbulent kinetic energy (TKE). The implementation of the model constant (β^*_∞) is very important in this premise, as will be seen in the upcoming discussion. The default value of the model constant (β^*_∞) implemented in each of these three codes is 0.09.

It is very clear from the figures (3.1, C.1 & C.2 in Appendix C) that the results from three different solvers show a large deviation in the computed values of the turbulence decay rate with each other (at least between FLUENT & STAR-CCM+). Looking at those results, one can anticipate that the observed deviation might be largely due to the difference in the implementation of the inlet boundary conditions in those codes for same specified turbulent inlet parameters. The following hypothesis was verified by initializing the simulations (without actually running them) in these three solvers and it was found that for a same specified inlet turbulence intensity (TI) of 10%, and inlet integral length scale (L_u) of 0.1m, the specific turbulence dissipation rate (ω) obtained from ANSYS solvers FLUENT, CFX is 54.53 s^{-1} and from STAR-CCM+ it is 8.94 s^{-1}. A closer look into these two values reveal that, for FLUENT/ CFX the specific dissipation rate is computed according to (ANSYS, 2013b)

$$\omega = \frac{k^{0.5}}{(\beta^*_\infty) L_u} \tag{3.1}$$

whereas, for STAR-CCM+ it is computed as (CD-Adapco, 2015)

$$\omega = \frac{k^{0.5}}{(\beta^*_\infty)^{\frac{1}{4}} L_u} \tag{3.2}$$

Hence, it is very clear from these two expressions that the specific turbulence dissipation rate (ω) computed in FLUENT, CFX and STAR-CCM+ are different since the model constant (β^*_∞) is raised to a different power in FLUENT and STAR-CCM+. In FLUENT it is raised to a power of 1 whereas for STAR-CCM+ it is raised to a power of 0.25. The specific turbulence dissipation rate (ω) controls the rate at which the turbulent kinetic energy (TKE) is dissipated into thermal energy per unit volume and time and, therefore, two distinct values of (ω) gives two different decay rates of TKE as observed for FLUENT and STAR-CCM+. As the initial specific dissipation rate is higher in FLUENT and CFX than STAR-CCM+, the FLUENT solver shows the turbulent kinetic energy being dissipated at a higher rate than STAR-CCM+.

One important thing to note here is that, even if the constant (β^*_∞) is tuned with similar values, different magnitudes of (ω) are obtained at the inlet (based on the above two equations), which ultimately affects the decay rate of TKE along the domain. So, for different inlet (ω), different rates of decay of TKE are obtained. In order to keep consistency across all the numerical simulations in different solvers, it is essential to have the same inlet specific dissipation rate (ω), that must be specified (instead of being computed) along with the TKE magnitudes at the inlet while tuning different value of the constant (β^*_∞). In this way, the variability of (ω) with (β^*_∞) can be eliminated and the performance of the model in these different CFD codes can be highlighted specifically in analysing the effect of the model constant (β^*_∞) on the decay rate of TKE. In such a scenario, the same specified inlet conditions (TKE, L_u and ω) can also be obtained for each and every case that are being investigated.

The abovementioned discussion tries to unify few of the primary differences observed while implementing the SST-k-ω model in three commercial CFD codes. If (ω) is specified to be the same at the inlet (i.e. 54.43s^{-1}) for both the FLUENT and STAR-CCM+ solvers, it is no longer computed at the inlet (since it is being specified) and, hence, similar results for the decay of TKE for FLUENT and STAR-CCM+ can be achieved. Also, similar results in CFX, specifying the (ω) and TKE at the inlet can be obtained since (ω) is computed in the same way in both FLUENT and STAR-CCM+.

However, at the end one should not use the model constant (β^*_∞) to control the magnitudes of the specific dissipation rate (ω) and L_u at the inlet, but rather use it to model the dissipation of turbulent kinetic energy (TKE) and production of the specific dissipation rate (ω), which it does anyway, as evident from the governing turbulence model equations given in ANSYS, (2013b).

3.3.1 Limitations of the RANS based CFD solvers

In this section, one of the fundamental limitation of the RANS based CFD model has been presented, that appeared while trying to examine the specified initial turbulent parameters (TKE, L_u and ω) from the SST-k-ω model, while comparing it to the initial

values of those parameters in the LES/experiments. Re-stating the inviscid estimate of the turbulent kinetic energy dissipation rate (ε), given by (refer to equation 2.41 in chapter 2)

$$\varepsilon \approx\sim -D\frac{u'^3}{L_u} \tag{3.3}$$

and considering turbulence to be nearly isotropic and homogenous in nature, $\overline{u'}$ in the equation (3.3) can be substituted with turbulent kinetic energy (k) as

$$u' = \sqrt{\frac{2}{3}k} \tag{3.4}$$

which gives equation (3.3) in the form of

$$\varepsilon \approx -0.544D\left(\frac{k^{1.5}}{L_u}\right) \tag{3.5}$$

This is the widely accepted form of the inviscid turbulent kinetic energy dissipation rate in free-shear and wall-bounded flows (Pope, 2000).

However, going through the RANS formulation stated in three-different CFD code manuals viz. (ANSYS, 2013b), (CD-Adapco, 2015), (ANSYS, 2013a), it has been found that the specific dissipation rates (ε) in those codes are defined as (Gerasimov, 2016)

$$\varepsilon = -\frac{k^{1.5}}{L_u} \tag{3.6}$$

One can clearly notice the differences in the estimation of the turbulent kinetic energy dissipation rate (ε) from the theoretical inviscid approximation (refer to equation (3.5)) and that from the CFD based RANS model (refer to equation (3.6)). In CFD RANS two-equation models, the constant in the formulation of (ε) which is typically (0.544D) has been overlooked for the sake of simplicity in modeling the closure problem of the Reynolds stress tensor. However, this difference in formulation of (ε) can affect the solution of the CFD problem and one must take care while comparing the values of the

initial turbulent parameters from the RANS based CFD model with the LES/experimental results. As (ε) is already pre-defined in all the commercial CFD codes and cannot be changed, one therefore needs to acknowledge this limitation while performing CFD simulations of turbulence decay.

3.4 Generic optimized SST-k-ω model for FLUENT, STAR-CCM+ and CFX

In this section, a new generic optimised SST-k-ω model is proposed for the three solvers with a modified value of the model constant coefficient (β_{∞}^{*}), that is seen to predict the decay of turbulence quite well.

3.4.1 New optimized SST-k-ω models for FLUENT

After pointing out the differences and the limitations of the three-different commercial CFD codes in the previous section, attempts have been made in the current section to fine-tune the model constant (β_{∞}^{*}) in FLUENT, with different magnitudes of the constant, in order to achieve results with better agreement in comparison to the present LES and the earlier experimental data. The choice of the new optimised values of the model constant is purely based on an empirical trial and error approach rather than any phenomenological (i.e. physics-based) approach and can be changed according to the need of the user. Fig. (3.2) shows the TKE profiles from the improved models for different values of (β_{∞}^{*}), ranging from (0.044-0.048), along with the results from the standard SST-k-ω model. The corresponding results from the LES simulations and the experimental data sets are also plotted in the same figure to examine the agreement of the improved models with those LES/experiments. From the figure it is seen that, any value between the range 0.044 to 0.048, can be selected as an optimised value for proper numerical modeling of the decay of freestream turbulence since decay from the new model prediction also achieves good qualitative agreement with the results of LES/experiments. Therefore, an intermediate value of 0.046 has been chosen being suitable for carrying out further numerical investigations on the flat plate boundary layer, as will be seen in the forthcoming section. The choice was made to emphasize more on

matching the LES results rather than the experimental results, because at the end the RANS models will suffice those studies that cannot be carried out through LES because of the available computational constraint.

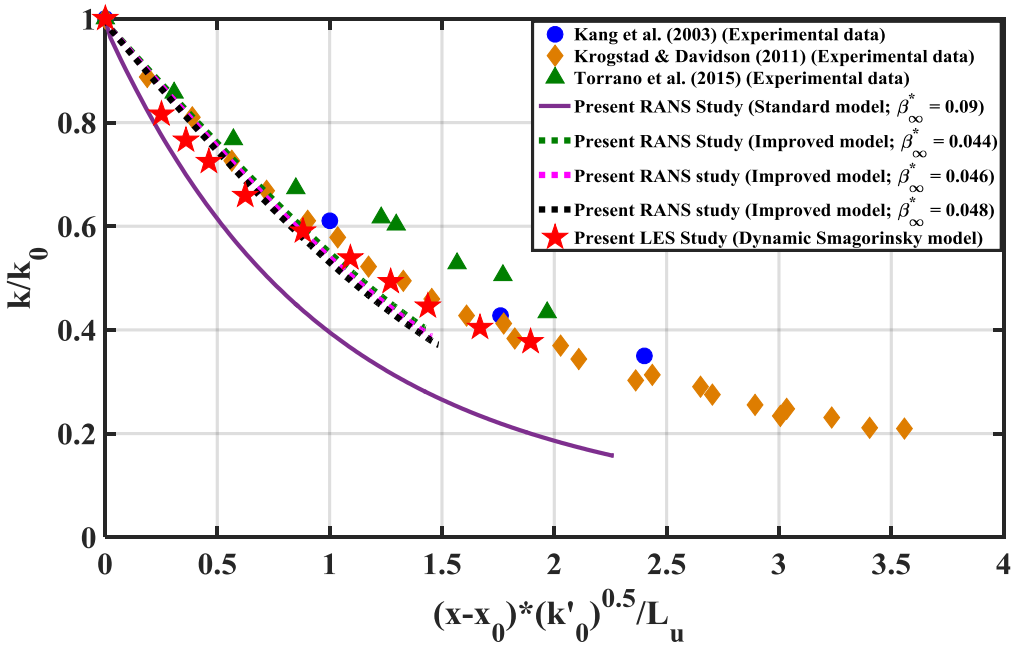

Figure 3.2 Spatial decay of TKE profiles obtained from the different optimized SST-k-ω RANS model compared with the LES and the earlier experimental studies, (FLUENT simulations)

Similar acceptable agreements between the TKE profiles obtained from the optimised model and LES/experiments are also observed in figure (3.3) and figure (3.4), where the scaling parameter has been changed from L_u to L_{u0} in fig (3.3) and to x only in fig. (3.4)) to see whether model constants in the range (0.044-0.048) still work for different non-dimensional scaling parameters of the prediction correlations derived in equations (2.49 & 2.50) (refer to chapter 2). Both the figures illustrate good agreement with the LES/experiments presented in figure (3.3) and figure (3.4).

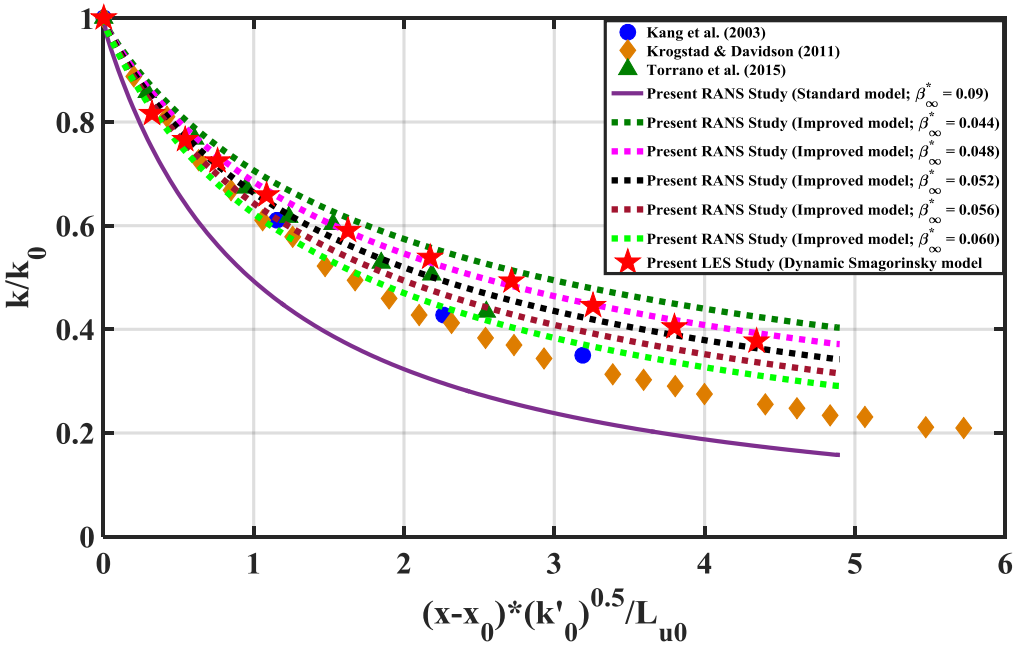

Figure 3.3 Spatial decay of TKE profiles obtained from the different optimized SST-k-ω RANS model compared with the LES and the earlier experimental studies, (FLUENT simulations)

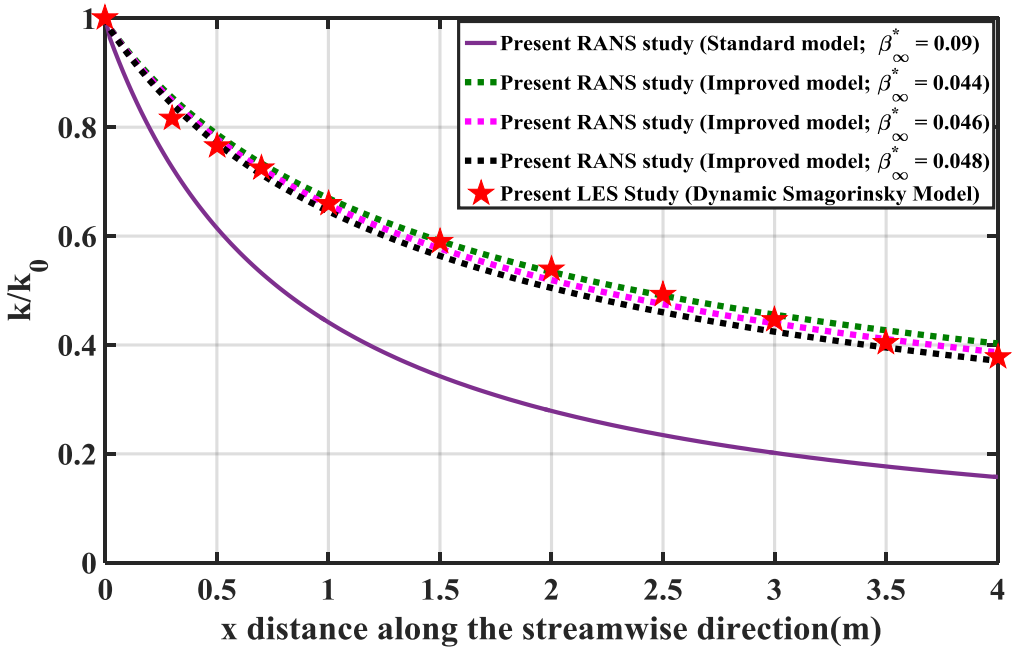

Figure 3.4 Spatial decay of TKE profiles obtained from the different optimized SST-k-ω RANS model compared with the present LES study along the streamwise distance x (FLUENT simulations)

3.4.2 New optimized SST-k-ω models for STAR-CCM+

As discussed in the previous section, the rationale for the choice of the new model constant (β^*_∞) is entirely based on an empirical approach and the range (0.044-0.048) has been found to work fairly well for modelling the decay of isotropic freestream turbulence in FLUENT. Hence, the following range of the improved model constant (β^*_∞) is retained and numerical simulations have been performed with the same range of constants in another commercial CFD package STAR-CCM+. The following approach was employed to examine whether a different commercial CFD code (STAR-CCM+ in this case) having the same range of given constants can reproduce similar results to FLUENT or not and, thereby, demonstrate a closer resemblance to the LES/experimental data. The plots of spatially decaying TKE profiles obtained from the standard SST-k-ω model employed in STAR-CCM+, for different optimised model constants are shown in figure (3.5). The experimental data sets along with the LES solutions are also plotted in

the same figure with the same non-dimensionless parameters for relative comparisons. The results from the improved model prediction exhibit very good agreement with the previous LES/experimental results. It is being re-emphasized here again that the any value of (β_{∞}^{*}) between the range (0.044-0.048) holds good in predicting the freestream decay of turbulence in STAR-CCM+.

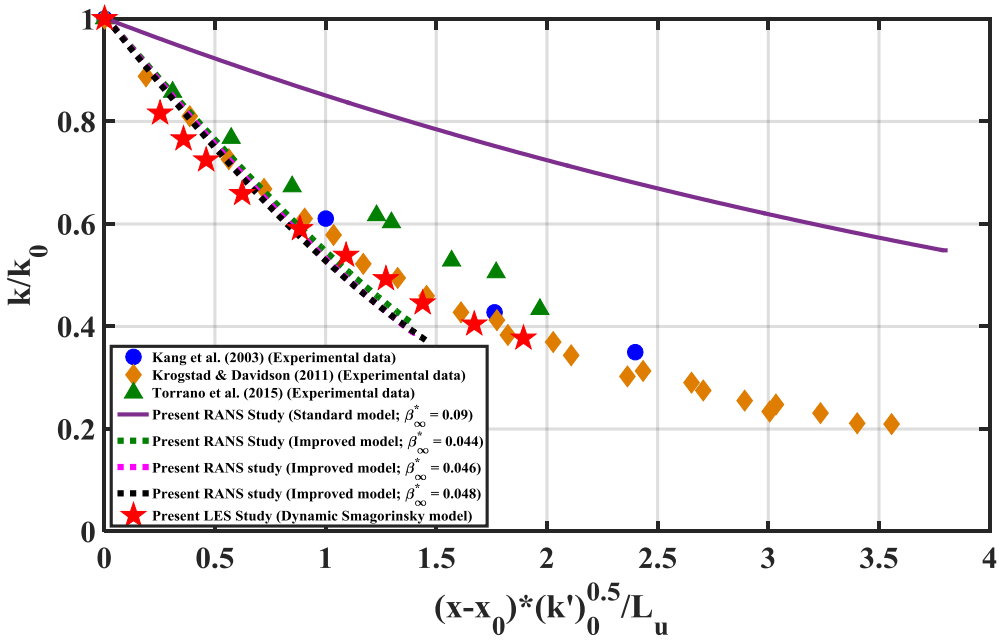

Figure 3.5 Spatial decay of TKE profiles obtained from the different optimized SST-k-ω RANS model compared with the present LES and the earlier experimental studies (STAR-CCM+ simulations)

The TKE profiles plotted against a different scaling parameter (i.e. x-axis variable scaled with initial integral length scale L_{u0}) also display analogous behaviour to the TKE plots already shown in figure (3.3) and, therefore, is not shown here. Also, the results for the TKE profiles plotted against the streamwise distance x are similar to those in figure (3.4). Those plots are presented in Appendix C (figure C.3 & figure C.4) for completeness.

3.4.3 New optimized SST-k-ω models for CFX

In this section the numerical results on the decay of TKE from the model simulations performed in a different commercial CFD software, CFX, are presented. The simulations

are performed to examine whether there are any differences in the numerical results between the ANSYS solver CFX with the previous results from FLUENT and the STAR-CCM+ solver. The investigation is also carried out to assess the applicability of the improved model constant (β_{∞}^{*}) range (0.044-0.048) in predicting the decay of turbulent kinetic energy (TKE) while running in ANSYS CFX. The outcome from the present simulations is presented in figure (3.6) where the non-dimensional TKE profiles for different magnitudes of (β_{∞}^{*}) in the range (0.044-0.046) are plotted against the non-dimensional parameter $(x-x_0)*(k_0^{'})^{0.5}/L_u$. The results illustrate good agreement with the LES studies and the earlier experimental data sets. The present discussion concludes that CFX achieves identical results relative to the earlier numerical results obtained from FLUENT and STAR-CCM+.

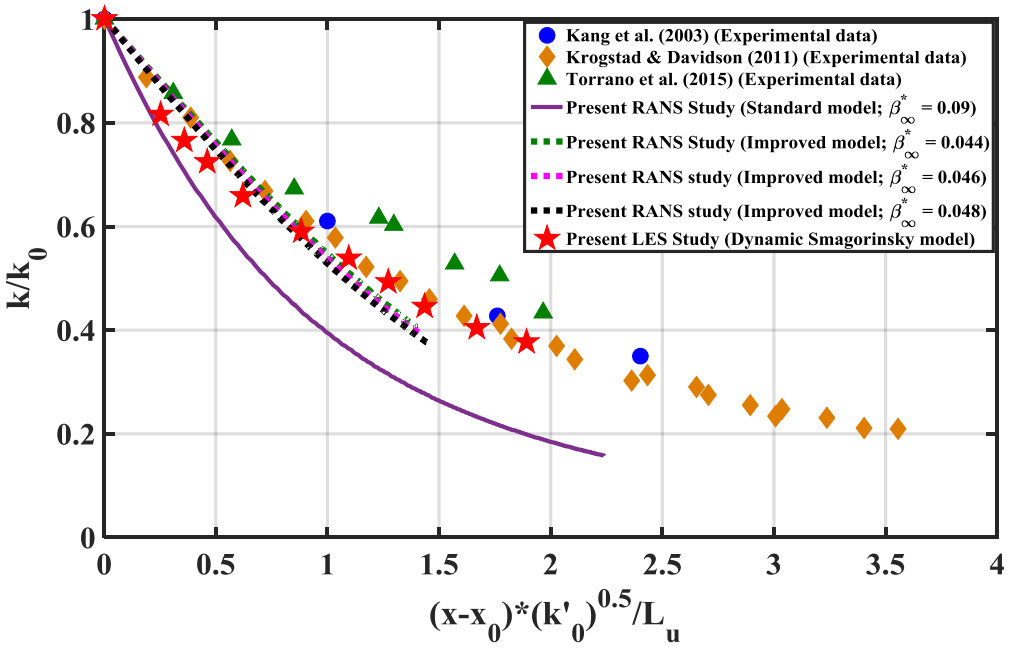

Figure 3.6 Spatial decay of TKE profiles obtained from the different optimized SST-k-ω RANS model compared with the LES and the earlier experimental studies, (CFX simulations)

The non-dimensional TKE profiles plotted against $(x-x_0)*(k_0^{'})^{0.5}/L_{u0}$ show similar

characteristics of turbulence decay already shown in figure (3.3) and, hence, they are not shown here but presented in Appendix C. The plots of the TKE profiles versus streamwise distance x, obtained from CFX exhibit similar attributes and are presented in Appendix C.

3.5 Applicability of the proposed generic SST-k-ω model for varying initial conditions

This section explores the effect of the varying initial turbulent conditions (TKE and L_u) on the improved SST-k-ω model and examines whether the new proposed model constants are accurate enough to predict the behaviour of turbulence decay in compare to the experiments/LES results. All the simulations shown in this section are performed in ANSYS software FLUENT with an inlet mean velocity ($\overline{U}$) = 4m/s. Similar results can be expected while modelling these cases in STAR-CCM+ and CFX with same initial and boundary conditions.

3.5.1 Applicability of the improved SST-k-ω model in predicting the turbulence decay for varying turbulence intensities at the inlet

In the following section, simulations with the improved model have been carried out by varying the turbulence intensity (TI) from 10% to 30%, whilst keeping the integral length scale (L_u) constant at 0.1m at the inlet. The simulations have been performed to check whether the optimised model constant in the range (0.044-0.048) generates results closer to the experimental/LES solutions, for predicting the decay of TKE in the case of varying turbulence intensities. Figures (3.7), (3.8) and (3.9) show the decay of non-dimensional TKE profiles (k/k_0) plotted against the non-dimensional parameter $(x - x_0) * (k_0')^{0.5} / L_u$ for inlet turbulence intensities (TI) of 10%, 20% and 30%. From the figures, it is clear that the given range of model constant shows results in close agreement with the LES data, having a little deviation from the experimental results. This deviation might be due to the inaccurate formulations of dissipation rate (ε) implemented in each of those softwares as presented in earlier section (3.3.1). Profiles of non-dimensional TKE for varying TI plotted against a different scaling parameter are shown in Appendix C (C.7-C.12).

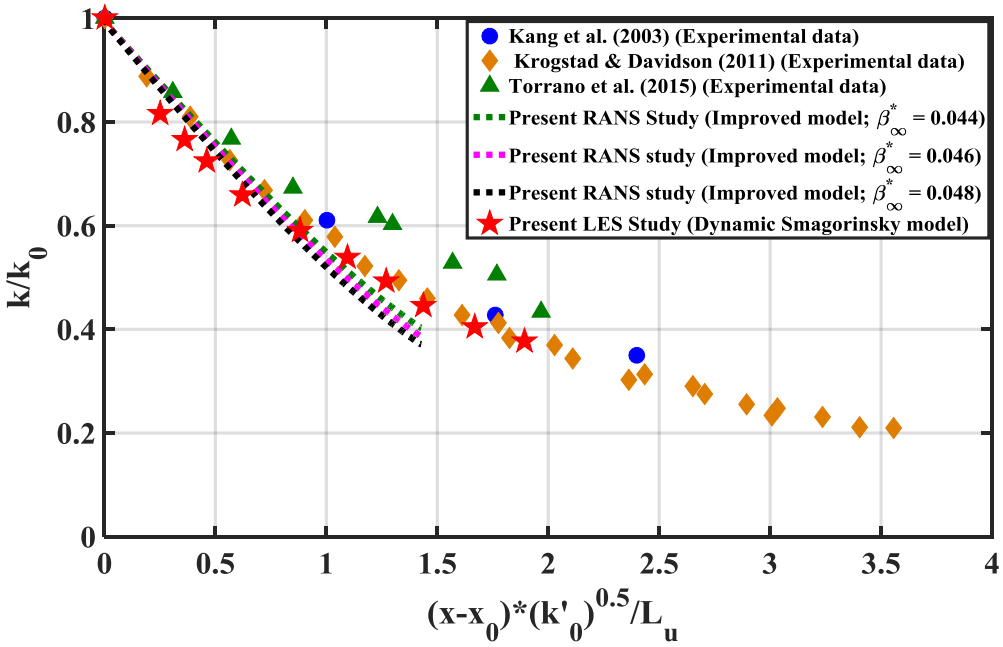

Figure 3.7 Spatial decay of TKE profiles from different optimized SST-k-ω model compared with the LES and the earlier experimental studies (TI = 20%, L_{u0} = 0.1m)

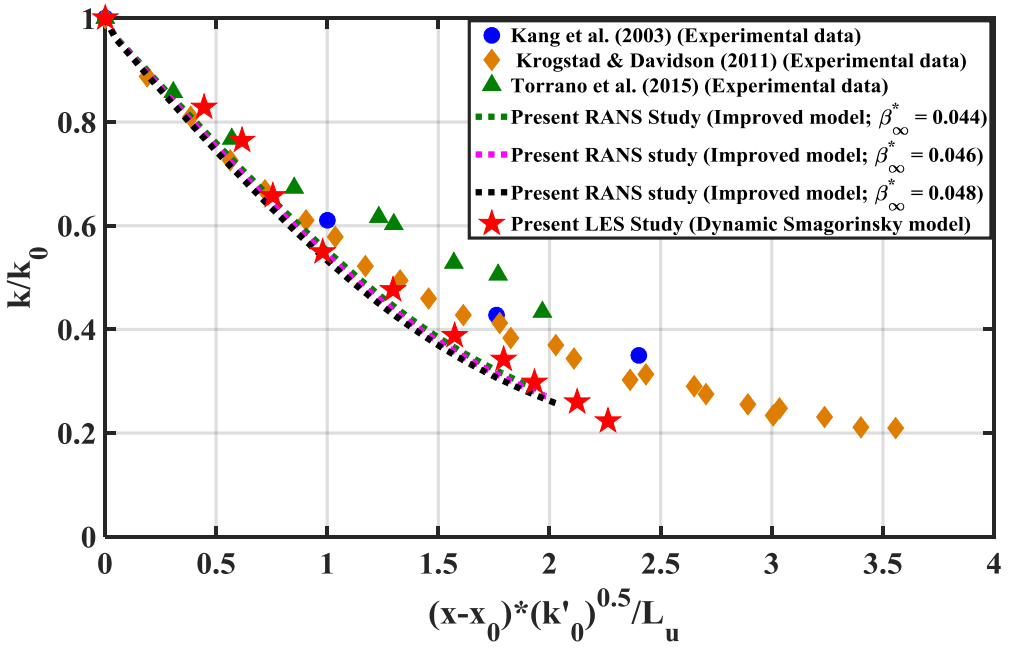

Figure 3.8 Spatial decay of TKE profiles from different optimized SST-k-ω model compared with the LES and the earlier experimental studies (TI = 20%, L_{u0} = 0.1m)

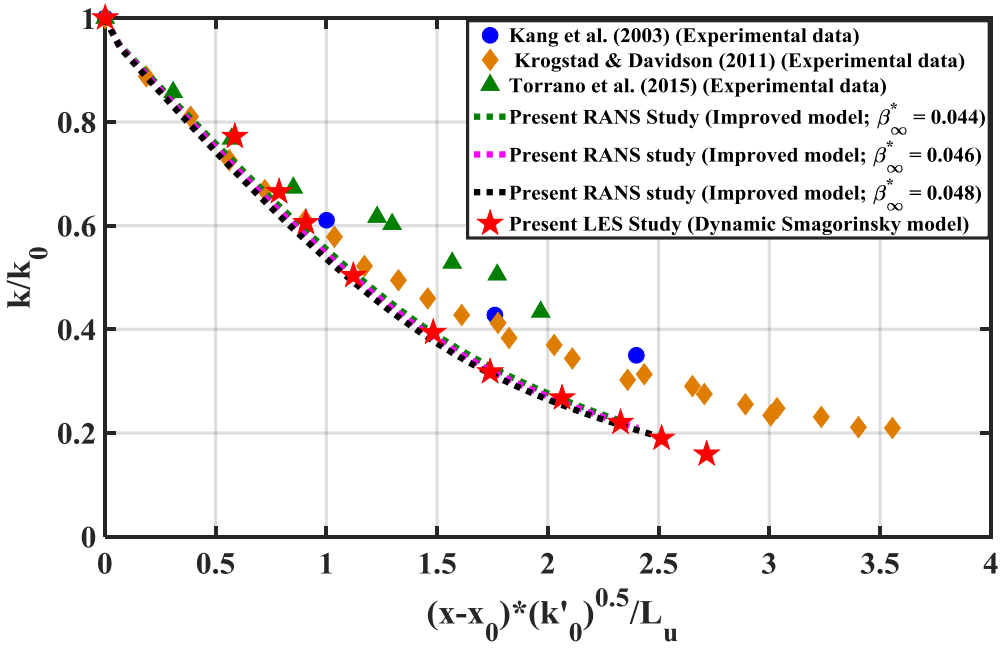

Figure 3.9 Spatial decay of TKE profiles from different optimized SST-k-ω model compared with the LES and the earlier experimental studies (TI = 30%; L_{u0} = 0.1m)

3.5.2 Applicability of the improved SST-k-ω in predicting the turbulence decay model for varying integral length scales at the inlet

Similar to the previous section, this section present results from the improved SST-k-ω model simulated for different integral length scales at the inlet (i.e. 0.02m, 0.05m and 0.10m) with a fixed turbulence intensity (TI) of 10% at the inlet. The model tests with varying integral length scales at the inlet are done to evaluate the applicability of the optimised model constant range in appropriately predicting the decay of TKE for different length scale values. Figures (3.10), (3.11) and (3.12) shows the dimensionless TKE profiles obtained for different initial integral length scale values with the optimised model constant range of (0.044-0.048). As expected, the modified constants display reasonable quantitative agreements with the previous LES study and the experimental results. Similar plots of TKE are shown in Appendix C (C.13- C.18) where the TKE profiles are plotted against different scaling parameters in the x-abscissa.

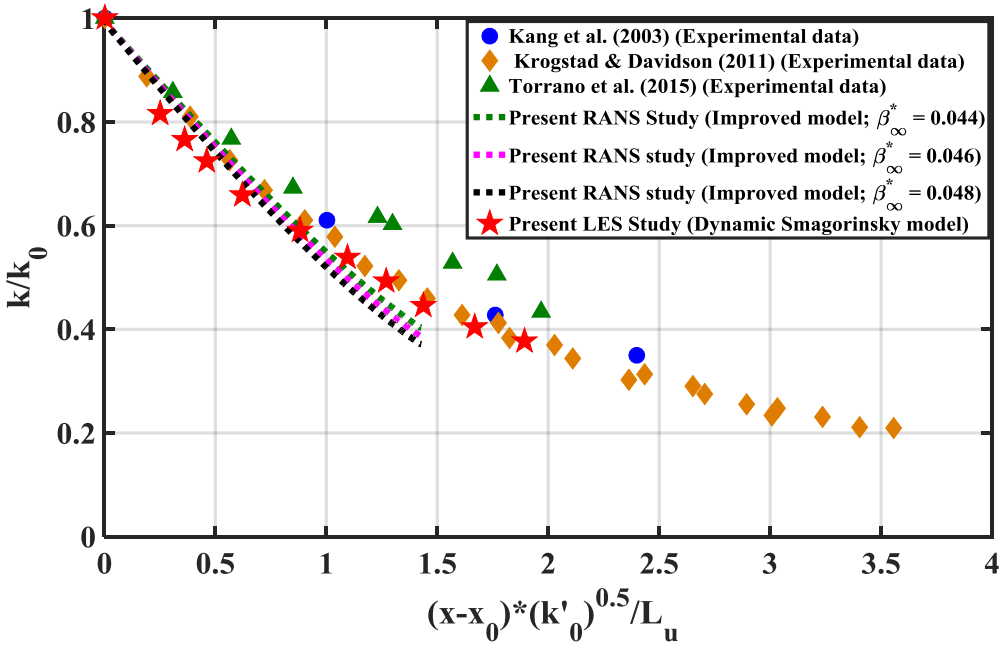

Figure 3.10 Spatial decay of TKE profiles obtained from optimized SST-k-ω model compared with the LES and the earlier experimental studies (TI = 10%; L_{u0} = 0.1m)

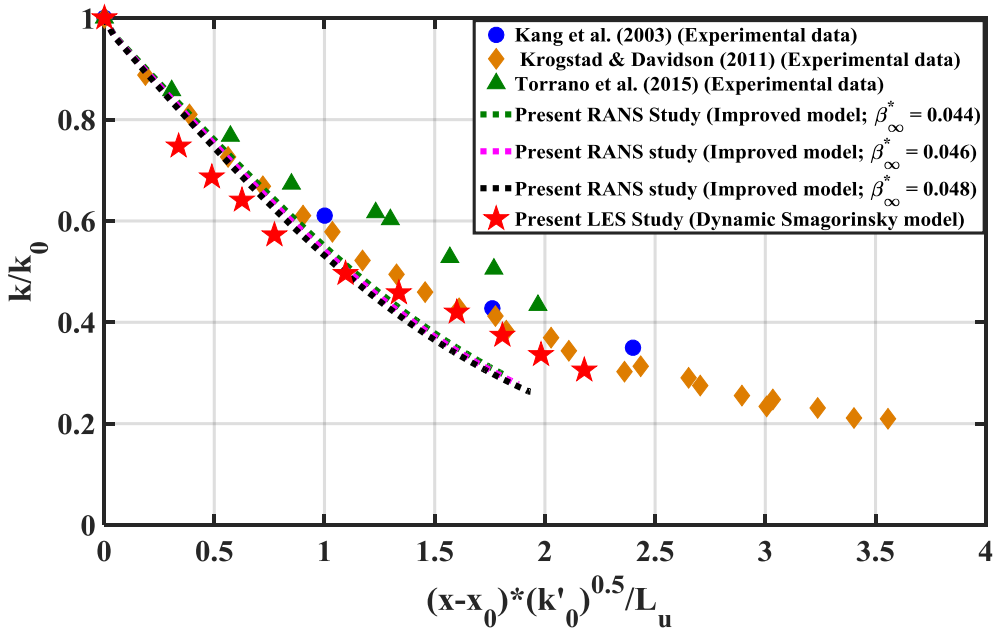

Figure 3.11 Spatial decay of TKE profiles obtained from optimized SST-k-ω model compared with the LES and the earlier experimental studies (TI = 10%; L_{u0} = 0.05m)

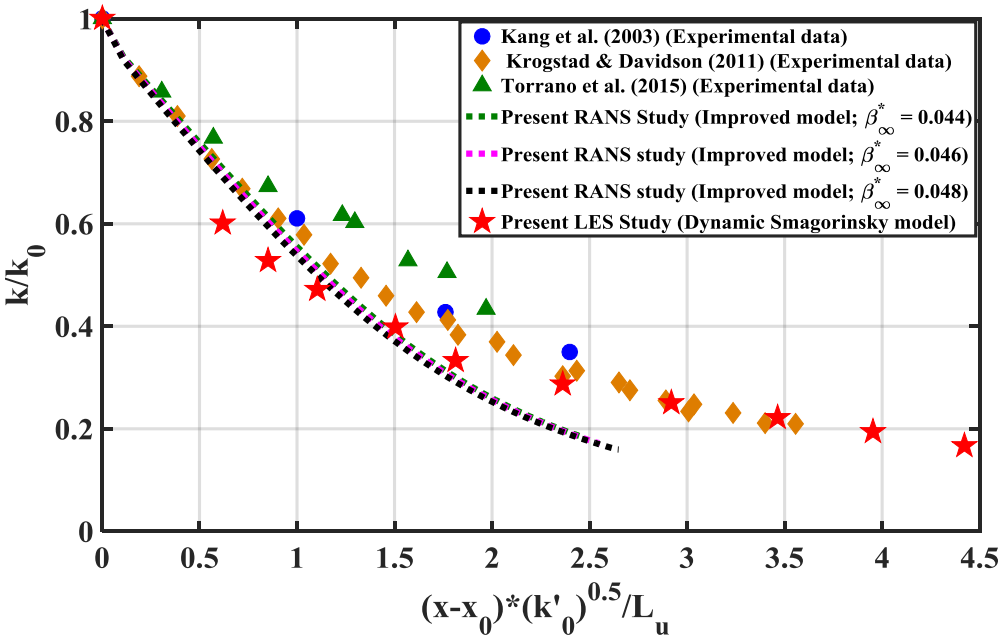

Figure 3.12 Spatial decay of TKE profiles obtained from the optimized SST-k-ω model compared with the LES and the earlier experimental studies (TI= 10%; L_{u0} = 0.02m)

3.6 Boundary layer validation for new optimized SST-k-ω model

3.6.1 Introduction

The present section examines the new optimized SST-k-ω model and investigates whether the revised model performs reliably for boundary layer flows. Details of the computational domain are presented in the section 3.6.2. Section 3.6.3 discusses the grid-generation technique along with near wall treatment of the boundary layers. Section 3.6.4 discusses the methodology used for the CFD modelling, which includes the turbulence models and the solution parameters. The boundary conditions are discussed in section 3.6.5. The grid-independence study is described in section 3.6.6. At the end, the boundary layer validation of the current optimized SST-k-ω model for flow over a horizontal flat plate is presented in section 3.6.7. The motivation behind the current study was to establish the improved RANS model as a generic model towards accurate prediction of boundary layer flow field over a flat plate.

3.6.2 Computational domain

The computational grid on which the steady RANS simulations were performed was designed to simulate a developing laminar and turbulent boundary layer incident on a smooth flat plane surface. A 3-D computational domain was generated according to the AIJ (Tominaga *et al.,* 2008) and Franke *et al.,* (2007) guidelines. The lateral and the top boundaries were situated at 0.5m from each other. A uniform smooth flat plane section of infinitesimally small unit node thickness was created at the mid-section of the computational domain which represents a flat plate immersed in a uniform free-stream turbulent flow. The plate with zero thickness was created to avoid any kinds of separation recirculation zone at the leading edge which might alter the turbulence intensities and the integral length scales in incident turbulent boundary layers over a three-dimensional bluff body. The top and bottom boundaries are at located at 0.25m from the plate surface that will allow enough eddies relevant to the boundary layer scales to convect past the plate and through the domain for a turbulent boundary layer flow. The outlet boundary is situated at 2.5m from the inlet boundary section which is in accordance with the spatial decay of turbulence kinetic energy profiles discussed in the previous chapter. The physical dimensions of the computational domain in the current study are L_x = 2.5m, L_y = 0.5m and L_z = 0.5m and the outlet boundary was free from any kind of recirculation zone.

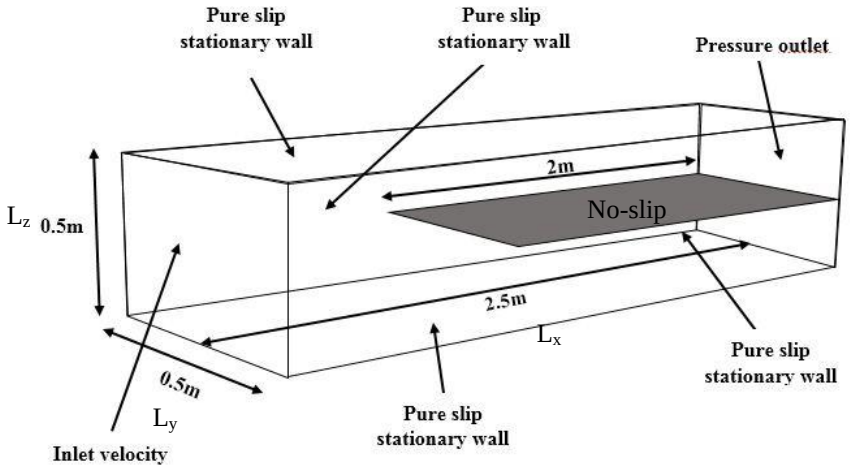

Figure 3.13 Schematic of the computational domain with the plate along with the boundary conditions

3.6.3 Grid-generation

In any CFD based numerical solution, an appropriate mesh is necessary for accurate solution, faster convergence and reduction of numerical diffusion. A commercial mesh generator, ICEM CFD^{TM} 16.0 was used to generate the grid. A perfectly structured hexahedral mesh pattern was generated throughout the domain, where a regular arrangement of the node elements was defined automatically using the software. The structured mesh elements offer a high degree of control of the node locations, better alignment with the flow directions, as well as require less computational memory with a significant reduction of computational cost when compared to an unstructured mesh.

Hexahedral meshes are preferred over polyhedral meshes because of their improved spatial discretization techniques for bounded unidirectional flows, since one can maintain the mesh faces that follow the flow direction. This is a consequence of the better accuracy of the hex-elements since the angle between the faces can be kept close to 90 degrees. For high Reynolds number turbulent flows, a very fine mesh spacing is required near to the wall of interest (the plate in this case case) and hexahedral grid units allow very fine wall-normal spacing without larger face skewness.

Creating the grid-nodes near the wall boundary (the plate in this case) is an important aspect to model the flow parameters in the near-wall region. More details about the near-wall treatment employed in the grid-generation technique are discussed in Appendix D.

3.6.4 Methodology

3.6.4.1 Solver

The commercial CFD software package, ANSYS FLUENT 16.0 was used in the current study, which uses the finite volume technique to solve the mass-conservation, momentum-conservation and energy-conservation equations. All the equations were solved using the double precision model, since double precision is more accurate than the single precision solvers for boundary layer heat transfer flows where there is a large difference between the extent of the biggest and the smallest cell in the domain (ANSYS, 2013b). A pressure-based algorithm was used since the present flow falls under the

category of low speed incompressible flow, whereas the density-based solvers are mainly developed for high speed compressible flows. More details on the pressure-based algorithm is already discussed in Chapter 2 (refer to section 2.5.1).

ANSYS FLUENT 16.0 uses a control volume cell-centred numeric for its conservation equations solution strategy with statistical iterative methods and are sometimes less accurate for certain complex flow problems such as turbomachinery compressor flows. However, it is mentioned once again that the FLUENT was used to carry out only the steady RANS simulations in the current study.

3.6.4.2 Turbulence models

In the present study, the SST k-ω model has been chosen to carry out the laminar boundary layer studies since the SST k-ω model with the Low Reynolds number modelling (LRNM) performed very well in terms of matching both the model scale wind tunnel velocity profiles over the windward roof of a low-rise building and the standard Nusselt number (Nu) correlation with Re for uniform flow over an isothermal flat plate (Karava *et al.*, 2011). Similarly, k-kl-ω transitional model was chosen as a suitable turbulence model to simulate the turbulent boundary layer phenomenon since this model can precisely predict the onset of transition in high Reynolds number boundary layer flows (Walters and Cokljat, 2008).

3.6.4.2.1 Shear-stress Transport k-ω model

The SST-k-ω model has already been discussed in detail in the previous chapter (Chapter 2; Section 2.5.4) with all the model equations and its variants. Hence further details about the SST k-ω model will not be discussed here. However, the Low Reynolds number modelling approach (LRNM) embedded in the SST k-ω model employed in the current study are explained in detail with the model equations in Appendix E.

3.6.4.2.2 k-kl-ω model Transitional model

This section describes the theory behind the k-kl-ω transitional model which is used to predict the boundary layer development and location of the transitional onset for medium to high Reynolds number flows. The k-kl-ω transitional model was developed by Walters

and Cokljat (Walters and Cokljat, 2008) and is based on the traditional k-ω model framework that represents a substantial refinement to a previous transition-sensitive model (Walters and Leylek, 2002). An additional third transport equation is included in two equation eddy-viscosity model which is used to represent pre-transitional velocity fluctuations that are identified as the precursors to the transition phenomenon. The kinetic energy of these pre-transitional velocity fluctuations is represented by kl, which is known as the laminar kinetic energy. Although the dynamics of the kl production is not very well understood, few researchers (Mayle and Schulz (1997); Walters and Leylek (2002)) have tried to shed light on the subject based on two contrasting theories. Whilst Mayle and Schulz (1997) proposed that the growth of laminar kinetic energy was due to the transport of energy from the freestream into the boundary layer due to the pressure diffusion term, Walters and Leylek (2002) stated that the production of the laminar kinetic energy is due to the interaction of the Reynolds stresses of the non-turbulent velocity fluctuations with the mean shear. This phenomenon is also verified from the LES simulations performed by Lardeau *et al.* (2007). The premise from the above discussion convey the fact that an additional model transport equation is required to solve kl, along with the transport equations of k and ω, to fully describe the transition process of the boundary layer. The model transport equations for k, kl and ω along with the model variants are described in Appendix F.

3.6.4.3 Solution parameters

For the steady RANS modelling (optimized SST-k-ω) of the boundary layer flow, the second order upwind discretization schemes were used for the pressure, momentum and turbulence parameters (turbulent kinetic energy and specific dissipation rate). The second-order schemes fare better than the first order discretization schemes near a solid-wall boundary due to their diffusive nature (low numerical discretization error) and increased damping, which allows one to model such flows correctly.

For the pressure velocity coupling the Semi-Implicit method for Pressure Linked Equations (SIMPLE) algorithm (Patankar *et al.* 1972) was used for the steady RANS as it is more suitable for steady state flows. For the evaluation of gradients and derivatives, the

Least square cell based gradient method is employed as it is more accurate and less expensive than other gradient methods on a structured hexahedral mesh.

3.6.5 Boundary conditions

For the steady RANS SST-k-ω and the transitional k-kl-ω model, a well-specified velocity boundary condition was defined at the inlet along with the turbulent parameters i.e. turbulent kinetic energy (TKE) and the specific dissipation rate (ω) for turbulent calculations. The pressure outlet boundary condition is specified with a gauge pressure of zero Pascals which physically relates to the atmospheric pressure to which the flow exits. The slip boundary condition was specified at all the other boundaries where the shear stress is assumed to be zero so that it had negligible effect on the boundary layer growth over the flat plate. A pure-no slip boundary condition was specified on the flat plate boundary which assumes that the tangential fluid-velocity adhering to the wall is zero (because of the existence of the viscosity of the fluid).

3.6.6 Grid-Independence study

Grid-independency is an important factor to check in any CFD simulation since the numerical results should not suffer from the discretization error arising from the spacing of the computational cells. A grid-independence study was carried out for two different boundary layer cases; 1) with a flow velocity of 4m/s developing a spatially evolving laminar boundary layer and 2) with a flow velocity of 40m/s thereby generating a spatially developing turbulent boundary layer. The grid-refinement strategy employed here was according to the COST guidelines (Franke *et al.*, 2007), which states that at least three systematically and substantially refined grids should be used and that the ratio of cells should be at least 1.5 in each dimension.

Three-grid resolutions L1, L2 and L3 of 462,500, 649,350 and 784,400 grid-cells, respectively, are used for the laminar boundary layer case to ensure a grid-independent solution. However, as the turbulence model with the (LRNM) approach is used for the laminar flow problem, a $y^+<1$ is employed which is a desired requirement for such a modelling approach for accurate prediction of laminar boundary layer near the wall. The

first cell height (Δy) from the wall chosen for the laminar boundary layer case is 1×10^{-4}m which is well under the desired requirements of the y^+ value of the wall-function grid.

Similarly, three independent grid resolutions T1, T2 and T3 with grid resolutions of 587,500, 824,850 and 996,400 cells are used for the developing turbulent boundary layer case. A $y^+<1$ is employed while constructing the grid-cells which is aimed at resolving the inner turbulent boundary layer until the viscous sub-layer of the flow. The first cell height (Δy) chosen for this case was at 1.6×10^{-5}m from the plate wall which falls under the desired y^+ for a LRNM model. It should be noted that the inlet mesh-nodes were fixed for all the six meshes used in the current study in order to keep consistent inlet velocity fields across all the cases.

The simulations for the laminar boundary layer case (4m/s) were run for an inlet mean velocity $\overline{U}$ = 4m/s, TI = 0.1% and L_u = 0.1m which corresponds to TKE magnitude of 2.4×10^{-5} J/kg and specific dissipation rate (ω) = $0.54s^{-1}$. The corresponding Reynolds number (Re_L) based on the plate length (L=2m) is 5.09×10^5 which comes under the category of the laminar flow. Similarly, the simulations for the spatially developing turbulent boundary layer case was run for an inlet mean velocity ($\overline{U}$) = 40m/s, TI = 0.1% and L_u = 0.1m. The corresponding values of the inlet TKE and specific dissipation rate (ω) are 2.4×10^{-3}J/kg and $5.44s^{-1}$ respectively. The corresponding Reynolds number of the flow based on the plate length (2m) is 5.09×10^6 which comes under the turbulent flow regime. The kinematic viscosity (ν) is taken as 1.57×10^{-5} based on the standard state temperature of 298.15k (25° C).

3.6.6.1 Grid-independency of the laminar boundary layer over the flat plate case

The grid-independency of three different grids (L1, L2 and L3) for spatially developing laminar boundary over the flat plate is assessed in terms of the local skin-friction coefficient (cf) (skin-friction is the ratio of the local shear stress to the dynamic characteristic pressure) and the corresponding velocity distributions along the normal direction to the boundary layer. Figure (3.14) shows the local skin-friction profiles for three different grids, along the centreline of the plate plotted against the local Reynolds

number (Re_X) where, X denotes the distance from the leading edge of the plate. A comparison between the local skin friction profiles for three different grids and the theoretical skin-friction profile is made to examine the accuracy of the applied CFD model. From the figure it is clear that, the local skin friction profiles are not very sensitive to the streamwise mesh density and that the increase in streamwise nodes for three different grids have very little effect on the modeled skin friction profiles. The (c_f) profiles obtained for three different grid-resolutions (L1, L2 and L3) almost overlap with each other on the top and demonstrate very good agreement with the theoretical laminar skin-friction profile.

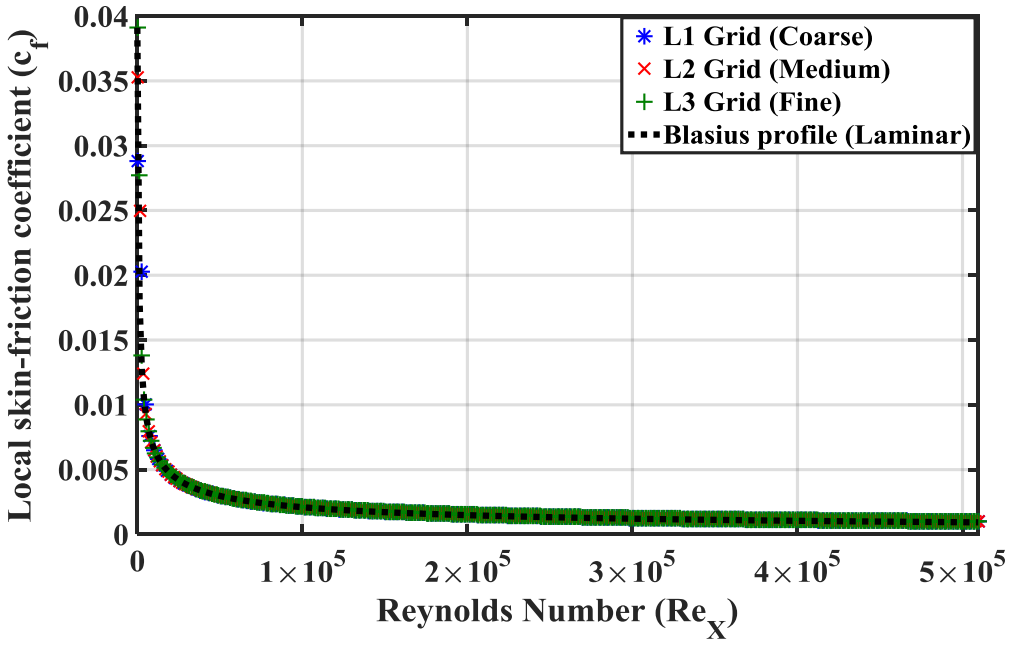

Figure 3.14 Local skin-friction profiles plotted for three different grids measured along the centreline of the plate

To characterize the velocity profiles inside the boundary layer, mean velocity magnitudes have been extracted at four different locations along the centreline of the plate. The location of those measurement points is shown in fig (3.15) for clarity in visualization and understanding.

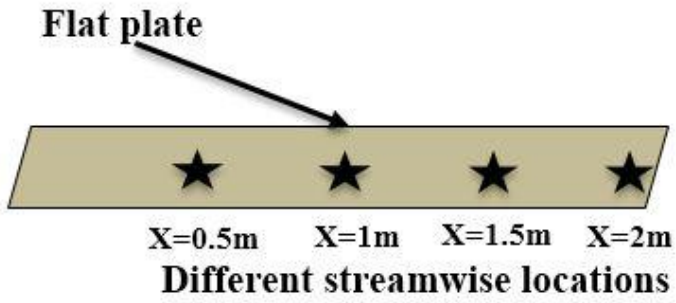

Figure 3.15 Schematic of the flat plate showing the location of four different measurement points along the centreline of the plate

The non-dimensional distances of these four different locations based on the streamwise distance from the leading edge of the plate (X) and the plate length (L) is shown in table (3.1).

Table 3.1 Non-dimensional distances of the four different locations along the centreline of the plate

Streamwise location No.	1	2	3	4
x	1m	1.5m	2m	2.5m
X/L	0.25	0.5	0.75	1

Figure (3.16) and figure (3.17) shows the normalized velocity ($\frac{u_i}{U}$) profiles plotted for three different grids measured at four different locations (x= 1m, x= 1.5m, x= 2m and x= 2.5m) along the centreline of the plate against a non-dimensional parameter ($\frac{y}{\delta}$). Fig (3.16) represents the velocity profile at X/L = 1 and X/L = 0.75 and figure (3.17) represents the velocity profile at X/L = 0.50 and X/L = 0.25, respectively (where X represents the distance from the leading edge of the plate). The thickness of the boundary layer, δ, is defined as the vertical distance from the surface of the plate to the location

where the local velocity reaches 99% of the freestream value and y represents the distance in the direction normal to the plate surface. The variability of the non-dimensional velocity profiles between the coarse and the medium grid and between the medium and the fine grid is negligible (less than 1%) which is clearly noticeable from the figures (3.16) and (3.17). Based on the above discussion, the medium grid L2 with 649,350 cells is chosen for all the CFD simulations in the current study which requires less computational time (than the fine grid) to simulate the boundary layer flow.

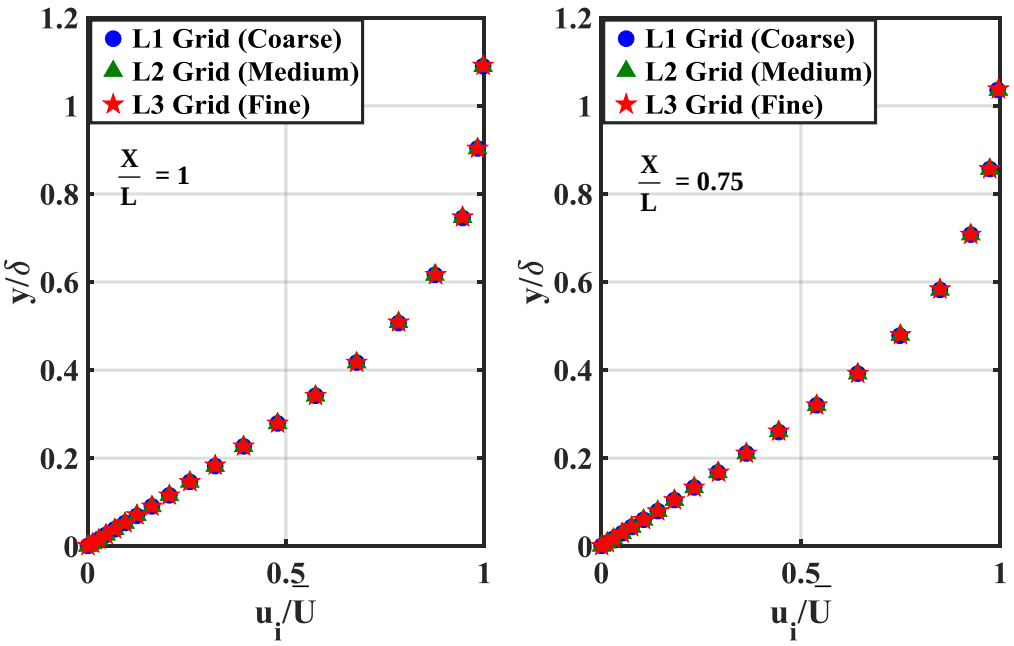

Figure 3.16 Normalized velocity profile plotted for three different grids along the centreline of the plate at x=2.0m (right) and x=2.5m (left)

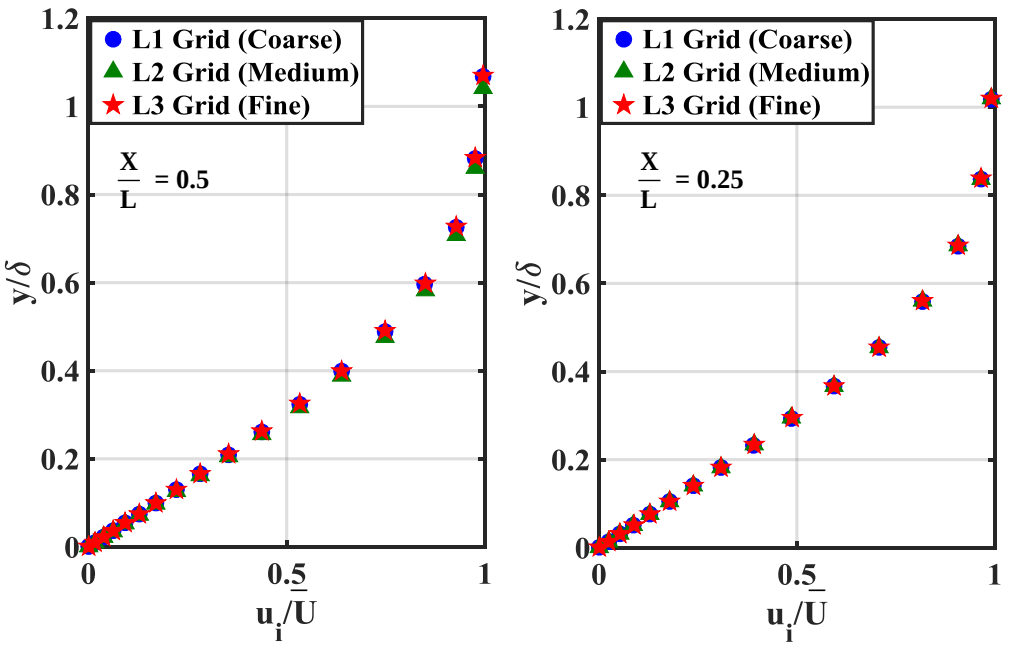

Figure 3.17 Normalized velocity profile plotted for three different grids along the centreline of the plate at x=1.0m (right) and x=1.5m (left)

3.6.6.2 Grid-independency of the spatially developing turbulent boundary layer over the flat plate

A grid independence study was also carried out on three different grids (T1, T2 and T3) for a spatially evolving turbulent boundary layer to check whether the boundary layer development is independent of the number of grid-cells in the domain. Figure (3.18) show the development of local skin-friction profiles for three different grids plotted against the local Reynolds number (Re_X) along the centreline of the plate. The results obtained from coarse, medium and fine grids show negligible differences, and for each grid the onset of natural transition is predicted roughly at local Reynolds number (Re_X) of 1.97×10^6. As the Reynolds number of the flow based on the plate length (2m) is 5.09×10^6, which is higher than the critical Re value for flow over a flat plate (White, 2016), it undergoes transition and subsequently changes to a more chaotic (than laminar) three-dimensional turbulent boundary layer. The sudden increase in skin-friction coefficient observed is due to this transition process occurring in the flow at high enough Reynolds number. The theoretical laminar and turbulent skin-friction profiles are also

plotted in the same figure (3.18) with the grid-resolution results to show that the skin-friction values predicted from grid-independent results match closely with theoretical skin-friction profiles.

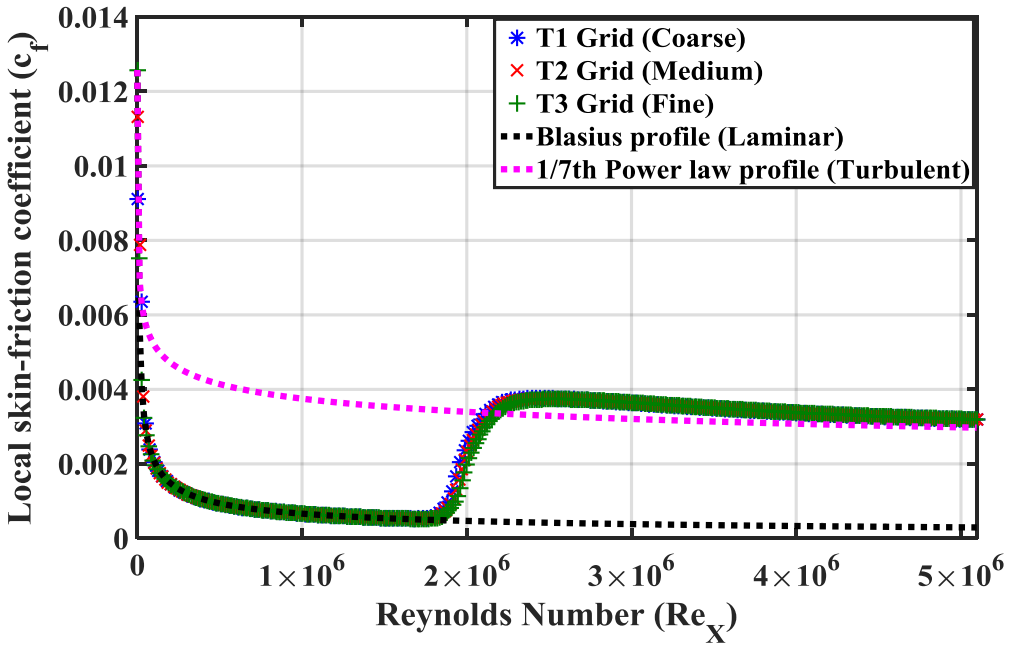

Figure 3.18 Local skin-friction profiles plotted for three different grids measured along the centreline of the plate

The velocity distributions for each of the three grids (T1, T2 and T3) along the centreline of the plate are plotted in figure (3.19) where the x-abscissa represents the non-dimensional velocity variable $(\frac{u_i}{U})$ and the y ordinate represents the dimensionless normal distance expressed as $(\frac{y}{\delta})$. The plots are shown only for two streamwise locations i.e. at x=2m and x=1.5m, since the turbulent boundary layer has already developed only over these regions. The flow prior to these locations are in a mixed transitional state and, therefore, are not shown here for grid-independent comparisons.

The three grids (T1, T2 and T3) employed in this study shows negligible variation (less than 1%) in both the local skin-friction profiles along the centreline and the velocity

distribution inside the boundary layer at the considered locations (x=1.5m and x=2m) and, therefore, the medium grid T2 with 824,850 grid cells is chosen to carry out the turbulent boundary layer analysis.

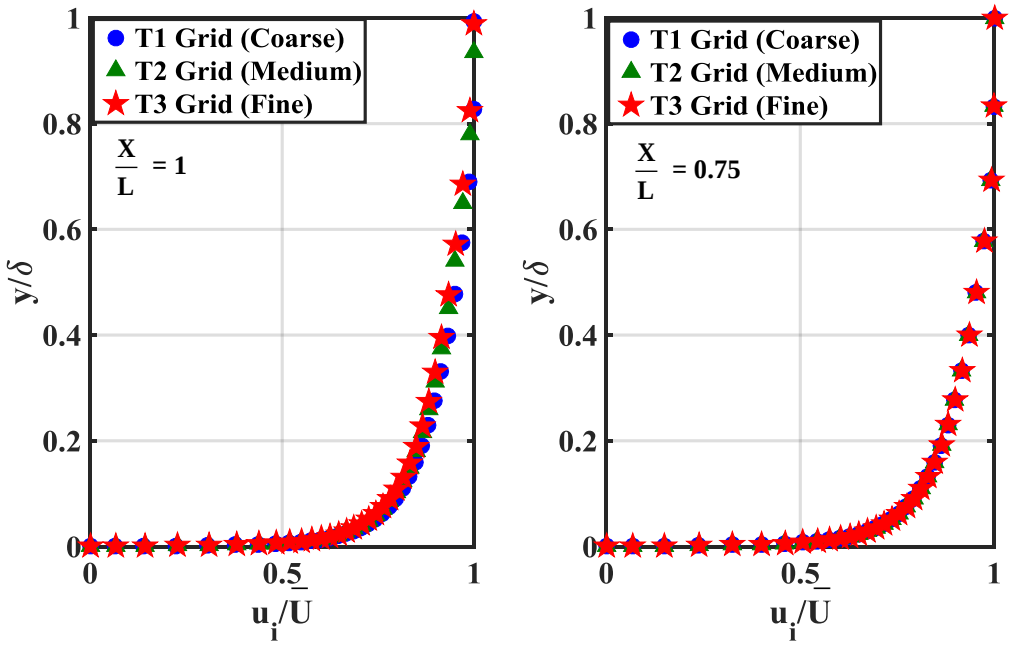

Figure 3.19 Normalized velocity profile plotted for three different grids along the centreline of the plate at x=2.5m (left) and x=2m (right)

3.6.7 Boundary layer validation

In this section, the flat plate boundary layer model results obtained from CFD simulations have been validated against the boundary layer solutions obtained from the theoretical boundary layer equations for steady incompressible laminar and turbulent flows. The comparisons between the newly devised improved RANS SST-k-ω model with a modified constant and the theoretical boundary layer solutions are shown to test the capability of these improved RANS model in reproducing the features of boundary layers in an accurate manner. In addition, the k-kl-ω model implemented with the optimised model constant is also tested against the flat plate theoretical turbulent boundary layer models.

3.6.7.1 Laminar boundary layer flow characteristics

The laminar boundary layer simulations have been carried out for the mean freestream velocity ($\overline{U}$) = 4m/s, negligible freestream turbulence intensity at the inlet (TI) = 0.1% and the inlet integral length scale (L_u) of 0.1m. At first, the local skin-friction profile obtained from the optimized SST-k-ω model is compared with the theoretical laminar skin-friction profile, which is determined according to the formula given by

$$c_f = \frac{0.664}{\sqrt{Re_X}} \tag{3.7}$$

where Re_X is the Reynolds number based on the distance from the leading edge of the plate X. The relative comparisons are shown in figure (3.20). Post-comparison it is revealed that the improved SST-k-ω model can reliably predict the near wall shear stress behaviour close to the solid boundary. Next, the velocity profiles obtained from the improved RANS model have been analyzed for further investigation.

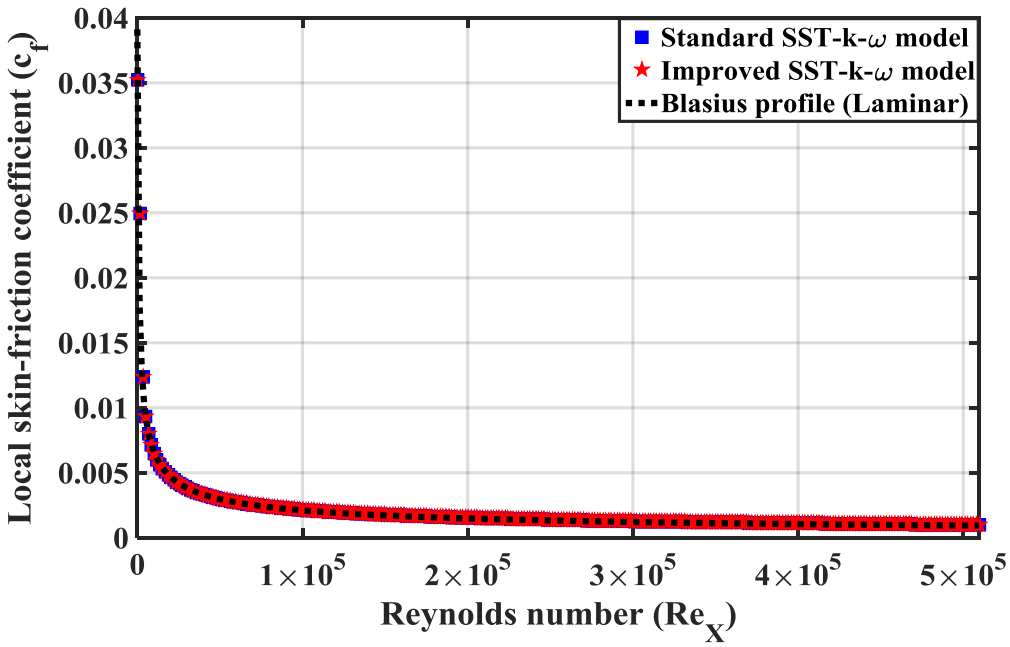

Figure 3.20 Comparison of the local skin-friction profiles obtained from the standard and the improved SST-k-ω model plotted against the theoretical laminar skin-friction profiles, measured along the centreline of the plate

The streamwise velocity magnitudes are extracted at four different points along the centreline of the plate. The location of these points on the plate section have already been shown in figure (3.15) along with the non-dimensional distances that are previously stated in table (3.1). The velocity profiles from the these four streamwise locations are presented in the current section since they all come under the laminar boundary layer flow regime. Figure (3.21) shows the plot of the normalized streamwise velocity component $(\frac{u_i}{\overline{U}})$ versus the non-dimensional normal distance $(\frac{y}{\delta})$ along the centreline locations of the plate at x=2.5m and x=2.0m. Similar plots for two other different streamwise locations (x= 1.5m and x=1.0m) are shown in figure (3.22). In order to examine the correctness of the obtained velocity distribution from the CFD models, it is necessary to discuss briefly about the widely accepted theoretical laminar boundary layer models. The laminar boundary layer velocity profile for an steady incompressible viscous flow over a flat plate was first predicted from the exact solution of the non-linear boundary layer equations given by Blasius (Blasius, 1908). Later, Von-Kármán (Kármán, 1921) in his theory proposed that the velocity profiles inside the laminar boundary layer may have an approximate parabolic shape that can be approximated by

$$u_i(x,y) \approx \overline{U}(\frac{2y}{\delta} - \frac{y^2}{\delta^2}) \qquad 0 \leq y \leq \delta\,(x) \tag{3.8}$$

A much better agreement with the exact solution of Blasius (Blasius, 1908) can also be achieved by more plausible assumptions of the velocity distribution satisfying the higher order polynomials (Duncan *et al.* 1970) such as cubic and quadratic velocity distributions, which are given by

$$u_i(x,y) \approx \overline{U}(\frac{3}{2}\frac{y}{\delta} - \frac{1}{2}(\frac{y}{\delta})^3) \tag{3.9}$$

$$u_i(x,y) \approx \overline{U}(2\frac{y}{\delta} - 2(\frac{y}{\delta})^3 + (\frac{y}{\delta})^4) \tag{3.10}$$

However, it should be noted that the cubic and the quadratic velocity distributions stated in equations (3.9) and (3.10) are plausible assumptions to the boundary layer solution by

Blasius and, hence, the reader is advised to examine the correctness of these assumptions by comparing the numerically obtained velocity profiles with the exact boundary layer solution of Blasius (1908). In this section, the velocity distributions obtained from the standard and the improved SST-k-ω model are compared with the Blasius, von-Kármán, cubic, quadratic velocity profiles (fig. (3.21) & fig. (3.22) to examine the accuracy of the improved RANS model in predicting the laminar boundary layer development. It is clear from these figures (figure 3.21 & 3.22), that the velocity profiles at those streamwise locations display a close match with all the theoretical profiles, with the closest being with the Blasius boundary layer velocity profile (numerical results lie within ±2% Blasius profile). Therefore, the results from the optimized SST-k-ω model confirm that the model is extremely reliable in reproducing the laminar boundary layer behaviour in the presence of zero pressure gradient.

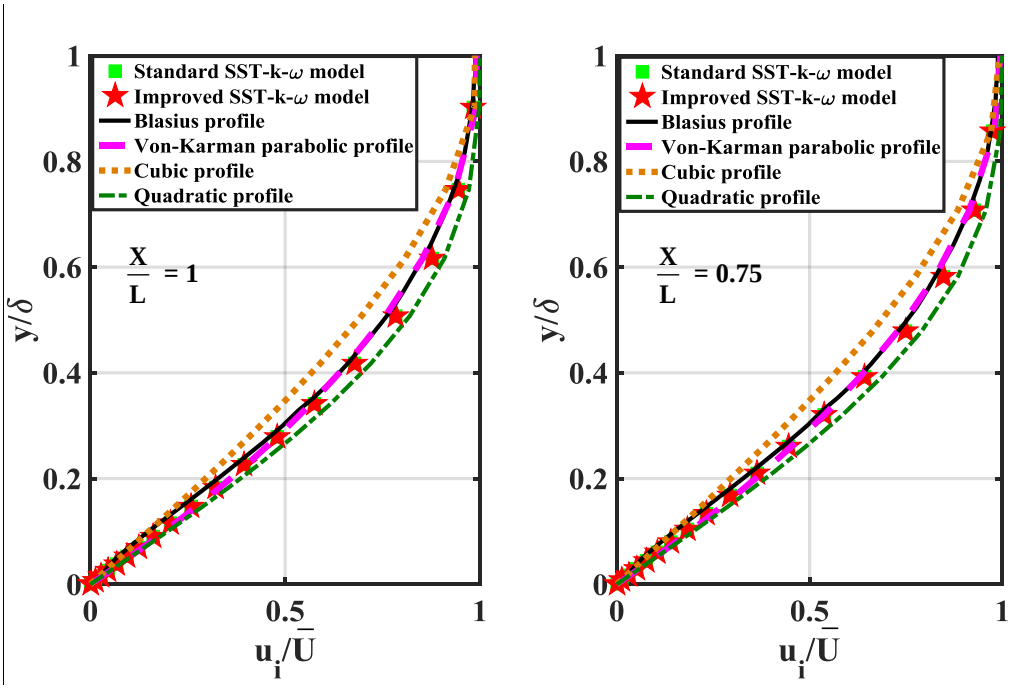

Figure 3.21 Normalized velocity profile obtained from the standard and the improved SST-k-ω model plotted against the theoretical laminar velocity profiles, measured along the centreline of the plate at x= 2.0m (right) and x= 2.5m (left)

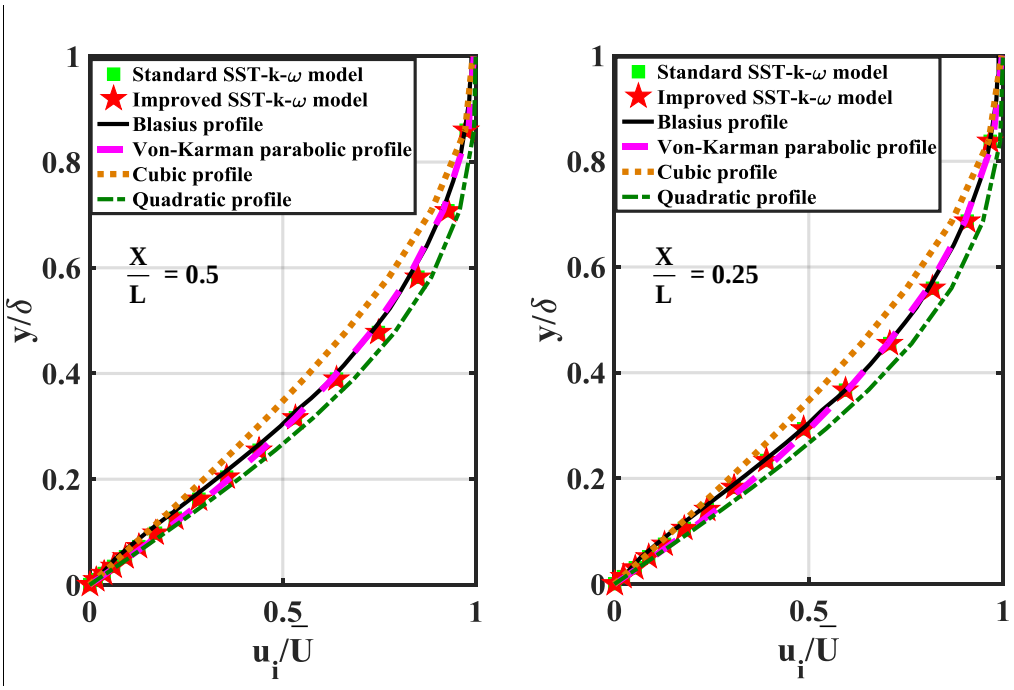

Figure 3.22 Normalized velocity profile obtained from the standard and the improved SST-k-ω model plotted against the theoretical laminar velocity profiles, measured along the centreline of the plate at x= 1.0m (right) and x= 1.5m (left)

In addition to the plots of the laminar velocity profiles and the skin-friction profiles shown, comparisons have been made in terms of displacement thickness (δ^*), momentum thickness (θ) and the shape-factor (H) obtained from the improved SST-k-ω model and that from the Blasius, cubic and quadratic profile. The displacement thickness (δ^*) is defined as the distance by which the external freestream flow is displaced outward due to the decrease in velocity in the boundary layer. Similarly, momentum thickness (θ) is defined as the distance by which the boundary layer has to be displaced in order to compensate for the reduction in momentum inside the boundary layer. The ratio of displacement thickness to the momentum thickness is called the dimensionless-profile shape factor (H). The comparisons of the non-dimensional displacement thickness, momentum thickness and shape factor are listed in table (3.2).

Table 3.2 Comparison between the dimensionless momentum thickness, displacement thickness and the shape factor obtained from the improved SST-k-ω model and the theoretical laminar velocity profiles

Variables	$\frac{\theta}{x}\sqrt{Re_X}$	$\frac{\delta^*}{x}\sqrt{Re_X}$	H (shape-factor)
Blasius velocity profile	0.66	1.72	2.59
Cubic velocity profile	0.65	1.74	2.70
Quadratic velocity profile	0.69	1.75	2.55
X/L = 1	0.72	1.84	2.56
X/L = 0.75	0.73	1.86	2.57
X/L = 0.5	0.73	1.87	2.57
X/L = 0.25	0.68	1.74	2.59

From the abovementioned table (3.2), it is evident that the non-dimensional form of momentum thickness, displacement thickness and velocity profile shape factor obtained from the numerical results demonstrate good quantitative agreement with the dimensionless form of these boundary layer variables derived from the theoretical boundary layer equations. The magnitudes of the momentum thickness and the displacement thickness are within 10% of the theoretical boundary layer values, whereas the shape factor lie within ±2% of the Blasius boundary layer solutions. Hence, it can be inferred that the SST-k-ω model can successfully predict the boundary layer growth over a smooth flat plate.

3.6.7.2 Turbulent boundary layer flow characteristics

The turbulent boundary layer flow characteristics obtained from the optimised k-kl-ω transitional model is investigated in the following section. The velocity profiles along the centreline of the plate at two locations (x=2.5m & x=2.0m) are plotted in figure (3.23). Only the velocity profiles at these two streamwise locations are presented, because the flow undergoes transition from a laminar to a turbulent regime prior to those locations. Therefore, the comparison of the numerically obtained velocity profiles, with the turbulent power-law velocity profile will be much more definite at those two streamwise positions. However, it is pointed out here that, the power-law velocity profile is an empirical velocity profile which is the simplest and widely accepted velocity profile for many engineering applications (pipe flows) that has a reasonably good fit to the velocity distributions inside the turbulent boundary layer (Nikuradse, 1950). The power law velocity profile can be expressed as

$$u_i(x,y) \approx \overline{U}\left(\frac{y}{\delta}\right)^{1/n} \quad \text{for } y \leq \delta \tag{3.11}$$

where the exponent n is a constant whose value depends on the Reynolds number (Re_X) of the plate flow, $\overline{U}$ denotes the mean-streamwise velocity, y represents the distance in the normal direction and δ is the boundary layer thickness. Note that in the approximation of equation (3.11), δ is "*not*" the 99% of the boundary layer thickness, but rather the actual edge of the boundary layer. The value of n generally increases with increasing Reynolds number (Re_X). The value of n = 7 approximates many flows in practice, and was suggested by Prandtl (Prandtl, 1904), as it forms an excellent fit to the low-Reynolds number turbulent data. The turbulent velocity profile is much fuller than the laminar one, and it becomes flatter as n increases. Figure (3.23) shows the non-dimensional turbulent velocity profile obtained from the numerical simulations plotted together with various power-law velocity profiles having n= 6, 7 and 8 for relative comparisons. The obtained velocity profiles illustrate good quantitative agreement with the empirical power law velocity profiles. In order to determine the precise exponent (n) of the velocity profiles obtained from the revised k-kl-ω model, a log-log plot of normalized velocity profiles is made which are represented in figures (3.24) and (3.25). In figure (3.24), the exponent n

is computed from the linear best-fit plot to the log-log profiles, and its magnitude is 7.60, for the velocity profile at x = 2.5m. Similarly, the exponent n obtained from the linear best-fit to the logarithmic velocity profiles measured at x = 2.0m is 7.42 (fig. (3.25)). Both the magnitude of exponents is remarkably close to the value of the exponent for the one-seventh power-law profiles (n = 7) which infers that the improved k-kl-ω model with an optimised (β_∞^*) succeeds remarkably well in predicting the development of the turbulent boundary layer over a flat plate.

It is emphasized over here that the turbulent power velocity profile represented in equation (3.11) is physically meaningless very close to the wall i.e. at $y \rightarrow 0$, since the normal velocity gradient, given by ($\frac{\partial u}{\partial y}$) will be infinite at $y \approx 0$, which is not close to the reality. Hence the equation (3.20) cannot be used to deduce the near wall shear stress (τ_w) along the length of the plate as it will yield a value of infinity (since, $\tau_w = -\mu(\frac{\partial u}{\partial y})$) close to the wall. Although, the slope of the tangent at any point close to the plate boundary will be very high in magnitude, it is nevertheless infinite. However, the large slope at the plate boundary will give rise to a very high wall shear stress and, correspondingly high local skin-friction coefficient (c_f). This phenomenon is quite evident from the plots shown in figure (3.26), where it is clearly noticed that after the onset of natural transition occurring approximately at Reynolds number (Re_X) of 1.98×10^6, the local-skin friction coefficient (c_f) undergoes a sudden jump to a relatively higher magnitude of coefficient values. It is important to mention that the skin-friction coefficient computed here is directly extracted from the numerical simulation results. A comparison between the numerical results and the theoretical skin-friction profiles is also demonstrated in the same figure which shows that the transitional k-kl-ω model with the improved model coefficient (β_∞^*) = 0.046 can effectively predict the turbulent boundary layer development and can address the transition of the boundary layer from a laminar to turbulent regime in a reliable manner. The turbulent boundary layer skin-friction profiles are determined empirically according to

$$c_f = \frac{0.027}{(Re_X)^{1/7}} \tag{3.12}$$

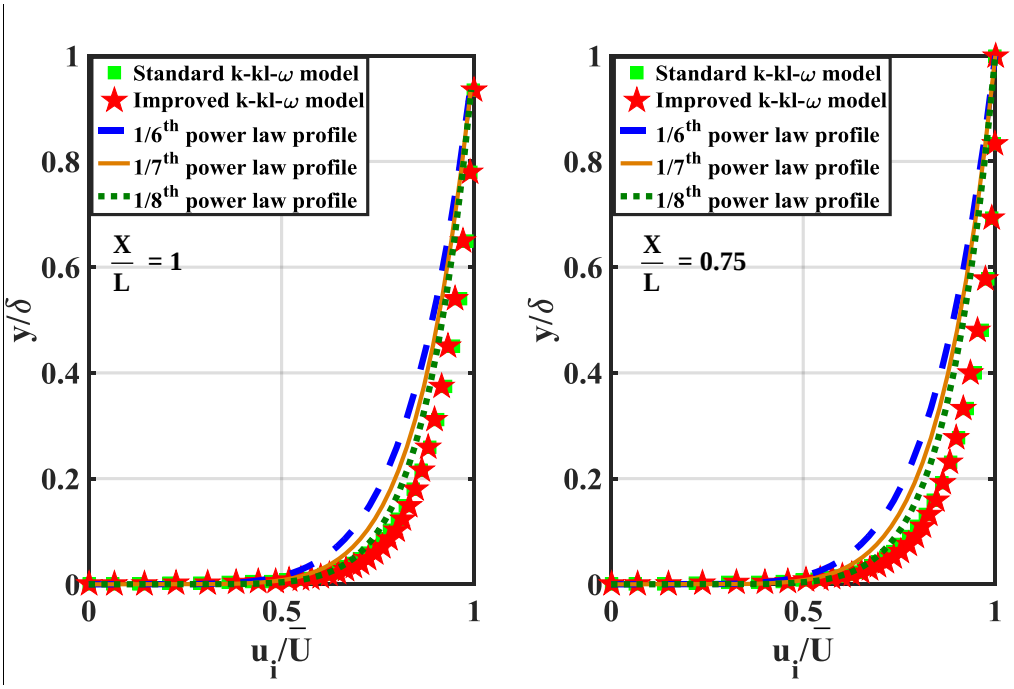

Figure 3.23 Normalized velocity profile obtained from the standard and the improved k-kl-ω model plotted against the theoretical turbulent velocity profiles, measured along the centreline of the plate at x=2.0m (right) and x=2.5m (left)

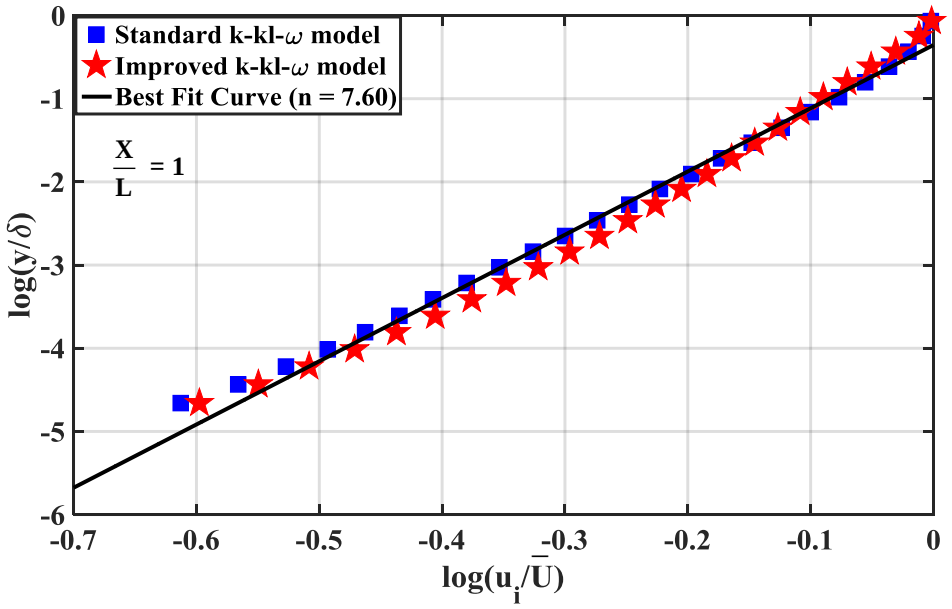

Figure 3.24 Plot of normalized velocity profile in the logarithmic form obtained from the standard and the improved k-kl-ω model measured at x=2.5m

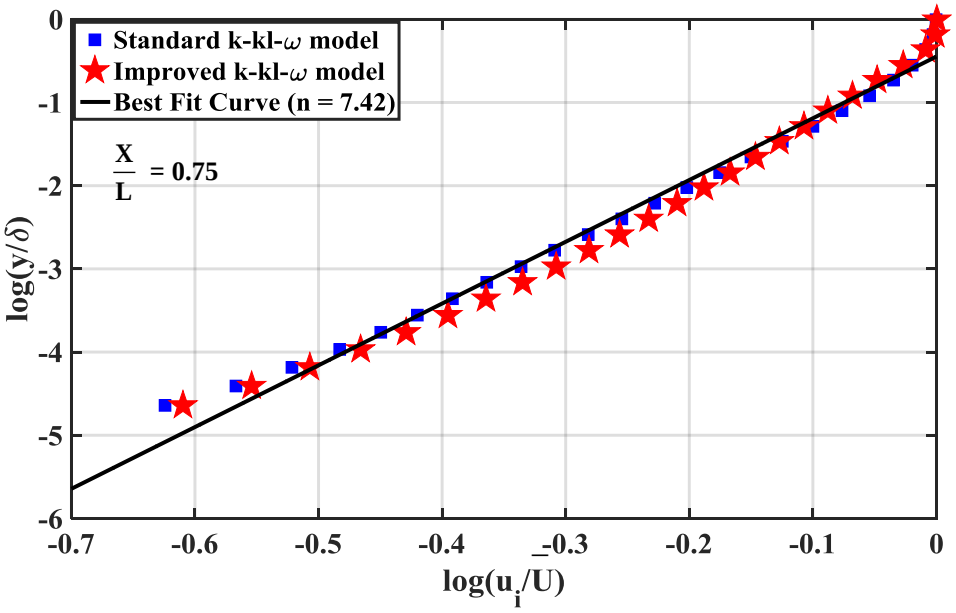

Figure 3.25 Plot of normalized velocity profile in the logarithmic form obtained from the standard and the improved k-kl-ω model measured at x=2.0m

The magnitudes of the dimensionless-profile shape factor (H) obtained from the revised k-kl-ω transitional model and those obtained from the different power law velocity profiles are summarized in table (3.3).

Table 3.3 Comparisons between the dimensionless velocity shape factor obtained from the improved SST-k-ω model and the theoretical turbulent velocity profiles

Turbulent velocity profiles	Velocity profile shape factor (H)
$1/6^{th}$ Power law velocity profile	1.33
$1/7^{th}$ Power law velocity profile	1.29
$1/8^{th}$ Power law velocity profile	1.25
X/L = 1	1.26
X/L = 0.75	1.27

The shape factor obtained from the velocity profiles at x = 2.5m and x =2.0m is relatively close and lie within the values of the shape-factor obtained from the semi-empirical $1/7^{th}$ and $1/8^{th}$ power-law velocity profile. The agreements are within ±2% from the theoretical turbulent profiles. Therefore, the optimised k-kl-ω transitional model demonstrates the ability to reproduce transitional and turbulent boundary layer behaviour in a correct manner.

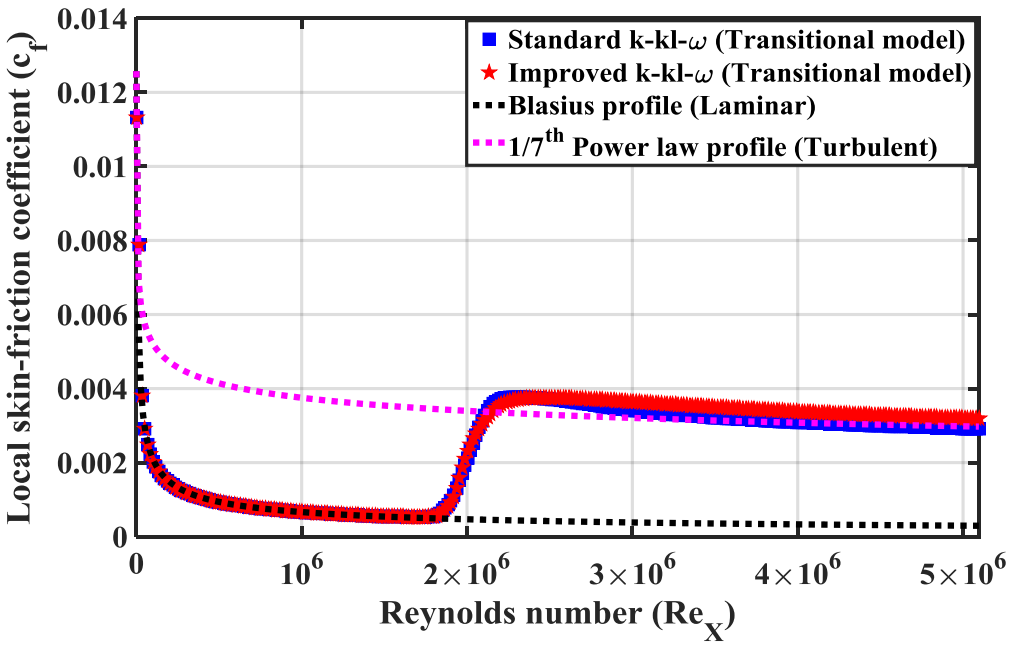

Figure 3.26 Comparison of the local skin-friction profiles obtained from the standard and the improved k-kl-ω model plotted against the theoretical turbulent skin-friction profiles, measured along the centreline of the plate

3.7 Summary

This section summarizes the overall results obtained from the optimized SST-k-ω and the k-kl-ω model simulations that are carried out in the preceding sections.

- The default standard SST-k-ω models employed in three commercial software codes (viz. FLUENT, STAR-CCM+ and CFX) are not accurate in predicting the decay of homogeneous isotropic turbulence downstream of an inlet. The discrepancy observed is due to the magnitude of the default model constants used in those software codes to solve the closure problem of two equation SST-k-ω model. Though the default values of these closure coefficients are derived empirically and have found to work quite well for wall-bounded and wall shear flows, it doesn't work accurately for grid-generated decaying isotropic turbulence.

- By tuning in the default values of the standard model constant (β_*^∞) of the SST-k-ω model in an appropriate manner (i.e. substituting $\beta_*^\infty \approx 0.046$) , a closer match of the FLUENT SST-k-ω results with the experiments and the LES results can be obtained for freely decaying isotropic homogeneous turbulence.

- Similar agreement for the two-other commercial CFD codes i.e. STAR-CCM+ and CFX can also be obtained by fine tuning the model constant in a similar manner, that can be applied to the studies of grid and computer generated isotropic homogeneous turbulence.

- The new optimized model constant when used with SST-k-ω low Reynolds number correction (LRNM) predicts the development of the laminar boundary layer in a correct manner and demonstrates good quantitative agreement with the Blasius boundary layer solution. Therefore, it can be concluded that modifying the constant to better predict freestream decay does not affect the laminar boundary layer development (e.g. local skin-friction profiles and the velocity boundary layer profiles).

- The transitional k-kl-ω model when used with the new optimized constant predicts the onset of natural transition quite well and the numerical results obtained for turbulent boundary layer velocity profiles show close resemblance to the empirical power law velocity profiles.

3.8 Conclusion

In this chapter, the capability of the standard SST-k-ω RANS based model in predicting the decay of isotropic and homogenous turbulence has been investigated in detail. Post-evaluation it is found that the standard SST-k-ω model doesn't predict the correct behaviour of the turbulence decay downstream in any of the three-available commercial CFD codes (FLUENT, STAR-CCM+ and CFX) because of the way the empirical closure coefficients are implemented as a precursor to the modelling simulation results. The differences and the limitations of these softwares in terms of different modelling

constants are highlighted for thorough understanding of the reader. In order to improve the pre-existing RANS modelling results, the standard SST-k-ω model in FLUENT has been used with a newly tuned model constant that successfully generates better results with a reasonable degree of accuracy, when compared quantitatively with the different experimental data sets and the present LES results. The new optimized model constant was then coupled with the SST-k-ω, a LRNM model and tested for a simple zero-pressure gradient flat plate, in order to assess the response of the new model constant in terms of laminar boundary layer predictions. Then the results are succinctly compared to the theoretical laminar boundary layer correlations. Similarly, the new model constant is also integrated with the transitional k-kl-ω model in the same way to address the transitional flow behaviour and match the turbulent boundary layer profiles with already established experimental and empirical flat plate turbulent boundary layer correlations. The simulation results disclose the fact that the improved model constant does not affect the laminar or turbulent boundary layer developments over a flat plate whilst working fairly well for freestream turbulence decay. Hence, the improved RANS SST-k-ω and k-kl-ω transitional models can be suitably extended to carry out studies on boundary layers over a flat plate in presence of oncoming freestream turbulence.

The next chapter present the conclusions from the present work, together with recommendations for future work.

REFERENCES

ANSYS (2013a) *ANSYS CFX-Solver Theory Guide*. pp. 1-372.

ANSYS (2013b) *ANSYS Fluent Theory Guide*. pp. 1-814.

Blasius, H. (1908) 'Grenzschichten in Flüssigkeiten mit kleiner Reibung', *Z. Angew. Math. Phys*, (56), pp. 1–37.

CD-Adapco (2015) *STAR-CCM + ® Manual*, pp. 1-12352

Chorin, A. J. (1968) 'Numerical Solution of Navier-Stokes Equations', *Mathematics of Computation*, 22(104), pp. 745–762.

Duncan, W. J., Thom, A. S. and Young, A. D. (1970) *Mechanics of fluids*, pp.1-723

Franke, J., Hellsten, A., Schlünzen, H. and Carissimo, B. (2007) Best practice guideline for the CFD simulation of flows in the urban environment, *COST action 732; Quality Assurance and Improvement of Microscale Meteorological Models*. Hamburg, Germany.

Gerasimov, A. (2016) *Quick Guide to Setting Up LES-type Simulations, Ansys Customer Portal*. Available at: http://www.tfd.chalmers.se/~lada/comp_turb_model/postscript_files/Quick_Guide_to_Setting_Up_LES_version_1.4_for_Lars.pdf.

Karava, P., Jubayer, C. M. and Savory, E. (2011) 'Numerical modelling of forced convective heat transfer from the inclined windward roof of an isolated low-rise building with application to photovoltaic/thermal systems systems', *Applied Thermal Engineering*, 31, pp. 1950–1963.

Kármán, T. von (1921) 'On laminar and turbulent friction', *Z. Angew. Math. Mech.*, 1(1921), pp. 235–236.

Lardeau, S., Li, N. and Leschziner, M. a. (2007) 'Large eddy simulation of transitional boundary layers at high free-stream turbulence intensity and implications for RANS modeling', *Journal of Turbomachinery*, 129(2), pp. 311–317.

Mayle, R. E. and Schulz, A. (1997) ‘The path to predicting bypass transition’, *Journal of Turbomachinery*, 119(3), pp. 405–411.

Nikuradse, J. (1950) ‘Laws of flow in rough pipes’, *Journal of Applied Physics*, 3(November), pp. 1–62.

Patankar, S. V, Spalding, D. B. and Road, E. (1972) ‘A calculation procedure for heat, mass and momentum transfer in three-dimensional parabolic flows’, *International Journal of Heat and Mass Transfer*, 15(10), pp. 1787–1806.

Pope, S. B. (2000) *Turbulent Flows*, *Cambridge University Press*. Cambridge University, pp. 1-810.

Prandtl, L. (1904) ‘Über Flussigkeitsbewegung bei sehr kleiner Reibung’, in *Verhandl. III, Internat. Math.-Kong.* Heidelberg, Teubner, Leipzig, pp. 484–491.

Spalart, P. and Allmaras, S. (1992) ‘A one-equation turbulence model for aerodynamic flows’, in *30th aerospace sciences meeting and exhibit*. Reno, Nevada, pp. 1–23.

Torrano, I., Tutar, M., Martinez-Agirre, M., Rouquier, A., Mordant, N. and Bourgoin, M. (2015) ‘Comparison of experimental and RANS-based numerical studies of the decay of grid-generated turbulence’, *Journal of Fluids Engineering*, 137(6), pp. 1–30.

Walters, D. K. and Cokljat, D. (2008) ‘A Three-Equation Eddy-Viscosity Model for Reynolds-Averaged Navier–Stokes Simulations of Transitional Flow’, *Journal of Fluids Engineering*, 130(12), pp. 1–14.

Walters, D. K. and Leylek, J. H. (2002) ‘A new model for boundary-layer transition using a single-point RANS approach’, in *ASME 2002 International Mechanical Engineering Congress and Exposition*. New Orleans,Louisiana, pp. 1–13.

Wilcox, D. C. (1998) *Turbulence Modelling for CFD*. 1st edn. California: DCW Industries, Inc, pp.1-522.

White, F. M. (2016) *Fluid mechanics*. 8th edn. Hill, Mc Graw, pp.1-848

Chapter 4

4 Conclusions and Recommendations

This chapter presents a number of concluding remarks from the present Computational Fluid Dynamics (CFD) work on the decay of homogeneous isotropic turbulence as well as several recommendations for the future research work.

4.1 Conclusions

The general objective of the thesis was to better understand the decay of turbulence upstream, prior to its interaction with any bluff body. The study was carried out as a part of the larger objective which is to accurately determine the heat transfer rates from a flat plate in presence of uniform freestream turbulence. Computational Fluid Dynamics (CFD) models have been developed using steady Reynolds averaged Navier-Stokes (RANS) and Large eddy simulation (LES) methods to characterize the spatial decay of freestream turbulence. The motivation behind the present study was to identify near constant TKE conditions in the computational domain to examine the effect of freestream turbulence on laminar and turbulent boundary layers. The main conclusions from the present study are as follows:

- A near homogenous and isotropic flow condition for LES simulations can be generated using a proper inlet turbulence generator i.e. (Consistent Discrete Random Flow Generation Technique) (Aboshosha *et al.*, 2015). The homogenous and isotropic flow conditions generated using this technique in the current study replicate similar inlet flow conditions obtained in grid-generated turbulence.
- The effect of the local turbulent root-mean square (r.m.s) velocity fluctuations (u') and the integral length scale (L_u) on the decay of turbulent kinetic energy is re-emphasized and it is found that the rate of decay of turbulent kinetic energy (TKE) solely depends on the local magnitudes of u' and L_u and viscosity, and no other upstream conditions have an effect on the spatial decay of turbulence. The findings are consistent with the earlier reports of Dryden (1943).

- The results from the Dynamic Smagorinsky LES model show very good qualitative and quantitative agreement with the previous experimental data, unlike those results obtained from the steady SST-k-ω RANS turbulence model which shows a much greater deviation with the experimental data sets. The anomaly of the results obtained from the current steady state RANS solution is due to the different formulation of the turbulence model constants implemented in commercial CFD codes (FLUENT, STAR-CCM+ and CFX) that are calibrated in different environments to work fairly well for wide range of flows, that may or may not include flows of decaying isotropic homogeneous turbulence.
- A new-correlation equation based on the local turbulent parameters (u' and L_u) have been developed to quantify the spatial decay turbulence for a uniform approach flow at the inlet. The results from the current study have been validated with the earlier relevant experimental studies based on the new formulated correlation equation, that highlights the applicability of the correlation equation to turbulent flows generated downstream from a conventional square grid.
- Based on the same numerical LES model, a set of three-correlation equations have been devised that can be used as a prediction tool for decay, to guide one to estimate the local values of turbulent kinetic energy (k) and length scale (L_u) from the initial values and, similarly, the estimation of the initial values from the local values of those turbulent parameters.
- A near-constant TKE condition is identified, which approximately extends from x = 2m to x = 4m in the numerical computational domain. This near constant region can be related and extended to actual physical locations in typical wind-tunnel experiment examining flow over three-dimensional bluff-bodies (such as cylinders or prisms) to quantify wind and thermal effects.
- The steady RANS models are revisited once again, in order to figure out its limitations in modelling the decay of homogenous isotropic turbulence. Thereafter, the steady RANS model has been implemented in three-different commercial codes (FLUENT, STAR-CCM+ and CFX) to highlight the differences in modelling of the specific dissipation rate (ω) in each of those softwares. Post-evaluation, it was found that the source of discrepancy between

the results from the experiments and the RANS model from the different software codes is due to the default value of the model constant (β_∞^*) raised to different power, that inherently controls the dissipation of turbulent kinetic energy (TKE) and the production of the specific dissipation rate (ω). Thereafter, fine-tuning of the model constant (β_∞^*) in each of three softwares was done with an optimized value of 0.046 that makes the results from three commercial CFD codes match with each other and also with the experimental/LES results on the spatial decay of turbulent kinetic energy.

- The new improved model constant when coupled with the SST-k-ω low Reynolds number correction model predicts the development of the laminar boundary layer over a flat plate in a correct manner. Similarly, the same model constant when integrated with the transitional k-kl-ω model demonstrates its ability to predict the laminar to turbulent boundary layer transition precisely along with the turbulent boundary layer development. In short, the improved version of the model constant reproduces results with reasonable degree of accuracy for spatially developing laminar and turbulent boundary layer flows.

4.2 Contributions

The original contributions of the present study to the scientific knowledge is provided below:

- A simple yet powerful prediction tool has been devised in the current study that can be used to estimate the local or initial turbulent parameters (i.e. TKE and L_u), downstream or at the inlet, in a typical wind-tunnel experimental facility, that would help one to estimate values of L_u which would be relevant for any bluff-body study. In addition, using the same prediction tool, one can also compute the values of TKE that would be generated by a conventional square-grid which will decay sufficiently at bluff-body leading edge, so that the freestream TKE would then be fairly-constant along the bluff-body surface. The maximum value that can be achieved for such a constant value can also be determined from the same prediction equations.

- An improved RANS SST-k-ω model with an optimized model constant value has been proposed, that can guide an appropriate numerical RANS approach to simulate freely decaying isotropic homogeneous freestream turbulence.

4.3 Recommendations

Based on the analysis of results and understanding from the present study, the following recommendations for future work can be made:

- In this study, the focus was entirely based on performing numerical simulations in order to investigate the freestream decay of turbulence in the streamwise direction. A lot of data on the earlier experimental grid-generated turbulence is available, but none of the earlier studies provides a universal single correlation equation having TKE and integral length scale embedded into that equation in near perfect isotropic homogeneous conditions. Most studies also don't comment on the spatial growth of integral length scales along the streamwise distance. So, it would be useful to carry out some experiments on grid-generated turbulence. Both passive and active grids of different dimensions should be used to generate turbulence and then characterize its spatial decay, each with different initial conditions (i.e. different mean free-stream velocities, initial integral length scales and turbulence intensities), since the effect of these parameters have not yet fully investigated in the past. This work could potentially bridge the gap on the discrepancies observed in the earlier results on the decay rate of multi-scale grid generated turbulent flows.

- Direct numerical simulations (DNS) can be carried out using the available commercial CFD codes (FLUENT, Star-CCM+, CFX) to assess their capability in reproducing grid-generated turbulence. In addition, the DNS computations can also provide detail data of turbulence statistics that will be free from any experimental uncertainties and, thereby, help one understand the basics of turbulent dynamics governed by the inviscid large scales and viscous small scales.

REFERENCES

Aboshosha, H., Elshaer, A., Bitsuamlak, G. T. and El Damatty, A. (2015) 'Consistent inflow turbulence generator for LES evaluation of wind-induced responses for tall buildings', *Journal of Wind Engineering and Industrial Aerodynamics*. Elsevier, 142, pp. 198–216.

Dryden, H. L. (1943) 'A review of the statistical theory of turbulence', *Quarterly of Applied Mathematics*, 1(1), pp. 7–42.

Appendix A

Solution method of the linear dependency of (k/k_0) with $(x-x_0)*(k'_0)^{0.5}/L_u$

The linear dependency of (k/k_0) with the non-dimensional variable $(x-x_0)*(k')^{0.5}/L_u$ is represented by the equation (2.57) (refer to chapter 2) and re-written once again to remind the reader

$$\frac{\frac{d}{dx}(k/k_0)}{\frac{d}{dx}(x-x_0)*(k')^{0.5}/L_u} \approx \text{constant} \qquad (A.1)$$

where k and k_0 are the local and initial value of the turbulent kinetic energy, k' is the local dimensionless turbulent kinetic energy, x (m) is the streamwise distance, x_0 is the virtual origin, and L_u represents the integral length scale (m).

In the upcoming section, the left-hand hand side of the equation (A.1) will be solved to prove the linearity of the relation observed in figure (2.34) (refer to chapter 2) and that there exits a linear functional relationship between the variables (k/k_0) and $(x-x_0)*(k')^{0.5}/L_u$. The expression $(x-x_0)$ will be denoted by x from now on for simplicity.

It has already been established in section (2.9.1) that (k/k_0) and (L_u/L_{u0}) evolves according to the power-laws in the streamwise direction hence their dependency can be written as equations in the form of

$$\frac{k'}{k'_0} = \frac{k}{k_0} = (a_1 x + 1)^p \qquad (A.2)$$

where a_1 is the power-law coefficient and p is the power-law exponent of the given equation (A.2). The values of a_1 and p obtained from the power-law best-fitting of the

data are a_1 = 1.15 and p = -1.06 (having 95% confidence bounds with an R^2 = 0.999), respectively.

Taking the spatial derivative of equation (A.2) yields,

$$\frac{d(k/k_0)}{dx} = pa_1(a_1x+1)^{p-1} \tag{A.3}$$

Similarly, (L_u/L_{u0}) varies with the streamwise distance x(m) in the form of

$$\frac{L_u}{L_{u0}} = (a_2x+1)^q \tag{A.4}$$

Where a_2 is the power-law coefficient and q is the power-law exponent of the given equation (A.4). The magnitudes of a_2 and q obtained from the power-law best-fitting curve are given by a_2 = 1.14 and q = 0.46 (having 95% confidence bounds with an R^2 = 0.999), respectively.

Now, substituting $k' = k_0'(a_1x+1)^p$ and $L_u = L_{u0}(a_2x+1)^q$ into the expression of the variable, $(x-x_0)*(k')^{0.5}/L_u$, gives

$$\frac{x.(k_0')^{0.5}.(a_1x+1)^{\frac{p}{2}}}{L_{u0}(a_2x+1)^q} \tag{A.5}$$

Taking the spatial derivative of the equation (A.5) yields

$$\frac{d}{dx}\left(\frac{x.(k_0')^{0.5}.(a_1x+1)^{\frac{p}{2}}}{L_{u0}(a_2x+1)^q}\right) = \frac{(k_0')^{0.5}}{L_{u0}}\left\{\frac{d}{dx}\left(\frac{x.(a_1x+1)^{\frac{p}{2}}}{(a_2x+1)^q}\right)\right\} \tag{A.6}$$

Approximating, $a_1 \approx a_2$, since, a_1 = 1.15 and a_2 = 1.14, both obtained from the best-fit curve of the power law, the right-hand side of the equation (A.6) can be written as

$$\frac{(k_0^{'})^{0.5}}{L_{u0}}\frac{d}{dx}\{x.(a_1x+1)^{\frac{p}{2}-q}\} \tag{A.7}$$

or, $$\frac{(k_0^{'})^{0.5}}{L_{u0}}(a_1x+1)^{p-1}.(a_1x+1)^{-\frac{p}{2}-q+1}.\{1+a_1.(\frac{p}{2}-q).x.(a_1x+1)^{-1}\} \tag{A.8}$$

Now, substituting $\frac{d(k/k_0)}{dx} = pa_1(a_1x+1)^{p-1}$ and,

$$\frac{d}{dx}(x-x_0)*(k_0^{'})^{0.5}/L_u =$$

$$\frac{(k_0^{'})^{0.5}}{L_{u0}}(a_1x+1)^{p-1}.(a_1x+1)^{-\frac{p}{2}-q+1}.\{1+a_1.(\frac{p}{2}-q).x.(a_1x+1)^{-1}\}$$

in equation (A.1) and thereby simplifying (A.1) gives

$$\frac{\frac{d}{dx}(k/k_0)}{\frac{d}{dx}(x-x_0)*(k')^{0.5}/L_u} = \frac{p.a_1.L_{u0}}{(k_0^{'})^{0.5}.(a_1x+1)^{-\frac{p}{2}-q+1}.\{1+a_1.(\frac{p}{2}-q).x.(a_1x+1)^{-1}\}} \tag{A.9}$$

Approximating, p ≈ -1 and q ≈ 0.5, since p = -1.06 and q = 0.46 are both obtained from the best-fit curve power law, the right-side of the equation (A.9) can be written after simplification as

$$\frac{\frac{d}{dx}(k/k_0)}{\frac{d}{dx}(x-x_0)*(k')^{0.5}/L_u} = \frac{pa_1L_{u0}}{(k_0^{'})^{0.5}} = \text{constant} \tag{A.10}$$

since, p, a_1 denotes the coefficient and exponent of the power-law equation given in (A.2) (which are constants), L_{u0} is the initial value of the integral length scale specified at the inlet (is a constant), and $(k_0^{'})$ is the initial non-dimensional value of the turbulent kinetic energy specified (and also is a constant).

Hence, it is proved that the variable $(\frac{k}{k_0})$ holds a linear relationship with $(x - x_0) * (k')^{0.5} / L_u$ and curve represented in figure (3.4) is linear in nature.

Appendix B

Sample calculations to estimate the initial turbulent scales (k'_0) and L_{u0}) based on the local TKE (k) and the integral length scale (L_u)

The set of three correlation-equations (equations 2.49, 2.50 and 2.60) presented in Chapter 2 are re-written here once again to remind the reader

$$\log(k') = \log(k_0') - n_1 \log(\frac{A_1 (k_0')^{0.5} (x - x_0)}{L_u} + 1) \tag{B.1}$$

$$\log(k') = \log(k_0') - n_2 \log(\frac{A_2 (k_0')^{0.5} (x - x_0)}{L_{u0}} + 1) \tag{B.2}$$

$$\frac{k}{k_0} = \frac{k'}{k_0'} = m(\frac{(x - x_0) * (k')^{0.5}}{L_u}) + C \tag{B.3}$$

The value of the decay coefficients (A_1 and A_2), decay exponents (n_1 and n_2) and the corresponding R^2 coefficients of the best-fit curve for the equations (B.1), (B.2) and (B.3) are summarized in table (B.1) and (B.2) for completeness

Table B.1 Constants obtained from best regression curve fitting procedure to equations B.1 and B.2 using the method of Non-linear least squares

Normalization parameter of the x ordinate	Decay exponent (n)	Decay coefficient (A)	R^2
k_0' and L_u	2.38	0.27	0.992
k_0' and L_{u0}	1.16	0.44	0.971

Table B.2 Constants obtained from best regression curve fitting procedure to equation B.3 using the method of Non-linear least squares

Normalization parameter of the x ordinate	m (slope)	C (intercept on the y ordinate)	R^2
k' and L_u	-0.51	1	0.953

Krogstad & Davidson (2010)

The applicability of the prediction correlation equations have been extended to previous experimental study of (Krogstad and Davidon, 2011) to estimate the initial values of the turbulent parameters at the grid inlet section with known local magnitudes of TKE and L_u at x = 2.02m (local values are extracted from (Krogstad and Davidon, 2011)).

The experimental data gives

k' = 0.00025 (approximately at $x-x_0$ = 2.02m)

L_u = 0.03m (approximately at $x-x_0$ = 2.02m)

Substituting these values in the equation (B.1) gives an equation with one unknown variable (k_0') which is

$$\log(0.00025) = \log(k_0') - 2.38\log\left(\frac{0.27\times(k_0')^{0.5}\times 2.02}{0.03}+1\right) \qquad \text{(B.4)}$$

Solving the equation (B.4) we get (k_0') =0.000594 or k = 0.108 (since $\bar{U} = 13.5\text{m/s}$)

Now substituting the value of (k_0') = 0.000594 in equation (B.2) gives a similar equation with one unknown variable (L_{u0}) which is

$$\log(0.00025) = \log(0.000594) - 1.16\log\left(\frac{0.44\times(0.000594)^{0.5}\times 2.02}{L_{u0}} + 1\right) \qquad (B.5)$$

Solving the equation (B.5) gives L_{u0} = 0.020m

Table (B.3) summarizes the predicted values and the actual known values of those parameters with the percentage difference between the actual and the known predicted values.

Table B.3 Comparison of the predicted and actual values of the inlet turbulent parameters (TKE and length scale) from the study of Krogstad & Davidson (2011)

Krogstad and Davidson (2011)	**Predicted**	**Actual**	**% difference in proportion to the predicted values**
Initial TKE (k'_0)	0.000594	0.000585	1.53
Initial integral length scale (L_{u0}) (m)	0.020	0.023	-15

As evident from table (B.4), the predicted value of TKE at the inlet (x-x_0 = 0m) is overestimated by 1.52% (< 2%), whereas the predicted value of integral length scale (L_u) is underestimated by 15%. Although, the predicted value of TKE show close proximity to the actual TKE value, the length scale (L_u) is underestimated by 15% which might be due to the deviation of the data from the actual fitted regression line given by R^2 = 0.971. As emphasized before, the integral length scale magnitudes are not off by several orders of magnitude and can be reliable to use it for boundary-layer wind tunnel experiments.

Sample calculations to estimate the local turbulent scales (k') and L_u) based on the initial (inlet) TKE (k'_0) and the integral length scale (L_{u0})

In this section, sample calculations have been shown to predict the local magnitudes of turbulent variables (k' and L_u) from the initial inlet turbulent scales (k'_0) and L_{u0}, in order to examine the validity of the of the correlation equations presented in equations (B.1), (B.2) and (B.3).

Krogstad & Davidson (2010)

The applicability of the prediction correlation equations have been extended to previous experimental study of (Krogstad and Davidon, 2011) to estimate the local values of the turbulent parameters TKE and L_u at x = 2.02m downstream from the inlet grid-section.

The magnitudes of TKE and integral length scales at $x\text{-}x_0$ = 0m are

$$k'_0 = 0.000585 \text{ (at } x\text{-}x_0 = 0\text{m)}$$

$$L_{u0} = 0.023\text{m (at } x\text{-}x_0 = 0\text{m)}$$

Substituting these values in equation (B.2), gives an equation with one-unknown variable (k') as

$$\log(k') = \log(0.000585) - 1.16\log\left(\frac{0.44\times(0.000585)^{0.5}\times 2.02}{0.023}+1\right) \qquad \text{(B.6)}$$

Solving, equation (B.6) gives (k') = 0.00027

Now substituting the value of (k') in equation (B.1) gives one equation with only one unknown variable (L_u) as

$$\log(0.00027) = \log(0.000585) - 2.38\log\left(\frac{0.27\times(0.000585)^{0.5}\times 2.02}{L_u}+1\right) \qquad \text{(B.7)}$$

Solving equation (B.7) gives $L_u = 0.034$m

Table (B.4) summarizes the predicted values and the actual known values of those parameters with the percentage difference between the actual and the known predicted values.

Table B.4 Comparison of the predicted and actual values of the inlet turbulent parameters (TKE and length scale) from the LES study

Krogstad & Davidson (2010)	**Predicted**	**Actual**	**% difference in proportion to the predicted values**
Local TKE (k′)	0.00027	0.00025	7.40
Local integral length scale (L_u) (m)	0.034	0.030	11.76

The deviation of the predicted levels of turbulence is not very high in magnitude (< 15%) and be used successfully used to estimate the local TKE and L_u from the initial magnitudes of TKE and L_u.

Identification of near constant TKE conditions (LES study)

Sample calculations have been shown to estimate the turbulent parameters downstream at x-x0 = 2m, x-x0 = 3m and x-x0 = 4m, to identify the near constant TKE conditions.

In order to know the unknown local turbulent variables (TKE and L_u) at $x-x_0 = 2$m, one needs to know the initial magnitudes of TKE and integral length scales at $x-x_0 = 0$m. The values obtained from the present LES study is

$$k_0^{'} = 0.0134 \text{ (at } x-x_0 = 0\text{m)}$$

$$L_{u0} = 0.107\text{m (at } x-x_0 = 0\text{m)}$$

Substituting these values in equation (B.2), gives an equation with one-unknown variable (k′) as

$$\log(k') = \log(0.0134) - 1.16\log\left(\frac{0.44\times(0.0134)^{0.5}\times 2}{0.107} + 1\right) \qquad \text{(B.8)}$$

Solving, equation (B.8) gives (k′) = 0.0062; k = 0.0992 (m^2/s^2) (since $\bar{U} = 4m/s$)

Now substituting the value of (k′) in equation (B.1) gives one equation with only one unknown variable (L_u) as

$$\log(0.0062) = \log(0.0134) - 2.38\log\left(\frac{0.27\times(0.0134)^{0.5}\times 2}{L_u} + 1\right) \qquad \text{(B.9)}$$

Solving equation (B.9) gives L_u = 0.17m

Similarly, using the above methodology, the values of TKE and L_u obtained at x-x_0 = 3m are

k′ = 0.0048; k = 0.0768 (m^2/s^2) (since $\bar{U} = 4m/s$)

L_u = 0.18m

Similarly, the values of TKE and L_u obtained, at x-x_0 = 4m are

k′ = 0.0040; k = 0.064 (m^2/s^2) (since $\bar{U} = 4m/s$)

L_u = 0.19m

It is clearly noticed from the values estimated at x-x0 = 2m, x-x0 = 3m and x-x0 = 4m that the turbulence levels reach near constant TKE conditions over this region extending from x = 2m to x = 4m, and the prediction correlation equations can be successfully applied to identify those regions in actual wind-tunnel bluff-body experiments.

Table B.5 summarizes the values of the TKE and length scales obtained at x-x0 = 2m, x-x0 = 3m and x-x0 = 4m

Table B.5 Summary of the local TKE and integral length scale magnitudes estimated from the prediction correlation equation (LES study)

Streamwise locations (m)	Local TKE (k) (m^2/s^2)	Local integral length scale (L_u) (m)
x-x0 =2	0.099	0.17
x-x0 =3	0.077	0.18
x-x0 =4	0.064	0.19

REFERENCES

Krogstad, P. A. and Davidon, P. A. (2011) 'Freely decaying, homogeneous turbulence generated by multi-scale grids', *Journal of Fluid Mechanics*, 680, pp. 417–434.

Appendix C

Comparisons between three different commercial codes against the spatial decay of isotropic homogeneous turbulence

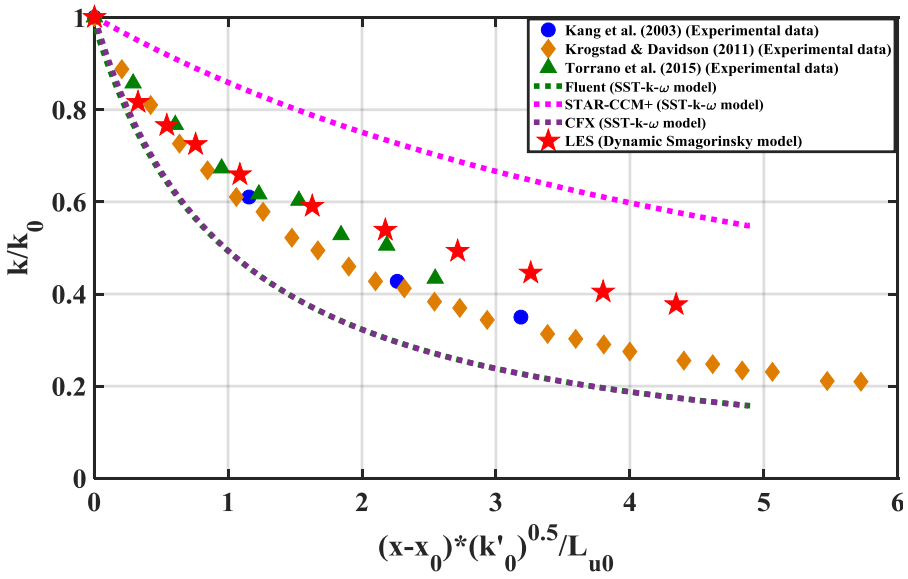

Figure C.1 Spatial decay of TKE profiles obtained from three different commercial codes (FLUENT, STAR-CCM+ and CFX) compared with the present LES study and previous experimental results, scaled with initial integral length scale (L_{u0}) ($\bar{U}$ =4m/s, TI =10%, L_{u0} = 0.10m)

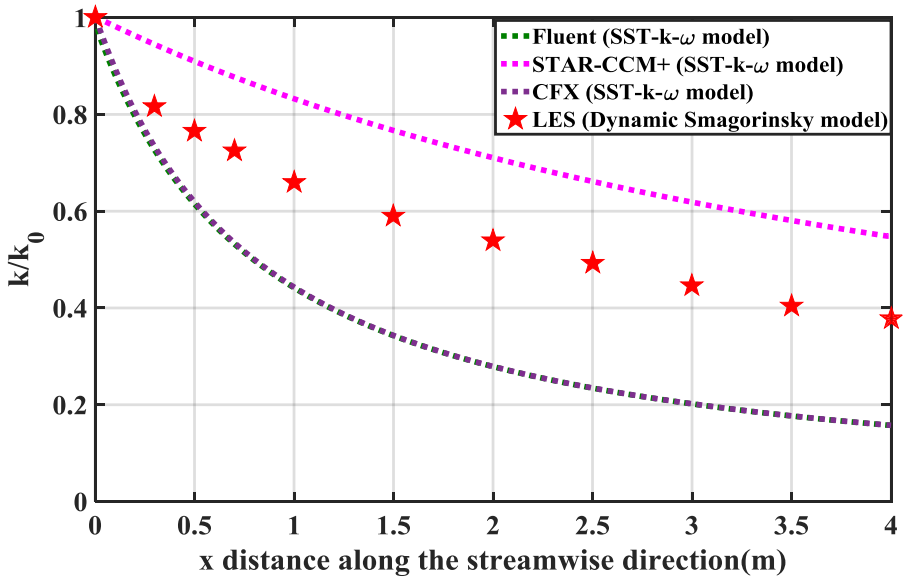

Figure C.2 Spatial decay of TKE profiles obtained from three different commercial codes (FLUENT, STAR-CCM+ and CFX) compared with the present LES study along the streamwise distance x ($\bar{U}$ =4m/s, TI =10%, L_{u0} = 0.10m)

New optimised SST-k-ω models for STAR-CCM+

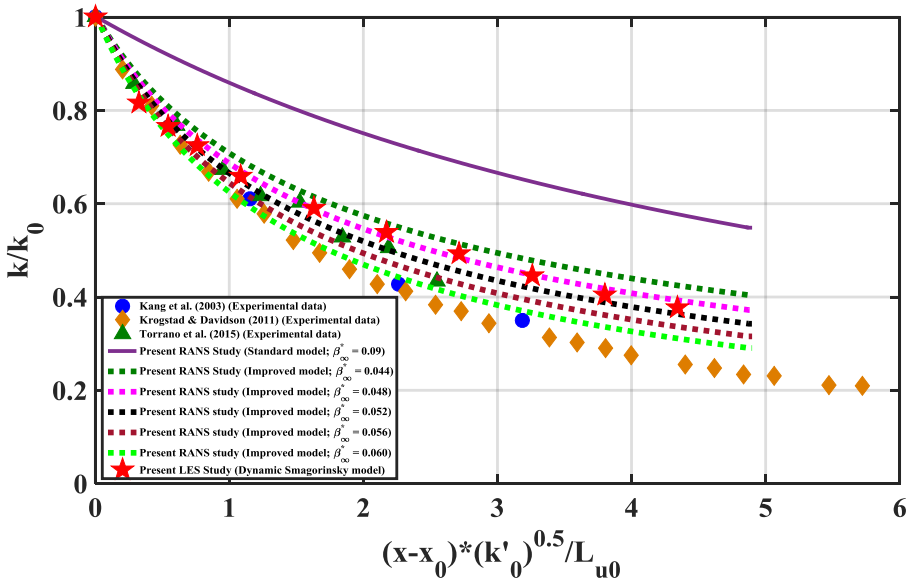

Figure C.3 Spatial decay of TKE profiles of the different optimized SST-k-ω RANS model compared with the present LES study and the earlier experimental studies, scaled with the initial integral length scale (L_{u0}) ($\bar{U}$ =4m/s, TI =10%, L_{u0} = 0.10m) (STAR-CCM+ simulations)

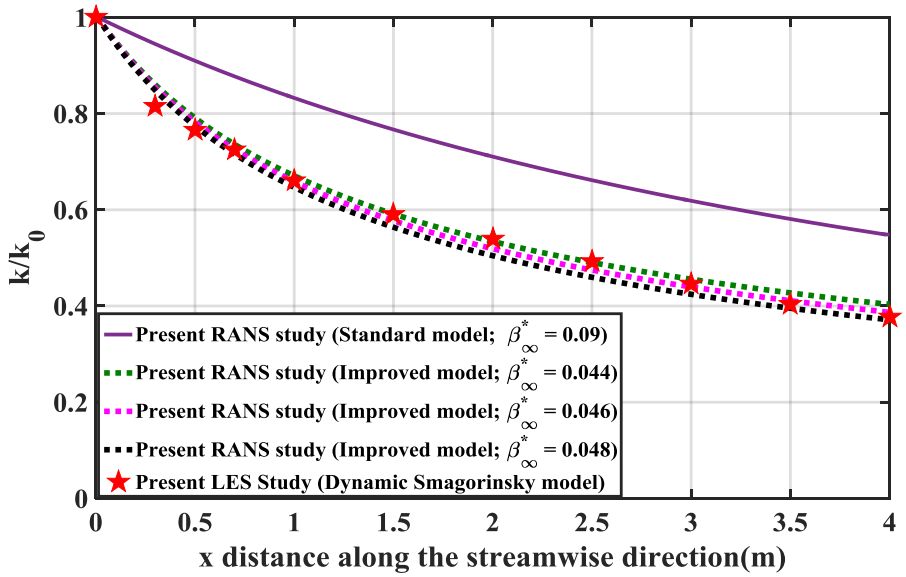

Figure C.4 Spatial decay of TKE profiles of the different optimized SST-k-ω RANS model compared with the present LES study along the streamwise distance x ($\bar{U}$ =4m/s, TI =10%, L_{u0} = 0.10m) (STAR-CCM+ simulations)

New optimised SST-k-ω models for CFX

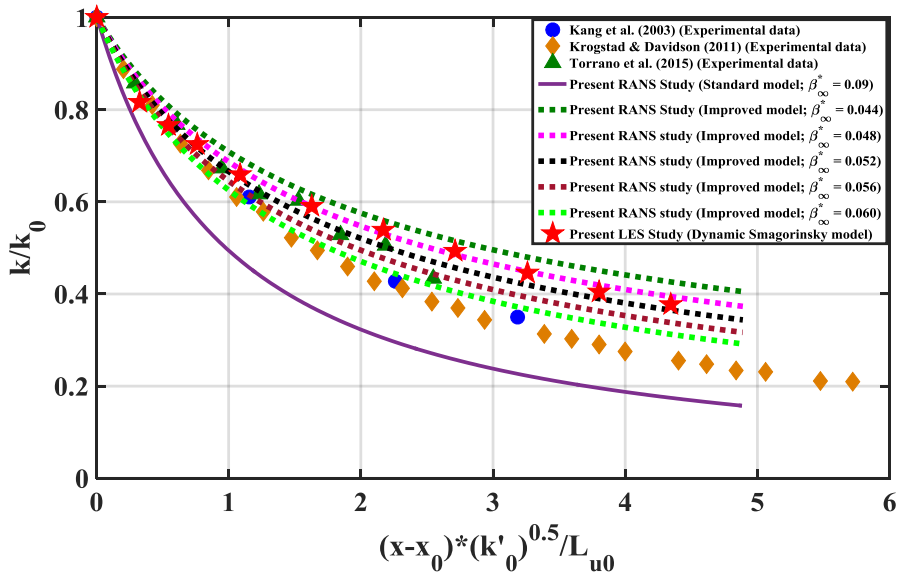

Figure C.5 Spatial decay of TKE profiles of the different optimized SST-k-ω RANS model compared with the present LES study and the earlier experimental studies, scaled with the initial integral length scale (L_{u0}) ($\bar{U}$ =4m/s, TI =10%, L_{u0} = 0.10m) (CFX simulations)

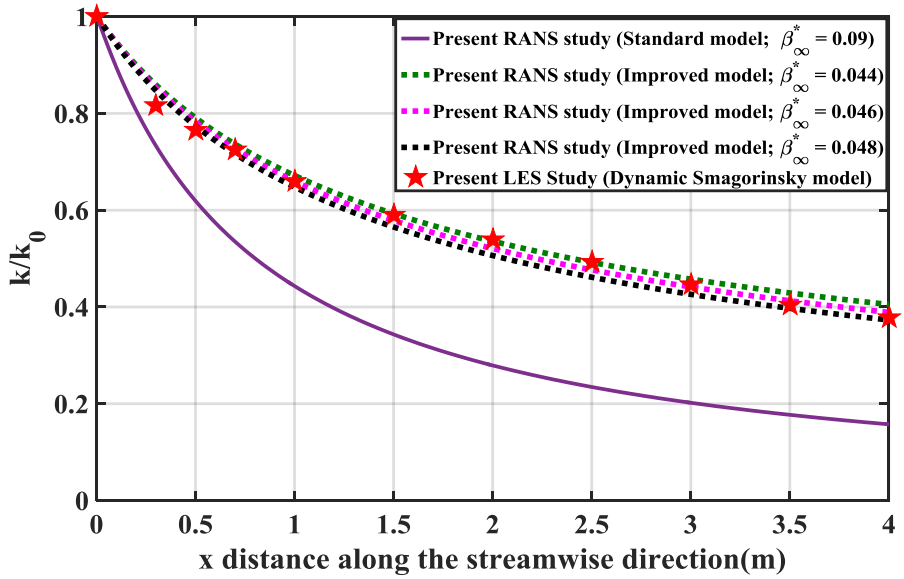

Figure C.6 Spatial decay of TKE profiles of the different optimized SST-k-ω RANS model compared with the present LES study along the streamwise distance x ($\bar{U}$ =4m/s, TI =10%, L_{u0} = 0.10m) (CFX simulations)

Applicability of the improved SST-k-ω model in predicting the turbulence decay for varying turbulence intensities at the inlet

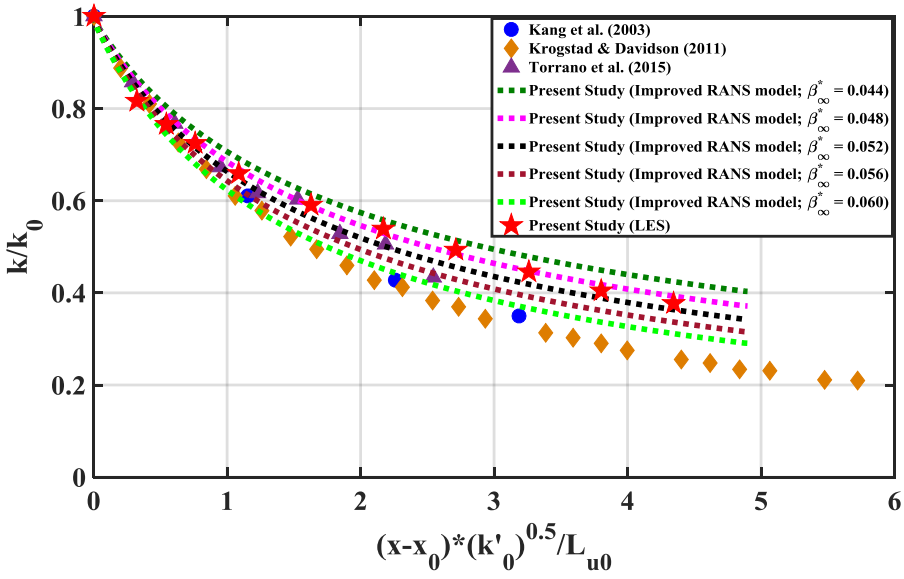

Figure C.7 Spatial decay of TKE profiles of the different optimized SST-k-ω RANS model compared with the present LES study and the earlier experimental studies, scaled with the initial integral length scale (L_{u0}) ($\bar{U}$ =4m/s, TI =10%, L_{u0} = 0.10m) (FLUENT simulations)

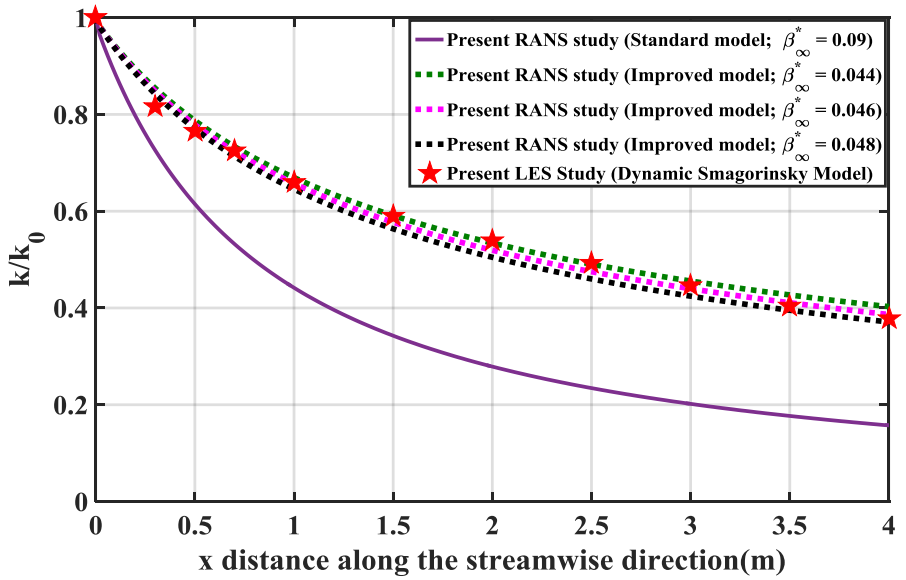

Figure C.8 Spatial decay of TKE profiles of the different optimized SST-k-ω RANS model compared with the present LES study and the earlier experimental studies, plotted against the streamwise distance x ($\bar{U}$ =4m/s, TI =10%, L_{u0} = 0.10m) (FLUENT simulations)

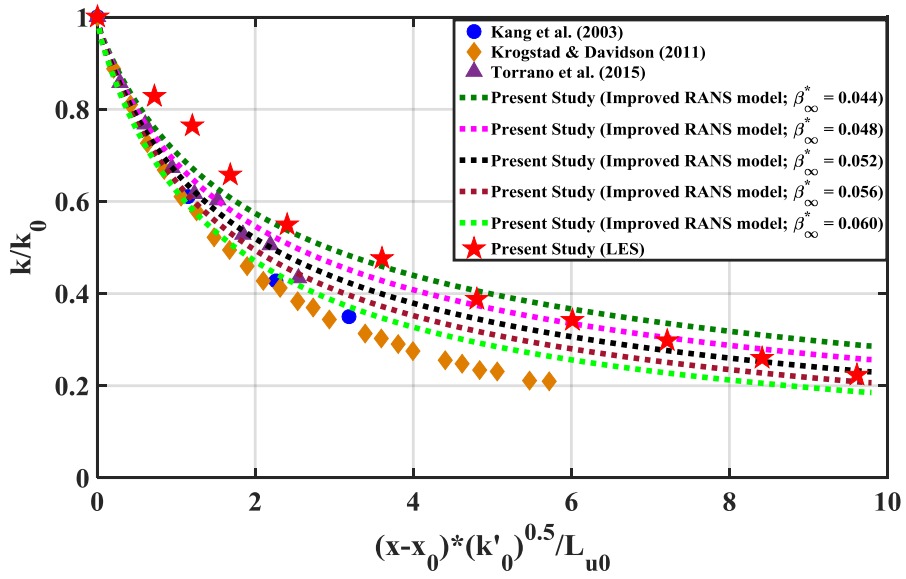

Figure C.9 Spatial decay of TKE profiles of the different optimized SST-k-ω RANS model compared with the present LES study and the earlier experimental studies, scaled with the initial integral length scale (L_{u0}) ($\bar{U}$ =4m/s, TI =20%, L_{u0} = 0.10m) (FLUENT simulations)

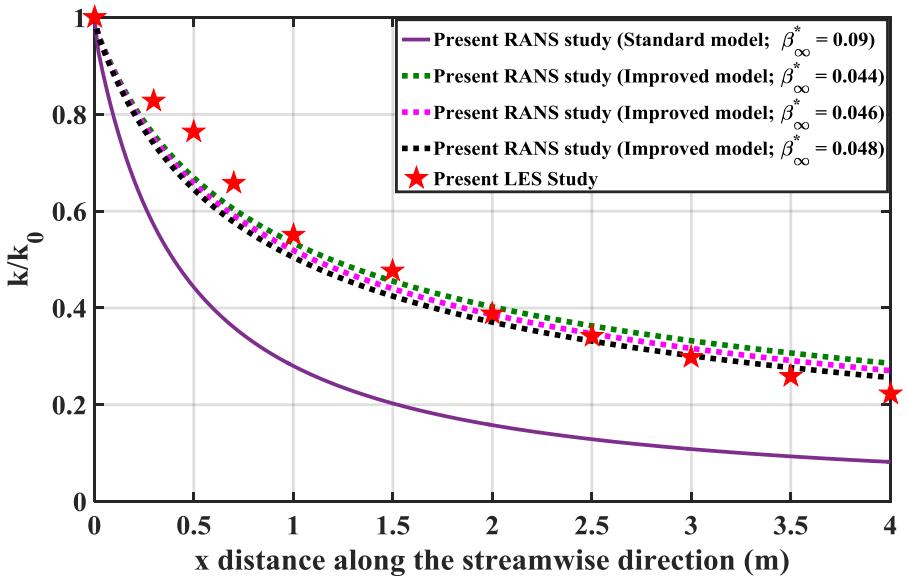

Figure C.10 Spatial decay of TKE profiles of the different optimized SST-k-ω RANS model compared with the present LES study and the earlier experimental studies, plotted against the streamwise distance x ($\bar{U}$ =4m/s, TI =20%, L_{u0} = 0.10m) (FLUENT simulations)

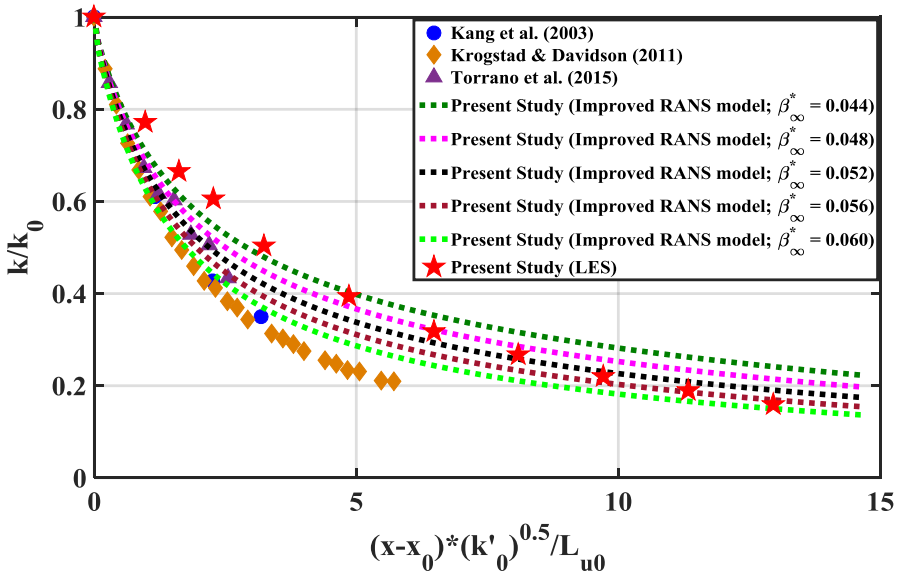

Figure C.11 Spatial decay of TKE profiles of the different optimized SST-k-ω RANS model compared with the present LES study and the earlier experimental studies, scaled with the initial integral length scale (L_{u0}) ($\bar{U}$ =4m/s, TI =30%, L_{u0} = 0.1m) (FLUENT simulations)

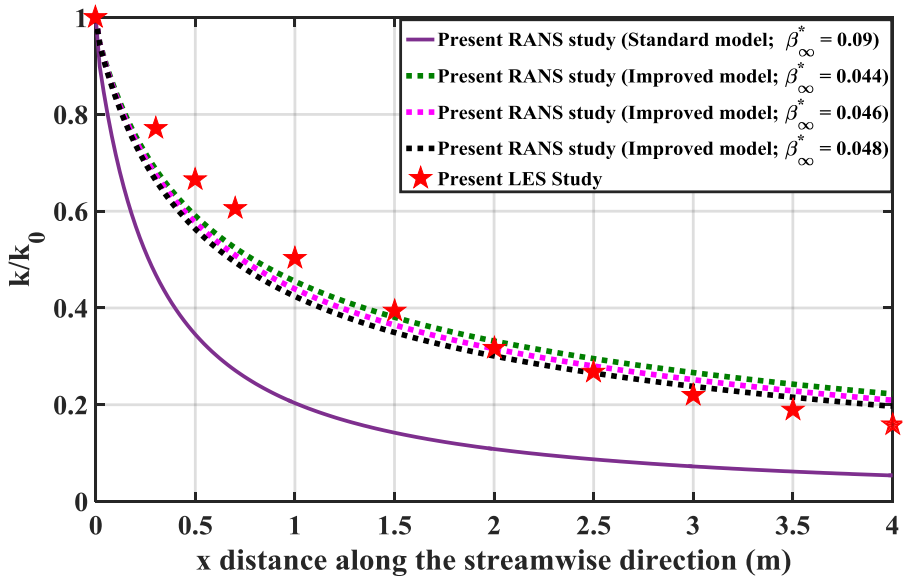

Figure C.12 Spatial decay of TKE profiles of the different optimized SST-k-ω RANS model compared with the present LES study and the earlier experimental studies, plotted against the streamwise distance x ($\bar{U}$ =4m/s, TI =30%, L_{u0} = 0.10m) (FLUENT simulations)

Applicability of the improved SST-k-ω model in predicting the turbulence decay for varying integral length scales at the inlet

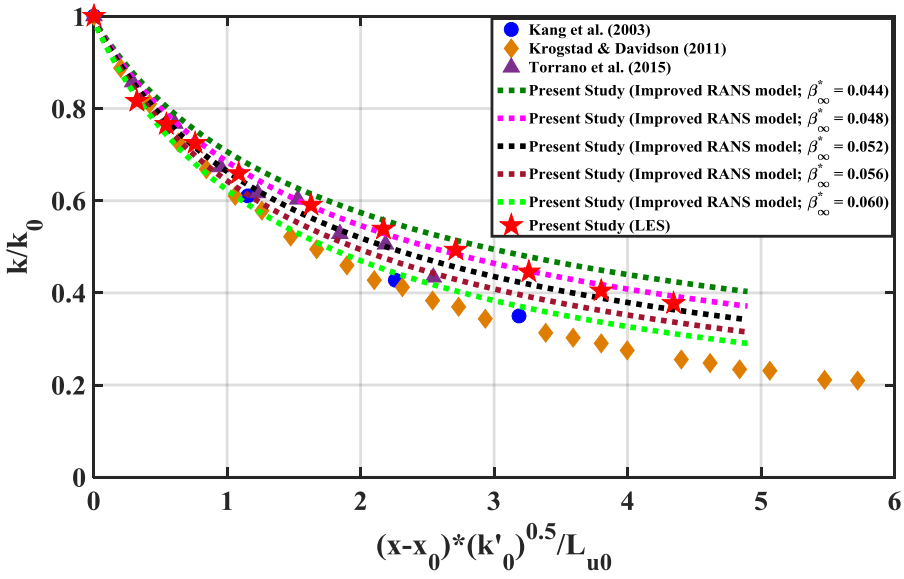

Figure C.13 Spatial decay of TKE profiles of the different optimized SST-k-ω RANS model compared with the present LES study and the earlier experimental studies, scaled with the initial integral length scale (L_{u0}) ($\bar{U}$ =4m/s, TI =10%, L_{u0} = 0.10m) (FLUENT simulations)

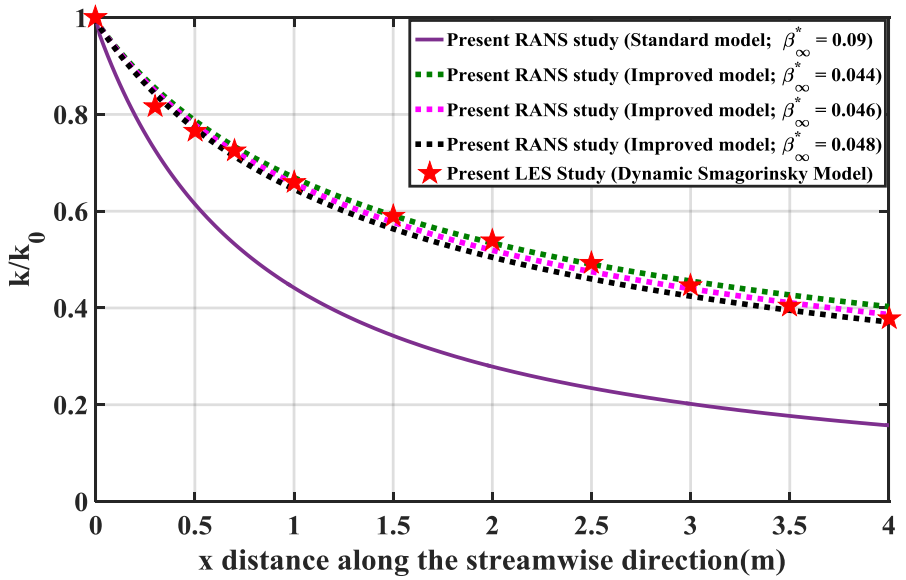

Figure C.14 Spatial decay of TKE profiles of the different optimized SST-k-ω RANS model compared with the present LES study and the earlier experimental studies, plotted against the streamwise distance x ($\bar{U}$ =4m/s, TI =10%, L_{u0} = 0.10m) (FLUENT simulations)

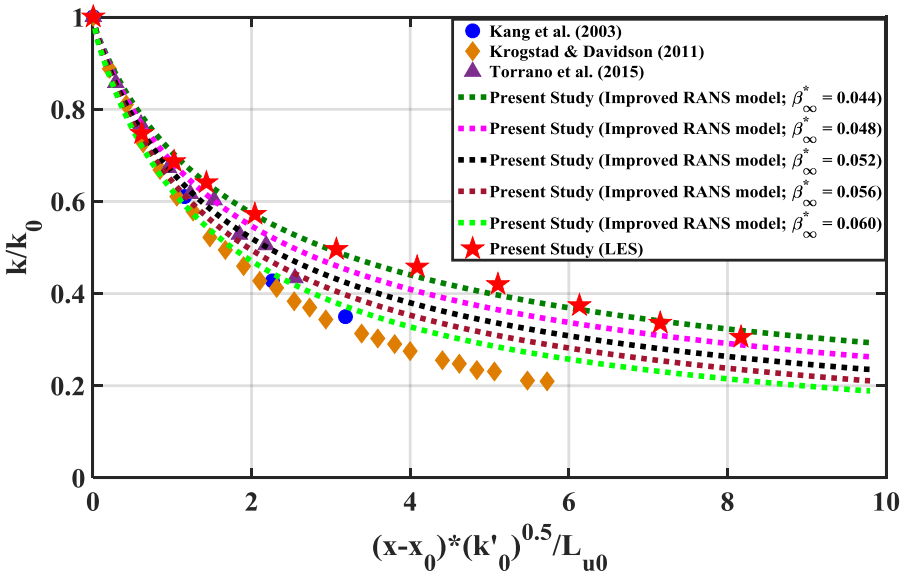

Figure C.15 Spatial decay of TKE profiles of the different optimized SST-k-ω RANS model compared with the present LES study and the earlier experimental studies, scaled with the initial integral length scale (L_{u0}) ($\bar{U}$ =4m/s, TI =10%, L_{u0} = 0.05m) (FLUENT simulations)

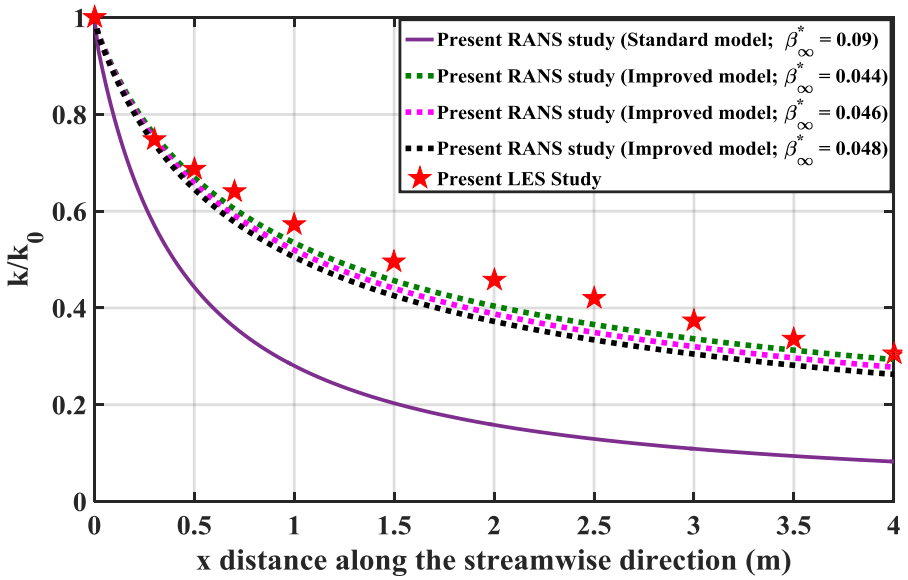

Figure C.16 Spatial decay of TKE profiles of the different optimized SST-k-ω RANS model compared with the present LES study and the earlier experimental studies, scaled with the initial integral length scale (L_{u0}) ($\bar{U}$ =4m/s, TI =10%, L_{u0} = 0.05m) (FLUENT simulations)

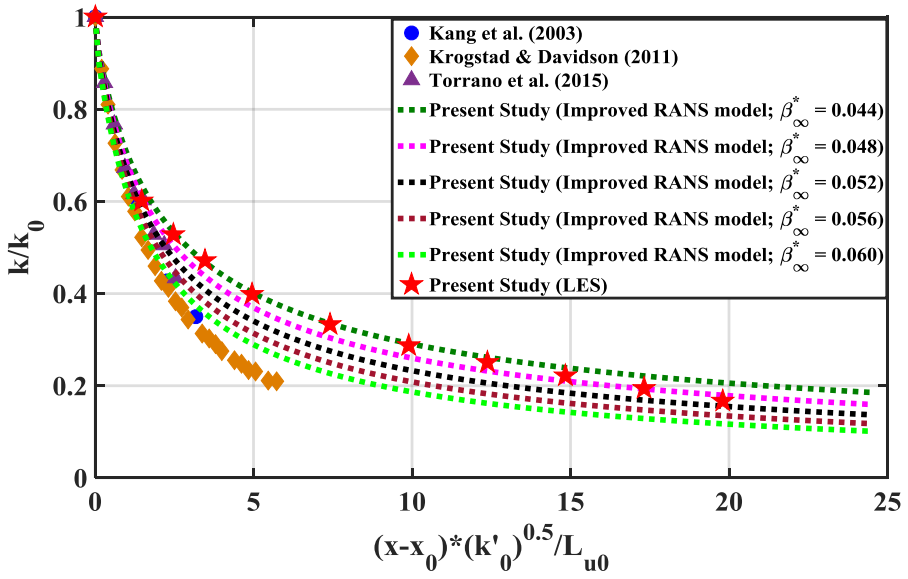

Figure C.17 Spatial decay of TKE profiles of the different optimized SST-k-ω RANS model compared with the present LES study and the earlier experimental studies, scaled with the initial integral length scale (L_{u0}) ($\bar{U}$ =4m/s, TI =10%, L_{u0} = 0.02m) (FLUENT simulations)

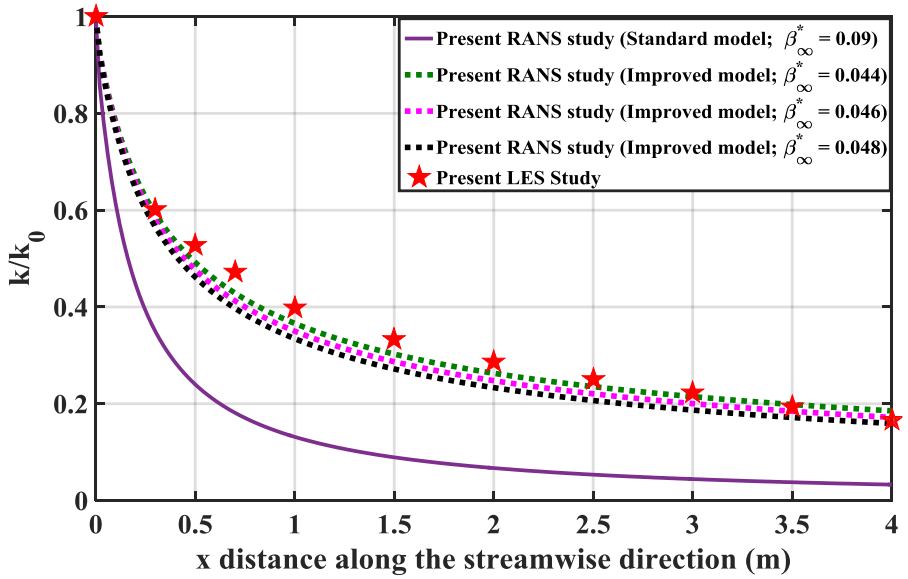

Figure C.18 Spatial decay of TKE profiles of the different optimized SST-k-ω RANS model compared with the present LES study and the earlier experimental studies, scaled with the initial integral length scale (L_{u0}) ($\bar{U}$ =4m/s, TI =10%, L_{u0} = 0.02m) (FLUENT simulations)

Appendix D

Near-wall treatment of boundary layers

The structure of wall bounded turbulent flows depends on how well the flow parameters on the layers near to the wall are resolved where the shearing of the eddies plays an important role in organizing the dissipation and momentum transfer. The free-stream parameters are no longer dominant, and the viscous effects are in action. Hence, in the immediate vicinity of the wall there is an extremely thin viscous sub-layer followed by the buffer layer and the logarithmic sub-layer. The number of mesh points required to resolve the details in a turbulent boundary layer is tremendously high and so wall functions are employed instead. There are two approaches available for modelling the near wall region. In the first approach a semi-empirical "wall function" (WF) is used where the viscosity-affected inner region is not resolved. In the other approach, known as the Low Reynolds Number modeling approach (LRNM), the viscosity-affected region is resolved through to the wall including the viscous sub-layer. LRNM requires high density grid resolutions near to the wall and is computationally expensive. A schematic representation of the two approaches is shown in fig (D.1). More details can be found out in (Versteeg and Malalasekera, 2007)

A non-dimensional wall distance y^+ for wall-bounded flow was used to characterize the grid resolution near the wall, where

$$y^+ \equiv \frac{\rho u_* y}{\mu} \tag{D.1}$$

where, ρ is the density of the fluid (air), u_* is the friction velocity, y is the distance of the nearest node in the normal direction from the wall and μ is the dynamic viscosity of the fluid (air). y^+ is often referred to as *yplus* and is commonly used in boundary layer theory in defining the law of the wall.

The main drawback of the wall functions (except the scalable wall function) is that the numerical results deteriorate considerably near to the wall when refined substantially in

the normal direction. y^+ values of less than 15 will gradually result in unbounded errors in wall shear stress and wall heat transfer. High quality numerical results will be obtained only if the overall resolution of the boundary layer is sufficient. The minimum number of cells required to cover the boundary layer accurately is 10 but a slightly higher value of 20 is mostly desirable (ANSYS, 2013). However, it is to be noted that an improvement in the boundary layer resolution of the flow variables can be obtained with a limited increase in the computational cost.

LRNM was used in the present work, which resolves the boundary layers through the viscous boundary layer, as suggested by (Blocken *et al.*, 2009). An appropriate LRNM grid should have a y^+ value of less than 5. The y^+ value also depends on the type of turbulence models used in any numerical solution. For models which can resolve the flow up to the wall, a mesh having $y^+ \leq 1$ is more accurate in thermal predictions occurring inside the viscous sub-layer. Hence, in all the simulations performed in the current study, a $y^+ \leq 1$ has been maintained which satisfies the requirements of the Low Reynolds number modelling. A growth factor of 1.2 was used to generate the viscous sub-layer, this being the maximum value recommended by COST (Franke *et al.*, 2007) guidelines. The generated grid covers more than 20 cells inside the boundary layer for better resolution of the flow field.

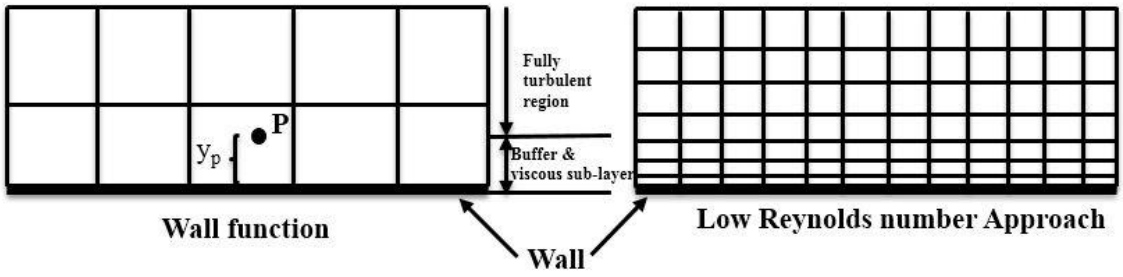

Figure D.1 A schematic representation of the wall approach method vs the LRNM grid approach

REFERENCES

ANSYS (2013) *ANSYS Fluent Theory Guide*. pp. 1-732.

Blocken, B., Defraeye, T., Derome, D. and Carmeliet, J. (2009) 'High-resolution CFD simulations for forced convective heat transfer coefficients at the facade of a low-rise building', *Building and Environment*. Elsevier Ltd, 44(12), pp. 2396–2412.

Franke, J., Hellsten, A., Schlünzen, H. and Carissimo, B. (2007) *Best practice guideline for the CFD simulation of flows in the urban environment, COST action 732; Quality Assurance and Improvement of Microscale Meteorological Models*. Hamburg, Germany.

Versteeg, H. K. and Malalasekera, W. (2007) *An Introduction to Computational Fluid Dynamics - The Finite Volume Method, Pearson Education*. pp. 1- 267.

Appendix E

Low Reynolds Number modelling approach

In wall bounded turbulent flows, the presence of solid walls is experimentally observed to have strong damping effect on the transport of turbulence characteristics. In numerical calculation of any turbulent flow, the velocity components and the turbulence energy will be set to zero to satisfy the *No-Slip* condition at the solid walls. The SST k-ω model may generate ambiguous results near the solid walls, achieving singular values of the turbulence dissipation parameters such as ε or ω which is not realistic in nature. Across a turbulent boundary layer, the flow undergoes a transition from fully turbulent to completely laminar within the thin viscosity dominated sub-layer adjacent to the solid surface. In this laminar and transitional layer, the molecular viscosity has a direct damping effect on the turbulence. This phenomenon is known as *Low Reynolds Number Turbulence* and is determined by the local turbulence Reynolds number Re_t which is given by $\frac{\rho k^2}{\mu\varepsilon}$ where k is the turbulence kinetic energy and ε is the turbulence dissipation rate. Two significant effects of the presence of the wall are:

a) Molecular viscosity dominates in the regions near to the solid wall which diffuses vorticity and damps turbulence. This is clearly manifest in the Reynolds stress transport equations near to the walls, where the viscous diffusion terms which are usually negligible compared to the other terms in the equation becomes one of the largest to be balanced by the other terms (Biswas, 2003).

b) There is a significant reduction of the velocity fluctuations normal to the solid wall by the *Pressure Reflection Mechanism* which is controlled by the non-viscous effects of the flow. Although this mechanism is not fully understood and is mostly found in acoustic wave damping phenomenon, the standard eddy viscosity models (k-ε or k-ω) cannot separate the second phenomenon from the usual eddy viscosity effect (Biswas, 2003).

In general, Low Reynolds number turbulence modelling can resolve the turbulence flow down to the wall (y+ <1). The damping of turbulence near to the solid surface due to molecular viscosity is simulated through some damping functions attached to the various terms of the transport equations which allows the flow model to have smooth change of the flow variable from small laminar sub-layer values to the fully turbulent values away from the wall. In CFD modelling, the coefficient α^* damps the turbulent viscosity causing the Low Reynolds number correction implemented in the SST k-ω model (ANSYS, 2013). It is given by

$$\alpha^* = \alpha_\infty^* \left(\frac{\alpha_0^* + \frac{\mathrm{Re_t}}{\mathrm{R_k}}}{1 + \frac{\mathrm{Re_t}}{\mathrm{R_k}}} \right) \tag{F.1}$$

where,

$$\mathrm{Re_t} = \frac{\rho \mathrm{k}}{\mu \omega} \tag{F.2}$$

$$\mathrm{R_k} = 6 \tag{F.3}$$

$$\alpha_0^* = \frac{\beta_\mathrm{i}}{3} \tag{F.4}$$

$$\beta_\mathrm{i} = 0.072 \tag{F.5}$$

In the high-Reynolds number form of the k-ω model, $\alpha^* = \alpha_\infty^* = 1$

REFERENCES

ANSYS (2013) *ANSYS Fluent Theory Guide*. doi: 10.1016/0140-3664(87)90311-2.

Biswas, G. (2003) 'Mathematical Model of Turbulance Flows', in *Compututional Fluid Flow and Heat Transfer*, pp. 1–46.

Appendix F

Governing equations of the k-kl-ω transitional model

The k-kl-ω model transitional model is considered to be a three-equation eddy viscosity type model which includes transport equation for turbulent kinetic energy (k), laminar kinetic energy (kl) and the inverse turbulent time-scale (ω). The model transport equations for k, kl and ω are given below

$$\frac{Dk}{Dt} = P_k + R_{BP} + R_{NAT} - \omega k - D_T + \frac{\partial}{\partial x_j}[(\nu + \frac{\alpha_T}{\sigma_k})\frac{\partial k}{\partial x_j}] \tag{F.1}$$

$$\frac{D(kl)}{Dt} = P_{kl} - R_{BP} - R_{NAT} - D_L + \frac{\partial}{\partial x_j}[\nu\frac{\partial (kl)}{\partial x_j}] \tag{F.2}$$

$$\begin{aligned}\frac{D\omega}{Dt} &= C_{\omega 1}\frac{\omega}{k}P_k + (\frac{C_{\omega R}}{f_\omega} - 1)\frac{\omega}{k}(R_{BP} + R_{NAT}) - C_{\omega 2}\omega^2 \\ &+ C_{\omega 3} f_\omega \alpha_T f^2{}_w \frac{\sqrt{k}}{d^3} + \frac{\partial}{\partial x_j}[(\nu + \frac{\alpha_T}{\sigma_\omega})\frac{\partial \omega}{\partial x_j}]\end{aligned} \tag{F.3}$$

The various terms in the model equations represent production, destruction, and transport mechanisms. In the transport equation of ω, the fully turbulent production, destruction, and gradient transport terms (first, third, and fifth terms on the right-hand side of equation (F.3) are analogous to the similar terms in the k and kl transport equations and similar to the terms that appear in the k-ω model forms discussed in chapter 2 (refer to section 2.5.4). The transition production terms (second term on the right-hand side) is intended to produce a reduction in turbulence length during the transition breakdown process. The fourth term on the right-hand side is included in order to decrease the length-scale in the outer region of the turbulent boundary layer, which is necessary to ensure correct prediction of the boundary layer wake region Walters and Cokljat (2008). All the other terms presented in the equations (F.1), (F.2) and (F.3) are not discussed here. Detailed information about all the model terms and its variants can be found in (Walters and Cokljat, 2008). Besides that, there are 27 model constants involved in this model, which

are more important to the overall model capability. The model constants are listed below for completeness

However, it should be noted that to capture the transitional and turbulent boundary layers correctly, the computational mesh must have a $y^+ \leq 1$ in order to predict the onset of transition location correctly. If the y^+ value is too large (≥ 5) the transition location moves upstream from the actual onset location. In the present numerical simulations, care has been taken to ensure that the y^+ is always a little less than 1 which accommodates more than 20 cells inside the boundary layer for accurate estimation of the turbulent flow field near to the solid plate surface.

Summary of the model constants of the three-equation Eddy-viscosity k-kl-ω model

$A_0 = 4.04$	$C_{INT} = 0.75$	$C_{\omega 1} = 0.44$
$A_s = 2.12$	$C_{TS,crit} = 1000$	$C_{\omega 2} = 0.92$
$A_\nu = 6.75$	$C_{R,NAT} = 0.02$	$C_{\omega 3} = 0.3$
$A_{BP} = 0.6$	$C_{11} = 3.4 \times 10^{-6}$	$C_{\omega R} = 1.5$
$A_{NAT} = 200$	$C_{12} = 1.0 \times 10^{-10}$	$C_\lambda = 2.495$
$A_{TS} = 200$	$C_R = 0.12$	$C_{\mu,std} = 0.09$
$C_{BP,crit} = 1.2$	$C_{\alpha,\theta} = 0.035$	$Pr_\theta = 0.85$
$C_{NC} = 0.1$	$C_{SS} = 1.5$	$\sigma_k = 1$
$C_{NAT,crit} = 1250$	$C_{\tau,1} = 4360$	$\sigma_\omega = 1.17$

REFERENCES

Walters, D. K. and Cokljat, D. (2008) ‘A Three-Equation Eddy-Viscosity Model for Reynolds-Averaged Navier–Stokes Simulations of Transitional Flow’, *Journal of Fluids Engineering*, 130(12), pp. 1–14.

Curriculum Vitae

Name: Dwaipayan Sarkar

Post-secondary Education and Degrees:

National Institute of Technology (NIT)
Durgapur, West-Bengal, India
2011-2015
Bachelor of Technology (Mechanical Engineering)

The University of Western Ontario
London, Ontario, Canada
2015- Present
Master of Engineering Science (Mechanical & Materials Engineering)

Honours and Awards:

Western Engineering Scholarship
2016-2018

Related Work Experience

Teaching Assistant
The University of Western Ontario
2016-2017

Research Assistant
The University of Western Ontario
2016-2018

Conference Proceedings:

Sarkar, D., Graat, K., Savory, E, (2017) "Effect of freestream turbulence on smooth flat plate heat transfer" *CFD Society of Canada Conference*, University of Windsor, Windsor, June 18-20, pp. 1- 11.

Publications:

Sarkar, D., Upadhyay, N., Roy, S., Rana., S.C. (2016) "Immersed Boundary simulation of flow through arterial junctions" *Sadhana, Academy Proceedings in Engineering Science*, 42(4) pp. 533-541.